Energy & Environmental Science

ROYAL SOCIETY OF CHEMISTRY

REVIEW

View Article Online
View Journal

Cite this: DOI: 10.1039/d6ee01264g

Contact interfaces in anodes with large volume strain for high-performance lithium-ion storage

Guangmao Yan,[a] Fei Wang, *[ab] Jieqian Liu,[b] He Zhou,[a] Xiong Lei,[a] Zhijun Wu,[e] Wubin Du,[e] Yixing Zhong,[a] Jing Feng,[a] Zhenhua Ge,[a] Yan Zhao,[b] Qiu He,[bc] Hongge Pan,[e] Hanyu Huo *[d] and Yan Yu *[d]

Silicon, germanium, tin, phosphorus, metal oxides, and their related compounds have emerged as promising anode materials for lithium-ion batteries owing to their high theoretical capacities. However, their practical application is severely hindered by large volume changes during lithiation and delithiation, which lead to electrode pulverization and rapid capacity fading. In addition, their intrinsically low electrical conductivity limits rate performance. To mitigate these issues, composite strategies—such as incorporating buffering matrices and conductive carbon—are widely employed, resulting in complex contact interfaces within the electrode. Nevertheless, the static and dynamic understanding of these interfaces remains insufficient. Under substantial volume strain, these contact interfaces undergo continuous evolution: point contacts may transform into surface contacts, while established interfaces may delaminate, ultimately governing electrode failure mechanisms. In this review, we systematically examine the nature and impact of contact interfaces in anodes undergoing significant volume strain. Contact interfaces are categorized into geometric types as well as physical and chemical interfaces, with particular emphasis on their *operando* evolution and coupling with solid electrolyte interphase chemistry. We critically evaluate advanced characterization techniques, including *operando* X-ray/neutron imaging and cryogenic electron microscopy, and present a comparative matrix outlining their respective capabilities. Furthermore, we bridge the gap between qualitative understanding and quantitative design principles by highlighting emerging advances in multiscale simulations as well as AI-assisted and data-driven interface engineering. Finally, we propose a roadmap linking laboratory-scale strategies to industrial scalability, offering a forward-looking framework for the rational design of next-generation Li^+ storage systems.

Received 26th February 2026,
Accepted 16th March 2026

DOI: 10.1039/d6ee01264g

rsc.li/ees

Broader context

The accelerating global demand for sustainable energy technologies highlights the urgent need for advanced electrochemical storage systems capable of supporting renewable energy integration and electrified transportation. Lithium-ion batteries (LIBs) remain the most widely adopted solution due to their high energy density and scalability; however, conventional graphite anodes, with a limited theoretical capacity of 372 mAh g^{-1}, cannot fully meet future performance requirements. High-capacity alternatives such as silicon, germanium, tin, phosphorus, and transition metal oxides offer promising energy densities but face critical challenges: large volume fluctuations during cycling that induce electrode pulverization, rapid capacity fading, and poor intrinsic conductivity. To mitigate these issues, composite strategies that incorporate buffering matrices and conductive additives have been developed, inevitably creating a complex network of contact interfaces. These interfaces not only accommodate mechanical strain but also regulate Li^+/electron transport, thereby exerting a decisive influence on electrochemical performance. Despite their importance, the functions and interactions of such interfaces remain insufficiently understood. This review provides a systematic framework for classifying and analyzing contact interfaces in high-capacity anodes, summarizing representative characterization techniques, and outlining strategies for interface engineering. By bridging the gap between interfacial structure and battery performance, it offers fresh insights for designing durable, high-energy LIBs.

[a] *Faculty of Materials Science and Engineering, Kunming University of Science and Technology, Kunming 650093, China. E-mail: echo1994wf@foxmail.com*
[b] *College of Materials Science and Engineering, Sichuan University, Chengdu 610065, China*
[c] *Institute of Nanotechnology, Karlsruhe Institute of Technology KIT, Hermann-von-Helmholtz-Platz 1, 76344 Eggenstein-Leopoldshafen, Germany*
[d] *Department of Materials Science and Engineering, University of Science and Technology of China, Hefei 230026, China. E-mail: hanyu.huo@ustc.edu.cn, yanyumse@ustc.edu.cn*
[e] *Institute of Science and Technology for New Energy, Xi'an Technological University, Xi'an 710021, China*

1. Introduction

As the energy demand continues to grow in human society, the increasing emissions of greenhouse gases from the combustion of fossil fuels have contributed to a steady rise in global temperature.[1–3] In response to this challenge, there has been a significant surge in research interest in energy storage and conversion technologies that are clean and renewable.[4,5] Among these technologies, electrochemical storage and conversion are

widely regarded as one of the most promising technologies, particularly for electric vehicle applications.[6] Hydrogen fuel cells, which directly convert the chemical energy of hydrogen and oxygen into electrical energy, offer exceptionally high energy densities and are considered one of the most viable solutions for electric vehicles.[7,8] However, despite its potential, hydrogen fuel cell technology has yet to be widely adopted in large-scale electric vehicles due to ongoing challenges in electrocatalysis and limitations in safe and efficient hydrogen storage systems.

Lead-acid, nickel–cadmium, nickel-metal hydride, and lithium-ion batteries (LIBs) are the four primary types of electrochemical energy storage devices commonly used today.[9,10] Among these, LIBs offer superior volumetric and gravimetric energy densities compared to lead-acid, nickel–cadmium, and nickel-metal hydride batteries, positioning them as the most promising energy storage solution for a wide range of applications.[11,12] A key factor contributing to the widespread adoption of LIBs is their commercial environmental compatibility. Since Sony first commercialized LIBs in the 1990s, they have been widely utilized as portable power sources in devices such as laptops, mobile phones, digital cameras, music players, and other electronic products. Looking ahead, LIBs are expected to capture a significant market share in the electric vehicle sector.[13–15]

LIBs are composed of several key components, including a polymer separator, a lithium salt electrolyte, a cathode electrode, an anode electrode, and cell shells. A typical commercial LIB features a carbon-based anode (*e.g.*, graphite), a transition metal lithium oxide cathode (*e.g.*, $LiCoO_2$ or $LiMn_2O_4$), and an organic electrolyte. During the charging process, Li^+ is released from the cathode and, under the applied voltage, travels through the electrolyte to intercalate into the anode.[16] At the same time, electrons flow through an external circuit from the cathode to the anode. During charge and discharge cycles, the directions of Li^+ and electron movement are opposite. The energy density of LIBs is primarily determined by the specific capacity and operating potential of both the cathode and anode.[17] The theoretical specific capacity of the commonly used graphite anode is only 372 mAh g^{-1}.[18] As a result, batteries using graphite anodes are increasingly insufficient to meet the growing energy demands of advanced electronic devices and electric vehicles. Replacing carbon-based anodes with novel materials that offer higher specific capacities could enable the development of LIBs with significantly higher energy densities.

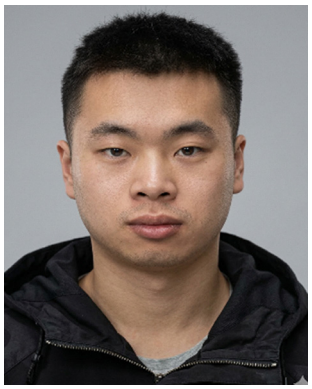

Guangmao Yan

Guangmao Yan is currently a PhD student at the Faculty of Materials Science and Engineering, Kunming University of Science and Technology. His research focuses on energy storage and conversion materials.

Fei Wang

Fei Wang is an associate professor at the Faculty of Materials Science and Engineering, Kunming University of Science and Technology. He was granted a Doctor's Degree from Sichuan University, majoring in materials science and engineering. His main research interests are batteries and relevant cross-scale simulations.

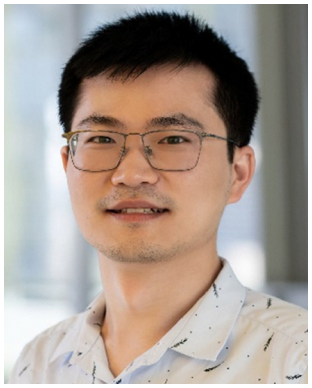

Hanyu Huo

Hanyu Huo is a Professor of Materials Science at the University of Science and Technology of China (USTC) and a recipient of China's National Overseas High-Level Young Talent Program. He received his PhD from the Shanghai Institute of Ceramics, Chinese Academy of Sciences. He conducted postdoctoral research at Tongji University, Justus Liebig University Giessen, and the University of Oxford. His research focuses on solid-state batteries, particularly electro-chemo-mechanical stability of solid–solid interfaces for fast ion transport.

Yan Yu

Yan Yu is a Professor of Materials Science at the University of Science and Technology of China (USTC). She received her PhD from USTC in 2006. Her research focuses on the design of nanomaterials for clean energy, particularly batteries and the fundamental science of energy-storage systems. She has been recognized as a Highly Cited Researcher in Materials Science and has received several honors, including the National Science Fund for Distinguished Young Scholars, the China Youth Science and Technology Award, and Fellowship of the Royal Society of Chemistry.

Over the past few decades, a range of high-specific-capacity anode materials, including silicon-based, tin-based, and transition metal oxide materials, have been proposed.[19–25] These materials typically achieve high specific capacities due to the alloying and conversion reactions, in which the molar volume of the electrochemical products is significantly higher than that of the reactants (anode materials).[26] To alleviate the volume strain associated with these anode materials, a common strategy is to incorporate carbon or high Young's modulus additives. These additives, which are typically electrochemically inactive or have a lower specific capacity, serve to suppress or buffer the expansion of the active materials.[27–29] For example, doping or incorporating carbon nanotubes or free carbon into silica at the atomic or molecular level has resulted in the formation of multiphase composite ceramics, such as SiOC,[30,31] which exhibit reduced volume strain. Consequently, significant heterointerfaces can be created between the anode materials and the additives. An analysis of publications in related fields in the Web of Science database (Fig. 1a) reveals a clear upward trend in the number of associated publications (many papers belonging to 2025 will be published in 2026), which has surpassed 14 000 in recent years (Fig. 1b). This suggests growing interest among researchers in addressing the challenges posed by anodes under high-volume strain.

Electrodes typically consist of multiple materials. In traditional electrode preparation methods, acetylene black is commonly used as a conductive agent, while polyvinylidene fluoride (PVDF) functions as a binder. This leads to the formation of numerous contact interfaces between the active materials, conductive agents, binders, and current collectors. With the ongoing advancements in materials science and technology, the electrode fabrication process increasingly incorporates additional additives, such as graphene and elemental metals, thereby creating a more intricate heterointerface system.[32–34] In battery systems, the transport of electrons and Li^+ depends on carriers or media. For multi-interface structures, electron and Li^+ transfer can only occur through the contact points at these contact interfaces.[35] The structure of these contact interfaces plays a crucial role in influencing the transport efficiency of electrons and Li^+, which in turn gives rise to a variety of intriguing phenomena.

Many previous works have reviewed surface and interface engineering for battery materials, but they predominantly focused on the liquid electrolyte/active material interfaces, such as SEI layers, surface coating, interface alloying, *etc.*[36–39] However, these research overlooks the critical internal contact interfaces buried within the composite electrode matrix, such as the solid–solid contact interfaces—comprising active material–active material, active material–conductive additive, active material–binder, and active material–current collector contacts—are highly abundant and play a decisive role in electron/ion percolation. These internal contact interfaces in high-volume-strain anodes undergo drastic geometric reconstruction, yet the fundamental mechanisms governing how these buried junctions evolve have also not been systematically analyzed. Furthermore, regarding theoretical modelling, a unified multiscale framework capable of describing the dynamic chemo-mechanical coupling at these evolving solid–solid interfaces is still unclear, leaving a gap between atomic-level bonding insights and macroscopic electrode failure.

In this review, we establish a systematic framework to analyze the contact interfaces of high-volume-strain anodes, moving beyond material-specific discussions. We introduce a dual-dimensional classification system defined by geometry (point-to-point (PtP), line-to-line (LtL), and surface-to-surface (StS)) and physical/chemical (weak *vs.* strong interactions and heterogeneous interfaces). Crucially, this framework is applied to reveal the dynamic evolution of contact interfaces---specifically, how contact modes transition and degrade under substantial volumetric strain. We further integrate these concepts with advanced characterization and simulation methodologies to establish quantitative structure–performance correlations. Finally, we distill these insights into generalizable design rules, providing a rational roadmap for engineering mechanically

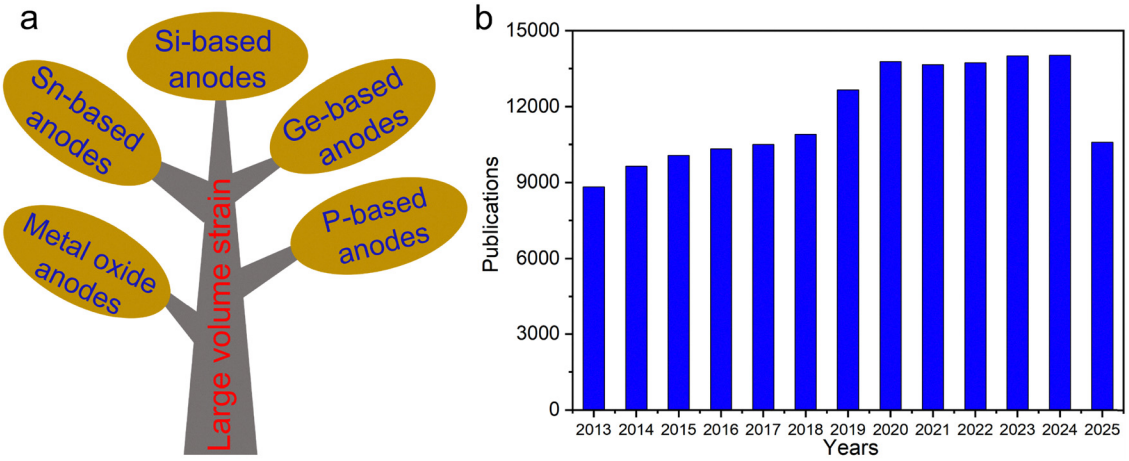

Fig. 1 (a) Anode materials with large volume strain. (b) The publications regarding the anode materials with large volume strain using the keywords (silicon anode OR "tin anode" OR "germanium anode" OR "metal oxide anode" OR "phosphorus-based anode" OR "volume strain" OR "volume expansion") in the "Web of Science" database. The search time range for the article is "2013-01-01 to 2025-11-20".

compliant and electronically percolated networks for next-generation batteries.

2. Typical anode materials with large volume strain

2.1. Si-based anodes

2.1.1. Volume strain effect. Silicon (Si) and oxygen (O), as the most abundant elements in the Earth's crust, are predominantly found in the form of silica and silicates. Leveraging their natural abundance and high theoretical capacities, Si-based materials—including Si and various silicon oxides—have emerged as some of the most promising candidates for next-generation LIB anodes.[40–42] Recent advancements in this field have led to the widespread development and commercialization of Si/C composite anodes, which are now regarded as representative systems for practical applications.[43–45] Companies such as BTR New Energy Materials Ltd have already adopted these materials in commercial LIBs.[46]

Despite these advances, current Si/C composites still face several critical challenges that limit their broader adoption and performance optimization: (1) The Si content in commercial Si/graphite composites remains relatively low (typically <10 wt%), restricting their reversible specific capacity to approximately 500 mAh g^{-1}.[47] (2) Si with inherently low electrical conductivity hampers its rate capability.[48] (3) Si-based materials undergo substantial volume strain—up to $\sim$300%—during lithiation and delithiation. This causes particle pulverization, continuous SEI formation, and consequently, rapid degradation of both cycling stability and coulombic efficiency.[49,50]

To address these issues, extensive efforts have focused on diversifying Si-based anode materials. These include pure Si, silicon monoxide (SiO), silicon dioxide (SiO_2), and non-stoichiometric amorphous silicon oxides (SiO_x, where $0 \leq x \leq 2$).[51–53] In addition, novel Si-based compounds—such as Li_2VSiO_5 and large intragranular cavity silica—have been introduced in recent studies to optimize electrochemical behavior further.[54,55] These materials exhibit a wide range of properties in terms of capacity, conductivity, cycling stability, safety, and cost.

Fig. 2 provides a comprehensive overview of the electrochemical performance of Si-based anodes. In general, increasing the oxygen content in Si-based materials leads to lower specific capacity, coulombic efficiency, and rate performance, improved cycling stability and safety and reduced raw material costs.[51] For instance, SiO_2 is an electrical insulator and, upon lithiation, predominantly forms non-conductive Li_2O and silicate phases—significantly degrading its rate performance compared to pure Si.[56,57] Similarly, in SiO_x materials, higher values of x correspond to increased formation of these insulating phases, resulting in progressively lower conductivity and rate capability.[55] This intrinsic trade-off highlights the critical need for structural and compositional optimization to enhance conductivity and electrochemical performance, especially under high-rate operating conditions.

Cycling stability remains a pivotal parameter in evaluating Si-based anodes. *In situ* transmission electron microscopy (TEM) studies reveal that pure Si anodes undergo volumetric strain of approximately 300% upon full lithiation, which induces particle fracturing and continuous SEI formation, leading to capacity fade over repeated cycles (Fig. 3).[59,60] In contrast, SiO anodes exhibit lower volume strain ($\sim$160%), and further increases in oxygen content (*e.g.*, in SiO_2) yield even greater dimensional stability.[61,62] For the broader SiO_x family, volume strain varies between $\sim$300% (pure Si) and $\sim$160% (SiO_2).[52]

Beyond performance concerns, volume strain in LIBs also poses significant safety risks, such as internal short circuits that may lead to combustion or explosion. Therefore, safety considerations are critical in the design of Si-based anodes.[63]

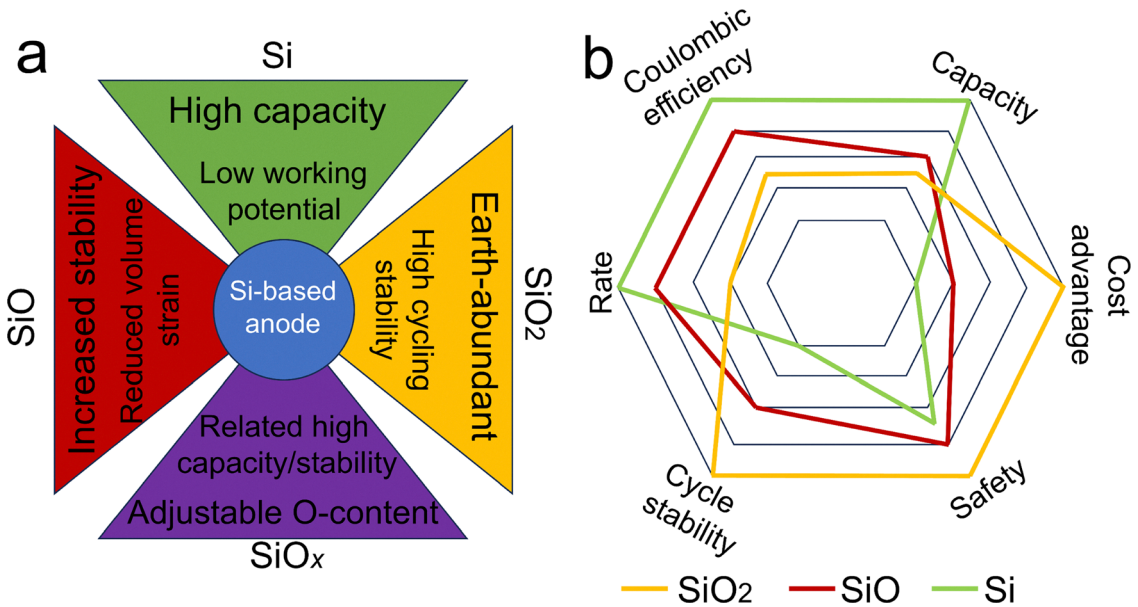

Fig. 2 The properties of various (a) Si-based anodes and (b) the comparison of various Si-based anode materials for the related factors in LIBs.

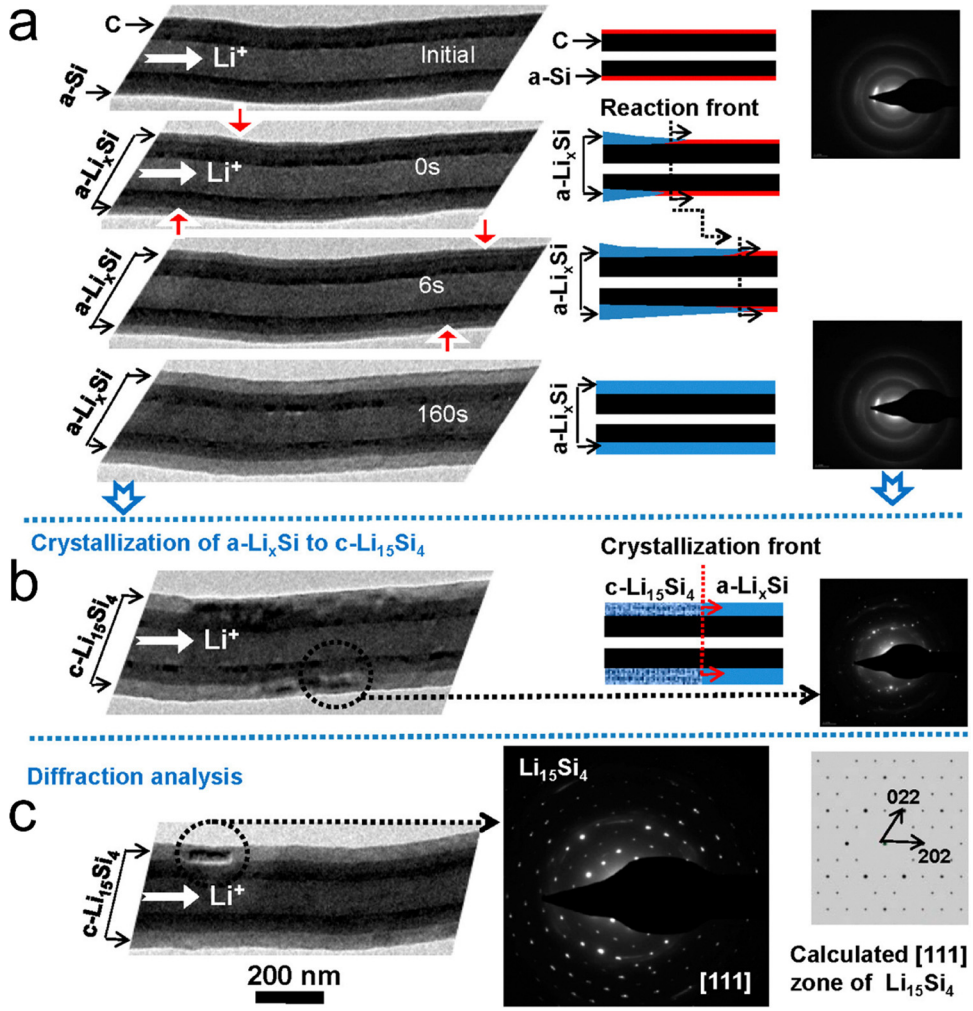

Fig. 3 Volume strain effect of Si anodes. (a) The *in situ* TEM morphology of the Si anode during lithiation. (b) and (c) The final crystalline $Li_{15}Si_4$ is formed after lithiation for Si. Reproduced with permission.[58] Copyright 2012, American Chemical Society.

SiO_2, in particular, is non-toxic, chemically stable, and non-flammable, with minimal volume strain during cycling. These characteristics significantly reduce the likelihood of separator puncture and short-circuiting, thereby enhancing battery safety.[64] Moreover, SiO_2 is cost-effective, being readily available from natural resources like sand, minerals, and biomass.[57,65] By selectively removing oxygen from SiO_2, it is possible to obtain SiO_x, SiO, or pure Si, enabling tunable electrochemical and physical properties depending on specific application needs.[66,67]

2.1.2. Lithiation mechanisms. Unlike graphite anodes, which rely on a Li^+ intercalation/deintercalation mechanism, Si stores Li^+ through an alloying/dealloying reaction (Fig. 4).[50] Coulometric titration experiments have identified four intermediate alloy phases ($Li_{12}Si_7$, Li_7Si_3, $Li_{13}Si_4$, and $Li_{22}Si_5$) formed at elevated temperatures (~415 °C) during lithiation. Among these, $Li_{22}Si_5$ exhibits the highest theoretical capacity, reaching 4200 mAh g^{-1}.[69] However, under ambient conditions, $Li_{15}Si_4$ is the terminal lithiation product, with a slightly lower theoretical capacity of 3589 mAh g^{-1}.

During the initial discharge (lithiation) in a half-cell, a voltage plateau typically appears between 0.05 V and 0.2 V[49,70,71] corresponding to the transformation of crystalline Si into amorphous Li_xSi:

$$Si + xLi^+ + xe^- \rightarrow Li_xSi \quad (2.1.1)$$

As the voltage drops below 0.05 V, amorphous Li_xSi further crystallizes into $Li_{15}Si_4$:

$$4Li_xSi + (15 - 4x)Li^+ + (15 - 4x)e^- \rightarrow Li_{15}Si_4 \quad (2.1.2)$$

During charging (delithiation), a sloping plateau at approximately 0.4 V reflects the decomposition of $Li_{15}Si_4$:

$$Li_{15}Si_4 \rightarrow 15Li^+ + 15e^- + 4Si \quad (2.1.3)$$

SiO anodes store Li^+ *via* two mechanisms: (1) a conversion reaction between SiO and Li^+, forming Li_2O and Si; (2) an alloying/dealloying reaction between the resulting elemental Si and Li^+.[72] However, the lithiation of SiO is complex due to irreversible reactions, particularly during the first cycle. The

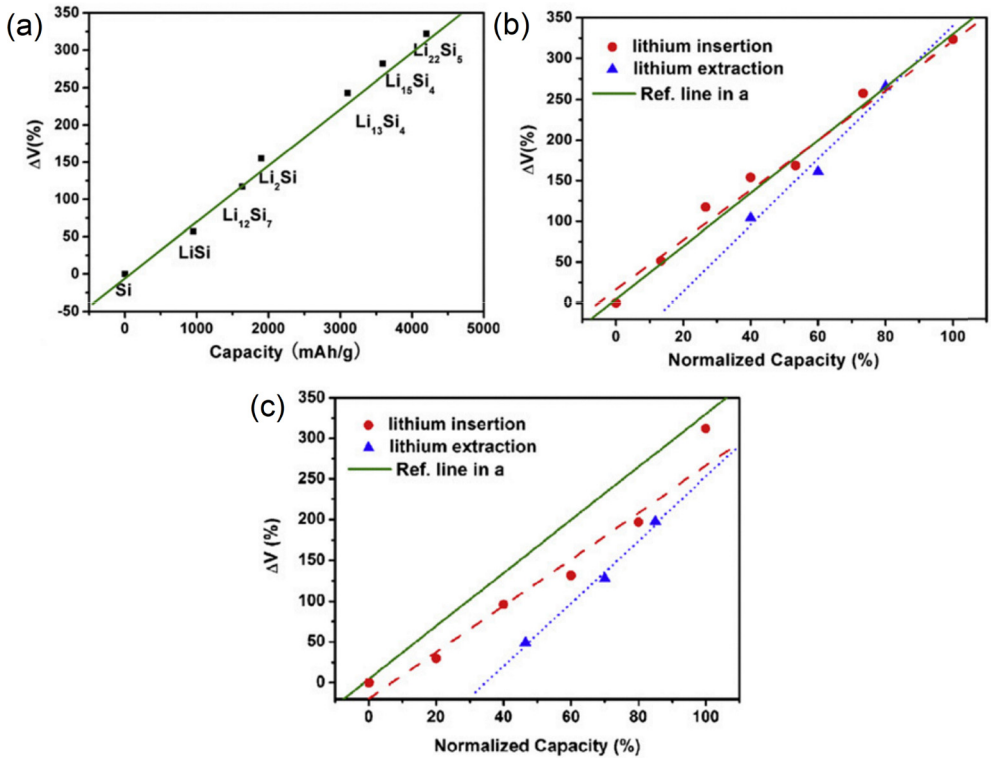

Fig. 4 Volume strain of (a) crystalline Li–Si alloys compared to Si. (b) Volume strain of amorphous and (c) crystalline Si during Li^+ insertion and extraction. Reproduced with permission.[68] Copyright 2012, Elsevier.

products formed vary with lithiation conditions, with lithium silicate compounds such as Li_4SiO_4, Li_2SiO_3, $Li_6Si_2O_7$, and $Li_2Si_2O_5$ being frequently reported. The major reactions are summarized as follows:[51]

$$SiO + 2Li^+ + 2e^- \rightarrow Li_2O + Si \quad (2.1.4)$$

$$SiO + Li_2O + 4Li^+ + 4e^- \rightarrow Li_4SiO_4 \quad (2.1.5)$$

$$3SiO + 2Li^+ + 2e^- \rightarrow Li_2SiO_3 + 2Si \quad (2.1.6)$$

$$7SiO + 6Li^+ + 6e^- \rightarrow Li_6Si_2O_7 + 5Si \quad (2.1.7)$$

$$5SiO + 2Li^+ + 2e^- \rightarrow Li_2Si_2O_5 + 3Si \quad (2.1.8)$$

$$Si + xLi^+ + xe^- \rightarrow Li_xSi \quad (2.1.9)$$

The reaction mechanism of SiO_2 with Li^+ is even less understood. However, several products, such as $Li_2Si_2O_5$, Li_2SiO_3, Li_4SiO_4, Li_2O, and Li_xSi, have been reported during the lithiation of SiO_2-based anodes.[57,73–75] Representative reactions include:

$$5SiO_2 + 4Li^+ + 4e^- \rightleftharpoons 2Li_2Si_2O_5 + Si \quad (2.1.10)$$

$$3SiO_2 + 4Li^+ + 4e^- \rightarrow 2Li_2SiO_3 + Si \quad (2.1.11)$$

$$2SiO_2 + 4Li^+ + 4e^- \rightarrow Li_4SiO_4 + Si \quad (2.1.12)$$

$$SiO_2 + 4Li^+ + 4e^- \rightarrow 2Li_2O + Si \quad (2.1.13)$$

Similar to SiO, the lithiation of SiO_2 occurs in two distinct steps: first, SiO_2 undergoes conversion to form electrochemically active phases (*e.g.*, $Li_2Si_2O_5$) and inactive phases (*e.g.*, Li_4SiO_4, Li_2SiO_3, and Li_2O), alongside elemental Si. In the second step, the elemental Si reacts with Li^+ to form reversible Li_xSi. During delithiation, the inactive phases remain, contributing to the low initial coulombic efficiency observed in SiO_2 anodes.[64]

The lithiation mechanism of SiO_x ($0 \leq x \leq 2$) combines both conversion and alloying/dealloying processes. During initial lithiation, SiO_x reacts with Li^+ to produce elemental Si and lithium-containing byproducts such as Li_2O and lithium silicates. The elemental Si then undergoes alloying with Li^+ to form Li_xSi.[76] The following reactions illustrate the lithiation pathways of SiO_x materials.[77–79]

$$SiO_x + 2xLi^+ + 2xe^- \rightarrow xLi_2O + Si \quad (2.1.14)$$

$$SiO_x + (6x/7)Li^+ + (6x/7)e^- \rightarrow (x/4)Li_4SiO_4 + (1 - x/4)Si \quad (2.1.15)$$

$$SiO_x + (2x/5)Li^+ + (2x/5)e^- \rightleftharpoons (x/5)Li_2Si_2O_5 + (1 - 2x/5)Si \quad (2.1.16)$$

$$SiO_x + xLi^+ + xe^- \rightarrow (x/4)Li_2O + (1 - x/4)Si \quad (2.1.17)$$

In conclusion, the lithiation mechanisms of SiO_2, SiO, and SiO_x anodes, unlike the relatively well-characterized behavior of pure Si, are still not fully understood. These materials often undergo irreversible structural transformations during initial cycling, which impact their capacity, cycling stability, and coulombic efficiency. Understanding the detailed reaction pathways, especially during

the first lithiation cycle, is essential for developing more stable, efficient, and safe Si-based anodes.

2.1.3. Summary. Si-based anodes (Si, SiO, SiO_2, and SiO_x) are among the most promising next-generation anodes because Si is earth-abundant and offers an exceptionally high theoretical capacity. In practice, however, commercial Si/carbon (often Si/graphite) composites still contain low Si fractions (typically <10 wt%), which limits the achievable reversible capacity ($\sim$500 mAh g^{-1}). Their broader development is further constrained by their poor intrinsic electrical conductivity and, most critically, the severe volume strain (up to $\sim$300%) during alloying/dealloying, which triggers particle fracture, repeated SEI rupture/reformation, rapid capacity fade, and reduced coulombic efficiency.

A key compositional trend across this family is that increasing oxygen content generally sacrifices capacity, initial coulombic efficiency, and rate capability, while improving cycling stability, safety, and cost. This trade-off shows that oxygen-rich systems form substantial amounts of electronically insulating Li_2O and lithium silicates during lithiation, lowering conductivity and kinetics but mechanically buffering strain (*e.g.*, reduced strain for SiO and even lower for SiO_2). Mechanistically, pure Si lithiates mainly *via* a crystalline-to-amorphous transformation followed by formation of crystalline $Li_{15}Si_4$ at deep lithiation, whereas SiO/SiO_2/SiO_x typically undergo an initial conversion reaction that generates Li_2O/silicates plus elemental Si, after which the generated Si participates in reversible Li_xSi alloying; the extent of irreversible byproduct formation (especially in the first cycle) remains a major origin of low initial efficiency. Overall, advancing Si-based anodes requires balancing the capacity–stability trade-off through a clearer understanding of first-cycle reaction pathways and rational structural/compositional design to maintain conductivity while mitigating volume strain.

2.2. Sn-based anodes

Since the 1990s, researchers have explored Sn-based amorphous oxides as high-capacity anode materials for LIBs, laying the groundwork for the development of Sn-based systems and sparking sustained academic and industrial interest.[80] A breakthrough occurred in 2005 when Sony introduced the first commercial Sn-based LIB, known as "Nexelion", which featured a Sn-based amorphous material as the anode. This battery exhibited a 30% capacity improvement over traditional graphite-based LIBs, further reinforcing the appeal of Sn-based anodes for next-generation energy storage systems.[81]

Current research on Sn-based anodes primarily focuses on four categories: Sn, Sn oxides, Sn sulfides, and other Sn-based anodes.[23,83–86] These materials offer several advantages, such as high theoretical specific capacity and an operating potential above the lithium plating threshold, reducing dendrite formation risks. However, these materials also face significant challenges, primarily, substantial volume strain during lithiation/delithiation, which can result in a volume expansion of $\sim$130% (Fig. 5d), leading to the pulverization and cracking of the active material, as well as detachment from the current collector, ultimately causing a rapid decline in cycling performance (Fig. 5).[82] Furthermore, low intrinsic conductivity, especially in Sn oxides and sulfides, limits their rate capability.[87,88]

2.2.1. Metallic Sn. Metallic Sn, a Group IVA element, undergoes reversible alloying reactions with Li^+, forming

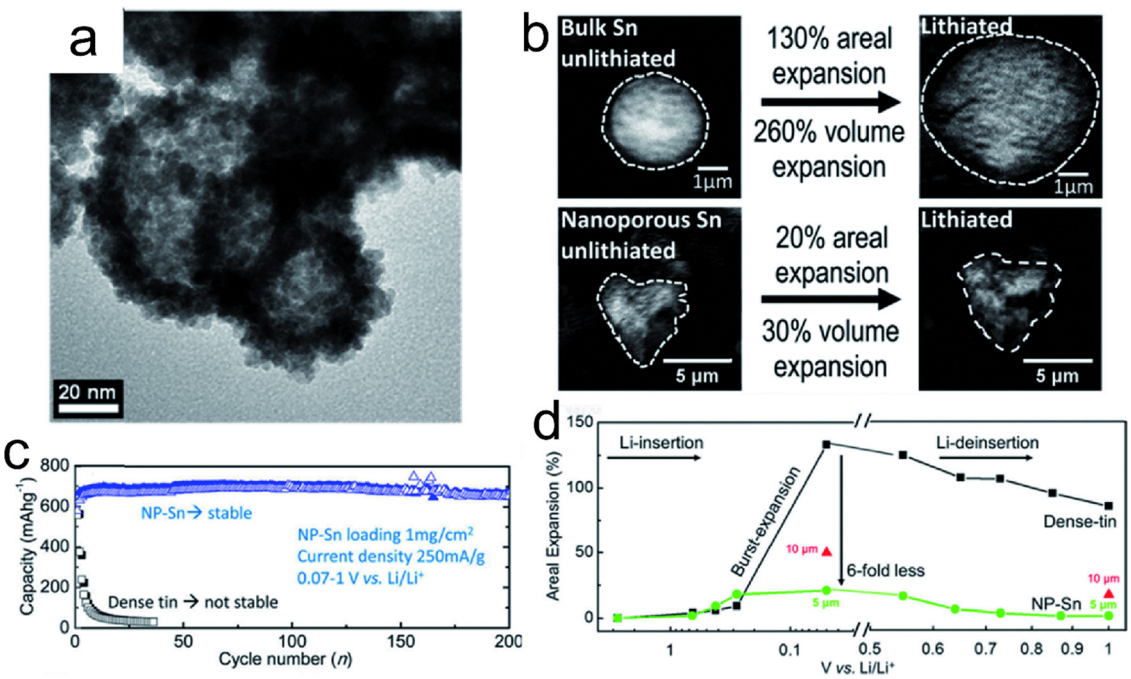

Fig. 5 (a) TEM morphology of Sn nanoparticles. (b) *In situ* TEM morphology of Sn nanoparticles before and after lithiation. (c) Cycling performance of bulk and nano-Sn anodes. (d) Areal expansion of bulk Sn and nano-Sn anodes at various voltages. Reproduced with permission.[82] Copyright 2017, Wiley-VCH GmbH.

various Li–Sn intermetallic phases. The overall lithiation/delithiation reaction is expressed as:[89]

$$Sn + xLi^+ + xe^- \rightleftharpoons Li_xSn \quad (0 \le x \le 4.4) \quad (2.2.1)$$

At maximum lithiation (x = 4.4), the resulting phase is $Li_{22}Sn_5$, yielding a theoretical specific capacity of 993 mAh g^{-1}, which is approximately 2.6 times higher than that of graphite.[90] This value is approximately 2.6 times greater than the capacity of commercially available graphite. The relatively higher working potential of Sn also helps reduce dendrite formation, improving battery safety.

Despite these benefits, the practical use of metallic Sn is limited due to extreme volume changes during lithiation. While shallow cycles result in minimal strain, full lithiation to $Li_{22}Sn_5$ induces 359% volume strain, leading to severe cracking and detachment of Sn particles from the current collector, thereby degrading cycling performance.[90]

2.2.2. Sn-based oxides. Common Sn-based oxides include SnO and SnO_2, both of which can store Li^+ through a two-step mechanism.[88,91–93] First step is the conversion reaction: reduction to metallic Sn and formation of Li_2O:[91]

$$SnO + 2Li^+ + 2e^- \rightarrow Sn + Li_2O \quad (2.2.2)$$

$$SnO_2 + 4Li^+ + 4e^- \rightarrow Sn + 2Li_2O \quad (2.2.3)$$

The second step is the alloying reaction:

$$Sn + xLi^+ + xe^- \rightleftharpoons Li_xSn \quad (0 \le x \le 4.4) \quad (2.2.4)$$

While the first step is largely irreversible, contributing to low initial coulombic efficiency, the second step is reversible, enabling repeated alloying/de-alloying. Based on this mechanism, the theoretical reversible capacities are 875 mAh g^{-1} for SnO and 782 mAh g^{-1} for SnO_2.[92,94] Interestingly, when particle sizes are reduced to the nanoscale, the first-step reduction becomes partially or fully reversible, allowing capacities to reach 1273 mAh g^{-1} (SnO) and 1494 mAh g^{-1} (SnO_2).[95] In this case, the amorphous Li_2O matrix, formed during Li^+ insertion, acts as a buffer that mitigates volume strain and prevents Sn agglomeration, thereby enhancing cycling stability.[96,97]

2.2.3. Sn-based sulfides. Among Sn-based sulfides, SnS_2 and SnS are the most studied. SnS_2 adopts a layered CdI_2-type structure, with weak van der Waals forces between adjacent layers, while SnS has a 1 : 1 Sn : S ratio with a similar layered configuration.[85,98] Like Sn oxides, Sn sulfides undergo a two-step reaction process.[99]

The first step involves reducing SnS_2 to Sn and Li_2S.[100]

$$SnS_2 + 4Li^+ + 4e^- \rightarrow Sn + 2Li_2S \quad (2.2.5)$$

The second step is the alloying reaction.

$$Sn + xLi^+ + xe^- \rightarrow Li_xSn \quad (0 \le x \le 4.4) \quad (2.2.6)$$

The theoretical specific capacity of SnS_2 is 645 mAh g^{-1}, based on the formation of $Li_{4.4}Sn$. If the first (currently irreversible) reaction could be made reversible, the capacity could reach 1232 mAh g^{-1}, corresponding to the uptake of 8.4 mol Li^+. In addition to high theoretical capacity, SnS_2 offers structural advantages. Its large interlayer spacing ($\sim$0.59 nm)[101] and the weak Sn–S bonds facilitate Li^+ diffusion and enhance electrochemical kinetics. Moreover, Li_2S formed in the first step serves as a mechanical buffer, suppressing Sn aggregation and alleviating volume strain. However, SnS_2 still suffers from low intrinsic conductivity and severe volume strain, which can lead to structural degradation and capacity fading over extended cycles.

2.2.4. Other Sn-based anodes. Beyond metallic Sn, Sn-based oxides, and Sn-based sulfides, a broad class of Sn-containing intermetallic compounds (including transition-metal stannides) have been explored as alternative anodes for LIBs. By introducing a second metallic component, these phases can partially decouple Li-storage activity from mechanical buffering and electronic transport: the metal sublattice provides high conductivity and a rigid/ductile framework that suppresses Sn coarsening and alleviates electrical isolation during repeated alloying/dealloying. The trade-off is that the gravimetric capacity is typically reduced because a fraction of the electrode mass is electrochemically inactive or only weakly active toward Li.[102]

From a mechanistic perspective, Sn-based intermetallic anodes can be broadly divided into two types. Insertion-type intermetallics accommodate Li^+ through a topotactic or two-phase insertion process while largely retaining a host framework. A representative example is η-Cu_6Sn_5. Li can be inserted into Cu_6Sn_5 to form $Li_xCu_6Sn_5$, with a theoretical capacity of $\sim$358 mAh g^{-1}.[103]

$$Cu_6Sn_5 + xLi + xe^- \rightleftharpoons Li_xCu_6Sn_5 \quad (2.2.7)$$

Such insertion-type intermetallics can exhibit improved mechanical integrity compared to fully lithiated Sn, but they remain susceptible to structural fatigue and require careful voltage window control to maintain high cycling efficiency. Another representative stannide is Mg_2Sn, where lithiation has been reported to proceed *via* initial Li insertion into the lattice followed by alloying reactions dominated by the Sn sublattice, producing initial discharge/charge capacities of $\sim$556/460 mAh g^{-1} in early reports.[104] Displacement/conversion–alloying-type stannides undergo partial breakdown of M–Sn bonding upon lithiation, generating nanoscale Li–Sn alloys embedded in a metallic M matrix. In the simplest approximation, many MSn_2-type phases can be described as:[105,106]

$$MSn_2 + 4.4Li^+ + 4.4e^- \rightleftharpoons M + 2Li_{4.4}Sn \quad (2.2.8)$$

Here, M (*e.g.*, Co or Fe) functions as an internal current collector and a stress-buffering scaffold, while the reversible Li-storage is dominated by the Sn-derived Li_xSn component. Recent colloidal nanoalloy studies on monodisperse $CoSn_2$ and $FeSn_2$ nanocrystals demonstrate that constructing a continuous metallic matrix and preventing Sn coarsening can dramatically extend cycling life. Mechanistic work on Fe–Sn compounds (*e.g.*, Sn_2Fe) further demonstrates that the extent of conversion and recombination, as well as the resulting phase evolution, critically governs reversibility and long-term stability. Similarly, Ni–Sn stannides (*e.g.*, Ni_3Sn_4) have been investigated as mechanically reinforced Sn hosts.[107] Nanocrystalline Ni_3Sn_4 can store Li^+ mainly through Sn-rich interfacial/grain-boundary regions, showing improved

cyclability compared with coarse-grained counterparts, especially when coupled to conductive frameworks.

In addition to transition-metal stannides, active–active intermetallic alloys such as SnSb have attracted attention because both Sn and Sb can alloy with Li^+, enabling a relatively higher theoretical capacity ($\sim$825 mAh g^{-1}). The sequential formation of Li_3Sb and Li_xSn can provide partial mutual buffering of strain:[108]

$$SnSb + 7.4Li^+ + 7.4e^- \rightleftharpoons Li_{4.4}Sn + Li_3Sb \quad (2.2.9)$$

Nevertheless, substantial volume strain still occurs, so practical SnSb electrodes typically rely on nanosizing, carbon coating, and hierarchical conductive scaffolds (*e.g.*, porous carbon nanofibers and core–shell composites) to preserve percolation pathways and suppress particle pulverization. Overall, Sn-containing intermetallics upon lithiation produce a multiphase nanocomposite (such as Li_xSn + M and Li_3Sb + Li_xSn) in which the inactive/less-reactive phase plays a role analogous to the Li_2O/Li_2S matrices in SnO_2/SnS_2, but with higher electronic conductivity, making them a useful platform for applying the interface-focused design rules discussed in later sections. Moreover, the Sn-based intermetallic compounds generally present relatively high density, which can bring about high volume energy density, although they present high volume strain (above 100%, Table 1)

2.2.5. Summary. Sn-based anodes have been intensively studied since the 1990s, and their practical potential was highlighted by Sony's ''Nexelion'' (2005) using a Sn-based amorphous anode. Current Sn-based anode research mainly covers four material families: metallic Sn, Sn oxides, Sn sulfides, and Sn-containing intermetallic compounds (including transition-metal stannides and SnSb). These systems provide high theoretical capacities and operate at potentials above the Li-plating threshold, but they are generally limited by pronounced lithiation-induced volume expansion and, for oxides/sulfides, relatively low intrinsic conductivity.

Metallic Sn stores Li^+ *via* reversible alloying to form Li_xSn ($0 \leq x \leq 4.4$) and forms $Li_{22}Sn_5$ at full lithiation with a theoretical capacity of 993 mAh g^{-1}, yet deep alloying causes severe volume strain and rapid loss of electrical contact. SnO and SnO_2 typically follow a conversion step to Sn + Li_2O followed by reversible Li–Sn alloying; their reversible theoretical capacities are 875 and 782 mAh g^{-1}, respectively, and nanosizing can improve reversibility and strain buffering through the Li_2O matrix. SnS_2 and SnS undergo analogous conversion to Sn + Li_2S and subsequent alloying; SnS_2 offers a theoretical capacity of 645 mAh g^{-1} based on $Li_{4.4}Sn$, with layered diffusion advantages and Li_2S-assisted buffering. Sn-containing intermetallics introduce a conductive metal framework and can proceed *via* insertion-type behaviour or displacement/conversion–alloying, while SnSb represents an active–active alloy system ($\sim$825 mAh g^{-1}).

Table 1 Densities and volume strains of different Li_xSn alloys

Phase	Density/(g cm^{-3})	Volume strain/%
Sn	7.29	260
Li_2Sn_5	6.11	122
LiSn	5.10	151
Li_5Sn_2	3.54	236
$Li_{22}Sn_5$	2.56	359
η-Cu_6Sn_5	8.28	266.27
$CoSn_2$	8.91	387.37
$FeSn_2$	8.54	373.33
$NiSn_4$	8.65	339.48
Mg_2Sn	3.51	121.64
SnSb	6.7	234.81

2.3. Ge-based anodes

Ge has emerged as a promising anode material for LIBs due to its high theoretical specific capacity of 1600 mAh g^{-1}, which, while lower than that of Si, is still significantly higher than that of graphite (Fig. 6).[110] More importantly, Ge possesses intrinsic properties that greatly enhance its rate performance. Its Li^+ diffusion coefficient is approximately 400 times higher, and its electronic conductivity is about 10 000 times greater than that of Si.[111] These properties make Ge-based anodes particularly suitable for high-power applications. Similar to Si anodes, the lithiation of Ge involves alloying reactions that result in significant volume strain ($\sim$370%) (Fig. 7). This expansion induces cracking, pulverization, and detachment from the current collector, which in turn degrades electrical contact. Furthermore, the continuous exposure of fresh surfaces leads to repeated formation and fracture of the SEI, consuming both the electrolyte and active lithium and accelerating capacity fading and eventual battery failure.

2.3.1. Ge and GeO_2. The most common Ge-based anodes are Ge and germanium oxide (GeO_2). And their mechanisms are similar to the previous elemental substances and oxides, so only a brief description will be given here. The lithiation mechanism of Ge-based anodes generally mirrors that of Si-based materials. For pure Ge, the reaction proceeds *via* a direct alloying reaction, as shown below (Fig. 7):[113]

$$4Ge + 22Li^+ + 22e^- \rightarrow Li_{22}Ge_4 \quad (2.3.1)$$

GeO_2 is also a common Ge-based anode, and the lithiation reactions can be divided into two steps as previously discussed anodes: a conversion reaction followed by an alloying reaction:[114]

$$GeO_2 + 4Li^+ + 4e^- \rightarrow Ge + 2Li_2O \quad (2.3.2)$$

$$Ge + 4.4Li^+ + 4.4e^- \rightleftharpoons Li_{4.4}Ge \quad (2.3.3)$$

Therefore, we will not continue to elaborate here. We will focus more on other special Ge-based oxides in the later contents.

2.3.2. Ge-based non-oxides. Beyond traditional Ge-based oxides, significant progress has been made in developing Ge-based non-oxide materials, including germanium selenides (GeSe), germanium sulfides (GeS_2, GeS), germanium phosphides (GeP), and Ge–Si solid solutions. These materials offer distinct advantages, such as high theoretical capacities and improved cycling stability compared to pure Ge, with different lithiation mechanisms that mitigate volume strain issues.

Among Ge-based non-oxide materials, GeP_5 has gained attention due to its ultrahigh theoretical specific capacity of

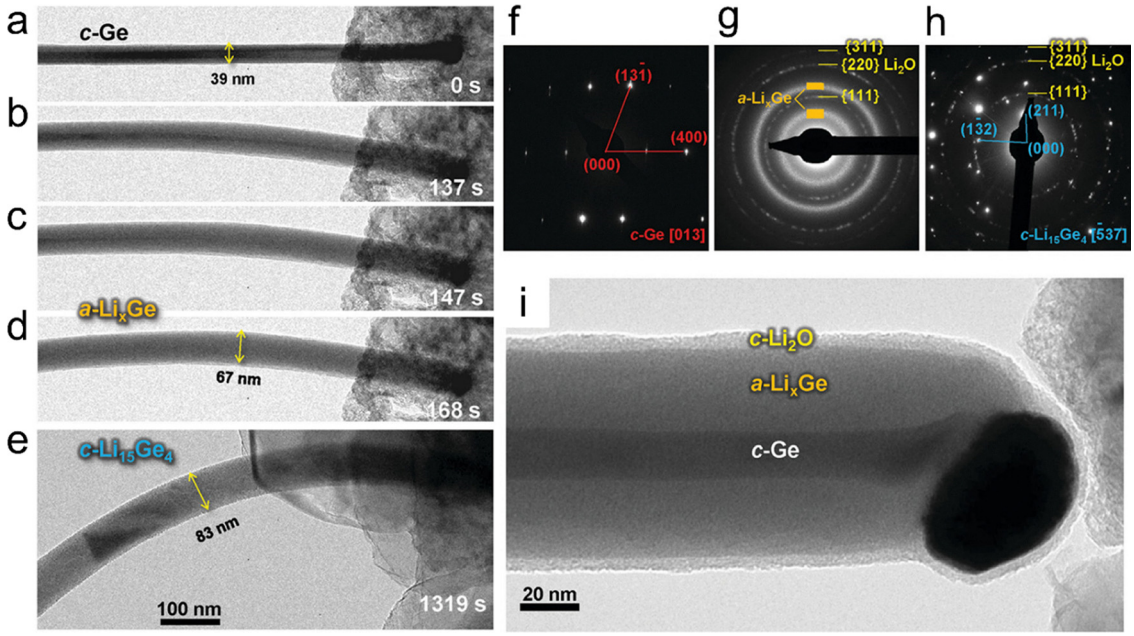

Fig. 6 (a)–(e) Volume strain effect of Ge nanowire anodes during lithiation observed by *in situ* TEM, resulting in a grey contrast due to the formation of Li_xGe. High-resolution TEM and selected area electron diffraction (SAED) patterns reveal the sequential phase transformations from (f) crystalline Ge (g) *via* amorphous Li_xGe to (h) the fully lithiated single crystalline $Li_{15}Ge_4$. (i) High-magnification image showing the intermediate state during lithiation. From the centre to the surface, the layers were a crystalline Ge core, an amorphous Li_xGe shell, and an amorphous Li_2O layer. Reproduced with permission.[109] Copyright 2014, Wiley-VCH GmbH.

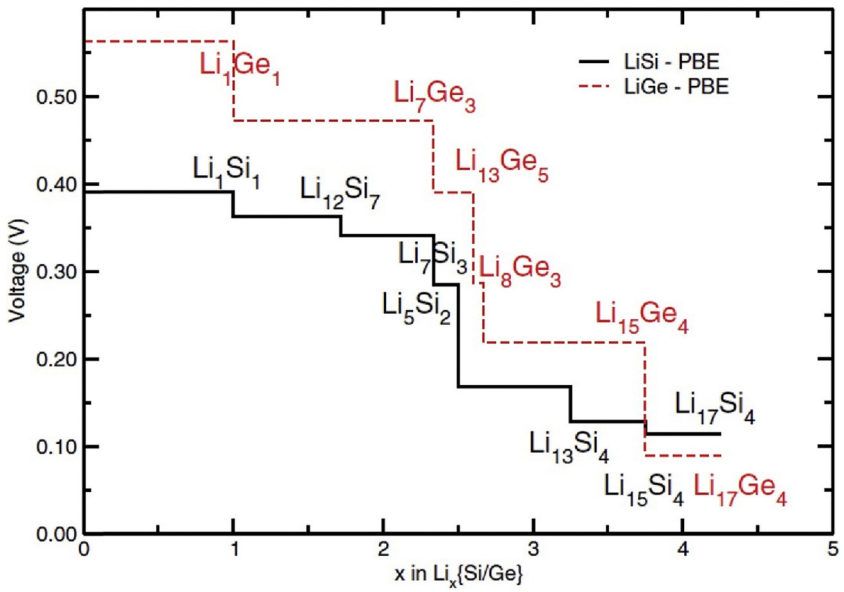

Fig. 7 Voltage *vs.* Li–Ge alloy curves from density functional theory (DFT) simulations. Reproduced with permission.[112] Copyright 2020, Elsevier.

2289 mAh g^{-1}.[115] However, similar to other high-capacity materials, GeP_5 suffers from significant volume strain, primarily due to the formation of high-molar-volume products like $Li_{4.4}P$. Its lithiation mechanism involves a two-step reaction:[116,117]

$$GeP_5 + 15Li^+ + 15e^- \rightarrow Ge + 5Li_3P \quad (2.3.4)$$

$$Ge + 4.4Li^+ + 4.4e^- \rightleftharpoons Li_{4.4}Ge \quad (2.3.5)$$

Moreover, particularly, the γ-phase, is emerging as a promising candidate for Li^+ storage. GeSe possesses a layered structure that facilitates Li^+ diffusion through its van der Waals gaps. The lithiation of GeSe follows a conversion–alloying mechanism, where the initial conversion to metallic Ge and Li_2Se is followed by the formation of Li–Ge alloys.[118]

$$GeSe + 2Li^+ + 2e^- \rightarrow Ge + Li_2Se \quad (2.3.6)$$

Additionally, sGe sulfides (GeS_2 and GeS) are another category of Ge-based non-oxides that have attracted attention for their potential as anode materials. GeS_2 adopts a layered CdI_2-type structure, while GeS has a 1 : 1 Ge : S ratio, both offering good Li^+ diffusion kinetics. The lithiation mechanism of GeS_2 is similar to that of other sulfides, consisting of a two-step process: first, a conversion reaction to form metallic Ge and Li_2S, followed by alloying of Ge with Li^+.[119]

$$GeS_2 + 4Li^+ + 4e^- \rightarrow Ge + 2Li_2S \quad (2.3.7)$$

The theoretical capacity of GeS_2 based on the formation of $Li_{4.4}Sn$ is 645 mAh g^{-1}, but if the first (irreversible) conversion reaction could be made reversible, the capacity could theoretically reach 1232 mAh g^{-1}. Li_2S formed in the first step serves as a mechanical buffer to suppress Ge aggregation and alleviate volume strain. GeS_2 nanostructures, such as nanosheets, have shown improved cycling stability and capacity retention by providing a higher surface area and facilitating more efficient Li^+ transport.

Specifically, Ge–Si solid solutions combine the benefits of both materials. The combination of Ge and Si results in an alloy system with tunable properties, where the high capacity of Si ($\sim$4200 mAh g^{-1}) is balanced with the structural stability of Ge. But the volume strain is still large, and structural stability is only relative to Si. The lithiation of Ge–Si alloys follows a typical alloying mechanism, where both components alloy with Li to form Li–Si and Li–Ge phases as follows.[120]

$$Ge_aSi_b + 4.4(a+b)Li^+ + 4.4(a+b)e^- \leftrightarrow aLi_{4.4}Ge + bLi_{4.4}Si \quad (a+b=1) \quad (2.3.8)$$

2.3.3. Ge-based oxides. Except for CeO_2, several Ge-based oxide anodes, such as $Ca_2Ge_7O_{16}$ and Zn_2GeO_4, have been reported.[121–123] However, the effects of volume strain in these materials have not been thoroughly studied. Therefore, only their Li^+ storage mechanisms are discussed here. For $Ca_2Ge_7O_{16}$, which has a theoretical specific capacity of 990 mAh g^{-1}, the lithiation mechanism is as follows:[124]

$$Ga_2Ge_7O_{16} + 28Li^+ + 28e^- \rightarrow 2GaO + 7Ge + 14Li_2O \quad (2.3.9)$$

$$7Ge + 30.8Li^+ + 30.8e^- \rightleftharpoons 7Li_xGe \quad (0 \le x \le 4.4) \quad (2.3.10)$$

In the first step, $Ca_2Ge_7O_{16}$ is converted to metallic Ge and Li_2O. This conversion is largely irreversible, with the formation of an insulating Li_2O matrix. In the second step, the metallic Ge formed in the first step alloys with Li^+ to form $Li_{4.4}Ge$ ($0 \le x \le 4.4$), which is the main reversible storage process. This is the typical alloying reaction for Ge-based anodes.[125]

For Zn_2GeO_4 with a theoretical specific capacity of 541 mAh g^{-1}, its lithiation mechanism also involves a conversion reaction first followed by an alloying reaction:[126]

$$Zn_2GeO_4 + 8Li^+ + 8e^- \rightarrow 2Zn + Ge + 4Li_2O \quad (2.3.11)$$

$$Ge + 4.4Li^+ + 4.4e^- \rightleftharpoons Li_{4.4}Ge \quad (2.3.12)$$

$$Zn + Li^+ + e^- \rightleftharpoons LiZn \quad (2.3.13)$$

In this conversion step, Zn_2GeO_4 is reduced to metallic Zn and Ge, forming Li_2O as a byproduct. This process is similar to the conversion reaction in other metal oxides, where Li_2O serves as a buffer to accommodate volume strain. In the following, the Ge formed during the conversion reaction alloys with Li to form $Li_{4.4}Ge$, completing the lithiation process. Finally, Zn can alloy with Li^+ to form LiZn, adding to the overall Li^+ storage capacity. This step is reversible and contributes to the capacity of the material.[127,128]

2.3.4. Summary. This section discusses Ge-based anode materials for LIBs, including their electrochemical performance and mechanisms. While pure Ge has a high theoretical capacity (1600 mAh g^{-1}) and significantly faster Li^+ diffusion and conductivity than Si, it suffers from massive volume strain ($\sim$370%) during lithiation. *In situ* TEM observations reveal that this expansion leads to severe particle pulverization and electrical isolation. To address this, many studies explored Ge-based derivatives, including oxides (*e.g.*, GeO_2 and Zn_2GeO_4) and non-oxides like phosphides (GeP_5), sulfides (GeS_2), and selenides (GeSe). These compounds typically utilize a two-step conversion-alloying mechanism. The initial conversion reaction creates metallic Ge embedded within a matrix (such as Li_2O or Li_2S). Crucially, this matrix acts as a mechanical buffer to accommodate volume strain and suppress aggregation, thereby improving cycling stability. Specific complex oxides like Zn_2GeO_4 further enhance performance by allowing both constituent metals (Zn and Ge) to reversibly alloy with Li^+, maximizing storage capacity while mitigating structural degradation.

2.4. Metal oxide anodes

Metal oxide (MO) anodes, particularly transition metal oxides such as Fe_2O_3, Co_3O_4, MoO_2, CuO, and Cu_2O, have attracted significant attention for LIBs.[129–133] These materials undergo complex redox reactions involving multiple electrons during Li^+ storage, which enables them to deliver high theoretical specific capacities.[134] Compared to graphite, metal oxides generally exhibit higher theoretical capacities. Moreover, unlike alloy-type anodes, MO anodes operate at higher voltages, which helps reduce the risk of lithium dendrite formation—a key safety concern in LIBs. Another advantage of MO anodes is the formation of inert reaction products (*e.g.*, Li_2O) after Li^+ insertion, which can act as a structural matrix that helps buffer volume strain and reduces electrode polarization. This contributes to maintaining the structural integrity of the electrode during cycling. However, a major drawback of MO anodes is their intrinsically low electrical conductivity, which severely limits their rate capability, particularly under high current conditions. This poor conductivity often leads to rapid capacity fading during repeated cycling.[135]

2.4.1. Conversion and alloying mechanisms. The lithiation/delithiation of MO anodes typically proceeds through a conversion reaction mechanism, especially in the early cycles. In this redox process, Li^+ reacts with the metal oxide to produce metal nanoparticles (M) and lithium oxide (Li_2O):[20,137,138]

$$M_xO_y + 2yLi^+ + 2ye^- \rightleftharpoons xM + yLi_2O \quad (2.4.1)$$

In some cases, the metal (M) generated from this reaction can undergo a subsequent alloying reaction with Li^+, forming Li_xM intermetallic compounds, further contributing to capacity:[139]

$$M + zLi^+ + ze^- \rightleftharpoons Li_zM \qquad (2.4.2)$$

Although these mechanisms enable high Li^+ storage capacity, they also result in large volume strain, which can lead to mechanical degradation of the electrode.

In practice, metal-oxide anodes can be broadly categorized into two classes based on their dominant lithiation mechanism. In conversion-type oxides (*e.g.*, Fe_2O_3, Co_3O_4, and MnO_2), the reaction in eqn (2.4.1) proceeds reversibly, and the active phase consists of nanosized metal particles dispersed in a Li_2O matrix. By contrast, in conversion–alloying (or alloying-type) oxides (*e.g.*, SnO_2, SnO, Zn_2GeO_4, and $CoSnO_3$), the metal generated by conversion further reacts with Li to form Li-rich M_xLi_γ alloys (eqn (2.4.2)). This additional alloying step increases the specific capacity but also induces much larger, often anisotropic, volume strain of the alloy domains.

2.4.2. Case study. An illustrative example of MO anode behavior is shown in Fig. 8, which depicts the *ex situ* TEM morphology of Co_3O_4 over a full electrochemical cycle.[136] Initially, pristine Co_3O_4 particles have an average diameter of approximately 57 nm. After lithiation, the particles expand to about 72.5 nm, accompanied by the formation of metallic Co and Li_2O. Upon delithiation, elemental Co is partially oxidized to CoO, and the average particle size decreases to approximately 64 nm. Assuming a spherical geometry, the overall volume strain during cycling is estimated to be 106%. This case study highlights a key challenge for MO anodes: the significant mechanical stress caused by repeated volume strain, which can result in particle fracture, loss of electrical contact, and ultimately, capacity degradation.

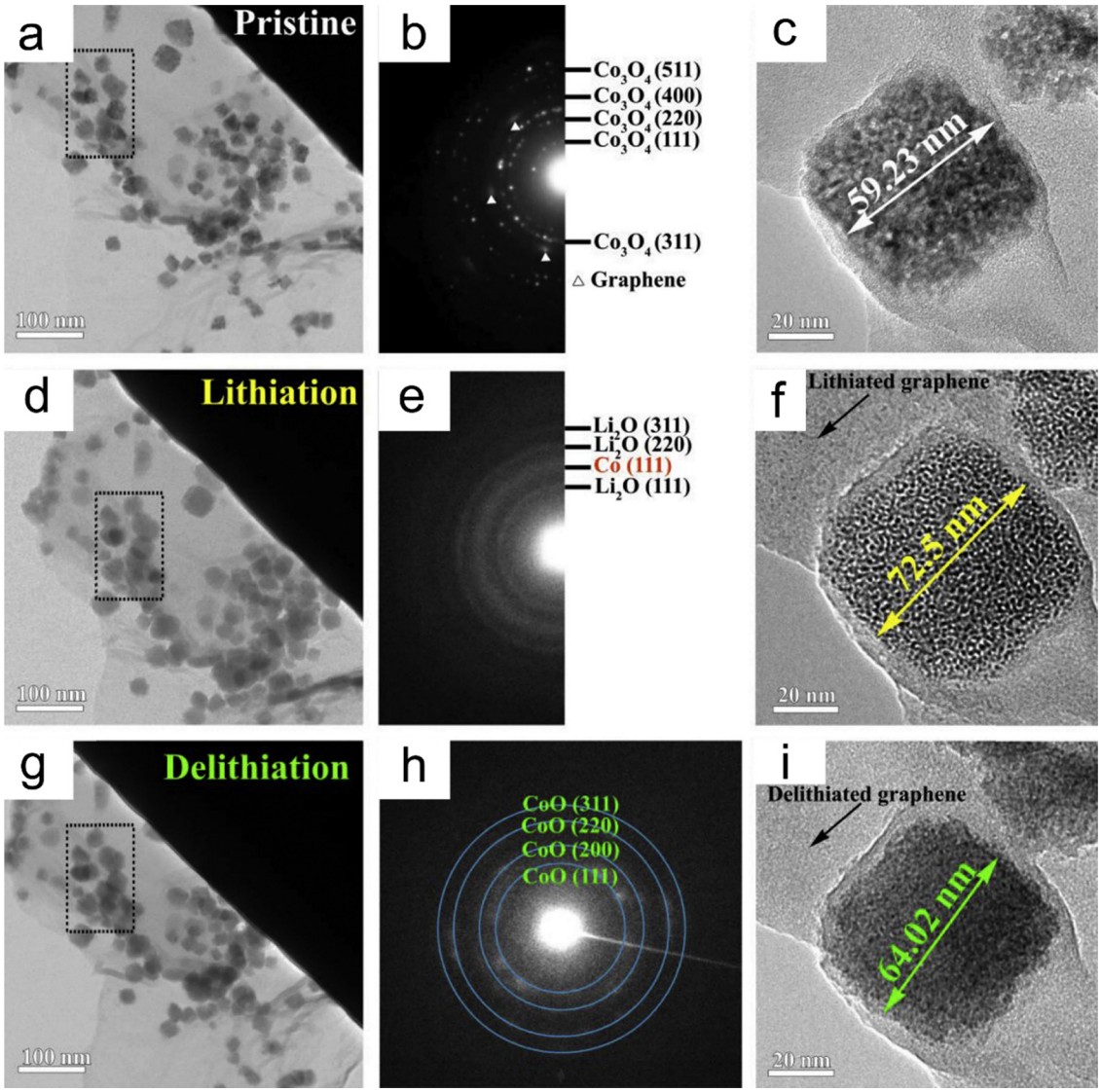

Fig. 8 The morphology and structures of Co_3O_4 anodes at (a)–(c) pristine, (d)–(f) lithiation and (g)–(i) delithiation states. Reproduced with permission.[136] Copyright 2018, Elsevier.

2.4.3. Summary. In MO anodes, the lithiation and delithiation processes typically involve a conversion reaction, where Li^+ reacts with the metal oxide to form metal nanoparticles (M) and lithium oxide (Li_2O). This is followed by an alloying reaction in some materials, where the metal produced during conversion further reacts with Li^+ to form Li_xM alloys, contributing to the overall capacity. These reactions allow for high Li^+ storage, but they also result in significant volume strain, which can cause mechanical degradation of the electrode material.

MO anodes can be classified into two main types based on their lithiation mechanism. The first type includes conversion-type oxides (*e.g.*, Fe_2O_3, Co_3O_4, and MnO_2), which undergo a reversible conversion reaction where metal nanoparticles are dispersed in a Li_2O matrix. The main challenge here is the loss of electronic connectivity due to the insulating nature of Li_2O and the coalescence of metal domains. The second is conversion-alloying-type oxides (*e.g.*, SnO_2, SnO, and Zn_2GeO_4). In these materials, the metal produced by conversion further alloys with lithium, forming Li-rich alloys. This step increases the capacity but also leads to larger and more anisotropic volume strain, causing cracking, debonding, and interfacial damage, which results in loss of electrical contact.

2.5. Phosphorus-based anodes

Phosphorus-based materials, including phosphorus allotropes and various phosphorus compounds (*e.g.*, Li_3P and Cu_3P), have emerged as promising candidates for anode materials in LIBs due to their exceptionally high theoretical capacities.[138–142] Compared to MOs, phosphorus-based materials typically possess narrower band gaps, resulting in better electronic conductivity. Moreover, elemental phosphorus features a layered structure, which facilitates efficient Li^+ diffusion during cycling (Fig. 9a).[143] Despite these advantages, the electrochemical performance of phosphorus-based anodes is strongly influenced by their discharge–charge mechanism and the associated volume strain. As illustrated in Fig. 9b, lithiation induces a gradual volume strain, reaching approximately 300% upon the formation of Li_3P, corresponding to a specific capacity of $\sim$2500 mAh g^{-1}.

2.5.1. Phosphorus allotropes. Phosphorus-based anodes have gained attention for their high theoretical capacities and distinct lithiation mechanisms. These materials can be categorized into red phosphorus (RP), black phosphorus (BP), and purple phosphorus (PP), which exhibit different structural characteristics and electrochemical behaviors.

RP is one of the most studied allotropes for anodes due to its relatively high theoretical capacity ($\sim$2596 mAh g^{-1}) and good electronic conductivity. The lithiation of RP involves a conversion reaction, where RP is first converted to amorphous phosphorus and then to lithium phosphide (Li_3P). This reaction is typically represented by:[144]

$$RP + 5Li^+ + 5e^- \rightarrow Li_3P \quad (2.5.1)$$

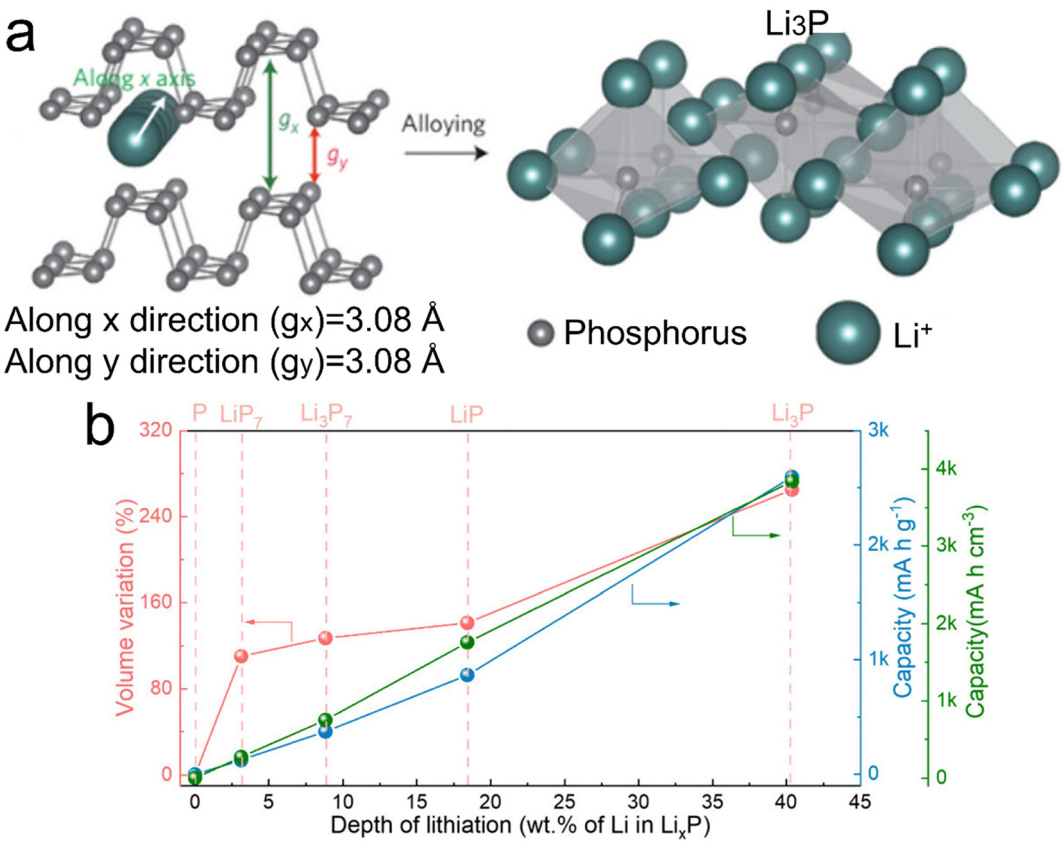

Fig. 9 (a) Structure and lithiated mechanism of a layered P anode. (b) Depth of lithiation *vs.* volume strain and capacity for BP anodes. Reproduced with permission.[143] Copyright 2024, American Chemical Society.

Despite its high capacity, the main limitation of RP anodes is the large volume expansion (~300%) during lithiation, which leads to significant mechanical degradation, particle fracture, and loss of electrical contact. To address these issues, nanostructuring and composite designs with conductive matrices (*e.g.*, carbon nanotubes) are often employed to mitigate strain and enhance cycling stability.[145]

BP is a 2D material that has garnered interest for its high capacity (~2596 mAh g^{-1}), excellent electronic conductivity, and unique anisotropic properties. The lithiation of BP follows a two-step conversion mechanism. Initially, BP is converted to lithium phosphide (Li_3P), followed by the formation of Li_xP alloys:[146]

$$BP + 3Li^+ + 3e^- \rightarrow Li_3P \quad (2.5.2)$$

$$Li_3P + xLi^+ + xe^- \rightarrow Li_xP \quad (3 < x \leq 3 + x) \quad (2.5.3)$$

The high surface area and tunable properties of BP make it a promising candidate for LIB anodes, but the main challenges include rapid degradation due to volume strain and surface oxidation in air. These can be mitigated through encapsulation in protective layers and composite strategies with carbon-based materials to improve mechanical stability and cycling performance.[147,148]

PP is another allotrope. Though less explored compared to RP and BP, PP has a layered structure that allows for relatively fast Li^+ diffusion, contributing to good rate capability. The lithiation of purple phosphorus also involves a conversion reaction, similar to RP:[149]

$$PP + 5Li^+ + 5e^- \rightarrow Li_5P \quad (2.5.4)$$

PP has a higher theoretical capacity than RP, but it suffers from more significant volume strain during the lithiation process, which leads to structural instability. The challenges associated with volume strain and cycling stability can be alleviated by nanostructuring and hybridizing with conductive agents, improving the mechanical properties and cycle life of the material.[150,151]

2.5.2. Phosphorus-containing silicon compounds. Silicon phosphides, including SiP, SiP_2, and SiP_3, have also garnered attention as phosphorus-based anode materials due to their high theoretical capacities, typically in the range of 1500–2000 mAh g^{-1}.[152–154] However, similar to elemental phosphorus, these compounds suffer from severe volume strain during lithiation, which presents a major obstacle to their practical application. Recent studies, particularly those employing DFT simulations, have focused on exploring the structural and electrochemical properties of these materials. SiP exhibits a layered 2D crystalline microribbon-like morphology, which is expected to promote rapid Li^+ intercalation and diffusion. SiP_2, a layered semiconductor with pronounced in-plane anisotropy, also supports fast Li^+ transport due to its unique crystal structure. SiP_3, while more structurally complex, encounters similar challenges related to volume strain and capacity fading. To mitigate these issues, various strategies have been investigated—most notably, carbon-based modifications. These modifications introduce conductive matrices and interfacial buffering layers, which enhance both mechanical stability and electrochemical performance.[155]

The lithiation mechanisms of phosphorus-rich silicon compounds such as SiP_2 have been explored through experimental studies. The lithiation process proceeds in multiple steps:[153]

$$SiP_2 + xLi^+ + xe^- \rightarrow Li_xSiP_2 \quad (x \leq 1.8) \quad (2.5.5)$$

$$Li_xSiP_2 + xLi^+ + xe^- \rightarrow Li\text{–}Si\text{–}P(\text{amorphous}) \quad (2.5.6)$$

$$Li\text{–}Si\text{–}P(\text{amorphous}) + xLi^+ + xe^- \rightarrow Li_{13}Si_4 + Li_3P \quad (2.5.7)$$

The subsequent delithiation occurs as follows:

$$Li_{13}Si_4 + Li_3P \rightarrow 4Si + Li_3P + 13Li^+ + 13e^- \quad (2.5.8)$$

$$Si + 2Li_3P \rightarrow SiP_2 + 6Li^+ + 6e^- \quad (2.5.9)$$

These reaction pathways highlight the complex phase transformations and amorphization phenomena that occur during cycling, which must be carefully managed to ensure long-term stability.

2.5.3. Non-metallic/metalloid phosphides. Phosphorus–sulfur (P–S) compounds represent an emerging class of materials with high theoretical capacities and unique electrochemical properties. These materials typically undergo a conversion reaction, followed by an alloying reaction, which makes them attractive candidates for high-capacity anodes. For example, phosphorus trisulfide (P_2S_5, which is a well-known P–S compound) exhibits a high theoretical capacity (~2000 mAh g^{-1}) and has shown promise for use as an anode material in LIBs.[156,157]

$$P_2S_5 + 10Li^+ + 10e^- \rightarrow 2Li_3P + 5Li_2S \quad (2.5.10)$$

In this reaction, P_2S_5 is reduced to Li_3P and Li_2S, with Li_2S acting as a buffering phase that helps alleviate volume strain. This material undergoes significant volume strain during lithiation, similar to other phosphorus-based compounds, but the sulfur component helps to mitigate some of the mechanical degradation by maintaining structural integrity.

Tin phosphide (SnP) is a promising metalloid phosphide that combines the high capacity of tin-based alloys with the structural benefits of phosphorus. The lithiation mechanism of SnP involves a conversion reaction where SnP is reduced to Li_3P, followed by the formation of Li_xSn alloys:[158]

$$SnP + 3Li^+ + 3e^- \rightarrow Li_3P + Sn \quad (2.5.11)$$

$$Sn + xLi^+ + xe^- \leftrightarrow Li_xSn \quad (0 \leq x \leq 4.4) \quad (2.5.12)$$

SnP combines the high theoretical capacity (~2380 mAh g^{-1}) of tin with the structural stability provided by the phosphorus component. While SnP suffers from volume strain during lithiation, its mechanical stability is often improved by composite electrodes that incorporate carbon or other stabilizing agents. Moreover, SnP's conductivity and rate capability are typically higher than those of other phosphorus-based anodes, making it a strong contender for high-power applications.

Germanium phosphide (GeP) is another metalloid phosphide that has been studied for its high capacity and electrochemical performance. GeP follows a similar lithiation mechanism to that

of SnP, involving a conversion reaction to Li_3P followed by alloying with Li^+:[159]

$$GeP + 3Li^+ + 3e^- \rightarrow Li_3P + Ge \quad (2.5.13)$$

$$Ge + xLi^+ + xe^- \leftrightarrow Li_xGe \quad (0 \le x \le 4.4) \quad (2.5.14)$$

GeP offers an enhanced electronic conductivity compared to SnP, making it suitable for high-rate applications. However, like SnP, volume strain during lithiation remains a challenge. To address this, nano-engineering and composite materials are often employed to improve cycling stability and prevent electrode degradation.

Non-metallic/metalloid phosphides, such as phosphorus-sulfur compounds, SnP, and GeP, offer high theoretical capacities and unique electrochemical behaviors, making them strong candidates for anodes.[160] These materials typically undergo conversion and alloying mechanisms, which contribute to their high storage capacities. However, the volume strain during lithiation and mechanical degradation remains a significant challenge.[158] Strategies like nanostructuring, composite electrodes, and interface engineering are being explored to mitigate these issues and enhance the cycling stability and rate performance of these materials.

2.5.4. Summary. Overall, phosphorus-based anodes include phosphorus allotropes (RP, BP, and PP), phosphorus-containing silicon compounds (SiP, SiP_2, and SiP_3), and non-metallic/metalloid phosphides (such as P–S compounds, as well as SnP and GeP). They are attractive for LIBs because their lithium storage mainly involves P to Li_3P conversion (often coupled with Sn/Ge alloying reactions), enabling exceptionally high theoretical capacities, while their relatively narrow band gaps and, in some cases, layered frameworks can facilitate charge transport and Li^+ diffusion. However, their electrochemical behavior is commonly accompanied by pronounced phase transformations and amorphization together with ~300% level volume strain, which induces particle pulverization, disruption of conductive networks, interfacial instability, and loss of electrical contact, ultimately leading to rapid capacity fading and limited cycle life. To realize durable high-capacity operation, current efforts focus on nano/microstructural engineering (*e.g.*, nanostructuring and hierarchical porosity) to mitigate stress accumulation, combined with carbon-based conductive/buffering matrices, protective coatings, and interface engineering to simultaneously enhance electron/ion transport and mechanical integrity. In particular, P–S systems can generate buffering phases (Li_2S) that partially accommodate volume strain, whereas SnP and GeP typically offer higher conductivity and better rate capability and still require composite and interfacial regulation to overcome strain-driven structural degradation.

2.6. Strategies for mitigating volume strain through compositing

As discussed in previous sections, many high-capacity anode materials—such as Si-based, Sn-based, Ge-based, MO-based, and phosphorus-based anodes—undergo significant volume strain during lithiation and delithiation. Generally, higher specific capacities are accompanied by more pronounced volume changes, which can lead to mechanical degradation, particle fracture, and loss of electrical contact.

To address these challenges, a variety of compositing strategies have been developed (Fig. 10). These approaches aim to engineer anode materials capable of accommodating large volume strain while preserving both structural integrity and electrochemical performance. The following are key compositing strategies used to mitigate volume strain:

(1) Core–shell structures: in this design, the active material (*e.g.*, Si) is encapsulated within a protective shell composed of materials such as carbon, graphene, or MO. The shell not only provides mechanical confinement to buffer volume strain but also enhances electronic conductivity, thereby improving overall battery performance. During cycling, the shell absorbs strain forces, reducing the risk of structural failure.

(2) Hollow/porous structures: creating anode materials with hollow or porous architectures introduces internal void space to accommodate strain without fracturing the structure. These features reduce material density and increase surface area, facilitating better Li^+ access and faster reaction kinetics.

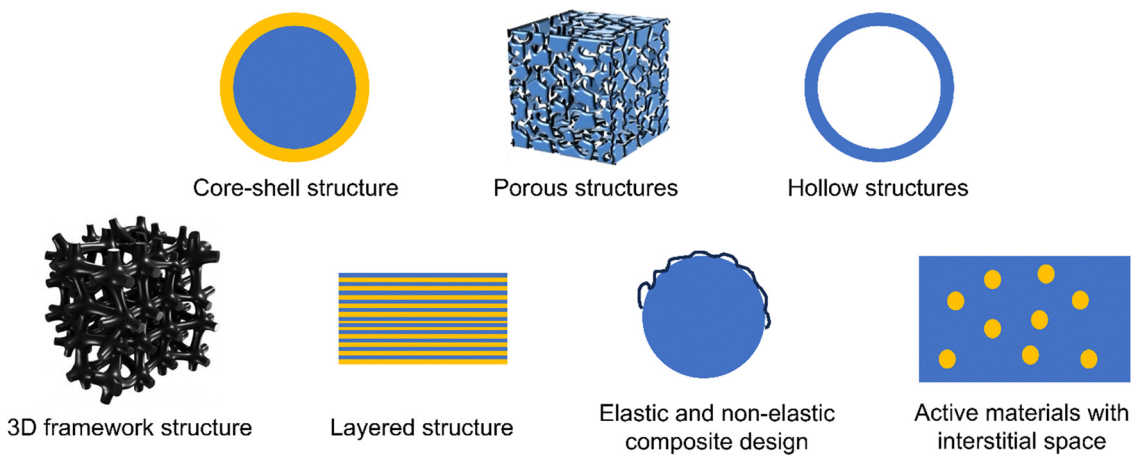

Fig. 10 Strategies for mitigating volume strain through compositing: core–shell, porous, hollow, 3D framework, and layered structure; elastic and non-elastic composite design and active materials with interstitial space.

Optimized porosity also contributes to strain accommodation while maintaining mechanical robustness.

(3) Three-dimensional (3D) network structures: a 3D conductive network—such as a carbon scaffold or metallic framework—can provide mechanical support and stress distribution for active particles undergoing volume strain. This interconnected framework serves as a structural backbone, ensuring the continuity of electron and ion transport pathways and maintaining the integrity of the electrode over extended cycling.

(4) Layered (multilayer) structures: multilayered designs incorporate alternating soft and rigid layers to absorb and dissipate mechanical stress during lithiation and delithiation. The soft layers act as cushions, reducing the likelihood of particle fracture, while rigid layers preserve structural order. This approach effectively enhances cycling stability by reducing internal stresses.

(5) Elastic and non-elastic composite designs: combining elastic materials (*e.g.*, flexible carbon frameworks or polymers) with non-elastic components (*e.g.*, metal oxides) allows for controlled strain distribution within the composite. The elastic matrix can deform reversibly to accommodate volume strain, while the non-elastic phase ensures structural coherence and contributes to electrochemical activity.

(6) Active materials with interstitial space: incorporating spherical particles with interparticle gaps into composite structures introduces interstitial spaces that serve as expansion buffers. These voids help absorb strain, reduce mechanical stress, and minimize particle pulverization, especially in materials like silicon that undergo extreme volumetric changes.

Compositing strategies not only mitigate volume strain but also generate abundant internal interfaces during fabrication. These contact interfaces play a pivotal role in enhancing electron and Li^+ transport, which in turn improves rate capability, cycling stability, and overall energy density. The subsequent section explores the crucial influence of these interfaces on Li^+ storage performance.

3. Geometric classification of contact interfaces

Because this work focuses on anode materials, the contact interfaces in this section refer to the contact interfaces within the active material itself. Based on geometric considerations, contact interfaces in electrode materials can be classified into three types (Fig. 11): (1) surface-to-surface (StS) contact; (2) line-to-line (LtL) contact; and (3) point-to-point (PtP) contact.[161] StS contact refers to a configuration in which two phases interact over a broad, continuous interface. This model enables efficient ion and electron transfer, making it highly desirable for

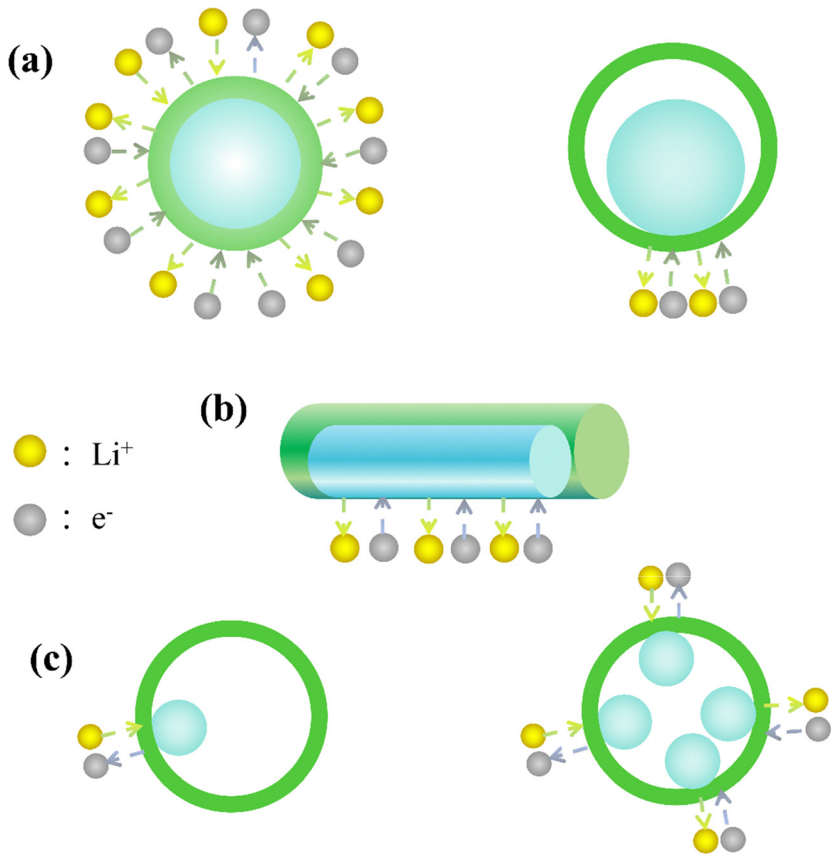

Fig. 11 Schematic illustrating the contact interfaces from geometric aspects: (a) surface-to-surface (StS), (b) line-to-line (LtL), and (c) point-to-point (PtP).

maximizing electrochemical performance. However, StS contact often compromises the porosity of the material, which may adversely affect the cycling stability of electrodes, particularly in systems undergoing significant volumetric strain during cycling.[162] In contrast, LtL contact typically occurs when one of the materials features a nanorod or wire-like geometry. The restricted contact area along a single line reduces ion and electron transport efficiency compared to StS. Nevertheless, the additional free volume in the LtL configuration provides greater tolerance for mechanical strain, improving structural stability during cycling. PtP contact represents the most geometrically constrained configuration, where only a single point connects the two phases. This minimal contact area severely limits ion and electron transfer, making PtP contact the least efficient in terms of electrochemical kinetics. Additionally, repeated volume changes during cycling can destabilize the interface, further degrading performance. Since electrochemical reactions require the simultaneous transport of ions and electrons, the contact model plays a critical role in determining both reaction kinetics and overall rate performance.[163]

3.1. Surface-to-surface contact (StS)

The most representative example of StS contact is the core@shell structure, where the active material is encapsulated by a shell layer. This design minimizes direct contact between the active material and the electrolyte, suppressing the formation of unstable SEI layers. Furthermore, if holes are made in the shell through a specific method, it is expected to solve the problem of slow Li^+ diffusion to a certain extent and enhance the rate performance.[164,165] The shell layer may even serve as a dual-functional component, replacing both the conductive agent and the electrolyte by facilitating rapid ion and electron transfer to the active core.[63,166]

StS interfaces can be further categorized into full and partial contact types. In full StS contact, the entire interface between the core and shell is engaged (Fig. 12a), whereas partial StS contact involves only localized contact, with other regions remaining electrically and ionically isolated (Fig. 12b).[167,168] The full contact configuration maximizes interface utilization, thereby enhancing charge transfer. However, it lacks internal free volume, meaning the shell must absorb all mechanical stresses during cycling. Repeated volumetric expansion and contraction can lead to shell cracking and loss of structural integrity.[169–171]

To mitigate this, voids or internal cavities are introduced into the StS structure.[172,173] The inclusion of such internal free space allows the surface coating to buffer the volume strain of the active material, while also providing a mechanism for strain release internally. These voids buffer the volume strain of the active core and relieve stress on the shell, thereby preserving structural stability without significantly compromising interfacial transport.[170,174,175] Nevertheless, such a void inclusion reduces the tap density of the material, lowering volumetric energy density.[176,177]

A notable example is the SiO_x@carbon anode developed by Wei's group. This composite features a continuous carbon shell tightly encapsulating the SiO_x core (Fig. 13a–d), achieving both enhanced charge transfer and effective stress buffering. As a result, the anode delivers a high specific capacity ($\sim$200 mAh g^{-1} at 5 A g^{-1}) and retains $\sim$80% of its initial capacity after 100 cycles, outperforming bare SiO_x electrodes (Fig. 13e–j). The carbon shell also limits electrode strain to 7.1%, compared to $\sim$99.6% for the uncoated version. However, despite these improvements, the cycling stability still lags behind that of other optimized SiO_x-based anodes due to the intrinsic limitations of the StS model in accommodating large volume changes during (de)lithiation.[178]

3.2. Line-to-line contact (LtL)

While LtL contact models provide a smaller contact area and therefore reduced ion/electron transport efficiency,[177] they offer substantial void space for strain accommodation, which is critical for long-term cycling stability.[179,180] As a result, this model helps reduce the stress on the shell material during

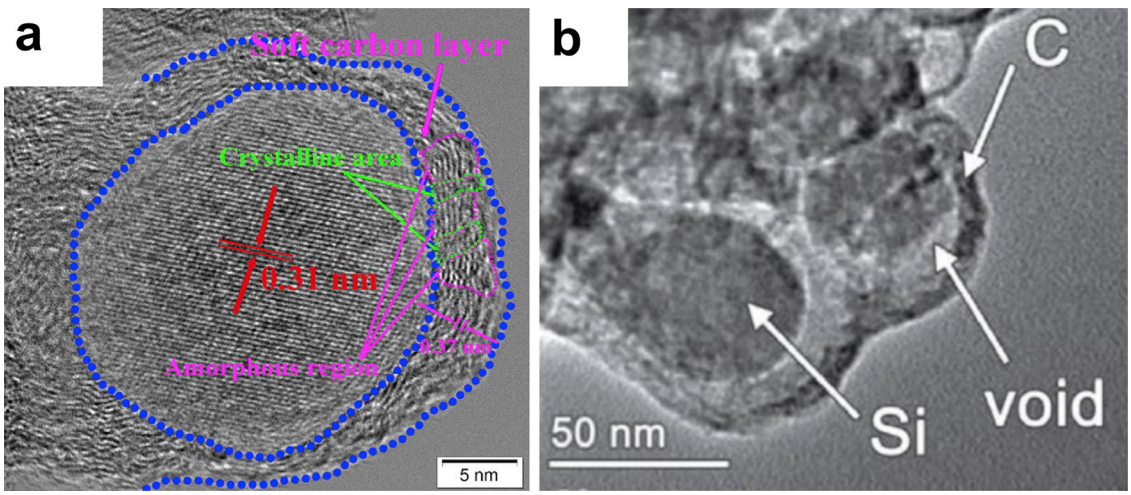

Fig. 12 TEM image of the (a) full and (b) partial StS model. Reproduced with permission.[172] Copyright 2012, Wiley-VCH GmbH.

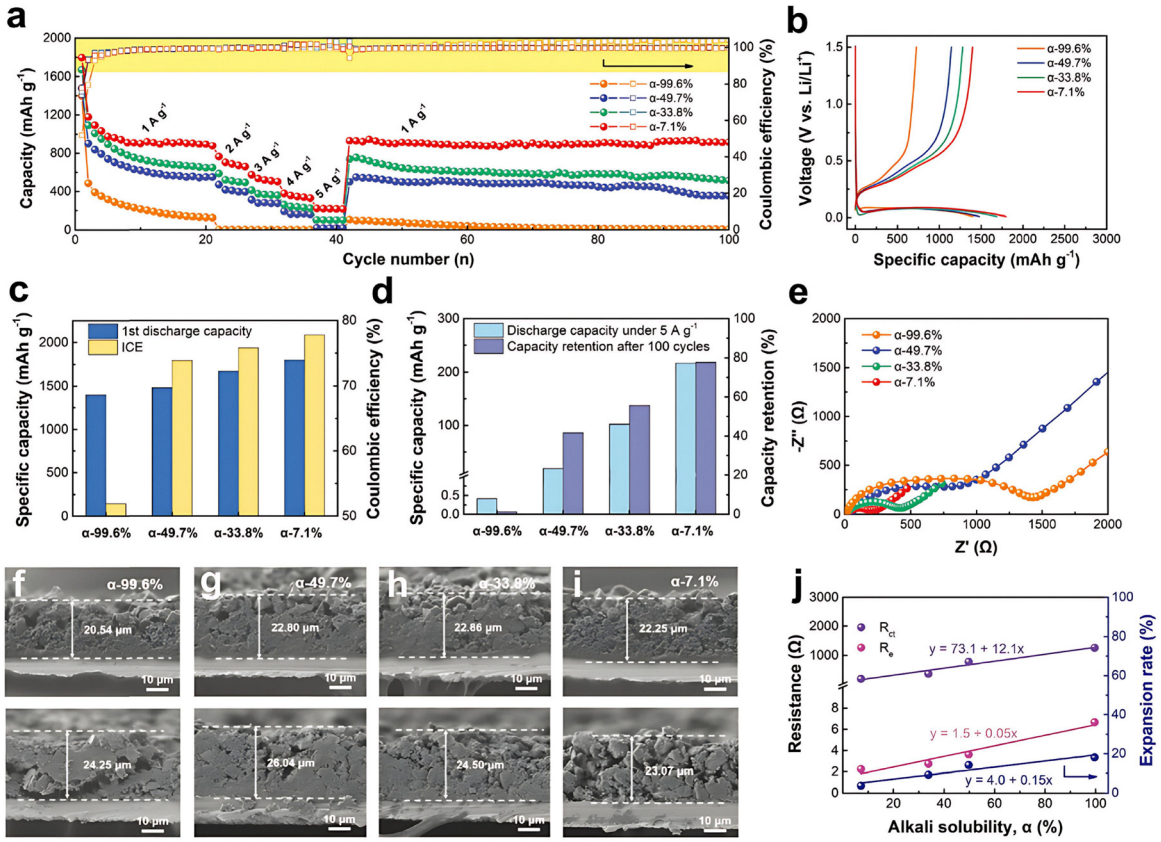

Fig. 13 (a) Rate performance, (b) discharge–charge curves, (c) specific capacity and initial coulombic efficiency, (d) capacity retention, (e) EIS plots, (f–i) thickness change, and (j) resistance *vs.* volume strain relationship of SiO_x@carbon. Reproduced with permission.[178] Copyright 2023, Wiley-VCH GmbH.

cycling, leading to improved long-term cycling stability.[181,182] This model is commonly found in nanowire-in-tube architectures, where a 1D nanowire is confined within a hollow tubular shell (Fig. 11b).[183] In this configuration, the contact occurs along a line, and the anisotropic structure supports progressive electrochemical reactions from the contact line outward.[184–186] However, because Li^+ must traverse the full diameter of the nanowire core, the maximum Li^+ diffusion length in LtL contacts is approximately double that in StS systems, reducing rate capability.[177,187] Assuming the contact model is the dominant factor influencing transport, the rate performance follows the trend: StS > LtL > PtP.

Chen *et al.* developed SnO_2 nanowires encapsulated in titanate nanotubes (SnO_2@C-HTO) as an anode material for Li^+ storage, using a combination of electrostatic spray deposition, annealing, and solution methods (Fig. 14). The resulting SnO_2@C-HTO exhibits excellent rate capability and cycling stability, attributed to the unique LtL structure. As the current density increases from 0.2 to 5 A g^{-1}, the specific capacity remains nearly constant, demonstrating the anode's superior electron and Li^+ transfer efficiency (Fig. 15). Compared to conventional SnO_2-based anode materials, SnO_2@titanate nanotubes show significantly enhanced rate performance, particularly at high current densities. Moreover, after 500 charge–discharge cycles, the anode maintains its specific capacity without noticeable degradation, highlighting its long-term stability. These findings suggest that the LtL structure, designed with careful consideration, contributes to achieving outstanding electrochemical performance in anode applications.

3.3. Point-to-point (PtP)

For materials experiencing large volume strain, two main design principles guide the development of stable electrodes: (1) minimizing direct contact with the electrolyte to reduce SEI formation[188,189] and (2) incorporating internal voids to relieve mechanical stress during (de)lithiation.[33,190] Although LtL contact models can fulfill these criteria, their fabrication often requires complex and expensive processes, such as chemical vapor deposition (CVD).[191–194] In contrast, zero-dimensional materials, typically spherical particles, are easier to synthesize due to their low surface energy.[195] However, they inherently form PtP contacts, severely restricting ion/electron transfer.[196] PtP contact can be subcategorized into single-point, multi-point, and bridge-contact models, each exhibiting distinct transport properties.[192,197]

In the single-point model (Fig. 11c), electron and ion transfer occurs through a single, isolated contact interface. Although strain during cycling may introduce new contact points, transport remains inefficient under high current conditions.[198] To improve performance, the multi-point model introduces several contact points, often by encapsulating nanoparticles within a conductive matrix.[199]

For example, Zhao *et al.* created a graphene-encapsulated Si composite using CVD and Ni templating (Fig. 16a and b). While

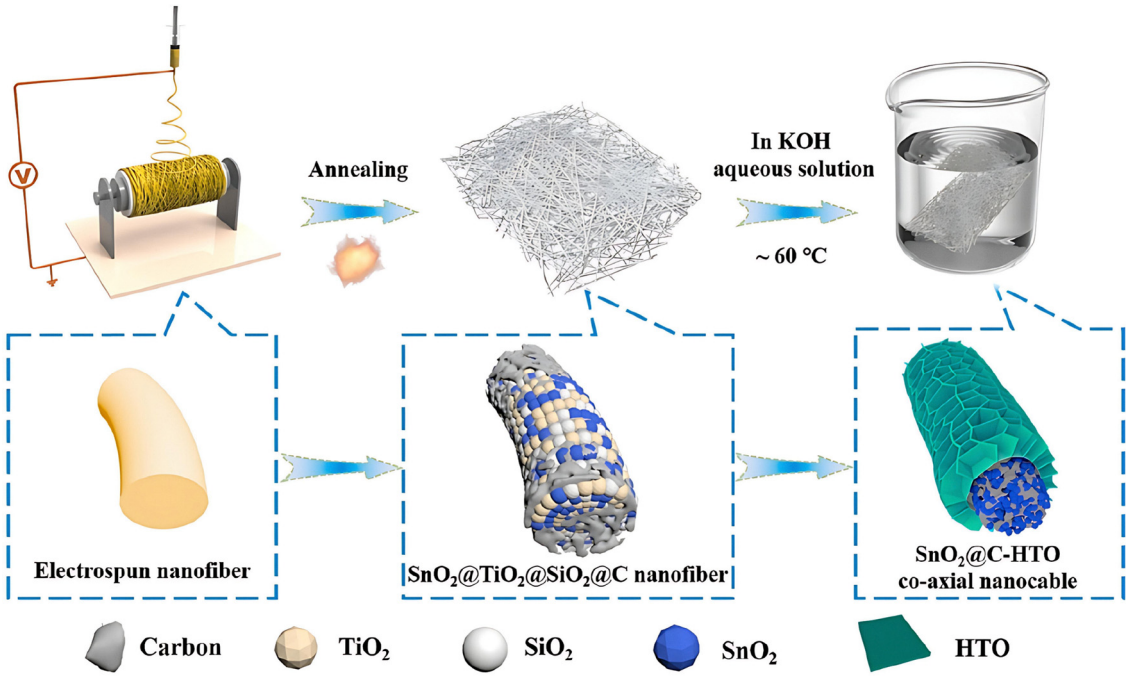

Fig. 14 Preparation of SnO_2 nanowires encapsulated into titanate nanotubes. Reproduced with permission.[87] Copyright 2024, Elsevier.

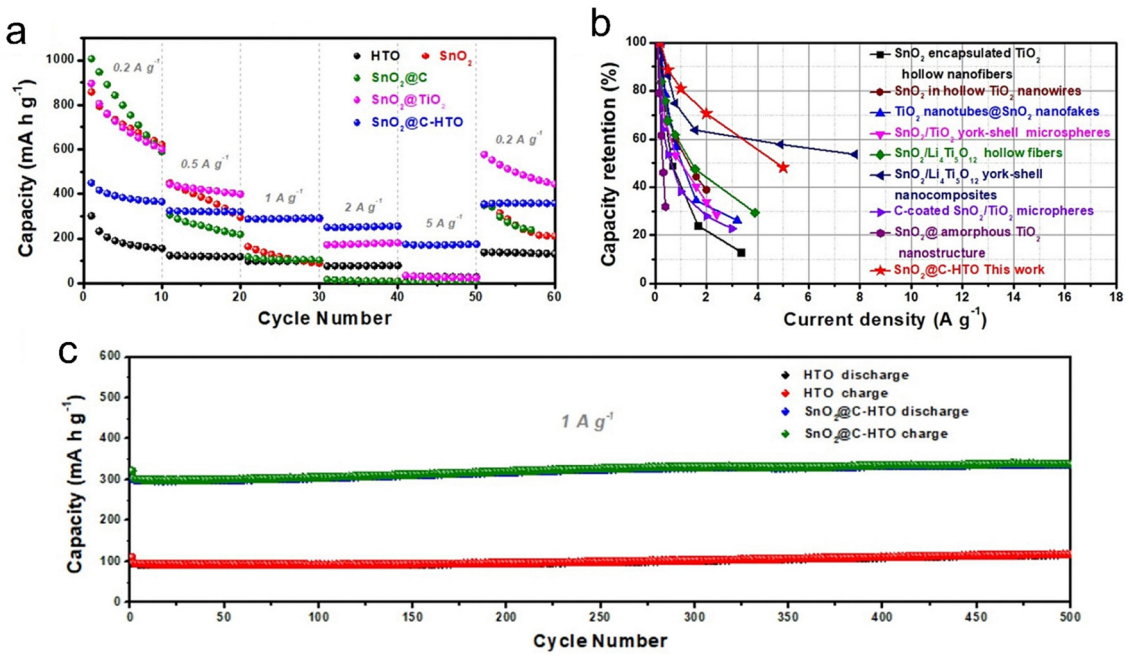

Fig. 15 (a) Rate-performance. (b) Performance comparison. (c) Cycling performance of SnO_2@ titanate nanotubes with the LtL model. Reproduced with permission.[87] Copyright 2024, Elsevier.

this structure enhances transport relative to the single-point model, it still has a smaller contact area compared to LtL and StS contact interfaces. It suffers from low volumetric density due to internal porosity.[200,201] For the single point contact model in the ideal situation, if the void in the shell can be filled due to the large volume train of active materials after lithiation, the void utilization would achieve 100% (Fig. 16c). However, the void generally cannot be fully packed, as in Fig. 16b. In multi-point contact structures, the space utilization increases with the increasing number of core materials under the condition that the void is not filled. If the void is filled, void utilization is inversely proportional to the number of particles filled.

For composite materials with single-point contact, the contact mode may shift from single-point to StS contact as the electrode material undergoes volume strain due to electrochemical reactions. In contrast, for the multi-point contact model,

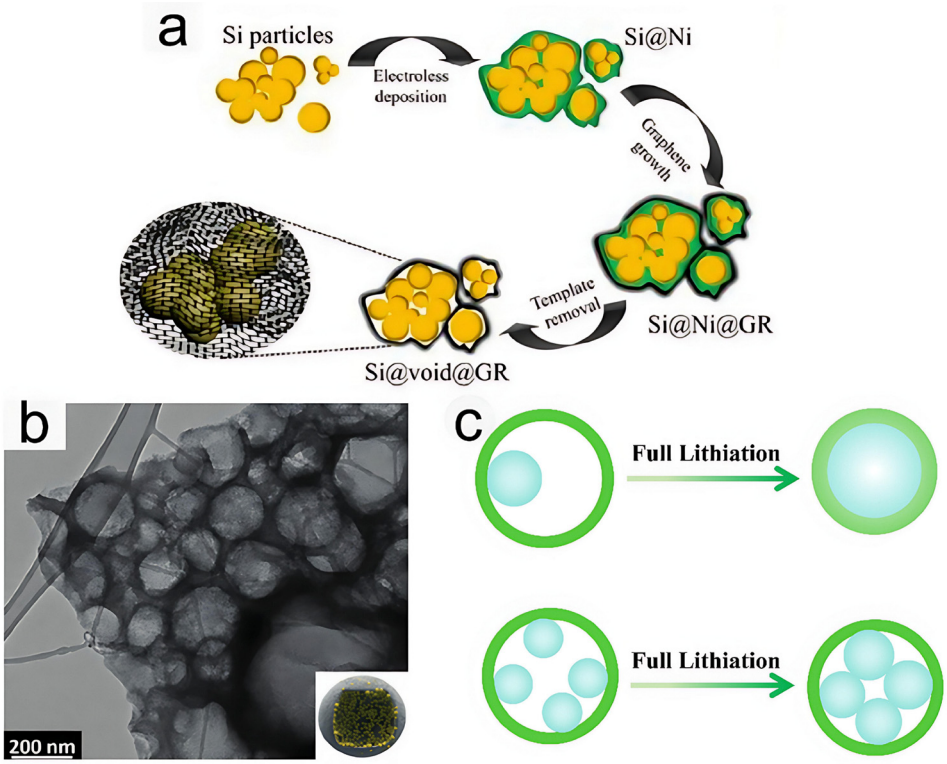

Fig. 16 (a) Schematic illustration and (b) TEM image of the PtP model. Reproduced with permission.[200] Copyright 2017, Wiley-VCH GmbH. (c) Comparison of the space utilization rate between multipoint contact and single point contact.

even after the strain of the electrode material, the contact mode remains multi-point contact due to the tangential relationships between multiple particles, with a significant number of pores still present inside the composite material.[200] To enhance the volumetric specific capacity of the multi-point contact model, two strategies can be employed: (1) increasing the size of the core materials and increasing their quantity, and (2) filling the unoccupied spaces with other materials.[172]

Further improvements of reaction kinetics can be achieved by incorporating bridge joint contacts, where one-dimensional (1D) carbon nanotubes (CNTs) or nanowires fill the voids between active particles (Fig. 17).[202] This approach enhances connectivity and transport efficiency, reducing electrolyte infiltration in turn, which minimizes SEI growth and improves coulombic efficiency.[202,203] A compelling example is the yolk shell Si@C composite (YS-Si/C), where CNTs are embedded within a hollow structure to form bridge contacts.[204] This design enhances both ionic and electronic transport while preventing excessive strain and structural degradation. EIS confirms reduced charge-transfer resistance and improved Li^+ diffusion (Fig. 18a). The composite maintains high capacities ($\sim$1700 mAh g^{-1} at 1–2 A g^{-1}) and excellent retention over 100 cycles (Fig. 18b–d), underscoring the effectiveness of bridge joint architectures.[202,205]

3.4. Coexistence of contact interfaces

The discussion above treats PtP, LtL, and StS contact interfaces as idealised geometries to clarify their individual transport and mechanical characteristics. In real composite anodes, however, these contact interfaces rarely appear in isolation. Instead, multiple contact interfaces are hierarchically organised from the primary particle level up to secondary agglomerates and the electrode scale.[206–209] Recognising this coexistence is essential for correctly interpreting electrochemical behaviour and for designing practical architectures.

In representative Si@C/CNT networks, Si nanoparticles are anchored onto interwoven CNTs, forming extended LtL contacts along the CNT sidewalls.[210] These LtL contact interfaces provide continuous, flexible electron pathways bridging multiple Si particles, effectively converting a collection of isolated PtP contacts into a connected line network, while the CNTs can accommodate part of the Si volume strain *via* bending and sliding.[211,212] Third, numerous Si/C composites employ conformal carbon or SiO_x shells on Si particles (Fig. 19a). In Si/CNT@C, for instance, a resorcinol–formaldehyde-derived carbon shell uniformly coats both Si nanoparticles and CNTs, welding them together into a three-dimensional porous structure.[213] Similarly, partial Si–C bond formation at Si/graphitic contact interfaces leads to strong adhesion between Si (or SiO_x) and the surrounding carbon matrix.[214] These contact interfaces can be viewed as local StS contacts that homogenise current distribution, stabilise the SEI, and buffer volume strain by converting Si strain into more uniform shell deformation.[215] As a result, a well-designed Si/C composite is not a pure PtP, LtL, or StS system, but a hierarchical combination of all three, with PtP contacts between primary particles, LtL connections along 1D conductive filaments, and

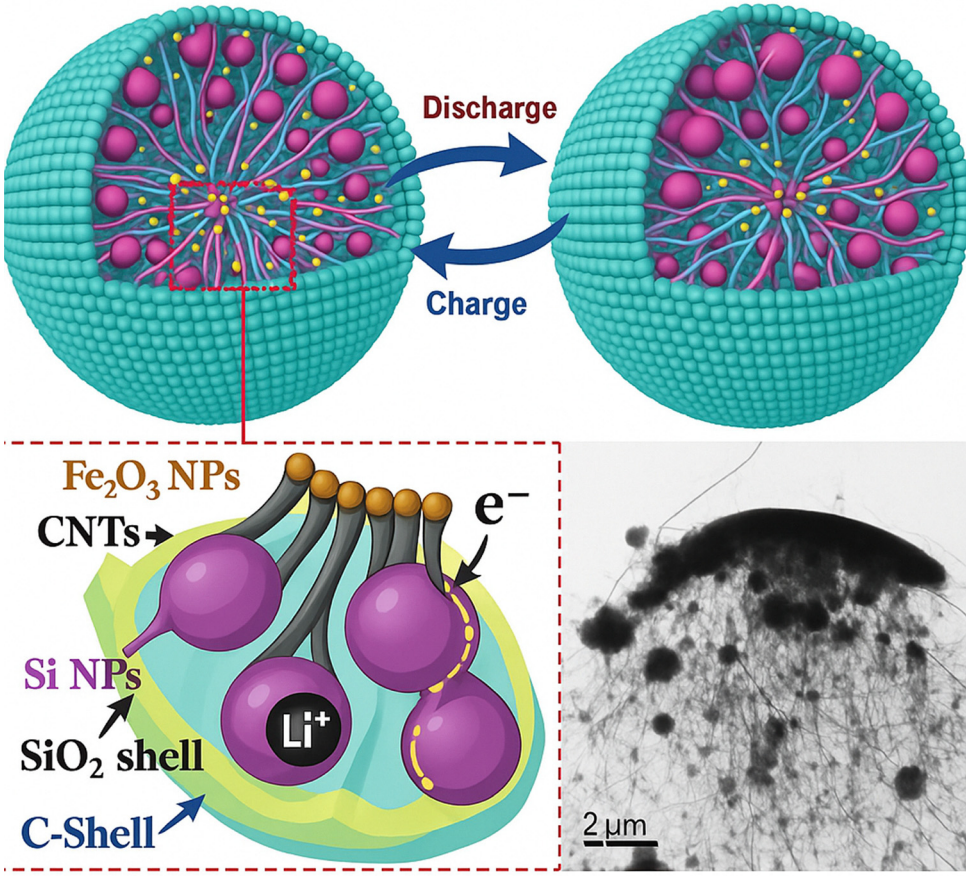

Fig. 17 Schematic and TEM morphology of bridge joint point contact. Reproduced with permission.[202] Copyright 2019, Wiley-VCH GmbH.

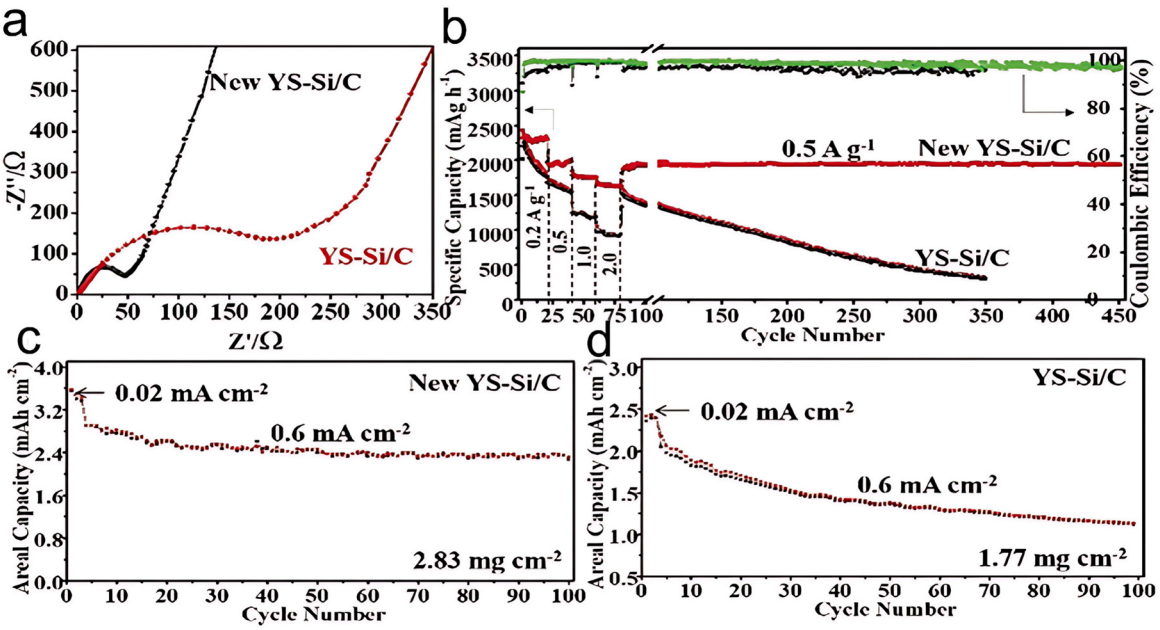

Fig. 18 (a) EIS plots, (b) rate performance, and (c) and (d) cycling stability of YS-Si/C. Reproduced with permission.[202] Copyright 2019, Wiley-VCH GmbH.

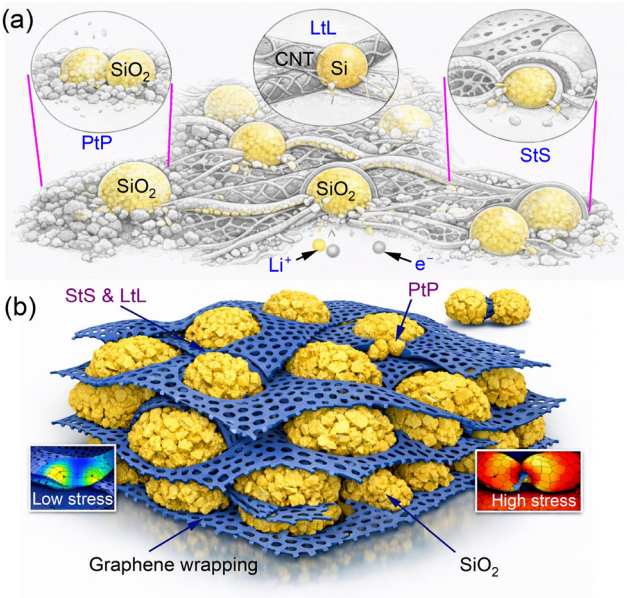

Fig. 19 (a) Hierarchical contact interfaces governing stress regulation and (b) electrochemical stability in HG@SiO_2 anodes.

StS core–shell or matrix–particle contact interfaces that dominate the mechanical and electrochemical stability.

A similar coexistence of PtP, LtL, and StS contact interfaces appears in other high-strain anode architectures, such as bioinspired mechanically interlocking holey graphene@SiO_2 (HG@SiO_2) anodes (Fig. 19b).[216] In this design, the interlocking regions between protruding SiO_2 domains and holey graphene sheets act as extended StS/LtL contact interfaces, transmitting strain from SiO_2 into the tougher graphene and reducing the maximum von Mises stress in the oxide. Overlapping and partially wrapped graphene edges form additional LtL connections that bridge neighbouring SiO_2 particles, while residual isolated SiO_2 particles or small clusters still interact with the conductive framework mainly *via* PtP contacts. Finite-element analysis (FEA) shows that these interlocking StS/LtL contact interfaces significantly reduce local stress and strain energy in SiO_2 compared with planar graphene@SiO_2, whereas PtP-dominated regions exhibit higher local stress and a greater tendency for debonding. The outstanding cycling stability of HG@SiO_2 (with high capacity at large current densities over thousands of cycles) can thus be understood as the result of a favourable hierarchy of contact interface geometries, where mechanically robust StS/LtL contact interfaces dominate but some PtP contact interfaces persist.

These examples highlight that our geometric classification is powerful when used as a multi-scale descriptor rather than as a set of mutually exclusive categories. Real composite anodes should be designed not to realise a single ideal contact interface, but to optimise the hierarchy and spatial distribution of PtP, LtL, and StS interfaces according to the specific requirements of ionic/electronic transport, mechanical compliance, and volumetric energy density.

3.5. Geometric state of the interface evolves dynamically

It is important to note that the classifications of PtP, LtL, and StS primarily correspond to the initial contact configurations established during material design or assembly. However, in high-volume-strain anodes, the contact interfaces are subjected to intense chemo-mechanical coupling, leading to continuous evolution in contact area, topology, and bonding strength during electrochemical cycling.[217] This evolution may manifest as either positive contact reinforcement (PtP/LtL to StS) or degradative contact loss (StS/LtL to PtP or discontinuous contact networks). The trajectory of this evolution is dictated by the magnitude of volume strain, stress dissipation pathways, and the mechanical toughness and adhesion strength of the interface/shell.[218,219]

For high-strain alloying materials, the expansion resulting from lithiation can substantially enlarge the actual contact area between particles or at the active phase–conductive skeleton contact interface.[220,221] This leads to a transition from discrete PtP or LtL contacts to quasi-StS configurations, which temporarily boosts electron and ion transport connectivity (Fig. 20a).[222] When SnO_2 nanoparticles are confined within ordered carbon pores or thin-walled carbon surface nanotubes, the lithiated Sn species swell to fill the channels, forming a broad surface contact with the carbon walls that far exceeds the initial point contact in efficiency. The theory of strain-promoted contact has been confirmed by correlating structural evolution with electrochemical performance.[223] In the case of Si anodes, *in situ* TEM has revealed that Si particles expand against their encapsulating shells or carbon networks, achieving a tighter fit that reflects a geometric shift from local to continuous contact. Consequently, as long as the outer contact interface preserves its integrity, this contact reinforcement can secure more stable conductive and mass transport channels.[224]

Although the expansion phase may enhance contact, the contact interfaces frequently suffer from debonding, cracking, and embrittlement under subsequent delithiation shrinkage and repetitive cyclic stress.[225] Consequently, originally continuous StS or LtL contact interfaces are fragmented into multiple PtP contacts or even disconnected voids, leading to the rupture of conductive networks and the repeated exposure of fresh surfaces. Extensive studies on core–shell or carbon-coated Si systems demonstrate that when the shell is excessively thin or interfacial adhesion is insufficient, the cycled shell gradually fractures and the contact interface delaminates. This results in a degradation of the contact geometry from the initial StS to discrete PtP or discontinuous LtL states, inducing continuous SEI regeneration and capacity decay (Fig. 20b).[226] Similarly, if high-strain particles like Si undergo pulverization during cycling, their contact with conductive agents or current collectors also degenerates from continuous surface contact into a fragmented point-contact network. This serves as one of the core origins of the dual mechanical-transport degradation in high-strain anodes.[227]

In addition to the bulk deformation of the active phase, interfacial SEI growth and the accumulation of side-reaction products fundamentally alter the real implications of geometric contact. For instance, in a typical yolk–shell Si@void@C

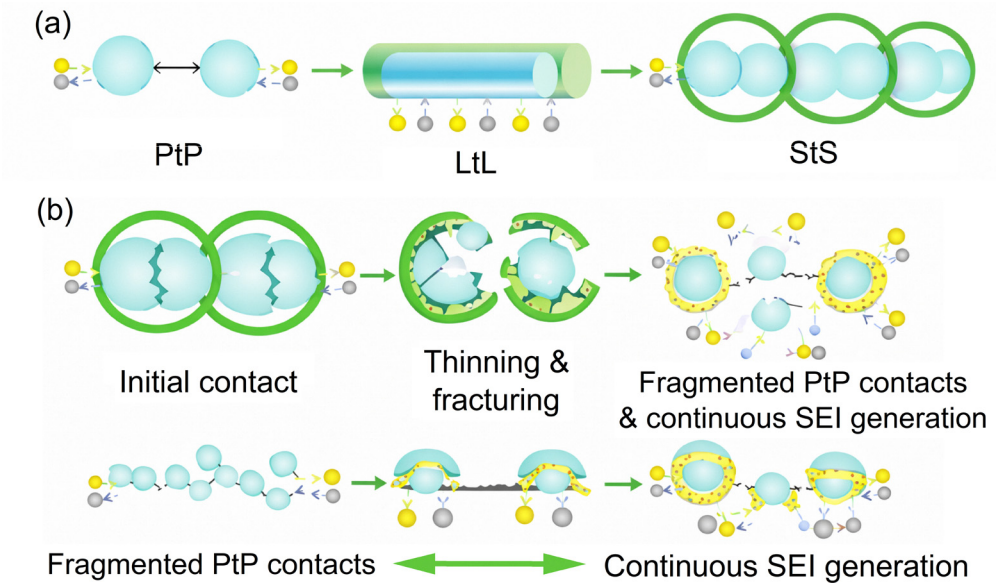

Fig. 20 Schematic diagram of high strain anode contact interface evolution. (a) Schematic of contact evolution from PtP to StS. (b) Schematic of degradation and SEI formation in high-strain anodes.

system, originally designed to feature weak or discontinuous contact (biased towards PtP/LtL) between the Si core and carbon shell with reserved void space, the SEI progressively accumulates inside the void and fills the gaps during cycling.[228]

This process transforms the assembly from a free-expansion core–shell structure to a Si@porous-SEI@C composite contact interface state. Consequently, the core is semi-fixed by the SEI, causing the contact geometry to transition from PtP/LtL to a more extensive quasi-StS configuration, while charge transport and stress distribution at the interface are reconfigured by this third phase of SEI.

3.6. Comparative analysis and design paradoxes

Each contact model, StS, LtL, and PtP, offers distinct advantages and limitations. As depicted in Fig. 21, transitioning from StS to PtP enhances structural stability but reduces volumetric energy density, illustrating the stability–capacity paradox. Simultaneously, the progressive reduction in contact area impairs charge transfer, giving rise to the stability–rate performance paradox. These trade-offs highlight the inherent challenges in optimizing electrode architectures. Achieving a balance among rate performance, cycling stability, and energy density remains a complex task, requiring innovative structural designs that transcend the limitations of traditional contact models.

To further substantiate the geometric classification, we summarize representative literature data that link the designed contact geometry with measurable kinetic parameters (Table 2). Although absolute values vary with contact models, the compiled cases consistently show that enlarging the real contact area (PtP to LtL to StS) tends to reduce interfacial polarization (lower R_{ct}), accelerate Li^+ transport (higher D_{Li}), and improve rate capability, whereas introducing line- or point-dominated contacts provides larger strain-buffering space and thus favors long-term structural integrity.

Although Si-based composites have been used as the primary model systems in this section, similar PtP/LtL/StS combinations have now been realised in other high-volume-strain anodes. SnO_2/SnS_x nanoparticles decorated on or encapsulated by carbon spheres and graphene sheets form mixed PtP–StS networks that closely mirror the SiO_x@C and graphene/SiO_2 architectures discussed above. BP/carbon composites typically feature BP platelets that are covalently tethered to graphitic

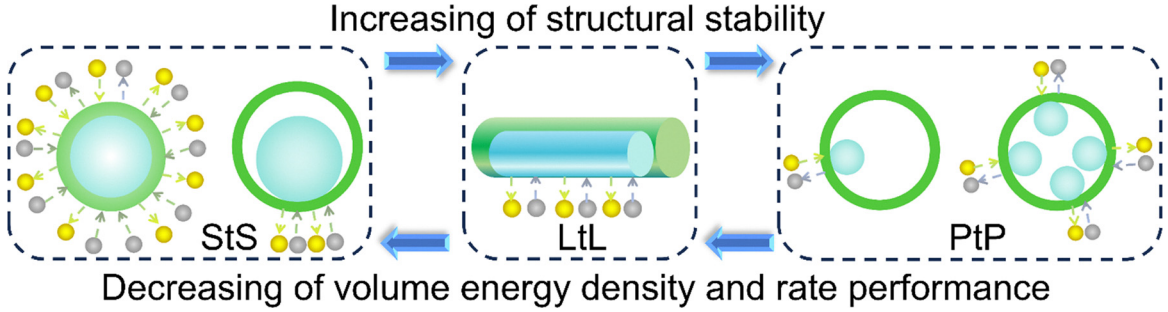

Fig. 21 Effect of electrochemical performance for the three types of models.

Table 2 Quantitative correlation between interface geometry and performance metrics

Geometry	Sample	R_{ct} value (Ω)	Li^+ diffusion coefficient	Cycling stability	Ref.
PtP	SS-SiNPs	253.6	—	A capacity retention of 90% after 200 cycles	229
PtP	Si NPs@SnO_2@C	70	10^{-12} cm^2 s^{-1}	A capacity retention of 60% after 500 cycles	230
LtL	CNTs–Si–CNTs	22	—	A capacity retention of 98% after 500 cycles	231
LtL	TH-Fe_2O_3@SnO_2	70.79	—	A capacity retention of 35% after 100 cycles	232
LtL	Si@PPy-2	78.20	1.46×10^{-12} cm^2 S^{-1}	A capacity retention of 95% after 1000 cycles	233
StS	SiO_2@NPC Y.S.	74.2	$K = 31.57$ Ω $s^{-1/2}$	A capacity retention of 94.3% after 300 cycles	234
StS	$CoNiO_2$@C	205.7	$K = 5.91$ Ω $s^{-1/2}$	A capacity retention of 83% after 200 cycles	235
StS	SGC pitch	85.3	5×10^{-19} cm^2 s^{-1}	A capacity retention of 99.38% after 200 cycles	236
StS	HG@SiO_2	21	—	A capacity retention of 90% after 8000 cycles	216
StS	Yolk–Shell Cu_2O@CuO@RGO	12	—	A capacity retention of 90% after 200 cycles	237
StS	Hp-SiOC@VG	12	6.7×10^{-13} cm^2 s^{-1}	A capacity retention of over 98% after 600 cycles	238
StS	SiO@2D-NC	50.37	7.12×10^{-10} cm^2 s^{-1}	A capacity retention of 88% after 200 cycles	239
StS	Si-CBPOD	12.1	$1.23–1.42 \times 10^{-10}$ cm^2 s^{-1}	A capacity retention of 75% after 1000 cycles	240
StS	PCSi-2	0.75	1.5×10^{-10} cm^2 S^{-1}	A capacity retention of 99% after 500 cycles	241
StS	Si-PLSA75	—	3.32×10^{-13} cm^2 S^{-1}	A capacity retention of 80% after 300 cycles	242

Note: The abbreviation is explained as follows. Secondary submicron Si materials composed of nanoparticles (SS-SiNPs); Si nanoparticles deposited with ultrasmall SnO_2 NPs and further coated by an ultrathin carbon on the surfaces (Si NPs@SnO_2@C). CNTs–Si–CNTs nanocomposites with the tubular sandwich structure (CNTs–Si–CNTs); terminal hollowed Fe_2O_3@SnO_2 heterojunction nanorods (TH-Fe_2O_3@SnO_2); one-dimensional linear polypyrrole-coated Si nanoparticles (Si@PPy-2) yolk–shell-structured SiO_2@N, P co-doped carbon spheres (SiO_2@NPC Y.S.); pitch-coated Si nanolayer–embedded graphite (SGC pitch); rambutan-like vertical graphene coated hollow porous SiOC (Hp-SiOC@VG); yolk–shell Cu_2O@CuO-decorated reduced graphene oxide (yolk–shell Cu_2O@CuO@RGO); the formation of uniform 2D-NC coating on SiO (SiO@2D-NC); robust nitrogen/sulfur Co-doped carbon frameworks (Si-CBPOD).

carbon and further wrapped by polymer or inorganic SEI layers, creating an interplay of PtP contacts between BP, LtL contacts along carbon nanotubes or nanosheets, and StS contacts at the BP/carbon or BP/SEI interfaces.[243,244] Transition-metal oxide/carbon and oxide/graphene hybrids likewise exhibit PtP contacts between oxide nanograins, LtL conduction along carbon filaments, and StS contact interfaces at oxide–carbon or oxide–electrolyte contact regions. These non-Si case studies confirm that the PtP/LtL/StS geometric framework is a general descriptor for internal contacts in alloy- and conversion-type anodes.[245,246]

However, due to inconsistent testing conditions (loading, voltage, electrolyte system, *etc.*) in different literature studies, it is challenging to attribute performance differences solely to contact geometry based on the capacity retention rate and number of cycles. Moreover, absolute values vary significantly and data are multidimensional depending on the specific contact models and material/electrochemical properties, and establishing their models and functional relationship is a challenge.

4. Physical/chemical classification of contact interfaces

In Section 4, contact interfaces in anode materials themselves with high-volume strain were classified based on geometric configurations. While useful, this classification does not fully capture the nature of interfacial interactions and the physical and chemical forces governing charge transfer and structural stability at the molecular and atomic levels. To address this limitation, this section reclassifies contact interfaces between anodes themselves based on their interaction mechanisms, as illustrated in Fig. 22. From a physical perspective, interfaces can be governed by weak interactions such as π–π stacking, hydrogen bonding, van der Waals forces, and electrostatic interactions. This also includes heterogeneous electronic junctions, such as homojunctions and heterojunctions, which influence charge transport behavior across material boundaries. From a chemical perspective, interfaces characterized

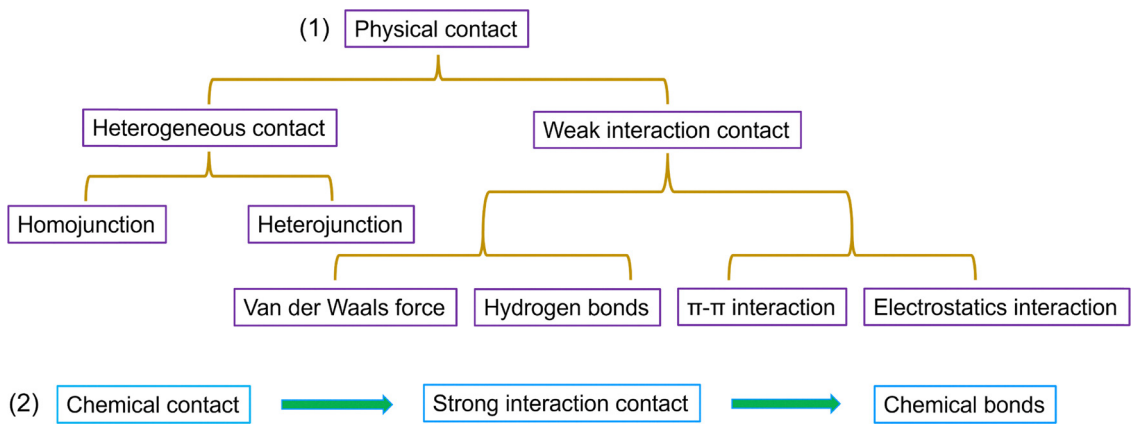

Fig. 22 Schematic illustrating the contact interfaces from physical and chemical aspects.

by strong interactions, the formation of covalent or ionic bonds, can dramatically alter interfacial stability, charge transfer efficiency, and mechanical anchoring of materials. The following sections discuss the impact of both weak and strong contact interfaces on the performance of Li^+ anodes under large-volume strain.

4.1. Weak interactions

Weak interactions, including π–π stacking (between aromatic systems), hydrogen bonding (involving F, O, and N atoms), van der Waals forces, and electrostatic interactions, are often referred to as non-covalent interactions.[247,248] These forces facilitate self-assembly and *in situ* polymerization without altering the inherent chemical structure of the constituent materials.[249,250] As a result, key properties such as mechanical strength, electronic conductivity, and electrochemical activity are largely preserved in the resulting composites. Moreover, due to their dynamic and reversible nature, weak interactions offer flexibility in modulating the performance of the composite materials during cycling.[250,251] However, they present challenges in constructing well-defined, uniform micro/nano-structured interfaces.[252]

Due to their high electrical conductivity, excellent mechanical properties, and easy contact interface modification, carbonaceous materials are widely used in composites for anodes with large volume strain. Moreover, Si/carbon composite materials are gradually achieving commercialization. Due to the unique sp^2 structure and ease of modification of carbon materials, various weak interaction forces are generated between them,[252] these include π–π interactions,[253,254] electrostatic interactions,[255] and hydrogen bonding,[256] as illustrated in Fig. 23.[257] As most carbon materials are part of a π-extended system, π–π interactions are commonly observed between carbon-based materials.[258] Additionally, the inherent modifiability of carbon materials results in a significant number of oxygen-containing functional groups (such as hydroxyl, carboxyl, and epoxy groups) on their surfaces.[259] Upon hydrolysis, these functional groups create electrostatic interactions at exposed sites with varying electrostatic properties. These sites can then interact with other sites of opposite polarity.[260] Furthermore, if the functional groups contain oxygen, nitrogen, or fluorine atoms, hydrogen bonds can frequently form between different functional groups.[248,261] The following section discusses the weak interactions between graphene and Si-based anodes, specifically in the context of self-assembled graphene aerogels.

Meng *et al.* synthesized a SiO_2-loaded epoxidized graphene hydrogel using graphene oxide (GO) and tetraethyl orthosilicate (TEOS) under hydrothermal conditions.[262] The formation of this anode material involves several weak interaction mechanisms, as illustrated in Fig. 23a. The hydrophilic oxygen-containing functional groups (such as carboxyl, hydroxyl, and epoxy groups) present on the GO surface facilitate its uniform dispersion in water, allowing it to form a stable precursor solution. The oxygenated groups on GO generate an electric double layer upon hydrolysis, resulting in a negative zeta potential and electrostatic repulsion between the graphene sheets, thereby ensuring their dispersion.[263,264] Following hydrothermal reduction, most of the epoxy groups on the GO surface are removed, leaving the graphene sheets clean and enabling them to stack together *via* π–π interactions, ultimately forming a hydrogel.[265] This graphene hydrogel, held together by weak forces, possesses an intricate internal pore structure that provides sufficient strain space for the SiO_2 anode material. Furthermore, the overlapping graphene sheets establish a conductive network, which significantly enhances the rate performance of SiO_2. Additionally, the hydrothermal process induces the formation of abundant hydroxyl groups on the SiO_2 surface. These hydroxyl groups interact with the oxygen-containing functional groups (such as hydroxyl, carboxyl, and epoxy groups) on the graphene through weak hydrogen bonding interactions. However, despite these advantages, the aerogels formed through these weak interactions suffer from poor mechanical properties and are prone to damage after repeated cycling.

Sun *et al.* synthesized SiO_x nanoparticles encapsulated in a graphene aerogel (SGA) through a hydrothermal method, where SiO_x interacts with the graphene aerogel *via* weak interactions. Due to the weak contact between SiO_x and graphene, the contact interface is prone to damage during the initial stages of cycling, which hampers the cycle stability at the beginning (Fig. 23b and 24). Interestingly, the specific capacity gradually stabilizes after experiencing initial attenuation. This phenomenon may be attributed to the reconstruction of the flexible interface (the weak contact region), which eventually reaches a more stable configuration over time.

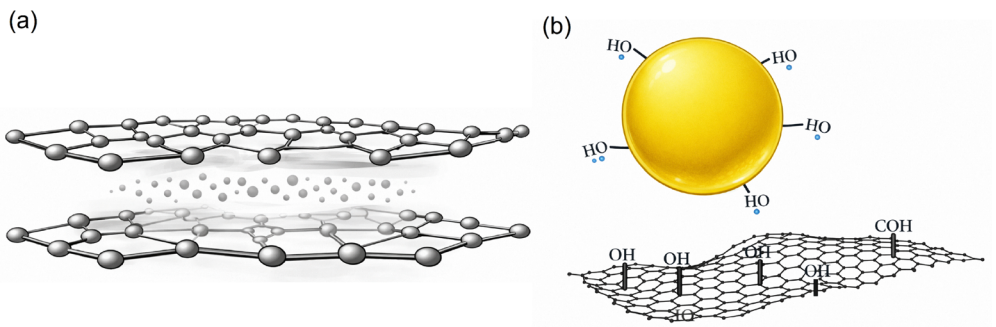

Fig. 23 (a) Schematic of electrostatic interaction, hydrogen bonding, and π−π stacking. (b) Hydrogen bonding interaction between graphene and SiO_2.

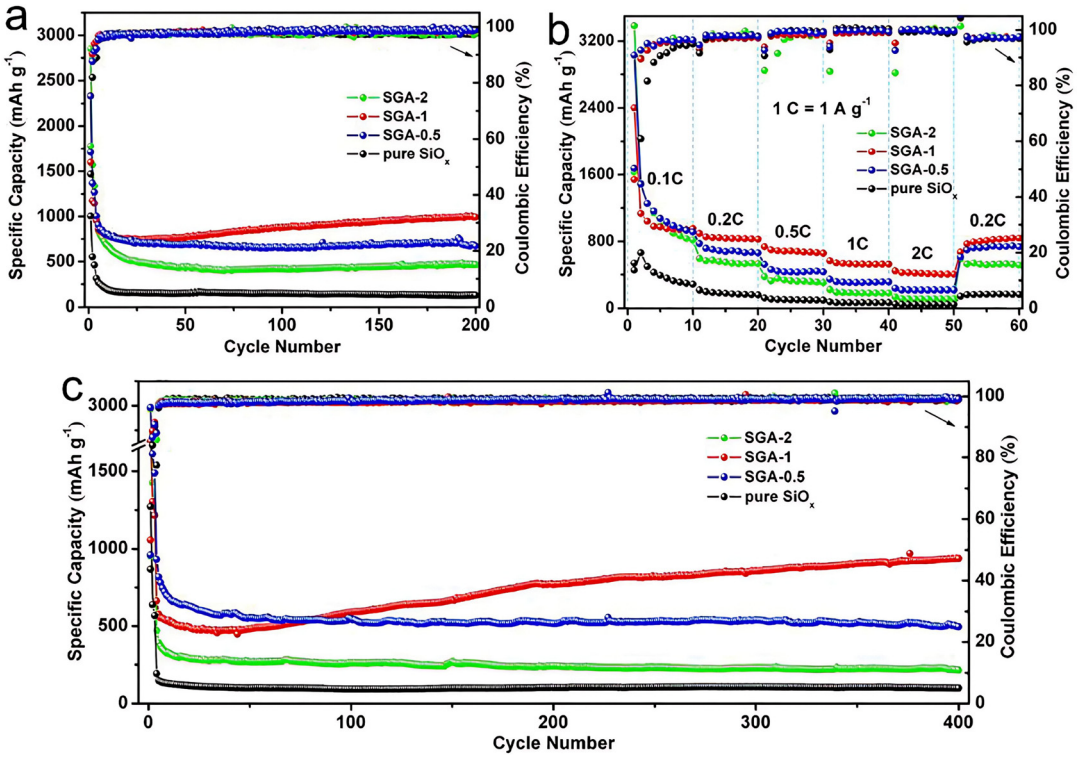

Fig. 24 (a) and (c) The cycling performance of SiO_x and SGA. (b) Rate performance of SiO_x nanoparticles encapsulated within a graphene aerogel. Reproduced with permission.[266] Copyright 2022, Elsevier.

4.2. Strong contact interfaces

A strong contact interface refers to a contact where the interfacial interaction goes beyond van der Waals physisorption and involves substantial chemical bonding or alloy formation, such as M–O–C bridges, covalent M–C bonds, or intermetallic M–Si phases. Contact interfaces with DFT-calculated adhesion or binding energies on the order of ~0.8–1.0 eV (or higher) per interfacial metal site, corresponding to works of adhesion W_{ad} > 0.5–1.0 J m^{-2}, are classified as strong, whereas purely van der Waals contacts typically exhibit binding energies of only a few tens of meV per atom and W_{ad} < 0.2 J m^{-2}.[267] Such strong contact interfaces ensure intimate electronic and ionic coupling and can partially clamp the active material, thereby modifying volume-strain behaviour and crack initiation; at the same time, excessively strong bonding may suppress beneficial interfacial sliding and induce stress concentration, so an optimal interaction strength rather than an arbitrarily large one is desired.[268,269]

Common methods for constructing such contact interfaces include CVD, condensation reactions, free radical polymerization, and hydrothermal reactions.[270–272] Compared to weak contact interfaces, those based on strong chemical bonding offer greater structural stability and enhanced interfacial coupling.[273] Moreover, the complex chemical reactions involved enable precise control over the morphology and functional properties of the resulting nanocomposites by tuning the synthesis conditions.[274,275] These methods are highly efficient and versatile for fabricating nanocomposites with well-defined structures and tailored performance.

Fe_3O_4/graphene composites with strong interfacial interactions (denoted as RG/Fe_3O_4) were synthesized *via* a high-temperature hydrothermal method, leveraging the formation of robust chemical bonds between graphene and Fe_3O_4.[276] Even after prolonged ultrasonic treatment, the Fe_3O_4 nanoparticles remained firmly anchored to the graphene surface, confirming the presence of strong contact interfacial bonding. Fig. 25a displays the EIS plots for composites with strong (RG/Fe_3O_4) and weak (Fe_3O_4 + rGO) interactions. The charge transfer resistance values, derived from fitting, were 47.4 Ω for RG/Fe_3O_4 and 87.7 Ω for Fe_3O_4 + rGO, indicating that strong interfacial interactions significantly enhance charge transfer efficiency.[277] In the low-frequency region of the EIS spectra, the Z_{re} *vs.* $\omega^{-1/2}$ plot shows that the RG/Fe_3O_4 electrode exhibits a lower σ value, suggesting more rapid Li^+ diffusion facilitated by the strong interfacial coupling (Fig. 25b).[278] Furthermore, as shown in Fig. 25c, the RG/Fe_3O_4 electrode demonstrates a higher Li^+ adsorption capacity, consistent with its greater theoretical specific capacity.[279] The density of states (DOS) diagram in Fig. 25d reveals a higher carrier density at the Fermi level for RG/Fe_3O_4, further underscoring the enhanced electronic conductivity resulting from the strong interaction interface.[280]

Such strong interfacial bonding substantially improves both electron and ion transport across the compositing contact interface. For anode materials subjected to high volume strain, strong interaction interfaces play a crucial role in anchoring the active material to the conductive matrix, thereby optimizing its buffering and conductive functions.[281–283] A representative

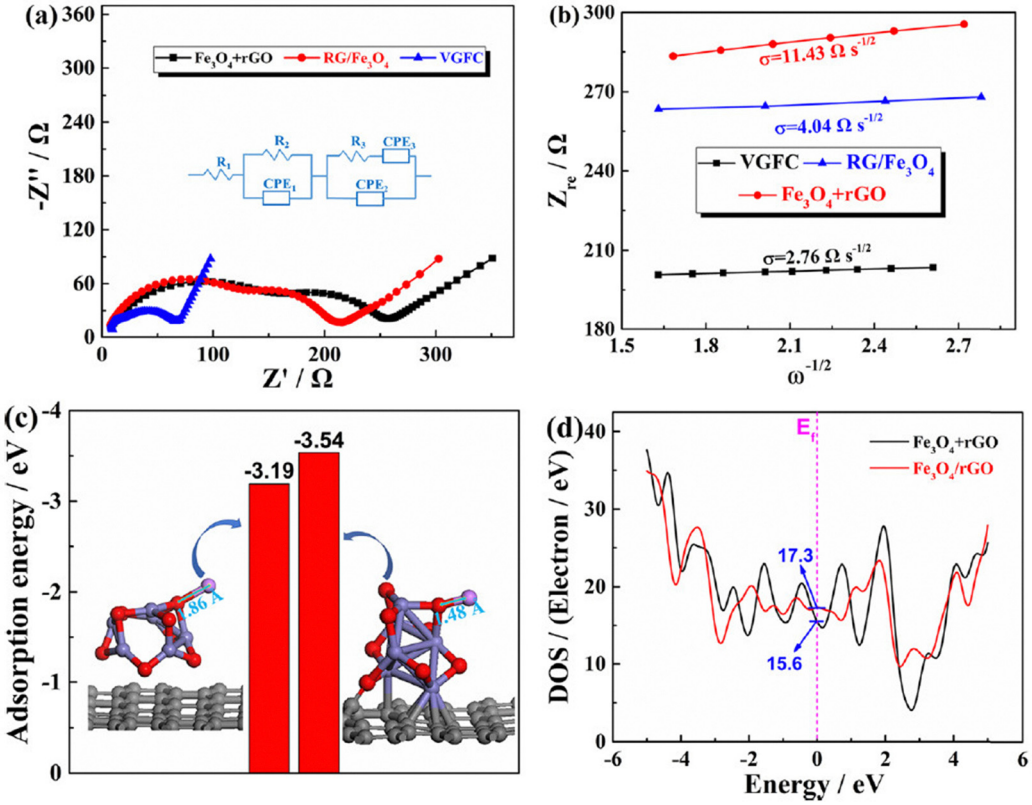

Fig. 25 (a) EIS plots of VGFC, RG/Fe_3O_4, and Fe_3O_4 + rGO and the corresponding equivalent circuit model (inset). (b) Z_{re} *vs.* $\omega^{-1/2}$ curves of the three electrodes. (c) E_{ad} values of Li^+ on Fe_3O_4 + rGO and Fe_3O_4/rGO and the corresponding optimized configurations. (d) DOS of Fe_3O_4/rGO and Fe_3O_4 + rGO (the Fermi level is set to zero). Reproduced with permission.[276] Copyright 2021, American Chemical Society.

example is the strongly coupled Si@soft carbon/graphene composite, synthesized *via* electrostatic self-assembly followed by sintering, forming stable Si–C bonds at the contact interface (Fig. 26a). This robust interfacial coupling facilitates efficient electron transport while effectively mitigating the volumetric strain of the Si core. In contrast, Si/graphene anodes fabricated *via* mechanical mixing, relying only on weak van der Waals interactions, suffer from poor cycling stability and limited rate performance. The Si@soft carbon/graphene composite, on the other hand, exhibits markedly superior electrochemical performance in terms of both cycling stability and rate capability (Fig. 26b–d).[63]

Generally, both strong and weak interaction interfaces are integral to contact interface chemistry. Due to the complexity of anode materials and battery systems, numerous strong/weak interaction interfaces with varying dimensions can exist, such as between inorganic materials, whether during material preparation or the charging and discharging processes. Therefore, designing and optimizing these strong/weak interaction interfaces in composite anode materials and battery systems is crucial for enhancing the overall performance of batteries.

4.3. Heterogeneous interfaces

The concept of a heterojunction originates from physics, where it refers to the contact interface formed between two different semiconductors (Fig. 27). Based on the conductivity types of the materials involved, these contact interfaces can be classified as homojunctions (P–p or N–n junctions).[284–286] or heterojunctions (P–n or p–N junctions).[287] In the context of anode materials, however, the concept takes on a broader meaning: two materials with different band gaps (electrostatic potentials) can be combined to form a heterojunction.[288–290] The mismatch in electrostatic potentials at the contact interface creates a built-in electric field,[291] which drives ions from the region of lower potential to higher potential. This interfacial electric field facilitates ion transport along the contact interface and also introduces additional ion storage sites, thereby enhancing the specific capacity of the anode material.[292]

Tong's group synthesized a series of anodes, including SiO_x@Si, SiO_x@Si/rGO, and c-SiO_x@Si/rGO anodes. The differences in work functions among Si, SiO_x, and graphene induce local electric fields at the heterointerfaces (Si/SiO_x and SiO_x/graphene), as illustrated in Fig. 28a–d. These interfacial electric fields promote the efficient transport of both electrons and Li^+. As a result, the SiO_x@Si/rGO anode exhibits the best rate performance among the three, maintaining a high specific capacity with minimal degradation even at a current density of 8 A g^{-1} (Fig. 28e). Additionally, the cycling stability is significantly enhanced by the presence of graphene, which improves the mechanical robustness of the composite electrode (Fig. 28f).

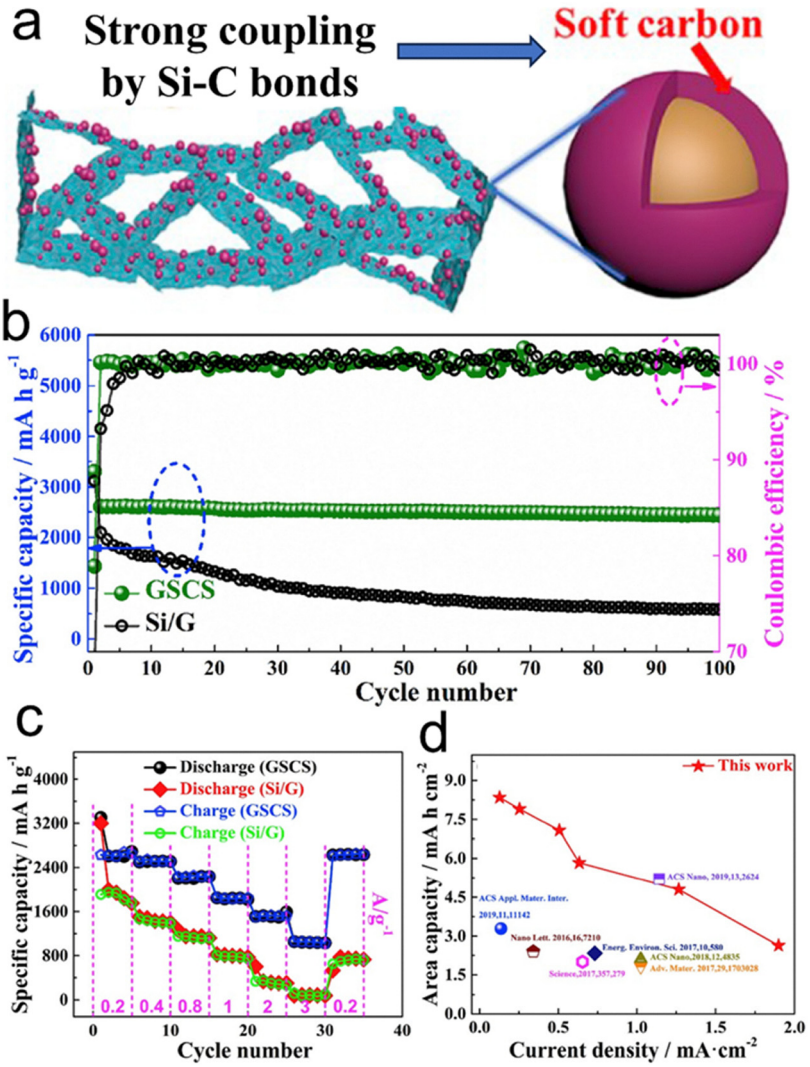

Fig. 26 (a) Schematic, (b) cycling stability, (c) rate performance, and (d) areal capacity of the Si@soft carbon/graphene anode material with a strong contact interface. Reproduced with permission.[63] Copyright 2020, Elsevier.

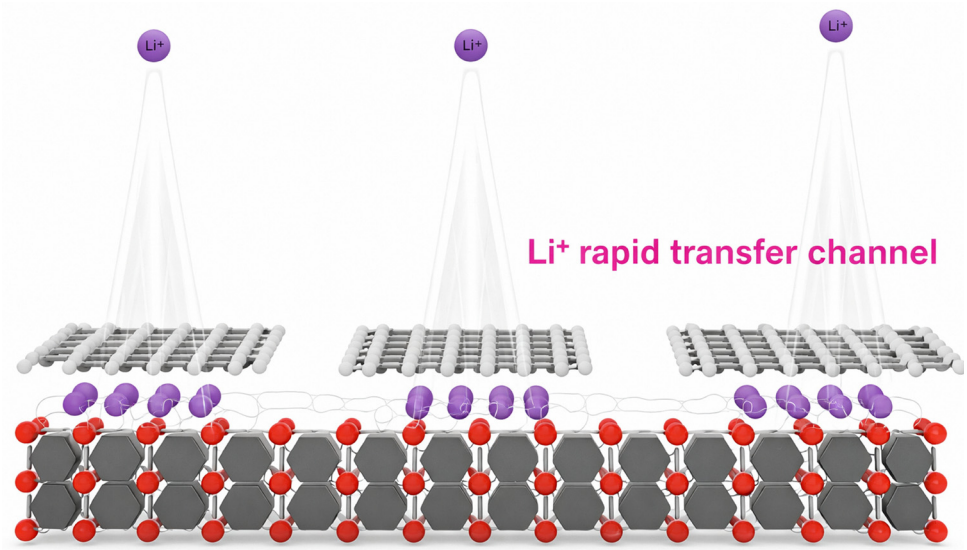

Fig. 27 Schematic diagram for designing a heterostructure electronic field between SiO_2 and graphene.

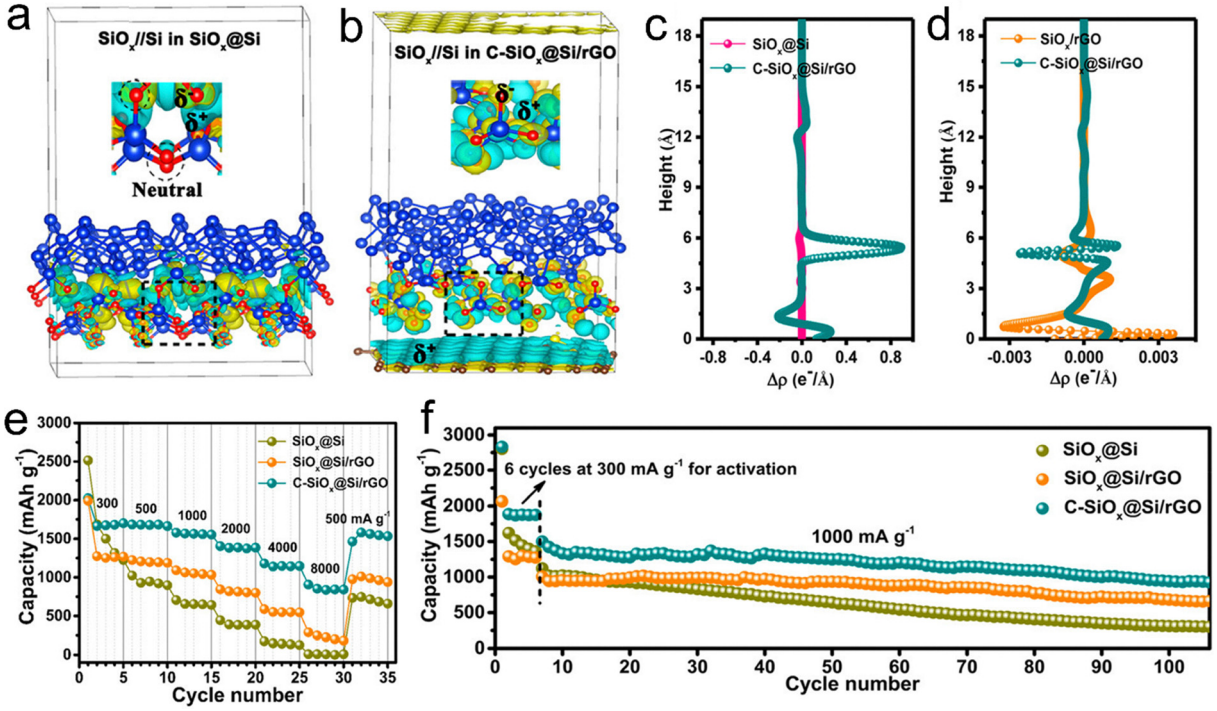

Fig. 28 The charge density difference of (a) SiO_x/Si and (b) SiO_x/Si/graphene hetero-contact interfaces, and corresponding charge distribution along the height for (c) SiO_x/Si and (d) SiO_x/Si/graphene hetero-contact interfaces. (e) Rate and (f) cycling performance of SiO_x@Si, SiO_x@Si/rGO, and c-SiO_x@Si/rGO anodes. Reproduced with permission.[293] Copyright 2020, American Chemical Society.

5. Contact interfaces in electrodes

In electrodes, the contact interfaces between active materials, conductive additives, and binders play a pivotal role in determining electrochemical performance, including the cycle stability and overall rate capability of the battery (Fig. 29).[294] Efficient charge transfer, robust mechanical integrity, and uniform ion diffusion are all critically dependent on the quality and design of these contact interfaces. Because this review mainly focuses on the anode materials, the following contents only discuss the contact interfaces between active materials and other components in electrodes (conductive additives, binders, and collectors).

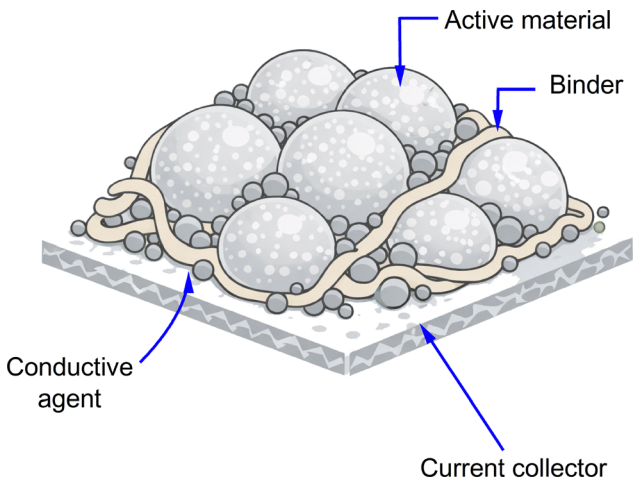

Fig. 29 Contact interfaces in electrodes.

5.1. Contact interfaces between active materials and conductive additives

The contact type between the conductive additives and the active material directly determines the efficiency of constructing the electronic conductive network inside the electrode, thereby profoundly affecting the rate performance, internal resistance, cycle life, and energy density of the battery.[295,296]

As discussed above, their contact interfaces can also be classified into PtP, LtL, and StS. In practical electrodes, these three types often coexist, and an efficient mixed 3D conductive network is constructed by combining different types of conductive agents.[297] The choice of conductive additives and their contact type is arguably one of the most critical factors in designing stable, high-performance anodes that experience large volume changes, with Si being the prime example.

5.1.1. PtP. For anodes like Si, which can expand by up to 300% during lithiation, the traditional PtP contact established by 0D carbon black (CB) is fundamentally insufficient on its own, which is typically established using quintessential 0D conductive additives.[298] CB can fill initial voids. The massive expansion and contraction of the anode with large volume strain during cycling creates a catastrophic mechanical environment. The rigid, PtP connections are easily severed as active particles swell, crack, pulverize, and move apart.

This leads to two critical failures. First, fragments of anodes with large volume strains become electrically isolated from the

conductive network, turning into a dead material that can no longer contribute to capacity. Second, the repeated breakage and reformation of the SEI on newly exposed anode surfaces leads to continuous electrolyte consumption and rapid capacity fade.[297] In essence, a conductive network based solely on point contacts is far too brittle to survive the mechanical turmoil within a Si anode, making it an inadequate solution for achieving long cycle life.

5.1.2. LtL. LtL contact interfaces created by 1D conductive additives, such as CNTs, become enhanced contact interfaces compared with PtP contact interfaces for anodes with large volume strain. CNTs offer a dual solution that addresses both mechanical and electrical challenges.[299] Their high aspect ratio, flexibility, and remarkable tensile strength allow them to act as a "nanoscale rebar" within the electrode.

When the anodes expand and inevitably crack, the interwoven CNT network physically holds the fragments together, preventing the complete pulverization and delamination of the electrode. More importantly, these flexible CNTs can bridge the newly formed cracks and gaps, maintaining electrical continuity to the anode fragments. They essentially create a resilient, conductive web that can stretch and adapt to the anode's breathing, ensuring that even fractured particles remain part of the electronic circuit. This ability to accommodate immense mechanical strain while preserving a long-range conductive pathway is a key reason why CNTs are indispensable in modern Si anode formulations.

As shown in Fig. 30, the CNTs are encapsulated onto the surface of active materials, achieving the LtL contact interfaces. The high-magnification inset highlights that the surface of these particles is uniformly covered by a dense, entangled network of CNTs. This hierarchical, high-surface-area structure is designed to facilitate efficient interaction with the electrolyte and provide robust electrical pathways, revealed by the decreased charge transfer resistance from the EIS plots. The enhanced cycling stability is also confirmed.

5.1.3. StS. StS is achieved mainly through the use of flexible 2D conductive additives, such as graphene. The strategy affects the electrochemical performance, such as the core–shell structure. By encapsulating an anode nanoparticle within a flexible, conductive graphene shell, a micro-environment is created that provides profound benefits.

First, this graphene cage acts as a mechanical buffer, physically constraining the strain and preventing the particles from pulverizing.[301] It holds the particle together from the outside in. Second, the graphene shell provides a stable, artificial surface for the SEI to form on. This prevents the SEI from forming directly on the Si anodes, which would otherwise rupture and reform with every cycle. A stable SEI is crucial for minimizing Li^+ loss and achieving high coulombic efficiency and long cycle life. Finally, this complete, conductive encapsulation ensures that the entire anode particle remains electrically connected throughout the charge–discharge process, maximizing its utilization. However, the StS contact interface would hinder the Li^+ diffusion, reducing the rate performance of anodes to a certain extent.[302]

5.2. Synergistic contact interfaces

For state-of-the-art anodes with large volume strain, the optimal strategy is a synergistic combination of all three contact types in a hierarchical 3D network. This multi-scale approach

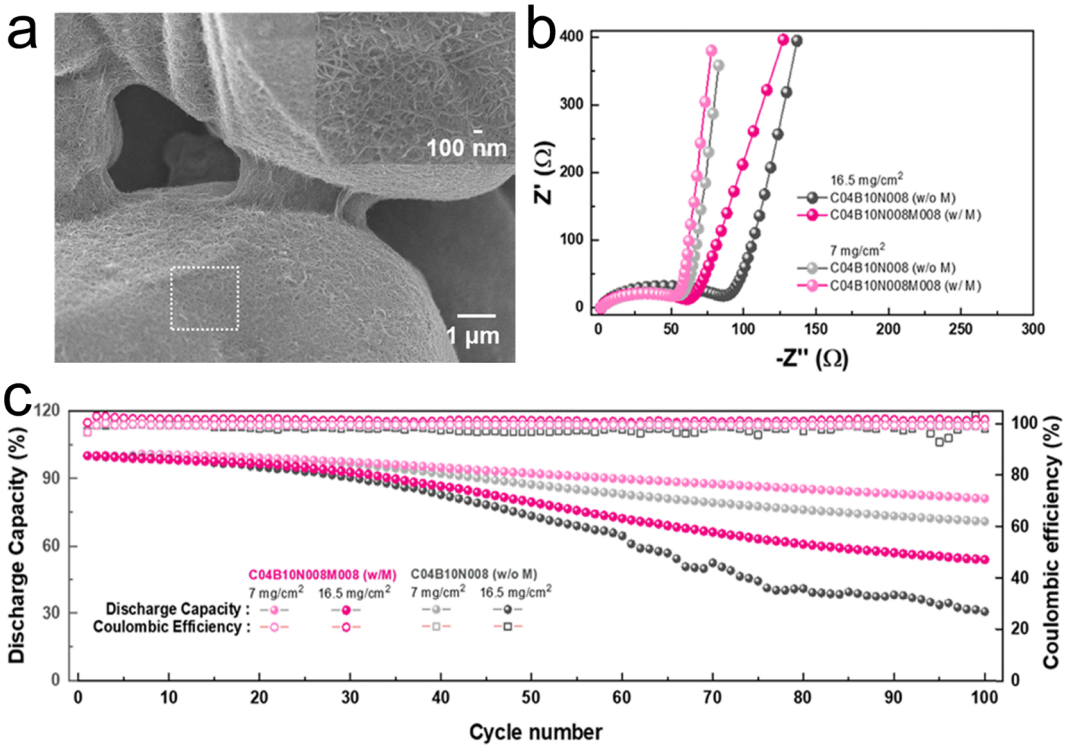

Fig. 30 (a) SEM morphology of the anode composite with CNTs. (b) EIS plots and (c) cycling stability of anodes using CNTs and normal conductive additives. Reproduced with permission.[300] Copyright 2021, American Chemical Society.

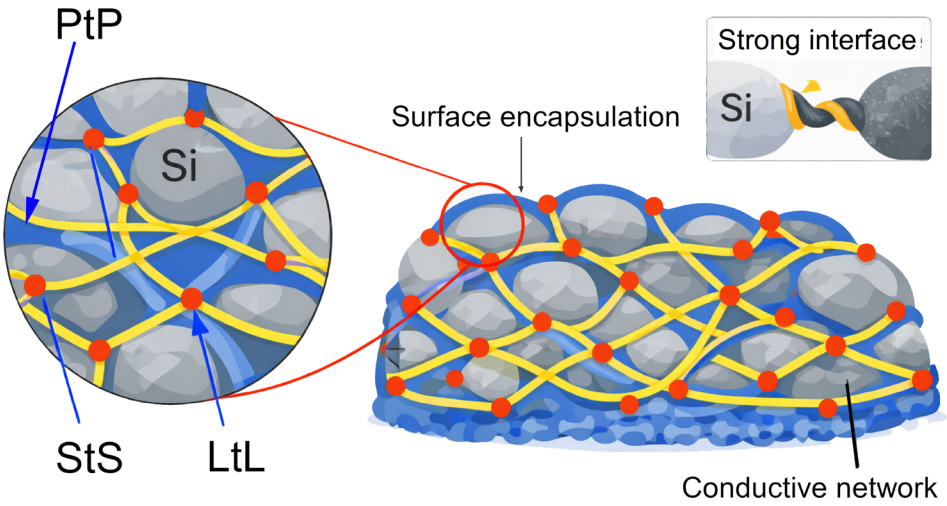

Fig. 31 Multiscale contact-interface engineering in high-volume-strain anodes.

leverages the unique strengths of each component to create an electrode that is both highly electronically and ionic conductive and exceptionally robust.[303]

In this design, StS contact interfaces ensure the encapsulation of individual anode particles to prevent pulverisation and stabilise the SEI. The LtL contact can weave between these encapsulated anode particles, building a long-range, flexible, and tough conductive skeleton that maintains the entire electrode's structural integrity and electrical conductivity during massive volume changes (Fig. 31). Furthermore, PtP contact interfaces can be used sparingly to fill any final, minute voids, ensuring that every part of the composite structure is electronically wired. This point-line-surface compositing network is not just a simple mixture; it is an engineered architecture designed to simultaneously manage the extreme mechanical stress and demanding electronic/ionic diffusion requirements of high-capacity anodes with large volume strain, paving the way for the next generation of high-energy-density batteries.[304]

It is worth noting that the interactions between conductive additives and active materials are generally weak interactions, such as the van der Waals force, dispersion force, *etc*. Therefore, the contact interfaces between conductive additives and active materials are weak. Therefore, developing contact interfaces between conductive additives and active materials with strong interaction forces is a trend.

5.3. Contact between active materials and binders

The contact interfaces of binder-active material are critical for dictating mechanical integrity and electrochemical function. A unified understanding of contact interfaces requires integrating the fundamental nature of physicochemical interactions with their resultant geometric architectures.[305] The evolution from weak physical interaction to strong chemical bonding directly drives a topological transition in the contact interfaces from discrete points to continuous lines, and ultimately, to holistic surfaces, which is paramount for harnessing the potential of these materials.[306] Therefore, the geometric and physicochemical contact interfaces are combined to discuss.

5.3.1. PtP governed by weak physical contact interfaces. The most elementary form of interaction is physical contact, dominated by weak and non-specific van der Waals forces. Conventional binders like polyvinylidene fluoride (PVDF) exemplify this category.[307] In solution, their coiled polymer chains result in a PtP geometry upon electrode fabrication, forming only sporadic, isolated anchor points on the active material's surface. For large volume strain anodes, this configuration is mechanically unstable. The immense stress generated during lithiation becomes highly concentrated at these few anchor points, leading to immediate contact interfacial delamination, catastrophic particle pulverization, and the rapid loss of electrical contact. This model, therefore, represents a fundamentally flawed contact interface that is incapable of preserving the electrode's structural integrity, resulting in precipitous capacity fade.

5.3.2. LtL enabled by mixed contact interfaces. A substantial leap in contact interfacial engineering is achieved with functional polymers like polyacrylic acid (PAA) and carboxymethyl cellulose (CMC), which leverage strong non-covalent chemical interactions and weak interfacial contact.[308,309] The high density of carboxyl functional groups along their linear backbones enables the formation of a continuous, 1D array of non-covalent chemical bonds with the surface hydroxyls of the active material.[310,311] This creates a LtL architecture, where the polymer acts as a flexible molecular tether. The key to its success lies in the dynamic and reversible nature of chemical bonds, which can break and reform to dissipate mechanical stress during volumetric strain. This mechanism effectively mitigates particle fracture and significantly enhances cycling stability. However, while vastly superior to point contacts, the 1D confinement of the LtL model still presents a limitation under extreme, multi-axial stress fields.

The formation mechanism of strong and weak contact interfaces between CMC and SiO_x is shown in Fig. 32. The diagram contrasts two potential pathways for the interactions. The top

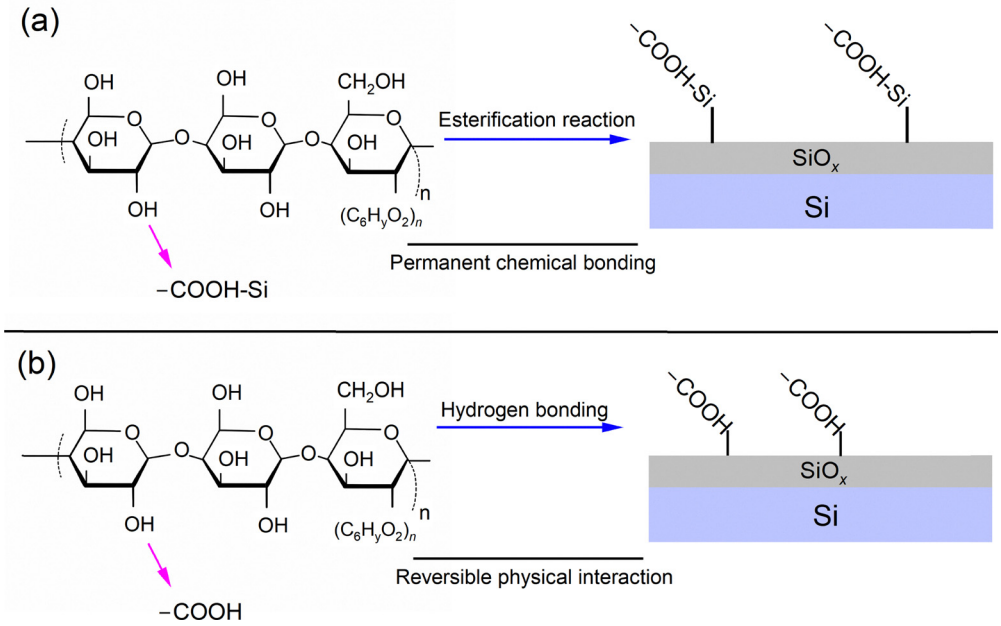

Fig. 32 Formation mechanism of (a) strong and (b) weak contact interfaces between active materials and binders.

path (Fig. 32a) depicts a covalent esterification reaction (chemical bonds), where a carboxyl group on the CMC polymer undergoes a condensation reaction with a surface hydroxyl group, resulting in the formation of a strong, permanent contact interface (–COO–Si) that chemically grafts the polymer onto the SiO_x surface. Alternatively, the bottom pathway (Fig. 32b) illustrates a weak contact interface based on hydrogen bonding, where the carboxylate groups on the CMC are first protonated to form carboxylic acid (–COOH) groups, which then establish a network of strong hydrogen bonds with the hydroxyl groups on the SiO_x surface.[312] In essence, the schematic contrasts direct chemical bond formation with strong physical adsorption as the primary modes of binder adhesion.

5.3.3. StS forged by mixed contact interfaces. The paradigm for achieving ultimate electrochemical stability is the creation of a StS contact interface, which relies on the strongest forms of chemical bonding: covalent linkages and intermolecular cross-linking.[313] This advanced architecture is realised through two primary routes: (1) covalently grafting the binder to the active material surface, for instance, *via* esterification between PAA and surface hydroxyls during thermal treatment, and (2) cross-linking the polymer chains themselves to form a robust, three-dimensional network. This surface architecture envelops the active particle in a conformal, elastic coating, functioning as an artificial exoskeleton. It transforms localised expansion stress into a globally distributed strain across the entire particle surface, effectively preventing pulverisation and maintaining electrical continuity even if the primary particle fractures. Critically, this robust network also mechanically buttresses the fragile SEI, preventing its rupture and continuous reformation. This holistic, multi-dimensional confinement represents the most effective strategy to accommodate extreme volume strain, ensuring the long-term cyclability and high initial coulombic efficiency essential for next-generation high-energy anodes. Due to the complexity of interface functional groups, the StS model also presents mixed weak and strong contact interfacial characterisation.

5.4. Contact between active materials and collectors

The contact interfaces between the active material and the current collector are also important within an electrochemical cell, acting as the primary conduit for electron transport. The structural and chemical nature of this contact interface directly governs the efficiency, rate capability, and long-term stability of the battery, especially for anodes with large volume strain.[314,315] Here, we analyse the contact interfaces based on two key dimensions: (1) contact geometry and (2) interaction force, and elucidate their profound impact on electrochemical performance.

5.4.1. Contact geometry

(1) PtP contact interfaces. This represents the least desirable contact mode, typically occurring between spherical or irregular particles and a planar current collector, where the contact area is confined to a few discrete, microscopic points. Consequently, the severely constricted electron transport pathways create enormous contact resistance, leading to severe polarisation, reduced energy efficiency, and poor rate capability.[316] The inhomogeneous current distribution, highly concentrated at these points, also accelerates localised material degradation and parasitic side reactions. For large volume strain anodes, this configuration is fatally detrimental. Although the strain of a Si particle may temporarily improve contact, the subsequent contraction during delithiation inevitably leads to its complete electrical isolation. This repeated connection/disconnection cycle results in the rapid and irreversible electrochemical inactivation of the active material, causing catastrophic capacity decay.

(2) LtL contact interfaces. A marginal improvement over point contact, this mode is common for 1D nanomaterials like nanotubes or nanowires randomly dispersed on a current collector, forming a linear contact zone.[317] The expanded pathway for electron transport lowers the interfacial impedance and improves rate performance to some extent. However, the contact interface remains vulnerable, especially when subjected to large mechanical stresses. For a typical Si nanowire anode, the significant radial strain exerts stress along the entire contact line, and during contraction, the material may slide or roll, leading to a partial or complete loss of electrical contact. While more stable than point contact, the accumulated mechanical fatigue over repeated cycles still results in interfacial failure and significant capacity fading.

(3) StS contact interfaces. This is the ideal contact configuration, achieved by directly depositing a thin film of active material onto the current collector or by conforming 2D materials flat against its surface.[318] This approach maximises the physical contact area, which in turn provides broad, unobstructed pathways for electron transport, minimising interfacial impedance dramatically. Crucially, for large volume strain anodes, StS contact provides the optimal anchoring effect to counteract the destructive forces of volume change.[319,320] The vast contact area effectively dissipates mechanical stress and robustly maintains the electrical connection, thereby suppressing the delamination of the active material from the current collector.[321] This principle is a core strategy in designing high-performance Si anodes. However, the StS contact interfaces would involve ionic diffusion, compromising the rate performance.

In summary, from a geometric classification perspective, the contact interfaces are similar to those of conductive additives/binders, with little difference. Therefore, examples will not be used for detailed analysis here.

5.4.2. Interaction force

(1) Weak contact interfaces. These contact interfaces are characteristic of conventional electrodes fabricated by slurry-casting, where adhesion of active materials and collectors relies primarily on weak, non-covalent van der Waals forces provided by a polymer binder like PVDF. The resulting contact interfaces are often insufficient to withstand the mechanical stresses from cell operation and can be weakened by electrolyte infiltration.[322] Furthermore, the electronically insulating nature of the binder introduces additional interfacial resistance. For large volume strain anodes, this type of contact interface is highly susceptible to failure, as the mechanical stress generated by the volume strain of the Si anode far exceeds the adhesion strength of conventional binders between them. This mismatch leads to the pulverisation of active particles and the complete structural collapse of the electrode.

(2) Strong interaction. This superior interface involves the formation of strong chemical bonds (covalent or ionic) between the active material and the current collector, achieved through methods like *in situ* growth or chemical grafting.[323] Chemical bonds, being orders of magnitude stronger than van der Waals forces, create a highly integrated and robust contact interface. This atomic-level connection enables seamless electron transfer, virtually eliminating contact resistance.[324] This is the definitive solution for achieving long-term cycling stability in large volume strain anodes. The powerful chemical bonds can effectively withstand and buffer the immense stress from volume changes, firmly anchoring the active material and ensuring the integrity of the electron transport pathway is maintained.[325] This strong interaction is the key to enabling both high-capacity retention and extended cycle life for these promising materials. However, this type of contact interface is complex to establish, costly, and may be difficult to achieve in large-scale applications.

In fact, the weak and strong contact interfaces between active materials and collectors are almost similar to the active material–binder contact interfaces. The biggest difference between them is that the current collector of the active material usually uses metal Cu, while it is difficult to form chemical bonds between inorganic active materials and metal materials. However, by surface modification of the metal current collector, strong contact interfaces are still expected to be achieved.[326]

5.5. Solid–solid contact interfaces in Si-based all-solid-state batteries

The discussion above has focused on internal contact interfaces within composite anodes operated with liquid electrolytes. However, the same high-capacity Si-based materials are increasingly being explored in all-solid-state batteries (ASSBs), where both the electrolyte and a large fraction of the electrode matrix are solids.[327–331] In this context, the solid–solid contact interfacial reactions between Si (or Si-based composites) and solid electrolytes (SE) introduce additional constraints that are conceptually related to, but practically distinct from, those in liquid-electrolyte cells.[332,333] The PtP/LtL/StS framework and the classification of weak *versus* strong (chemo-mechanically bonded) interfaces can be naturally extended to these solid–solid contacts, providing a unified methodology to analyse interfacial contact, mechanical compliance, and interphase chemistry in Si-based ASSBs.[334–336]

5.5.1. Geometric solid–solid contact modes and mechanical compliance. In Si-based ASSBs, Li^+ transport across the contact interface relies on intimate solid–solid contact between Si (or Si/C and SiO_x/C composites) and the SE.[337] In ideal thin-film model cells, the Si/SE interface is a nominally continuous StS contact that can sustain uniform current flow and homogeneous interphase formation.[338,339] Thin-film studies with sulfide SEs such as Li_3PS_4, $Li_{10}GeP_2S_{12}$, and related glasses demonstrate that, under moderate volume strain and appropriate stack pressure, such StS contacts can maintain low contact interfacial resistance and stable cycling.[340]

However, when scaling to composite μ-Si or SiO_x electrodes with large strain (≈300–400%), this idealised StS geometry is rarely preserved: local debonding, crack opening and pore formation at the Si/SE interface rapidly convert nominal StS contacts into effective PtP-like contacts with limited real contact area.[341]

Electrochemo-mechanical studies of Si–Li_6PS_5Cl and Si–LGPS composite anodes highlight the central role of stack pressure and

stiffness matching in controlling these geometric transitions.[342] Without sufficient external pressure, lithiation-induced strain of Si can push against the comparatively brittle SE network, causing microcracks, interfacial voids, and tortuous contact-loss paths within the composite; these defects manifest macroscopically as rising interfacial resistance and heterogeneous current distribution.[343] Conversely, excessively high fabrication or stack pressures (>300 MPa) can densify the composite but also induce particle fracture and shear bands in both Si and SE, again degrading connectivity.[344]

From the PtP/LtL/StS perspective, one key design target for Si-based ASSBs is therefore to maintain continuous StS contact at the Si/SE contact interface and within Si–SE composite domains, while avoiding the transition to isolated PtP-like contacts that occur when cracks and voids nucleate along the contact interface.[345] To this end, several geometric strategies have been proposed to embed LtL-type supporting networks and compliant interlayers into Si-based ASSB anodes.[346] For instance, Si or SiO_x particles infiltrated into porous, percolating frameworks of sulfide SEs, oxide scaffolds, or polymer/SE composites can generate mixed LtL/StS contact networks in which the SE and conductive backbone jointly share load and maintain multi-point attachment to each Si domain.

Such designs are analogous to the LtL-supported PtP/StS networks discussed for liquid-electrolyte cells, but now the lines carry not only electrons but also Li^+ through mixed-conducting or ion-conducting phases. Embedding elastomeric binders or polymer-rich SE domains at critical junctions further introduces mechanically compliant pathways that allow small interfacial sliding or deformation without complete loss of contact.[347] Si-based ASSBs should be engineered so that the macroscopic Si/SE contact interface is not a single, brittle StS plane, but a hierarchical PtP/LtL/StS network in which load and transport are distributed across multiple, partially redundant contact paths.[348]

5.5.2. Strongly interacting solid–solid contact interfaces. In silicon-based ASSBs, long-term stability is not dictated by contact interfaces (PtP/LtL/StS) alone, but by the coupled effects of interfacial interdiffusion/reactions and the transport properties of the resulting interphases.[349] Under intimate StS contact between Si and SEs (*e.g.*, LPSCl and LGPS), continuous reduction/decomposition and element migration generate multiphase products (Li_2S, Li_3P, LiCl, and Si–S related species). Critically, the performance is governed less by a simplistic "thicker means more resistive" narrative than by whether the interphase establishes electron blocking or electron percolation. When the interphase is Li^+-conductive yet electronically insulating, interfacial reactions can become self-limiting, forming an intimate, strong-contact interface that improves adhesion/real contact while passivating further decomposition. In contrast, when reaction products evolve into a mixed ionic-electronic conductor (MIEC) with percolating electronic pathways, a harmful strong-contact interface emerges, sustaining ongoing SE reduction and active-Li depletion even without an exceptionally large apparent impedance.[350] Cryo-TEM on μ-Si/LGPS directly evidences this scenario: a thick (~10–20 μm) reaction layer forms, containing needle-like Li_2S and Li–Ge precipitates; the electronic conductivity associated with Li–Ge supports an MIEC-like interphase, enabling sustained decomposition and rapid capacity decay.[350]

In Si/LPSCl composites, ToF-SIMS and XPS depth profiling reveal that sulfide-derived decomposition products (Li_3P/Li_2S/LiCl) decay with sputtering depth, while SiO_x contributes closer to the Si side, forming SiO_2 and Li_xSiO_y, yielding a gradient structure from sulfide products to oxygen/silicate-rich species; signatures such as SO_3^{2-} further indicate more severe degradation driven by SiO_x involvement.[351] Such gradients imply spatially varying electronically insulating, redistributing Li^+ flux and local current density, and preconditioning chemo-mechanical damage.[352]

These examples illustrate how strongly interacting StS contacts can be both beneficial and detrimental: chemical bonding and interphase formation can enhance adhesion and ensure intimate solid–solid contact (mechanically strong contact interfaces), but uncontrolled reactions can produce thick, mixed-conducting layers that chemically destabilize the electrode.[350,352] Extending the weak/strong/heterointerface classification to Si-based ASSBs, the contact interfaces can be distinguished as follows. The first type is a non-reactive and thermodynamically stable interface (Fig. 33a), where no reaction occurs between the solid electrolyte and Li metal, resulting in a stable 2D contact interface with both phases in thermodynamic equilibrium. The second type is a reactive and mixed-conducting interface (Fig. 33b), where chemical reactions between Li metal and the solid electrolyte form a 3D interphase. This interface alters the properties of the solid electrolyte, creating a mixed-conducting interphase with both ionic and electronic conductivity, leading to potential self-discharge of the battery. The third type is a reactive and metastable SEI (Fig. 33c), where the reaction products are mostly non-conductive or have low electronic conductivity, limiting the interphase growth to a thin stable layer, similar to the SEI formed in liquid electrolyte batteries. The performance of this type of SEI depends critically on its ionic conductivity.[353] For pure Si anodes, a 2D Si/SE interface is formed, which leads to more pronounced stress accumulation due to the volume expansion of Si during cycling (Fig. 33d). This 2D interface can result in a less uniformly distributed SEI, contributing to mechanical instability and poor cycling performance. In contrast, composite Si/LPSCl anodes, where the electrolyte is mixed with Si, form a 3D Si/SE interface. This configuration not only promotes a more homogeneous stress distribution but also leads to a higher SEI formation rate. The increased interface area facilitates more extensive SEI growth, while contributing to a higher SEI formation rate, allowing for better accommodation of the volume changes during cycling. The 3D interface provides more space for stress relief, leading to improved mechanical stability and enhanced cycling performance.[354]

Similarly, alloy- or nitride-based interlayers and molecular-layer-deposited alucone coatings have been used at Li metal/sulfide SE interfaces to block electron flow while preserving Li^+ conduction; analogous strategies are now being adapted to Si-based ASSBs to convert highly reactive StS contacts into controlled heterointerfaces with tailored ion/electron transport and adhesion.[355,356] Within the PtP/LtL/StS framework, these efforts can be viewed as attempts to transform mechanically fragile,

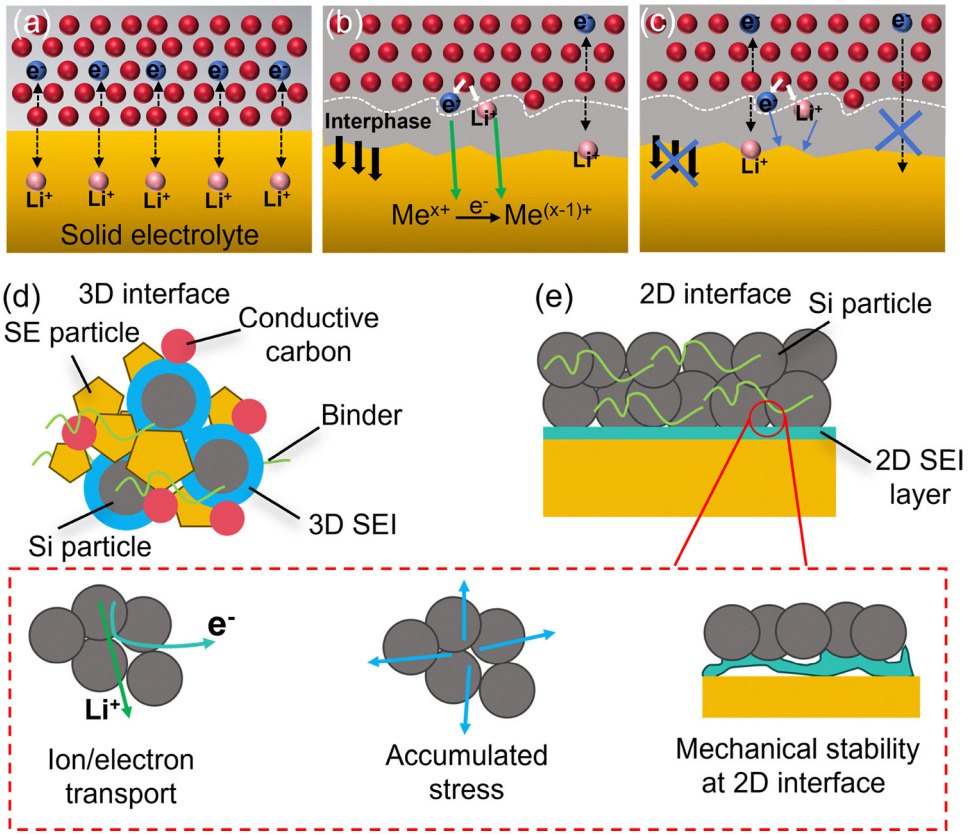

Fig. 33 Types of interfaces between lithium metal and a solid Li^+ conductor. (a) Non-reactive and thermodynamically stable interface, (b) reactive and mixed conducting interphase (MCI), and (c) reactive and metastable SEI. Critical issues in Si-based anodes with (d) 3D and (e) 2D contact interfaces.

chemically unstable StS contact interfaces into strong, chemically buffered contact surfaces that remain robust under repeated alloying–dealloying.[357]

5.5.3. Weak solid–solid contact interfaces. At the other end of the interaction are weakly contact interfaces, where direct chemical reactivity between Si and the SE is suppressed, and mechanical compatibility is improved by soft or composite interlayers.[358] Conceptually, such contact interfaces resemble the weak contacts discussed earlier for liquid-electrolyte cells dominated by van der Waals, polymer entanglement, or physically adsorbed layers, but in ASSBs, they must still provide sufficient Li^+ conduction across solid–solid boundaries.

One class of strategies employs polymer or gel-rich interlayers between Si and the rigid inorganic SE (Fig. 34).[359,360] For instance, polymer–sulfide hybrid electrolytes and solidified localized high-concentration electrolytes (S-LHCEs) have been used to replace or wet the immediate vicinity of the Si surface, forming LiF-rich and polymer-supported interphases that can deform with Si and maintain contact interfaces under large strain.[361,362] In geometric terms, these compliant layers effectively thicken the StS contact region while reducing its effective modulus, allowing Si domains to expand and contract without generating large stress concentrations in the brittle SE. At the same time, the hybrid interphase can be engineered to remain

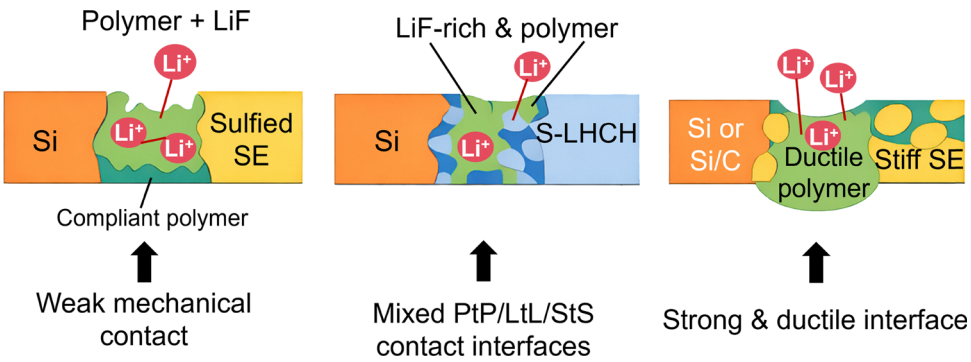

Fig. 34 Compliant contact interfaces for Li^+ transport in solid-state batteries.

electronically blocking, thereby suppressing long-range decomposition of sulfide SEs even if local redox reactions occur at the interface.

A second class involves composite SE frameworks in which the brittle sulfide or oxide SE is percolated with ductile polymers or compliant inorganic phases.[363] Such composites naturally generate mixed PtP/LtL/StS contacts: stiff SE grains make StS contact with Si or Si/C, while polymers fill gaps and act as soft bridges that sustain LtL-type paths for Li^+ transport and redistribute stress.[364] From the weak/strong contact interface viewpoint, these hybrid contact interfaces are weak in the sense that they avoid direct, extensive chemical bonding between Si and the inorganic SE, but they are mechanically strong and damage-tolerant because they allow controlled sliding and deformation without abrupt debonding.[365] As advanced *operando* tomography and cryo-EM studies of Si-based ASSBs begin to quantify how contact interfacial voids, cracks, and third phases evolve in such composites, these design concepts can be refined into quantitative criteria on local compliance, percolation, and interphase growth.[334]

Overall, the emerging picture is that Si-based ASSBs require a deliberate combination of geometric and interaction-type design at the solid–solid contact interfaces. Continuous StS contact must be preserved where Li^+ must cross the contact interface, but should be buffered by compliant or chemically stable interlayers; LtL pathways need to be provided for both ions and electrons through mixed-conducting or hybrid phases; and PtP-like contacts—inevitable in composite electrodes—should be managed so that they act as strain buffers rather than bottlenecks for transport. The PtP/LtL/StS framework, extended with weak/strong/heterointerface classification, thus offers a concise model to compare liquid–electrolyte and solid–state Si anodes and to guide the design of mechanically compliant, chemically controlled solid–solid contact surfaces for next-generation Si-based ASSBs.

5.6. Coupling geometric contact interfaces with SEI evolution

Recent work has shown that LiF-rich, inorganic-dominated SEIs can provide high mechanical robustness and low resistance when they are thin, uniform, and well supported by an appropriate substrate.[366] Cross-linked polymeric or silane-derived SEIs offer superior elasticity and tolerance to repeated strain–contraction, but may become resistant if they grow too thick. Electrolyte and additive engineering (*e.g.*, weakly solvating electrolytes and silane additives) is now routinely used to tune the LiF/polymer ratio and nanostructure of SEI layers on Si and Si/C electrodes.[367] However, the ultimate effectiveness of a given SEI chemistry depends critically on the geometric contact mode (StS, LtL, or PtP) on which it is formed, because SEI growth not only passivates surfaces but also acts as a stress source that can reshape PtP/LtL/StS stability.[368]

At StS, such as Si@C or SiO_x@C core–shell structures and the interfaces between secondary particles and current collectors or solid electrolytes, SEI growth typically occurs on extended, quasi-planar surfaces (Fig. 35a). When a thin, LiF-rich inorganic SEI is formed uniformly on a mechanically compliant StS contact interface (for example, on a carbon shell with an internal void space), the combination of high modulus and good adhesion can suppress repeated cracking, limit continuous electrolyte reduction, and support stable cycling with a very small electrode thickness increase.[369,370] In contrast, if a rigid, inorganic-dominated SEI grows on a stiff StS contact without accommodation space, such as a flat Si film directly bonded to a metal current collector, large in-plane strain is concentrated into the SEI, leading to extensive fracture, delamination, and rapid capacity loss.[371] Repeated repair cycles of fracture and regrowth then further weaken the bonded interface and progressively reduce the effective StS area. In such cases, introducing an intermediate polymeric or cross-linked organic interlayer that can host LiF nanodomains (hybrid inorganic–organic SEI) has been shown to enhance both mechanical compliance and interfacial stability, converting a fragile StS contact into a chemically and mechanically robust strong interface.[372]

In LtL contacts, exemplified by Si or SiO_x particles anchored on carbon nanotubes, nanofibres, or graphene edges, the SEI forms along quasi-1D conductive backbones that are responsible

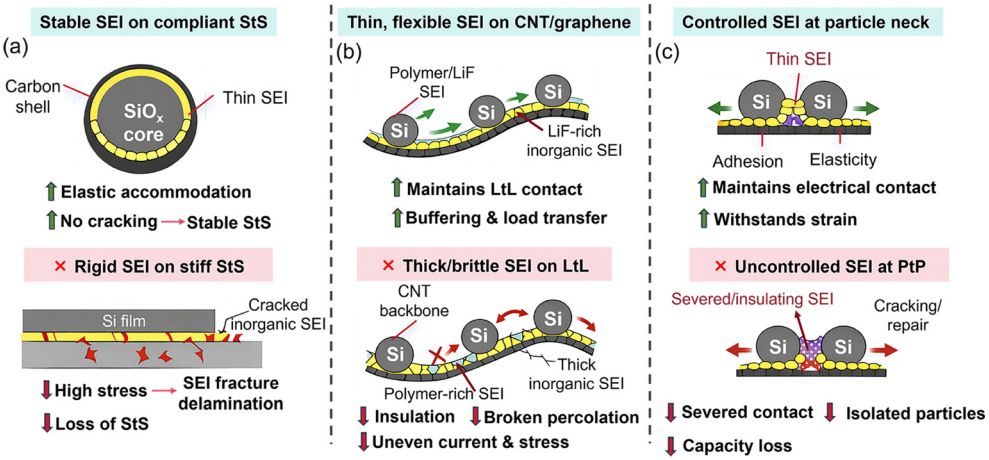

Fig. 35 Impact of SEI chemistry on stability of contact interfaces in Si-based anodes. (a) StS contact interface with a rigid inorganic SEI and cracking and delamination. (b) LtL contact interface with a thick inorganic SEI and loss of conduction. (c) PtP contact interface with a brittle inorganic SEI and contact breakage.

for long-range electron transport and sometimes also assist Li^+ transport (Fig. 35b). Ideally, the SEI on these scaffolds should be thin, ionically permeable, and mechanically robust enough to maintain intimate a LtL contact interface while allowing the backbone to bend and slide relative to the expanding active phase.[373] If the SEI on the conductive skeleton becomes too thick or too rich in brittle inorganic components, line contacts can be "choked" or insulated, breaking percolation even if the active particles themselves remain structurally intact. Conversely, appropriately engineered polymer-rich SEIs or artificial coatings on CNT/graphene can act as lubricating, adhesive layers that preserve LtL connectivity and homogenise current distribution, thereby mitigating local hot spots of SEI growth and stress.[374] Over many cycles, however, even beneficial SEIs on LtL backbones can alter their cross-section and stiffness; if not controlled, this gradual evolution can undermine the redundancy of the LtL network and make the overall contact architecture more susceptible to local failures.[375]

In PtP contact interfaces between neighbouring Si, Sn, or P particles are the most vulnerable to SEI-induced isolation and illustrate most clearly the bidirectional coupling between SEI evolution and internal contacts (Fig. 35c). Because PtP constrictions concentrate current and stress into small areas, they tend to develop highly heterogeneous SEI necks that are either too fragile (cracking under strain) or too insulating (blocking both electron and Li^+ transport).[376] Thick inorganic SEIs at PtP junctions can effectively sever the contact, creating electrically dead particles, whereas very soft, purely polymeric SEIs may initially hold particles together but progressively thicken and increase resistance. Each cycle of SEI cracking and repair at these necks adds an extra fatigue cycle to the underlying contact, so that PtP contact interface gradually transitions from load-bearing connectors into sites of irreversible isolation.[377] Consequently, PtP contacts are best relegated to secondary roles providing local buffering space and accommodating sliding while their direct exposure to electrolyte is minimised by surrounding StS shells or binder domains. Where PtP contacts are unavoidable, SEI chemistries that form thin, adhesive, and moderately elastic interphases (*e.g.*, mixed inorganic/organic necks) are preferable.[224]

These considerations suggest that SEI evolution and geometric contact interface design must be co-optimised and treated as a coupled system. StS contact interfaces that carry the majority of the current should be paired with mechanically reinforced, LiF-rich yet compliant SEIs or artificial interphases.[368] LtL conductive scaffolds require SEIs that protect against side reactions without insulating the backbone or excessively stiffening it; and PtP contacts should be minimised in number, carefully shielded from excessive SEI growth, and designed so that any necessary interphase is thin, adhesive and fatigue-resistant.[378] At the same time, internal contact loss feeds back to SEI evolution by exposing fresh surfaces and concentrating current into fewer remaining pathways, thereby accelerating electrolyte decomposition and interphase thickening. By explicitly linking SEI chemistry (inorganic-rich *vs.* polymeric or hybrid structures) to PtP/LtL/StS contact modes and acknowledging these feedback loops, the interface framework developed provides a mechanistic basis for understanding why nominally similar SEI compositions can lead to very different long-term stability and offers practical guidelines for designing contact surfaces and interphases that remain functional under the extreme volume changes of high-capacity Si-based anodes.[332,368]

5.7. Mechanistic chain: from strain generation to interface degradation and electrochemical failure

High-capacity alloy- and conversion-type anodes such as Si, Sn, Ge, MOs, and P-based compounds typically undergo 100–400% volume strain during lithiation. The strain is often inhomogeneous, because Li^+ insertion starts at the surface and propagates inward, and because many materials exhibit anisotropic crystal structures or multiphase compositions.[379] In secondary particles and composite agglomerates, neighbouring grains and the surrounding conductive/binder matrix mechanically constrain local strain, which further amplifies stress gradients and leads to the build-up of plastic deformation and damage over repeated cycles.[380]

This strain is transmitted through internal and electrode-level contact interfaces, and the way it is transferred depends strongly on the contact geometry and bonding. In PtP contacts (*e.g.* Si nanoparticle–Si nanoparticle or Si–carbon black), stress is concentrated at small contact spots, so cracks and debonding occur easily, and particles are gradually disconnected from the percolation network.[381] In LtL contact interfaces (*e.g.*, Si attached along CNTs or nanofibres), strain is distributed along longer line contacts, and 1D skeletons can bend, twist, or slide, giving better tolerance to mismatch.[382] In StS contact interfaces (*e.g.*, conformal Si@C or SiO_x@C shells, mechanically interlocking graphene@SiO_2), stresses are spread over an area; ductile or graded shells can smooth stress and delay fracture, whereas overly rigid shells crack and locally revert to PtP contact interfaces.[324] Similar processes occur at the active material–binder, active material–conductive additive, and active material–collector interfaces, where weakly bonded contact interfaces detach and form voids, while strong and mechanically compliant contact interfaces deflect cracks, dissipate energy, and delay delamination.

Mechanical evolution is tightly coupled to contact interphase chemistry and transport. When StS/LtL contacts fracture into PtP contact or open gaps, fresh surfaces are exposed to electrolyte, and the SEI repeatedly ruptures and reforms, consuming Li^+ and electrolyte and thickening the interphase (Fig. 36).[368,383] Delamination at active material–binder/collector contact interfaces generates electronically isolated but electrochemically reactive regions that continue to form unstable SEIs.[384] Crack networks and internal voids facilitate deeper electrolyte penetration into conversion-type materials, promoting ongoing transformation into inactive products.[385] At the same time, the loss of StS/LtL contacts and the growth of PtP contact interfaces break electronic and ionic percolation pathways, increasing R_{ct}, lowering apparent Li^+ diffusion coefficients, and creating current hot-spots that accelerate further local damage.[386]

The macroscopic consequence of this chain is mechanical and electrochemical failure. Mechanically, electrodes exhibit

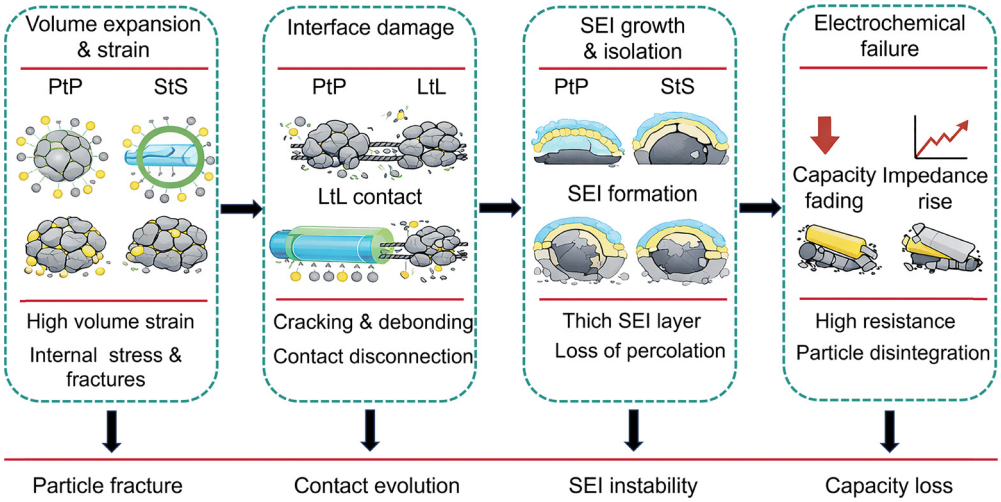

Fig. 36 Mechanistic cascade linking strain evolution, interface degradation, and electrochemical failure in high-strain anodes.

particle pulverisation, loss of cohesion, detachment from the current collector, and irreversible thickness changes.[387] Electrochemically, this appears as rapid capacity fading, low coulombic efficiency in the early cycles due to repeated SEI formation, progressive impedance growth, and poor rate performance at high current densities.[388] Systems dominated by PtP contacts tend to lose percolation early and fail catastrophically, whereas composites with a hierarchical mixture of PtP–LtL–StS contact interfaces degrade more gradually and maintain usable performance for much longer.[389]

Core–shell StS architectures and graded shells mainly moderate strain and stress transfer at the particle level. LtL networks (such as CNTs) provide flexible and redundant electronic pathways that remain connected even when some local debonding occurs.[224,390] Strong chemical bonding at active material–binder and active material–collector contact interfaces slows sliding and delamination, while artificial interphases or SEI-regulating strategies mitigate the chemical consequences of fracture.[391] In practice, suppressing failure in high-strain anodes therefore requires not only reducing the absolute volume change, but also deliberately designing the geometry and chemistry of internal contact interfaces so that the chain "strain generation to contact interface evolution to electrochemical failure" is interrupted at multiple stages.

6. Characterization of contact interfaces

6.1. Characterization of geometric classification

For the geometric characterization of materials, available methods are relatively limited and primarily depend on electron microscopy techniques (*e.g.*, SEM and TEM) in combination with focused ion beam (FIB) etching and 3D reconstruction technologies.[392–399] In contrast, other analytical approaches, including spectroscopy, mass spectrometry, and electrochemical techniques, are generally less effective for characterizing contact interfaces, especially when it comes to physical classification.

To verify the mechanical interlocking structure within the porous graphene/SiO_2 composite representative of a StS contact interface, the material was sectioned using FIB techniques and analyzed *via* EDS (Fig. 37a).[6] Through the integration of SEM and EDS (Fig. 37b), supported by FIB, the contact interface was preliminarily examined. However, the detailed structural features of the porous graphene/SiO_2 interface still require further investigation.

3D reconstruction technology, incorporating an expectation-maximization algorithm, was employed to investigate the growth contact interface between Li and Cu. By analyzing images from multiple perspectives and cross-sectional views, the 3D spatial relationship among Li, Cu, and the current collector was revealed (Fig. 38).[400] In a freshly fabricated Li metal anode, spherical Li deposits and a distinct SEI layer were clearly observed. After a 10-hour resting period, however, internal voids appeared, and the SEI evolved into a concave structure. A comprehensive understanding of the spatial features of active electrode materials and the contact interfaces between electrodes and electrolytes is essential for elucidating electrode processes, identifying failure mechanisms, and formulating effective strategies to improve battery lifespan.

However, current characterization methods still offer limited resolution and details when it comes to analyzing interfacial structures. Even advanced techniques, such as SEM combined with FIB and 3D reconstruction, are often insufficient for capturing finer interfacial features.[401,402] Going forward, it is crucial to develop more sophisticated analytical tools capable of revealing precise information about contact interfaces, including atomic configurations, chemical bonding, and coordination environments.

6.2. Characterization of physical/chemical classification

Compared to the geometric classification of contact interfaces, a wider range of techniques are available for analyzing their physical and chemical properties. These include X-ray photoelectron spectroscopy (XPS), Raman spectroscopy, X-ray absorption near-edge structure (XANES), and Fourier transform infrared

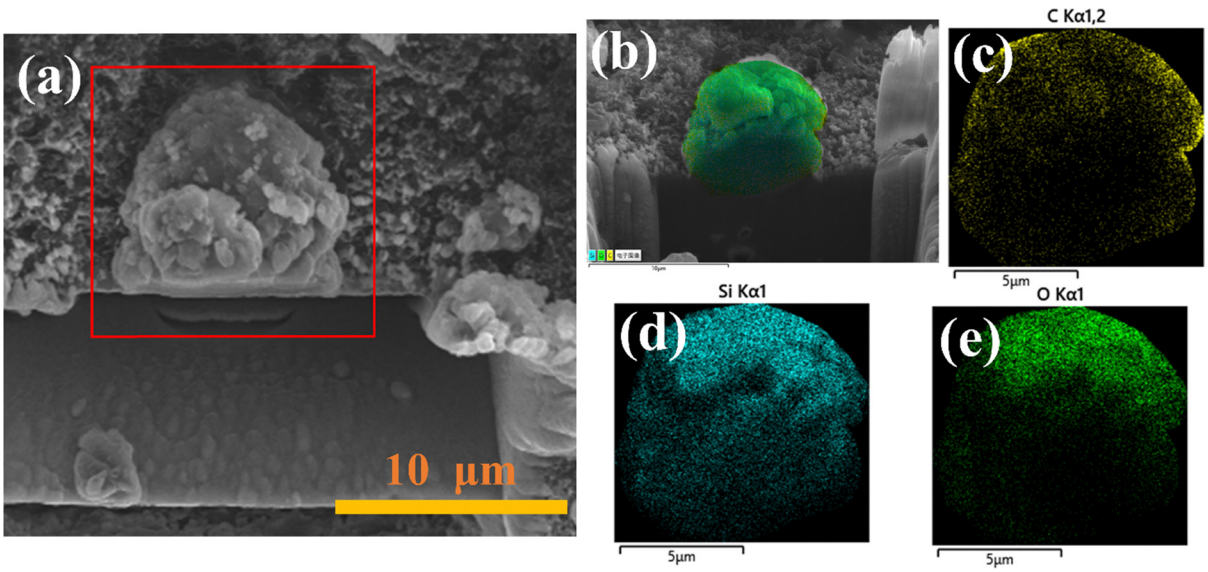

Fig. 37 (a) The morphology of the porous graphene/SiO_2 cut by the FIB. (b) Exposed fresh cross-section morphology and corresponding EDS elemental mapping. (c) C, (d) Si, and (e) O elements. Reproduced with permission.[6] Copyright 2022, Wiley-VCH GmbH.

spectroscopy (FT-IR).[403–405] At physical or chemical contact interfaces, local electric fields can form due to differences in the work functions of specific crystallographic planes. Moreover, atomic-level contact interactions at these interfaces can introduce localized strain. As a result of these interfacial electric fields and strain, spectral features often exhibit noticeable shifts compared to their bulk counterparts. By analyzing the nature of chemical bonding, it is also possible to classify different types of contact interfaces.

Using an epitaxial *in situ* growth strategy, Sun *et al.* successfully synthesized a graphene@SiC heterostructure, in which strong interfacial interactions are present between graphene and SiC (Fig. 39).[406] XPS and XANES analyses confirmed the existence of a robust contact interface. In comparison to pristine SiC, the XPS spectra of Si 2p and C 1s, as well as the XANES data for graphene@SiC, show significant peak shifts, indicating the formation of a built-in electric field at the contact interface. Additionally, the appearance of a new sp^2 carbon signal suggests charge redistribution between the two materials, further validating the presence of strong interfacial coupling.

Even in the case of weak contact interfaces, peak shifts can still be observed, despite the absence of new chemical bond formation. For example, graphene, with its aromatic ring structure, exhibits π–π interactions between adjacent six-membered rings. As shown in Fig. 40, the Raman spectrum of stacked graphene displays a clear shift compared to that of pristine, non-interacting graphene, confirming the existence of weak π–π interactions at the graphene contact interface.[248]

6.3. *Operando* and *in situ* characterization of buried contact interfaces

While the above techniques are powerful for the identification of contact interface types, buried contact interfaces in high-volume-strain anodes evolve dynamically during cycling, calling for *operando*/*in situ* probes.

Directly probing the evolution of buried contact interfaces remains experimentally challenging. First, these contact interfaces are typically nanoscale and deeply embedded, so direct probing requires either high penetration depth or destructive sectioning. Any sample thinning, cutting, or polishing may perturb the native contact interfacial topology, especially when soft SEI or polymeric phases are involved. Second, buried interfaces are often chemically fragile and beam-/air-sensitive. SEI-rich regions, lithiated intermediates, and metastable phases can be altered by electron/ion beams, moisture, or temperature fluctuations, leading to artefacts that obscure the genuine interfacial state. Third, the interface evolution is highly transient and multiphase. The measured signals in *operando*/*in situ* experiments are generally averaged over spatially heterogeneous regions and coexisting contact modes (PtP/LtL/StS), making quantitative interpretation strongly model-dependent. Finally, *operando* cell designs usually require modified geometries (thin electrodes, large windows, and special current collectors), which may change the real electrochemistry and mechanical boundary conditions relative to practical cells. Therefore, careful validation and cross-checking of *operando*/*in situ* setups are indispensable.

Among emerging tools, 3D/four-dimensional (4D) X-ray and neutron imaging has become a key route for visualising interface evolution under realistic cycling conditions.[407] High-throughput *operando* X-ray computed tomography (X-CT) can track crack formation, layer delamination, pore growth and electrode swelling in real time, providing a direct view of how PtP/LtL/StS contact networks evolve across hundreds of micrometres to millimetres.[408] In Si-containing graphite anodes, *operando* diffraction-assisted X-ray CT (XRD-CT) has been used to correlate local lithiation states with structural degradation and heterogeneous strain, revealing regions where high Si content promotes local strain, layer buckling and contact loss within wound commercial cells.[409–411] Correlative 4D experiments that combine

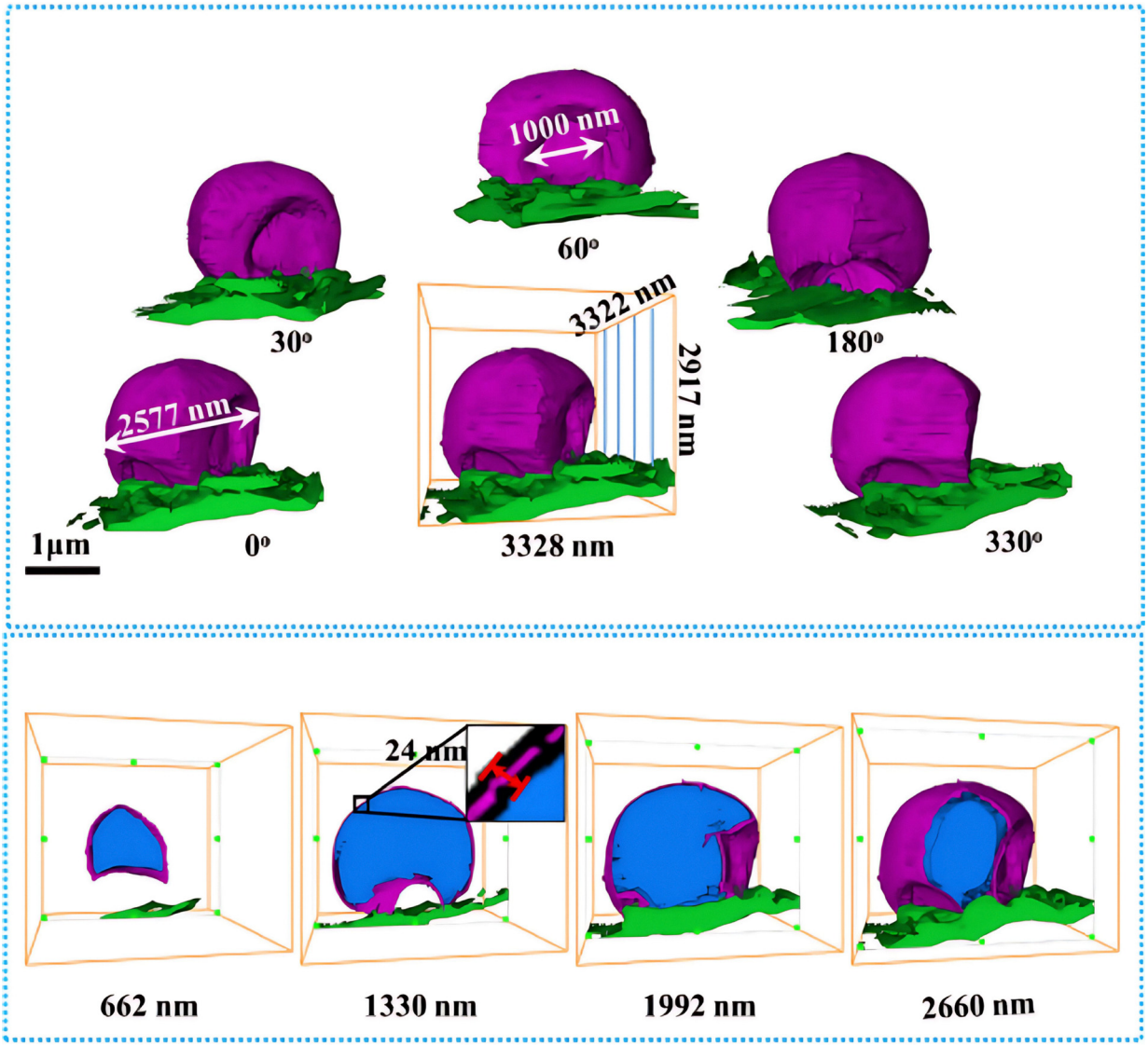

Fig. 38 Colored 3D reconstruction of a Li-metal anode after placing the Cu-TEM-grid in the coin cells for 10 h: Li deposition (blue), SEI layer (purple), and Cu current collector (green). Reproduced with permission.[400] Copyright 2021, Elsevier.

X-CT with neutron CT further exploit the complementarity between electron-density and nuclear-density contrast: X-CT resolves morphology (cracks, gaps, and pore coalescence), while neutron CT, with high sensitivity to Li and H, maps Li redistribution, electrolyte depletion, and gas evolution across the same volume.[412,413] Virtual unrolling and digital volume correlation (DVC) techniques then convert these time-resolved tomograms into quantitative displacement and strain fields, making it possible to track when continuous StS contacts effectively degrade into PtP-like contacts as cracks and voids nucleate at buried interfaces.[414–416]

Among emerging tools, cryo-TEM/cryo-EM provides a powerful route to visualise sensitive buried interfaces at near-atomic resolution.[417,418] By rapidly freezing cycled electrodes, cryo-techniques preserve the native SEI and interfacial morphology while alleviating beam-induced damage, enabling direct interrogation of contact integrity, fracture, and interphase reconstruction.[419] Nonetheless, cryo-TEM is still largely a quasi-*operando* snapshot approach rather than continuous real-time tracking. The method is also limited by low-dose requirements, a small field of view, and the possibility that sample extraction/transfer introduces selection bias. Consequently, cryo-TEM is most convincing when combined with statistical imaging and complementary *operando* probes that supply kinetic and chemical information over larger length scales.

Operando/*in situ* XRD excels at monitoring bulk phase transitions and lattice-strain evolution, which can be correlated with interface migration or decohesion in high-strain materials and with graphite or SiO_x phase evolution under different cycling protocols.[420,421] While conventional XRD has limited direct sensitivity to nanometer-scale contact interfaces, advanced XRD-CT schemes, as noted above, can resolve spatially heterogeneous lithiation and structural damage within individual electrodes, providing indirect but spatially resolved fingerprints of where contact loss and mechanical failure initiate.[422] *Operando*/*in situ*

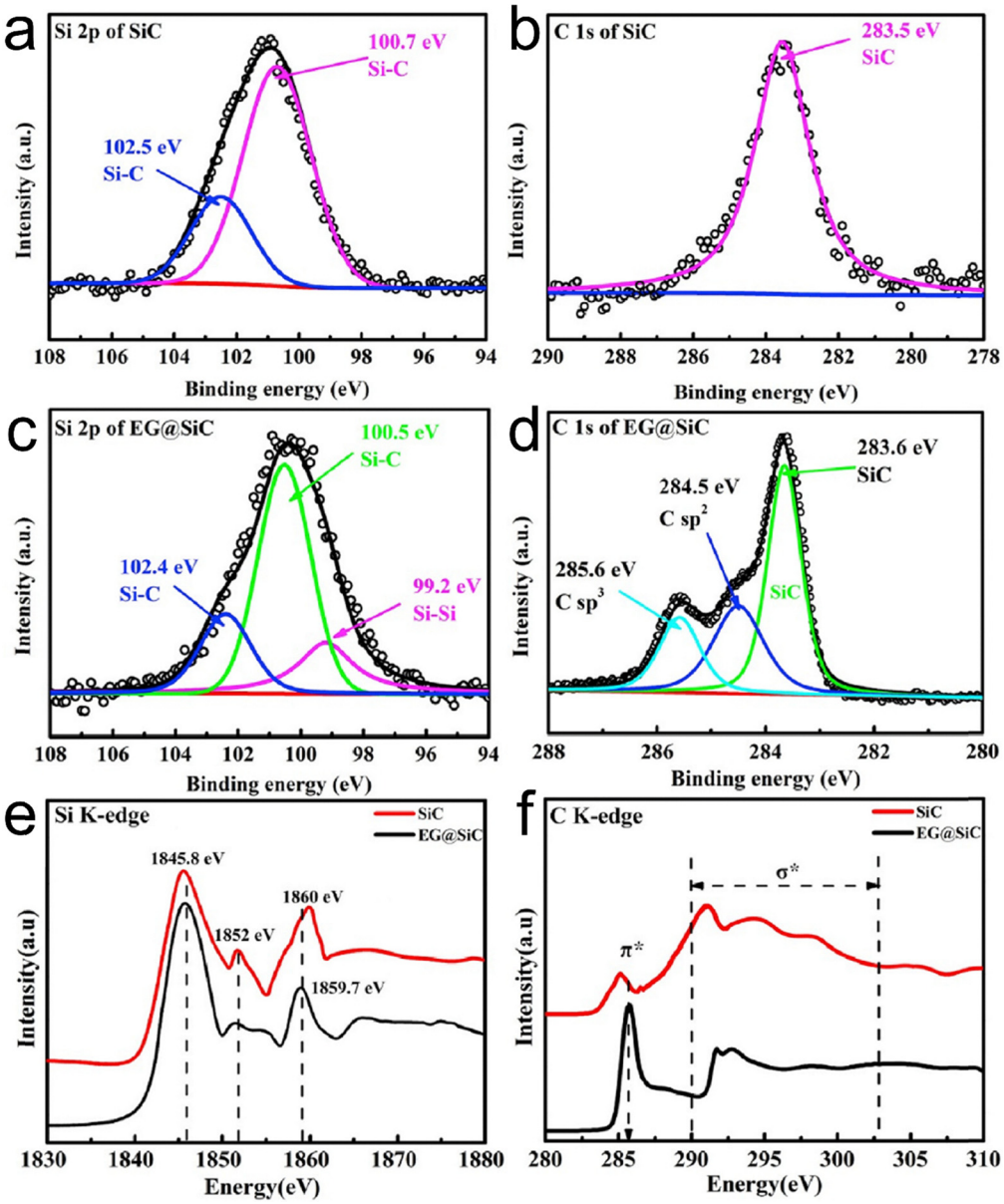

Fig. 39 XPS Si 2p for (a) SiC and (c) EG@SiC. XPS C 1s for (b) SiC and (d) EG@SiC. (e) Si and (f) C K-edge XANES spectra of pristine SiC and EG@SiC. Reproduced with permission.[406] Copyright 2020, Elsevier.

X-ray absorption spectroscopy (XAS) offers element-specific local structural and valence information, and in surface- or interface-sensitive modes it can directly follow the chemical reconstruction of near-surface contacts and SEI-regulated interphases.[423] Yet, *operando* XAS may suffer from beam-induced effects, self-absorption or fluorescence complications, and the intrinsic difficulty of deconvoluting interface signals from bulk contributions, particularly in thick composite electrodes. Recently, *operando* nano-focus wide-angle X-ray scattering (nWAXS) has been demonstrated as a powerful probe of solid–solid contact interfaces in solid-state batteries, resolving the nucleation and growth of LiF- and Li_3N-rich interphases at Li/electrolyte contacts in real time and linking interphase nanostructure to dendrite suppression.[424] Conceptually similar nWAXS approaches could be used to monitor how the SEI nanostructure evolves at PtP/LtL/StS contacts in high-volume-strain anodes, although suitable cell designs and scattering geometries remain an active area of development.

Neutron-based techniques (neutron diffraction/scattering/reflectometry and neutron CT) are especially promising for buried interfaces because of their deep penetration and high sensitivity to light elements such as Li and H.[425] In principle, *operando* neutrons can map lithiation distribution across composite architectures and track the evolution of Li^+-containing interphases without disturbing the electrode. 4D neutron CT has already been used, in combination with X-CT, to follow lithium distribution, electrolyte wetting, and electrode strain in commercial cells, offering a direct view of how transport

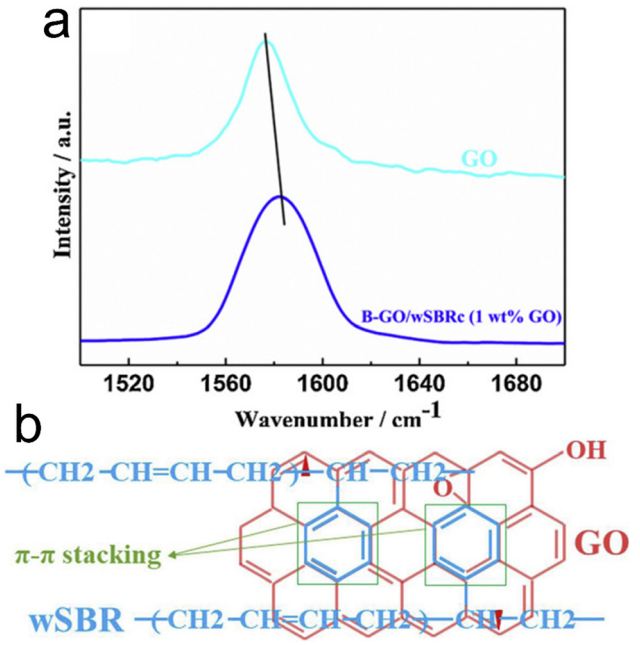

Fig. 40 (a) Employing the Raman spectra to analyze the π–π contact interaction and (b) the corresponding schematic. Reproduced with permission.[248] Copyright 2019, Elsevier.

heterogeneities and mechanical degradation develop in spirally wound architectures.[412] However, neutron experiments require large sample masses and long acquisition times to achieve sufficient signal-to-noise ratios, which may compromise realistic electrode designs or temporal resolution. Moreover, strong background from hydrogen-containing electrolytes and limited instrument availability remain practical bottlenecks, especially for high-throughput studies of Si-rich anodes.

Overall, no single *operando*/*in situ* technique can fully resolve the dynamic, buried contact interfaces in high-volume-strain anodes. A rational strategy is to combine high-resolution cryogenic imaging (for native interfacial snapshots) with *operando* 3D/4D imaging (X-CT/XRD-CT/neutron-CT for morphology and lithium distribution) and element-specific spectroscopy or scattering (XRD/XAS/nWAXS for phase and interphase chemistry), assisted by multi-scale simulations.[412,426] Going forward, the development of more realistic *operando* cells, low-damage probes, and data–model co-interpretation frameworks will be critical for establishing a full-lifecycle picture of contact interfaces and their evolution.[427] Within such integrated workflows, the PtP/LtL/StS framework can serve as a common protocol to interpret how different experimental signatures, strain fields, phase maps, lithium distribution, and interphase composition collectively reflect the progressive degradation or stabilisation of contact interfaces during cycling.

To make the practical capabilities of these techniques more transparent for interface studies, Table 3 summarises the typical depth sensitivity, chemical/electronic resolution, and contact interface-detection capability of the methods discussed in this section. In particular, it compares XPS/X-ray absorption near-edge structure (XANES)-based spectroscopies with vibrational spectroscopies (Raman, attenuated total reflection Fourier transform infrared spectroscopy (ATR-FTIR)) and emerging tools such as cryo-TEM and neutron diffraction/scattering.[428] Altogether, these complementary probes span length scales from the SEI and nanometre-scale solid–solid contacts (cryo-TEM and surface-sensitive XPS/XANES) to bulk electrode and full-cell structural evolution (hard X-ray XANES/EXAFS and neutron methods), providing a toolbox for dissecting buried contact interfaces in high-volume-strain anodes.

To directly connect the characterization toolbox in Section 6 with the geometric contact interface framework in Section 3, Table 4 further maps each technique onto the contact interface types for which it can probe most effectively. In this matrix, the three geometric contact modes—PtP, LtL, and StS—are used as columns, while representative techniques from Sections 6.1–6.3 (electron microscopy and tomography, spectroscopies, cryogenic and *operando* X-ray/neutron methods) are listed as rows. The qualitative scores (“++”, “+”, and “–”) indicate, respectively, direct geometric sensitivity, partial or indirect sensitivity, and negligible specificity to a given interface type. This contact interface–method matrix is intended as a practical guide: it allows readers to select appropriate characterization routes when they wish to visualize discrete particle contacts (PtP), 1D skeletons (LtL), or extended/core–shell interfaces (StS) in composite anodes under large volume strain.

6.4. Simulations for contact interfaces

As discussed earlier, contact interfaces involve complex atomic arrangements that are difficult to probe using current experimental techniques. To address this challenge, simulation methods—primarily DFT,[447–452] molecular dynamics (MD),[453–457] and FEA—have been extensively employed to investigate the structure and behavior of contact interfaces. These computational tools offer valuable insights into atomic-scale and mesoscale interactions that are often inaccessible through experimental means due to the intricacies and dynamic nature of contact interfacial systems.[458]

6.4.1. DFT calculations. DFT is especially powerful for accurately describing electronic structures and energetics at the quantum mechanical level.[459,460] It enables the prediction of properties such as adsorption energies, charge and ion transfer characteristics, and electronic configurations at contact interfaces. DFT’s ability to model electronic behavior at the atomic scale makes it indispensable for designing materials with tailored interfacial properties. Simulations complement DFT by capturing the dynamic evolution of interfacial systems over time. By solving Newton’s equations of motion for large atomic ensembles, MD enables the study of molecular interactions, ion diffusion, and phase transformations under realistic conditions, including the effects of temperature and pressure. FEA, particularly through the finite element method (FEM), offers a macroscopic view of mechanical and physical fields across contact interfaces. By discretizing materials into finite elements, FEM allows precise modeling of stress distribution, strain, and Li^+ diffusion and concentration gradients, all of which influence contact interfacial reactions. Importantly, FEM can simulate the influence of external conditions such as

Table 3 Typical depth sensitivity, chemical resolution, and contact interface-detection capability of characterization techniques

Technique	Depth sensitivity	Chemical/electronic resolution	Interface detection capability
XPS	~1–3 nm (surface)	≤0.3 eV; oxidation state and bonding *via* chemical shifts	Excellent for SEIs and electrolyte/active contact interfaces; limited access to buried active/carbon or active/current-collector contact interfaces without sputtering
HAXPES	~10–30 nm	Similar to XPS, sub-eV at synchrotron	Probing buried interfaces under thin coatings/SEI without sputtering; suitable for realistic composite electrodes
Soft XANES–TEY	~5–10 nm	Highly sensitive to the oxidation state and coordination (edge shifts and pre-edge features)	Element-specific probe of outermost solid–liquid/solid–solid interfaces; blind to deeper interfaces
Soft XANES – TFY/PFY	~100–300 nm	The same intrinsic chemical sensitivity as TEY; possible self-absorption in thick electrodes	Averageing near-surface and subsurface regions; tracking average redox/interphase evolution in porous electrodes
Hard X-ray XANES/EXAFS	Tens to hundreds of μm (bulk)	Oxidation state, coordination number, bond lengths (limited by core–hole lifetime)	*Operando* view of bulk structural/redox changes across entire electrodes; individual PtP/LtL/StS contacts inferred only indirectly
Micro-Raman	~0.1–10 μm (material-dependent)	~0.5–3 cm^{-1}; phases, bonding motifs, disorder	Mapping phase transitions, amorphisation and carbon framework near surfaces; interface selectivity is limited unless using model geometries
ATR-FTIR	~0.5–5 μm	0.5–4 cm^{-1}; functional-group	Very sensitive to electrolyte and SEI species at planar electrode/electrolyte interfaces; less direct for internal solid–solid contact interfaces in thick electrodes
Cryo-TEM/cryo-STEM	Electron-transparent lamella (~50–200 nm thick)	Sub-nm spatial resolution; with EELS/EDS, ~0.5–1 eV energy resolution	Direct, near-native imaging of SEIs and buried solid–solid contacts (PtP/LtL/StS) at the nanoscale; limited field of view and statistics; demanding sample preparation
Neutron diffraction/scattering	Hundreds of μm to cm (whole electrodes/cells)	Precise lattice parameters, phase fractions, Li site occupancy are sensitive to light elements	Bulk-averaged structural and lithiation information under realistic conditions; cannot resolve individual nanoscale interfaces, but reveals macroscopic heterogeneity and strain linked to contact evolution

temperature, pressure, and environmental factors, reducing the need for extensive physical testing and enabling exploration of scenarios difficult to replicate experimentally.

For instance, DFT simulations have demonstrated the advantages of the LiF/C contact interface for Li^+ transport.[450] Along individual diffusion pathways, the energy barriers for Li^+ migration on LiF and C are approximately 0.2 eV and 0.25 eV, respectively (Fig. 41a–c). However, at the LiF/C contact interface, this barrier drops to ~0.13 eV, suggesting enhanced ion mobility due to the interfacial electric field (Fig. 41d). Additionally, the LiF/C heterointerface exhibits stronger adsorption for electrolyte molecules compared to either component alone, indicating improved electrolyte wettability and, consequently, better Li^+ transport (Fig. 41e). These results highlight how DFT can uncover properties that are challenging to measure experimentally, such as diffusion pathways and adsorption energies (Fig. 41f).[461]

Analyzing the data in Table 5, a quantitative distinction emerges that contact interfaces governed by weak physical adsorption (*e.g.*, van der Waals forces in Gr/SiO_2 or Gr/BP) typically exhibit low adhesion energies (<0.8 J m^{-2}), which are often insufficient to anchor high-strain particles. In contrast, stable architectures characterized by chemical bonding consistently show binding energies exceeding a critical threshold of ~1.0 J m^{-2} (or >1.0 eV per atom), suggesting this range as a target design criterion for resisting delamination under large volume strain.

6.4.2. MD simulations. MD simulations have been used to explore the lithiation mechanism of Si anodes, particularly from the contact interface (Fig. 42).[476] At elevated temperatures, characteristic oscillations of Li layers in the body-centered cubic (bcc) phase diminish, indicating amorphization. Amorphous Si, with its inherently disordered structure, exhibits a heterogeneous bonding network at the Si/Li interface, featuring 3-, 4-, and 5-fold coordinated Si atoms. Li and Si atom distributions oscillate around their respective bulk concentrations (bcc-Li at 0.080 mol cm^{-3} and amorphous Si at 0.082 mol cm^{-3}) under ambient conditions (298.15 K, 1 atm).

Upon full lithiation ($x \approx 3.9$), a Li layer forms at the contact interface in the Li_xSi structure, stabilizing thermodynamically unfavorable Si dangling bonds. This interfacial Li layer appears as a subtle peak ~0.2 nm thick with a density of ~0.01 mol cm^{-3}. The observed concentration drop at the Li–vacuum interface reflects the system's bounded nature. In contrast, an inward concentration decrease highlights repulsive interactions between the Li_xSi phase and the interfacial Li layer. Furthermore, the system undergoes thermal contraction between 500 and 600 K due to Li vaporization at the Li–vacuum boundary. Such atomistic insights into lithiation-induced structural evolution are challenging to capture experimentally, but are effectively revealed through MD simulations.

However, while classical MD successfully captures phase evolution, it often struggles to describe the complex bond-breaking and forming events associated with interface fracture and SEI degradation under large volume strain. To address this, reactive force field (ReaxFF) MD has been increasingly adopted to investigate chemo-mechanical failure mechanisms. Unlike non-reactive potentials, ReaxFF can dynamically simulate chemical bond scission and formation, revealing how mechanical stress accumulation at the expanding Si/C or Si/SEI interface triggers specific decomposition reactions and physical delamination.[477] Furthermore, a significant recent leap in modelling capability comes from machine learning potentials (MLPs), such as deep potentials (DP). These data-driven

Table 4 Contact interface types (PtP, LtL, StS) *vs.* characterization methods in composite anodes ("++": direct and highly sensitive; "+": partially or indirectly sensitive; "–": little or no specificity to that geometry)

Technique	PtP	LtL	StS	Brief remarks for contact interfaces	Ref.
2D SEM/TEM (plan-view, cross-sectional, FIB-assisted)	++	++	+	Direct imaging of particle–particle (PtP) and particle–fibre (LtL) contacts; cross-sections reveal local StS core–shell or laminated interfaces such as porous graphene/SiO_2 and Si@C shells	429,430
3D FIB–SEM tomography/ X-ray 3D reconstruction	+	++	++	Resolves the full 3D network of active, carbon/binder and pore phases; quantifies connectivity, tortuosity and contact areas for mixed PtP–LtL–StS networks in realistic electrodes, including buried contact interfaces	431,432
AFM/conductive-AFM/ nano-mechanical mapping	+	+	++	Probes local topography, stiffness and conductivity at planar electrode surfaces and coatings; particularly useful for evaluating roughness, adhesion and mechanical compliance of StS contact interfaces (*e.g.*, active/binder and active/current-collector) and for identifying local PtP "hot spots" in rough composites	433,434
XPS/HAXPES/soft XANES (surface and near-surface)	+	+	++	Chemically classifies strong *vs.* weak contact interfaces through core-level shifts and DOS/coordination changes; most sensitive to outer StS interfaces (*e.g.*, SEIs, coatings, and graphene@SiC heterointerfaces) but can also probe chemically distinct PtP asperities and LtL fibre surfaces in model systems	435
Raman/ATR-FTIR (vibrational spectroscopies)	+	+	+	Detecting bonding motifs, disorder, and strain near interfaces; π–π stacking in weak PtP/LtL contact interfaces. ATR-FTIR is well-suited to planar StS electrode/electrolyte contact interfaces	436–438
Cryo-TEM/cryo-STEM (lamellae of cycled electrodes)	++	+	++	Provides near-atomic-resolution snapshots of buried solid–liquid and solid–solid contacts with the SEI frozen in its native state; directly resolves discrete Li dendrites and SEI-covered PtP contacts, as well as layered StS interfaces in Li/solid–electrolyte and Si/SEI systems, including multi-layer SEI architectures	439–441
Operando XRD/SAXS/X-ray imaging	–	–	+	Primarily sensitive to bulk phase transitions, crystallographic strain, and density changes; geometric interface information (PtP/LtL/StS) is inferred indirectly by correlating lattice-strain evolution and phase heterogeneity with known interface models in high-strain materials	442,443
Neutron diffraction/reflectometry/imaging	–	–	+	Deep-penetration probes of Li distribution and interphase thickness across entire cells; especially suited to buried StS contacts in solid-state cells, where nm-scale interphases and their evolution under bias can be resolved without dismantling the device	444–446

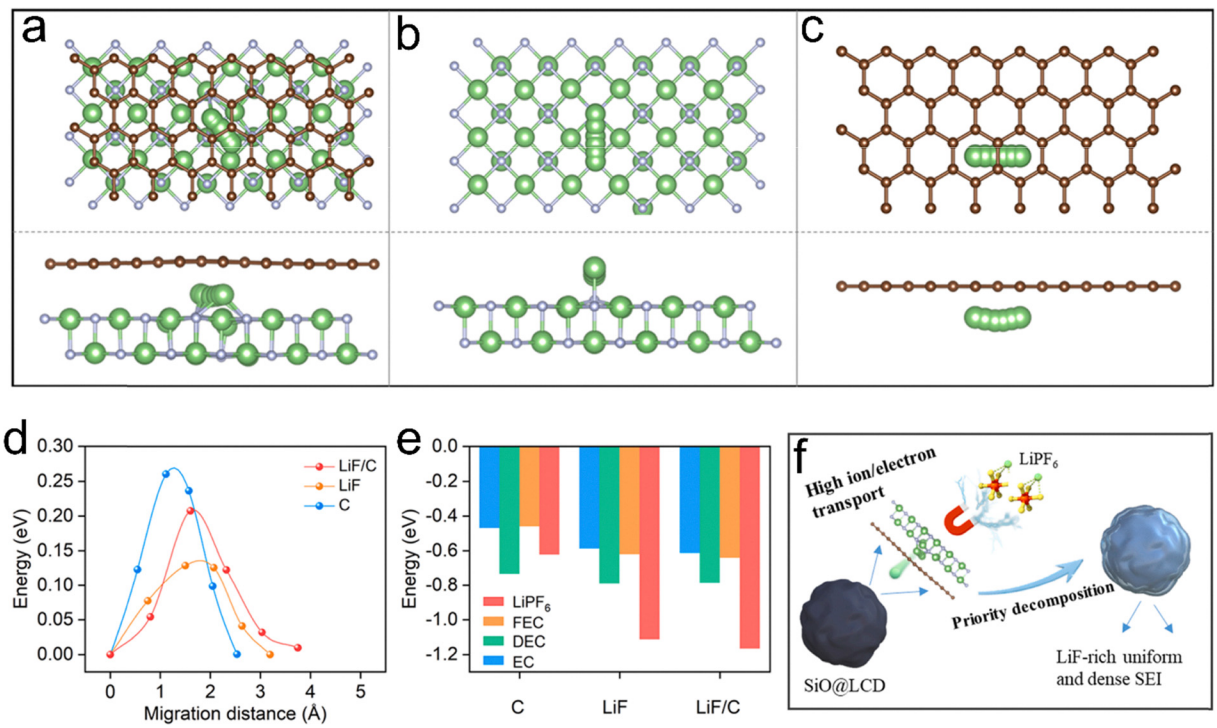

Fig. 41 DFT calculations for studying the contact interface of the LiF/C anode. Li^+ diffusion at the (a) LiF/C, (b) LiF, and (c) C contact interfaces and corresponding (d) diffusion barrier. (e) Adsorption energy of pristine C, LiF, and LiF/C for the electrolyte. (f) Schematic of the advantages of LiF/C for Li^+ storage. Reproduced with permission.[450] Copyright 2023, Elsevier.

Table 5 Calculated adhesion energy for various contact interfaces

	Interface description	Adhesion energy	Ref
1	Gr/c-SiO_2	0.349 J m^{-2}	462
2	Gr/OH-SiO_2	0.242 J m^{-2}	
3	Gr/SiO_2 + H_2O ML	0.211 J m^{-2}	
4	Si/SiC(0001) (isolated)	7.1 eV	463
5	Si/SiC(0001) ($\theta < 0.25$ ML)	6.7 eV	
6	Si/SiC(0001) ($\theta > 0.25$ ML)	5.0 eV	
7	Si/SiC(0001) ($\theta > 0.4$ ML)	4.2 eV	
8	Si_3/(5,5) CNT	−5.2 eV	464
9	Si_6/(5,5) CNT	−0.28 eV	
10	Si_6/COOH-(5,5) CNT	−0.88 eV	
11	Si/poly (generic)	−1.6 to −2.08 J m^{-2},	465
12	Si-H/poly (inert)	−1.28 to −1.92 J m^{-2}	
13	Si-OH/poly (polar)	−1.92 to −2.88 J m^{-2}	
14	SiO_2–C (Dia)	≈ 1.8 eV $Å^{-1}$	466
15	Si–C (non-ox)	≈ 0.3 eV $Å^{-1}$	
16	C_2H_2/SiO_2	2.32 J m^{-2}	467
17	Gr/OH-SiO_2	0.52 J m^{-2}	
18	Gr/c-SiO_2	0.31 J m^{-2}	
19	CH_4@ SnO_2/(8,0)-CNT (phy)	−0.21 to −0.26 eV	468
20	CH_4@ SnO_2-cluster (O-top, diss)	−1.66 eV	
21	CH_4@ SnO_2-cluster (C-top, mol)	−0.66 eV	
22	Sn_4/N-C	−4.29 eV	469
23	Sn_4/ED-C	−4.11 eV	
24	Sn_5/Gr	−4.32 eV	
25	Sn_{10}/Gr	−5.40 eV	
26	P@C/EC-host	∼67.3 J m^{-2}	470
27	P/C-Mix	∼0.1–0.3 eV $Å^{-2}$	
28	P/graphene	<0.1 eV $Å^{-2}$	
29	Gr/BP	−0.722 J m^{-2}	471
30	Sb/BP	−3.759 J m^{-2}	
31	Fe_3O_4/rGO-mixed	−3.19 eV	472
32	Fe_3O_4/Gr-coupled	−3.54 eV	
33	Fe_3O_4/Gr-non-aligned	−3.30 eV	
34	Fe_3O_4/N-Gr-coupled	−3.65 eV	
35	GeS/Gr	−0.060 eV	473
36	a-GeO_2/C	−0.422 J m^{-2}	474
37	GeO_x/T-Nb_2O_5(001)	−19.06 eV	475

Note: Abbreviations are explained as follows. Graphene on crystalline SiO_2 (Gr/c-SiO_2); graphene on a hydroxylated SiO surface (Gr/OH-SiO_2); graphene on SiO_2 with an interfacial H_2O monolayer (Gr/SiO_2 + H_2O ML); single Si atom adsorption on SiC(0001) (Si/SiC(0001) (isolated)); low-coverage Si adsorbed on SiC ($\theta < 0.25$ ML) (Si/SiC(0001) ($\theta < 0.25$ ML)); medium-coverage Si adsorbed ($\theta > 0.25$ ML) (Si/SiC(0001) ($\theta > 0.25$ ML)); high-coverage Si adsorbed SiC ($\theta > 0.4$ ML) (Si/SiC(0001) ($\theta > 0.4$ ML)); Si_3 cluster on (5,5) carbon nanotubes (Si_3/(5,5) CNT); Si_6 cluster on (5,5) carbon nanotubes (Si_6/(5,5) CNT); Si_6 cluster on carboxyl-functionalized (5,5) carbon nanotubes (Si_6/COOH-(5,5) CNT); generic Si/polymer interface (Si/Poly (generic)); Hydrogen-terminated Si/inert polymer (*e.g.*, polyethylene, polypropylene) (Si-H/Poly (inert)); hydroxyl-terminated Si/polar polymer (*e.g.*, epoxy, polyamide) (Si-OH/poly (polar)); silica–diamond contact (C–Si bond rupture peak force) (SiO_2–C dia)); non-oxidized silicon–carbon contact (Si–C bond rupture peak force) (Si–C (non-ox)); acetylene molecule on an SiO_2(0001) surface (C_2H_2/SiO_2); graphene on a hydroxylated O-terminated SiO_2 surface (Gr/OH-SiO_2); graphene on crystalline SiO_2 (α-quartz (0001)) (Gr/c-SiO_2); graphene on a Si-terminated SiO_2 surface (Gr/Si-SiO_2); methane (CH_4) physisorbed on various sites of the SnO_2-decorated (8,0) SWCNT composite (CH_4@ SnO_2/(8,0)-CNT (phy)); dissociative chemisorption of methane (C–H bond cleavage) at the oxygen-top site of a SnO_2 cluster (CH_4@ SnO_2-cluster (O-top, diss)); molecular chemisorption of methane at the carbon-top site of a SnO_2 cluster (CH_4@ SnO_2-cluster (C-top, mol)); tetrameric tin (Sn_4) cluster supported on a nitrogen-doped carbon substrate (Sn_4/N–C); tetrameric tin (Sn_4) cluster anchored on electron-deficient carbon nanofibers (Sn_4/ED-C); pentetrameric tin (Sn_5) cluster supported on a graphene substrate (Sn_5/Gr); decameric tin (Sn_{10}) cluster supported on a graphene substrate (Sn_{10}/Gr); decameric tin (Sn_{10}) cluster supported on a nitrogen-doped carbon substrate (Sn_{10}/N–C); tetrameric tin (Sn_4) cluster supported on a boron–nitrogen co-doped carbon substrate (Sn_4/BN-C); RP covalently anchored *via* P–C bonds on an engineered carbon host (P@C/EC-host); physically mixed RP and carbon (non-covalent) (P/C-mix); RP on an inert substrate (*e.g.*, pristine graphene) (P/graphene); graphite physically mixed with BP flakes (control interface) (Gr/BP); metallic antimony covalently bonded to a BP interface (Sb/BP); Fe_3O_4 with rGO *via* simple mechanical mixing (Fe_3O_4/rGO-mixed); aligned Fe_3O_4 on graphene with a strong coupling interface (Fe_3O_4/Gr-coupled); non-aligned Fe_3O_4/graphene composite interface *via* a hydrothermal method (Fe_3O_4/Gr-non-aligned); Fe_3O_4 on N-doped graphene with a strong coupling interface (Fe_3O_4/N-Gr-coupled); germanium sulfide/graphene van der Waals heterostructure as an anode for Na-ion batteries (GeS/Gr); amorphous GeO_2/carbon matrix interface (a-GeO_2/C); amorphous germanium oxide (GeO_x) thin film on an orthorhombic T-Nb_2O_5(001) surface (GeO_x/T-Nb_2O_5(001)).

approaches bridge the gap between the high accuracy of DFT and the large time/length scales of classical MD. By training on high-fidelity *ab initio* data, MLPs enable the simulation of realistic, rough, and amorphous contact interfaces with quantum-mechanical accuracy but at a computational cost orders of magnitude lower than DFT.[478] This breakthrough allows for the observation of stress-dependent ion diffusion and crack nucleation at the atomic scale over nanosecond timescales.

Ultimately, to fully elucidate the mechanical failure of contact interfaces at the electrode level, atomistic MD simulations must be bridged with continuum mechanics. MD serves as a critical tool for extracting fundamental constitutive parameters, such as interfacial adhesion energies, traction-separation laws for decohesion, and stress-dependent diffusion coefficients, which are otherwise difficult to measure experimentally.[479] Feeding these atomic-scale parameters into macroscopic FEA models enables a hierarchical understanding of how local bond-breaking events propagate into large-scale interface delamination and particle pulverization. This multiscale modelling approach represents the frontier of contact interface engineering, offering a predictive framework that links intrinsic material properties to the cycle life of high-volume-strain anodes.[480]

6.4.3. FEA simulations. FEA has also been employed to evaluate the mechanical behavior of bioinspired interlocking contact interfaces (Fig. 43).[6] In a conventional graphene@SiO_2 anode with an encapsulated contact interface, lithiation induces uniform SiO_2 strain (Fig. 43c), with stress and displacement peaking at $\sim 1.4 \times 10^{11}$ N m^{-2} and ∼10.5 μm, respectively (Fig. 43e). In contrast, the bioinspired interlocking contact interface significantly suppresses deformation near the SiO_2 interface, limiting stress to below 0.5×10^{11} N m^{-2} (Fig. 43b) and displacement to ∼4.2 μm. However, this interlocking configuration introduces moderate stress ($\sim 2 \times 10^{11}$ N m^{-2}) into the graphene matrix. Notably, stress at the graphene/SiO_2 interface reaches $\sim 4.7 \times 10^{11}$ N m^{-2} (inset in Fig. 43b), indicating strong interfacial bonding, which helps prevent SiO_2 detachment and enhances cycling stability. These findings underscore the value of FEA in understanding interfacial mechanics and guiding the design of contact interfaces for high-strain electrode materials.

Moving beyond static stress analysis, recent computational advances have focused on simulating the dynamic failure processes of contact interfaces, specifically utilizing cohesive zone models (CZM) and phase-field fracture methods.[481] The traditional FEA often assumes perfect bonding or simple friction. CZM introduces traction-separation laws to describe the progressive degradation of

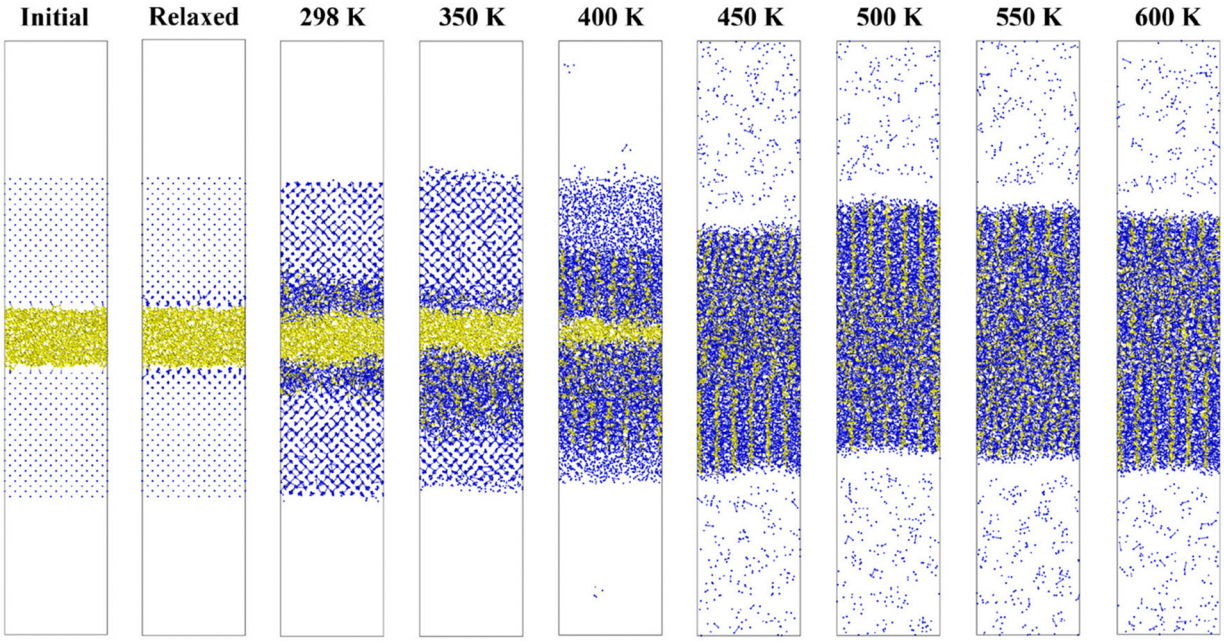

Fig. 42 MD simulations for studying the reaction of Si and Li at various temperatures for 1 ns. The blue and yellow spheres are Li and Si, respectively. Reproduced with permission.[476] Copyright 2024, American Chemical Society.

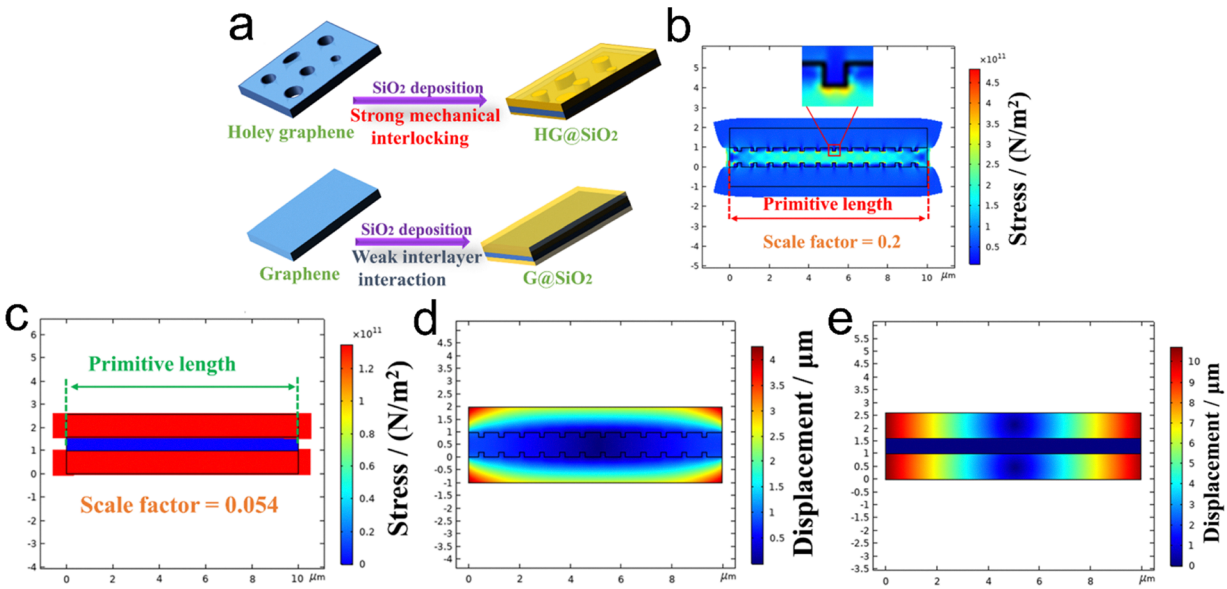

Fig. 43 FEM simulations for studying the bioinspired contact interfaces for an HG@SiO_2 anode. (a) Schematic of general encapsulated and bioinspired mechanical interlocking contact interfaces. Stress and strain of a graphene@SiO_2 anode with (b) mechanical interlocking and (c) encapsulated contact interfaces after lithiation. Displacement of a graphene@SiO_2 anode with (d) mechanical interlocking and (e) encapsulated contact interfaces after lithiation. Reproduced with permission.[6] Copyright 2022, Wiley-VCH.

interfacial adhesion. This allows researchers to quantitatively predict the onset of delamination and the transition from continuous StS contact to isolated PtP configurations when the stored elastic energy exceeds the interfacial fracture toughness.[482] Furthermore, phase-field fracture modelling has emerged as a powerful tool for capturing complex, arbitrary crack propagation paths within high-strain particles and SEI layers without the need for pre-defined crack tips.[483] This diffuse-interface approach is particularly effective in revealing how geometric features, such as surface roughness and local curvature, act as stress concentrators that nucleate cracks and sever electronic connectivity during repeated volume strain.[484]

Crucially, the evolution of contact interfaces is governed by strong chemo-mechanical coupling, a phenomenon that modern FEA frameworks must address.[485] It is not merely that lithiation causes strain; conversely, the generated mechanical stress field significantly modulates electrochemical kinetics.

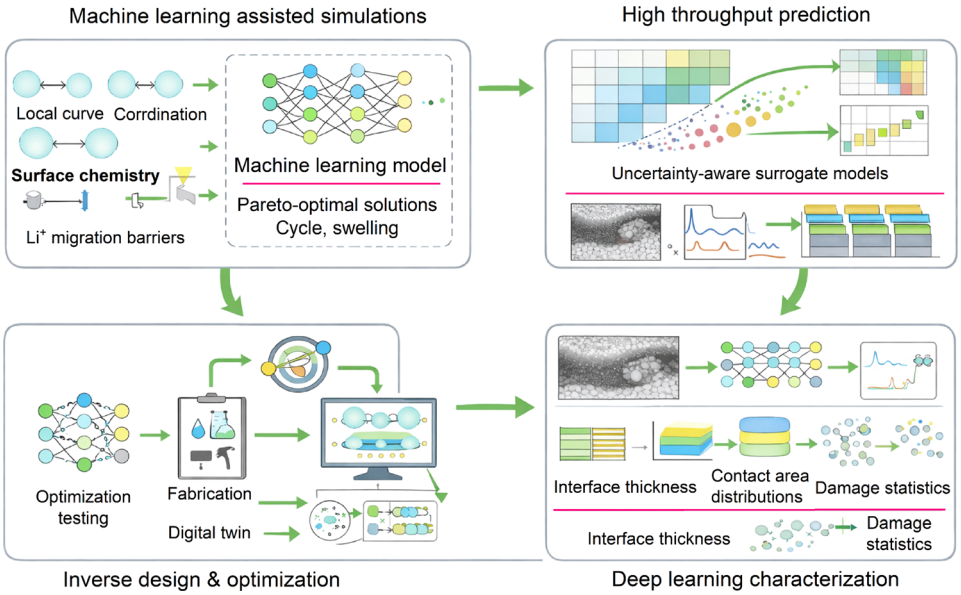

Fig. 44 AI- and data-driven closed-loop contact interface design for high-volume-strain anodes.

High hydrostatic stress at contact interfaces has been shown to retard Li^+ diffusion and reduce the thermodynamic driving force for lithiation, creating blocking effects that lead to inhomogeneous reaction current.[486,487] Advanced coupled models now integrate stress-dependent diffusion equations with mechanical constitutive laws, elucidating a feedback loop. Volume strain generates contact stress, which in turn hinders local lithiation, potentially protecting the contact interface from over-stressing but also limiting the accessible capacity. Understanding this bidirectional coupling is essential for optimizing the trade-off between interfacial mechanical integrity and fast charging capability.

6.4.4. Summary. At the atomic scale, DFT can map interfacial energetic landscapes as a function of Li concentration and local bonding, thereby identifying whether a designed interface is thermodynamically stable or prone to reconstruction during cycling.[488] For example, DFT-derived adhesion/binding energies and charge-transfer characteristics can be used to evaluate whether a PtP or LtL contact will spontaneously densify into a larger-area StS contact upon strain, or instead become chemically weakened by interfacial alloying and SEI-induced passivation.[489] Moreover, DFT-based screening (including high-throughput or descriptor-guided workflows) enables rapid selection of coatings, interlayers, or dopants that optimize interfacial bonding strength and ion-transfer barriers, thus biasing the system toward favorable evolution trajectories rather than a single initial state.[490,491]

MD simulations provide the complementary time dimension, allowing direct observation of contact migration, phase redistribution, and interphase growth under realistic thermo-electrochemical conditions.[492] Classical or reactive MD can capture the nucleation of lithiated phases near contact, the emergence of interfacial Li-rich layers, and the progressive densification or fragmentation of contacts over repeated lithiation/delithiation.[493] In addition, MD is increasingly combined with machine-learning interatomic potentials to access longer timescales and larger interfacial domains, enabling more quantitatively faithful prediction of interface decohesion, crack initiation, and SEI-mediated third-phase reconstruction that are difficult to resolve experimentally.

To link atomic-level interfacial processes with electrode-level degradation, multiscale modeling frameworks are indispensable. Parameters derived from DFT/MD (*e.g.*, interfacial adhesion energy, Li diffusivity, elastic moduli, or reaction-induced eigenstrain) can be fed into phase-field or continuum FEM models to predict stress redistribution, contact loss, and geometric-state transitions across particles, shells, and conductive frameworks. Such multiscale coupling allows one to evaluate not only an interface's instantaneous function, but also its lifetime-level evolution under practical cycling conditions, thereby providing actionable guidance for designing contact interfaces that remain transport-efficient and mechanically coherent over long service times.[494]

6.5. AI and data-driven contact interfaces

Fig. 44 illustrates a unified, closed-loop framework for artificial intelligence (AI)- and data-driven contact-interface engineering in high-volume-strain anodes, structured around four tightly coupled modules. Machine learning-assisted cross-scale simulations translate atomistic, mesoscopic, and continuum descriptors into interface-level performance metrics, enabling efficient screening beyond single-scale modelling.[495] High-throughput prediction then explores the vast combinatorial design space of interface chemistry, geometry, and mechanics using uncertainty-aware surrogate models, identifying Pareto-optimal trade-offs rather than isolated optima.[496] Deep learning-assisted characterization converts complex, multimodal experimental signals into evolution-aware, interface-native descriptors, such as contact-mode distributions, interphase thickness, and damage statistics bridging the gap between buried nanoscale interfaces and model inputs. Finally, inverse design and closed-loop optimization integrate prediction

and characterization with fabrication and testing, allowing iterative refinement of interface chemistry, topology, and processing under realistic constraints.[497] Altogether, this framework shifts contact interface engineering from static, trial-and-error optimisation toward an evolution-aware, data-accelerated paradigm, where PtP/LtL/StS contact states provide a common descriptor layer linking chemistry, mechanics, and electrochemical reliability across scales.

6.5.1. Machine learning assisted multiscale simulations. AI and data-driven methods are rapidly becoming a practical complement to physics-based simulations for contact-interface engineering in high-volume-strain anodes. Because the design space encompasses interface geometry (PtP/LtL/StS), interaction strength, SEI chemistry, and multiscale mechanics, descriptor-based learning offers an efficient approach to mapping interfacial structure to function.[498] In a typical workflow, carefully chosen descriptors, such as local coordination number and curvature at PtP/LtL/StS contact interfaces, chemical composition and roughness of the interphase, adhesion and cleavage energies from DFT, Li^+ migration barriers from nudged elastic band (NEB) calculations, and elastic, plastic, and fracture parameters from MD/FEA are assembled into feature vectors.[499,500] In contrast, experimentally accessible quantities such as charge-transfer resistance, apparent DLi, swelling strain, and cycle-life statistics serve as labels. Machine-learning models trained on such combined DFT/MD/FEA and experimental datasets can then rapidly screen coatings, interlayers or composite architectures and enable *in silico* screening and inverse design of contact interfaces that achieve Pareto-optimal trade-offs between kinetics, mechanical robustness, and volumetric performance rather than optimising each metric in isolation.[501]

6.5.2. High-throughput prediction. High-throughput prediction seeks to convert the vast combinatorial space of contact-interface design into a tractable search. For high-volume-strain anodes, design variables extend beyond material selection (Si/SiO_x/Sn/Ge/oxides/P and carbon/binders/current collectors) to interphase chemistry (SEI and artificial interlayers/coatings) and interface geometry (PtP/LtL/StS).[502] Because contact interface failure arises from coupled transport–mechanics–chemistry, an effective scheme should prioritize interface-level metrics causally upstream of cell-level outcomes, rather than directly regressing capacity retention from formulation metadata.[503,504]

A practical approach is to define a compact yet expressive target set aligned with the PtP/LtL/StS framework and the strain contact-loss chain:[505–507] (i) thermodynamic stability of contacts/interphases during lithiation, (ii) kinetic descriptors, (iii) mechanical integrity metrics, and (iv) evolution-aware quantities describing whether PtP/LtL contacts densify into StS or instead weaken and delaminate under SEI growth and interfacial reactions. This is consistent with the earlier emphasis that DFT-derived adhesion/binding energies, charge-transfer characteristics, and Li^+ migration barriers can screen coatings/interlayers/dopants and bias interfaces toward favorable evolution trajectories rather than a single initial state.

Data generation typically follows two complementary streams. High-throughput computation uses DFT to evaluate adhesion, charge redistribution, and reaction energetics for simplified interfaces with NEB providing Li-migration barriers. MD adds the time dimension by capturing interphase growth, contact sliding/necking, and early decohesion, and supplies coarse-grained transport/fracture parameters for mesoscale models.[508,509] The key is to curate both streams into a contact interface-centered database annotated by geometry (PtP/LtL/StS descriptors), chemistry (SEI/interlayer composition), and mechanics (modulus/toughness proxies), preventing learning from degenerating into purely empirical correlations.

Prediction is most powerful when implemented as uncertainty-aware surrogate modeling. Instead of running expensive DFT/MD/FEA for every candidate, regression/classification surrogates (*e.g.*, Gaussian processes or ensemble trees for small–medium datasets; message-passing models for atomic graphs) predict the targets with calibrated uncertainty.[510] Candidates are then ranked by multi-objective criteria maximizing adhesion/toughness while minimizing Li-transfer barriers and suppressing deleterious reactions, yielding Pareto fronts that reflect stability–capacity–rate trade-offs. Uncertainty also enables active learning, guiding the next round of simulations/experiments toward the most informative candidates rather than brute-force sampling.[511,512]

The key value of high-throughput prediction is its ability to output actionable PtP/LtL/StS design rules: which interlayers increase StS adhesion without penalizing Li^+ transfer, which binder motifs stabilize LtL under multi-axial strain, and which processing windows shift contact-state distributions toward percolated yet compliant architectures.[513] These outputs naturally feed into the subsequent digital-twin and closed-loop optimization concepts, where screened interface genes are translated into electrode-level lifetime forecasts under realistic constraints.[514]

6.5.3. Deep learning-assisted characterization. A central bottleneck in contact-interface engineering is that the most informative contact interfaces are nanoscale, buried, chemically fragile, and dynamically evolving, so conventional characterization often yields noisy or averaged signals. Deep learning (DL) alleviates this by translating high-dimensional, multimodal measurements into quantitative, interface-native variables consistent with the PtP/LtL/StS framework *e.g.*, contact-mode fractions, contact-area/connectivity distributions, crack statistics, SEI/interphase thickness maps, and their temporal evolution.[515]

For 3D/4D imaging (*operando* X-ray/neutron tomography and digital volume correlation), DL improves sparse-view reconstruction/denoising, robust phase–interface segmentation (active/carbon–binder/pore/SEI), and temporal tracking of the same particles/contacts across cycling, enabling evolution-aware descriptors of contact loss and delamination.[516] For cryo-EM/TEM, DL increases throughput and statistical reliability by automating segmentation and quantification of heterogeneous SEI layers and failure motifs (neck debonding, interphase cracking, and loss of LtL tether continuity), which is critical when small fields of view risk selection bias.[517] For spectroscopy/scattering (XPS/Raman/FTIR/XANES/EXAFS), DL-assisted unmixing and physics-guided regression help disentangle interface signals from bulk contributions, yielding compositional and bonding descriptors that can be mapped back to contact integrity.[518]

Equally importantly, DL can learn relationships between electrochemical/chemo-mechanical signatures (EIS, hysteresis, and strain) and hidden interface states, especially when constrained by occasional imaging labels; this turns characterization into a continuous state-estimation problem rather than isolated snapshots.

6.5.4. Inverse design and closed-loop optimization. To move from forward prediction to true inverse design, the contact interface problem must be reformulated as an optimisation task: given target performance vectors (*e.g.*, low charge-transfer resistance, high capacity retention, limited swelling/porosity loss, and stable SEI impedance growth) identify the combination of interface chemistry, geometry, and processing conditions that satisfies these targets under realistic constraints.[519] In high-volume-strain anodes, the design variables are intrinsically high-dimensional and strongly coupled, spanning (i) contact topology (PtP/LtL/StS fractions, contact-area distributions, and percolation redundancy), (ii) interphase/SEI descriptors (composition gradients, elastic/viscoplastic compliance, adhesion spectrum, and effective ionic/electronic transport), and (iii) manufacturing parameters (binder type and content, conductive additive morphology, calendering pressure, drying protocol, formation protocol and duty-cycle history).[514] Importantly, because the best contact interface is rarely optimal with respect to a single metric, inverse design should be posed as a multi-objective optimisation, explicitly trading off kinetics, mechanical robustness, and volumetric efficiency, consistent with the design paradoxes discussed earlier.[520]

A practical approach is to combine surrogate models (trained on DFT/MD/phase-field/FEM and experimental data) with modern optimisation engines. Bayesian optimisation is particularly attractive because it couples exploitation with uncertainty-aware exploration, allowing expensive experiments (high-fidelity simulations) to be allocated where they maximally improve the model. For highly discrete design spaces (*e.g.*, binder chemistries, coating recipes, and electrolyte additive sets), evolutionary algorithms or reinforcement-learning policies can be used to discover non-intuitive recipes, while generative models (*e.g.*, graph-based generators for interphases, or microstructure generators constrained by PtP/LtL/StS grammar) can propose physically plausible candidates rather than random perturbations.[521] In all cases, explicit constraints, scalability, slurry rheology, areal loading, safety windows, and cost/sustainability should be incorporated as hard feasibility filters or soft penalties to avoid solutions that are optimal only in the lab but not manufacturable.

The end goal is a closed-loop workflow that iteratively co-optimises contact interface design and validation: (I) propose candidates using the optimiser (with uncertainty estimates), (II) fabricate/prepare interfaces or electrodes within a controlled processing window, (III) rapidly characterise the resulting PtP/LtL/StS states and interphase attributes (ideally with *operando*-informed metrics), (IV) test electrochemical–mechanical performance under standardised protocols, and (V) update the surrogate/digital-twin model with the new data. Digital twins provide the natural ''state estimator'' in this loop by continuously assimilating time-resolved measurements into a predictive representation parameterised by PtP/LtL/StS and SEI-growth kinetics. Over repeated iterations, the loop shifts contact interface engineering from expert-driven trial-and-error to data-accelerated, evolution-aware optimisation, where models learn not only which interface works initially, but which one remains stable as contacts migrate, the SEI thickens, and stress localises. Ultimately, using PtP/LtL/StS as a shared descriptor layer across scales can unify atomistic chemistry, mesoscale topology, and cell-level reliability into a single optimisation language, accelerating the discovery of robust, scalable contact interfaces for next-generation high-capacity anodes.

7. Summary and perspectives

7.1. Summary

High-capacity anode materials that offer large volume changes (*e.g.*, Si, Sn, Ge, and P) offer theoretical capacities far beyond those of graphite. Still, they experience volumetric strain during lithiation/delithiation. Such extreme strain commonly induces particle pulverization and cracking, loss of contact with the current collector or conductive network, and repeated rupture/reformation of the SEI. These coupled effects progressively sever electronic pathways, consume active lithium and electrolyte, and ultimately lead to rapid capacity decay and short cycle life, which constitutes the central barrier to practical deployment of high-strain anodes. To mitigate these issues, a wide range of composite and interfacial engineering strategies (*e.g.*, nanosizing, porous/hollow architectures, elastic scaffolds, and core–shell encapsulation) have been developed to buffer volumetric deformation and preserve transport continuity. In this context, the structure and properties of contact interfaces become decisive factors governing both electrochemical performance and mechanical integrity.

Building on this motivation, this review classifies internal contact interfaces using a geometric framework, which are PtP, LtL, and StS, and further discusses their coupled physical/chemical attributes. PtP contact interfaces are the most constrained, providing minimal contact area and thus limited charge/ion transport, while also concentrating mechanical stress at discrete junctions, making them highly vulnerable under cyclic strain. LtL contact interfaces (often enabled by 1D conductive networks) offer improved percolation and better stress redistribution than PtP, whereas StS interfaces provide the most continuous transport pathways and are, in principle, the most favorable for kinetics and contact stability (Fig. 45). Importantly, real composite electrodes rarely contain a single ideal contact mode. Instead, PtP/LtL/StS contact interfaces often coexist in hierarchical, mixed networks. More critically, contact interfaces are not static. Under severe chemo-mechanical coupling, interface geometry can dynamically evolve during cycling, which includes strain-induced densification that transiently enhances contact, or debonding and cracking that convert initially continuous StS/LtL contacts into isolated PtP contacts or even complete disconnection. Such geometric evolution is strongly coupled to

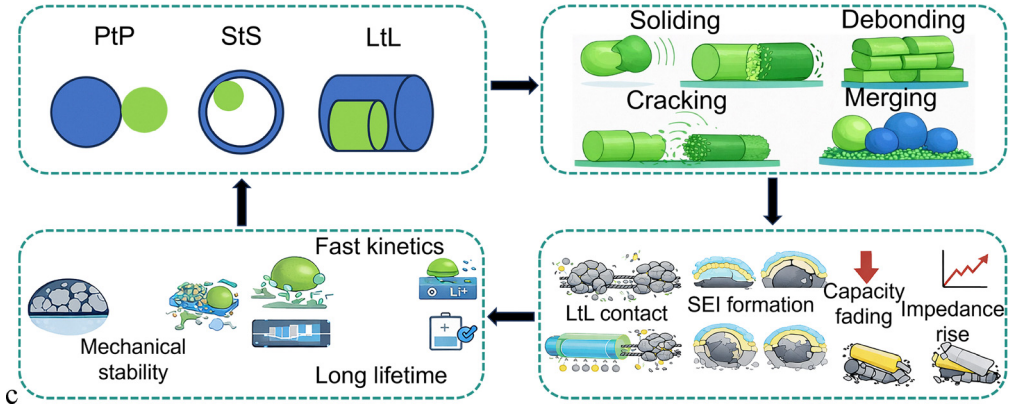

Fig. 45 Unified contact-interface design framework for high-strain anodes.

the physical/chemical nature of the interface, including interaction strength, bonding character, interphase composition, and SEI formation/stability, which together dictate how contact area, adhesion, and transport pathways change over time. Consequently, achieving simultaneously high conductivity, high stability, and high energy density requires co-optimization of interface geometry and interfacial chemistry.

At the electrode scale, robust 3D hierarchical contact networks can be engineered by combining 0D conductive fillers (initial PtP contacts), 1D percolating wires (LtL bridges), and 2D coatings or shells (StS contact and protective skins), together with functional binders that enhance adhesion and mechanical compliance. Meanwhile, advanced characterization and modeling approaches enable the observation of buried, fragile, and transient interfaces. *Operando* and *in situ* imaging (including X-ray/neutron methods) tracks morphological evolution and cracking, spectroscopies resolve bonding and interphase chemistry, and multiscale simulations (DFT/MD/FEA) reveal ion transport, stress distribution, and failure initiation at interfaces. Emerging AI- and data-driven workflows further accelerate screening and optimization by mapping high-dimensional structure–property–performance relationships and enabling inverse design of interface architectures. Despite substantial progress, several open challenges remain, including balancing stability with rate capability and volumetric energy density, achieving controllable and scalable fabrication of optimized interface networks, and closing the gap between idealized models and realistic electrode behavior.

7.2. Perspectives

Contact engineering has emerged as a powerful strategy to enhance the electrochemical performance of high-capacity anode materials subjected to large volumetric changes. However, several critical issues remain to be addressed (Fig. 46).

7.2.1. Lack of clear definitions. The geometric definition of contact interfaces remains ambiguous. For instance, the boundary between PtP and StS contact is not clearly defined. Should an atomic-scale contact still be classified as PtP, or does it transition to StS at the nanoscale? In practice, this ambiguity is amplified by multiscale roughness and deformation: a nominal PtP interface may consist of discrete micro-asperity junctions, while a point contact may rapidly spread under plasticity, creep, or interphase growth. As a result, different researchers often apply different implicit criteria. Electrochemists may emphasize charge-transfer accessibility and ionic pathways. In contrast, mechanics-focused studies may classify contacts by load-bearing area and stress concentration, and materials chemists may prioritize the presence of an interphase, bonding motifs, or interfacial reconstruction.

Similarly, the classification of physical and chemical interfaces into weak and strong interactions lacks a quantitative basis. Should interaction energy thresholds be established to distinguish between them? Beyond simple "bond strength", the effective interaction relevant to cycling stability is time- and environment-dependent, shaped by electrolyte wetting, SEI formation, interphase viscoelasticity, frictional sliding, and damage accumulation. Without shared, operational definitions, cross-study comparisons become unreliable, meta-analyses and data aggregation are weakened, and design rules derived from one platform may not generalize to others. This also limits the interpretability of emerging AI and digital-twin approaches, because labels such as PtP/LtL/StS or weak/strong can be inconsistently assigned across datasets. Future research should aim to propose precise and quantitative criteria for defining contact interface types, ideally through a standardized descriptor set (*e.g.*, real contact-area fraction, contact-length/area density, coordination/connectivity metrics, adhesion/work-of-separation, and interphase thickness/chemistry) that can be measured or inferred reproducibly across scales and cycling states.

7.2.2. Fundamental paradoxes in geometric design. Several fundamental paradoxes intrinsically constrain geometric interface engineering for large-volume-strain anodes, because the same geometric features that improve one performance dimension often degrade another.[522]

A first paradox is the contact-area paradox: enlarging the real contact area by moving from PtP toward StS generally lowers local current density, reduces charge-transfer resistance, and homogenizes stress distribution, yet it can also increase constraint on the active phase. Under extreme expansion, overly tight StS-like confinement may elevate triaxial stress, accelerate cracking or interphase fracture, and promote catastrophic debonding once

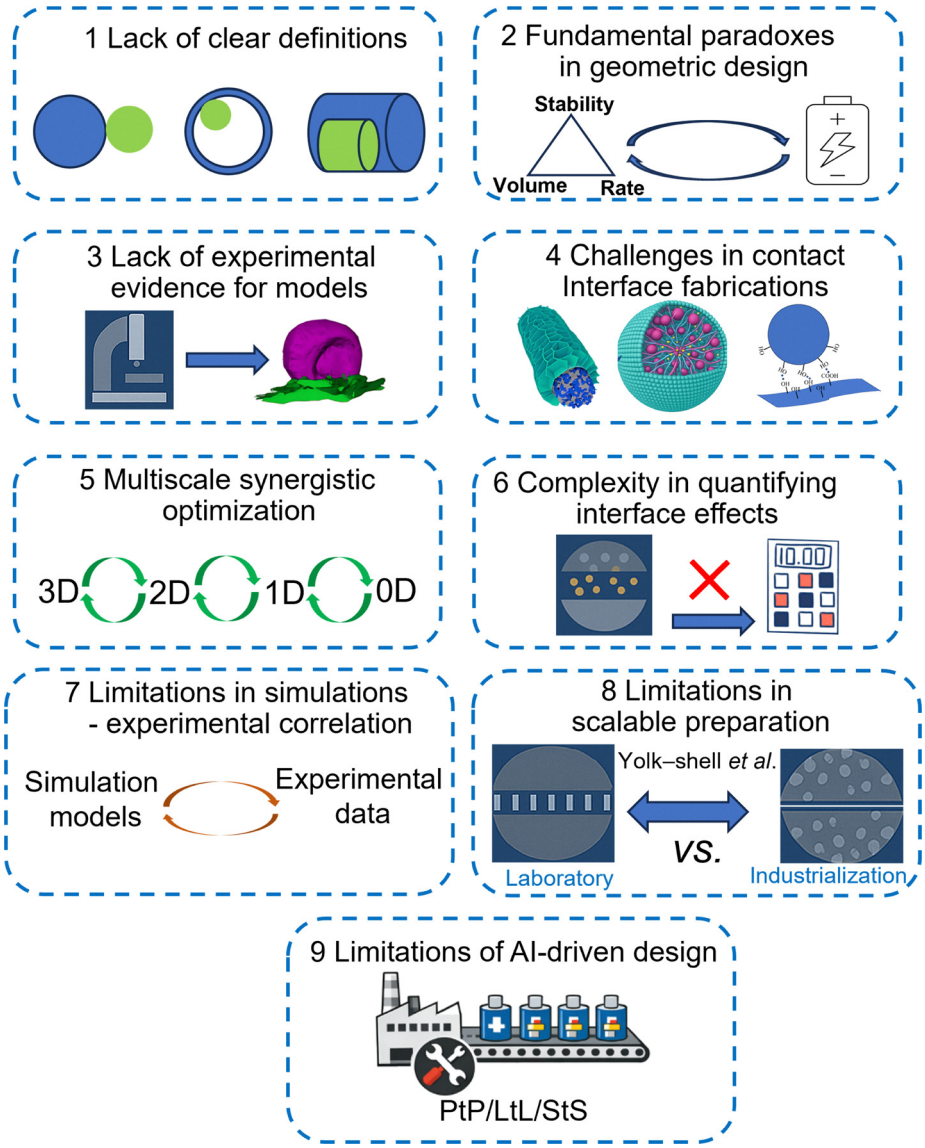

Fig. 46 The perspectives of study in contact engineering proposed in this work.

the adhesion limit is exceeded.[523] Conversely, intentionally sparse PtP-like contacts can relieve constraint and accommodate deformation, but they simultaneously amplify stress concentration at discrete junctions and dramatically reduce electrical percolation robustness, making the electrode vulnerable to sudden disconnection. A second paradox is the porosity–connectivity–energy-density trade-off. Many architectures that convert PtP into LtL/StS networks rely on high porosity, open scaffolds, or low-density conductive frameworks to preserve pathways during breathing. These designs can be highly effective in half-cells, but the same geometric free volume reduces tap density and volumetric energy density and may exacerbate electrolyte consumption by increasing accessible surface area for SEI growth. Increasing electrode densification and calendaring improves volumetric metrics, yet it can collapse engineered void space, hinder ion transport, and mechanically intensify interface damage. The third paradox concerns hierarchical length scales: optimizing contacts at the primary particle level does not guarantee stability at the secondary particle or electrode level, where particle rearrangement, binder relaxation, and interphase accumulation continuously rewrite the effective PtP/LtL/StS topology. Addressing these paradoxes requires geometry-aware, multiscale co-design, where contact type, connectivity, void space, and mechanical compliance are tuned together, rather than pursuing a single "ideal" contact geometry.

7.2.3. Lack of experimental evidence for theoretical models. Despite significant advancements in theoretical modeling of stress transfer, ion transport, and failure mechanisms at contact interfaces, experimental validation remains a critical gap in current research. Theoretical models, often grounded in DFT, MD, and FEA, provide valuable insights into atomic-scale interactions, stress fields, and ion migration paths. However, these models often rely on idealized assumptions, such as static interfaces and simplified geometries, which fail to account for

the dynamic, evolving nature of real-world interfaces. This discrepancy is particularly problematic given that contact interfaces undergo continuous morphological and chemical changes during (de)lithiation, making direct validation challenging.

One of the core difficulties is the dimensions of contact interfaces. They are typically at the atomic or nanometer scale, which makes them exceedingly difficult to observe directly in real time, particularly under operational conditions. This limitation hinders the validation of stress transfer and failure mechanisms, such as crack propagation, delamination, and SEI growth, that are central to interface degradation. Although computational models predict these phenomena with increasing sophistication, there remains a lack of experimental evidence to confirm their behavior in a practical, dynamic setting.

Emerging *in situ* characterization tools, such as TEM, AFM, and *operando* techniques like X-ray tomography and neutron diffraction, offer the potential to bridge this gap. These tools are beginning to provide real-time, high-resolution images of interface evolution, capturing key processes like ion insertion, interphase formation, and crack nucleation during cycling. By integrating these experimental insights with theoretical models, future research can validate and refine our understanding of contact interface dynamics, providing a more accurate foundation for designing next-generation anodes.

7.2.4. Challenges in interface fabrication. Interface configurations such as bridge-joint PtP contacts and heterogeneous junctions are difficult to synthesize due to the precision required in controlling interfacial structure. This fabrication challenge limits their scalability and practical application. Hence, new fabrication techniques enabling precise construction of targeted interfacial architectures are urgently needed.

Beyond laboratory performance, the industrial feasibility of contact-interface designs is ultimately constrained by tap/areal density, scalable processing, and long-term mechanical reliability. Commercial Si-based anodes are still dominated by simplified SiO_x–graphite or low-Si composites made through continuous, low-cost routes (pitch/resin coating, spray drying, mechanochemical blending, and conventional carbonization), which naturally favor density-preserving StS/PtP-rich composite contacts rather than delicate hollow or ultraporous 3D networks. In contrast, many lab-scale hollow/3D architectures rely on multistep templating/etching or low-throughput self-assembly and often sacrifice volumetric metrics; even in yolk–shell systems, excessive void space can reduce volume energy density and raise practical concerns if not densified or mechanically reinforced. Encouragingly, several interface concepts are already converging toward industrially compatible forms: robust pitch-coated Si-nanolayer/graphite composites maintain low, commercially acceptable swelling ($\sim$48% after 50 cycles) and high full-cell retention under industrial electrode density ($\sim$1.6 g cm^{-3}), illustrating that strong StS protection can be achieved without sacrificing manufacturability. Likewise, high-tap-density yolk–shell microspheres that integrate conductive inner CNT highways show a realistic pathway to couple void-buffered strain accommodation with density and areal-capacity targets.

7.2.5. Multiscale synergistic optimization. Multiscale structural engineering has emerged as a critical strategy for optimizing high-performance anodes by simultaneously addressing mechanical resilience, charge transport, and energy density. At the macroscopic level, the design of electrode architectures often focuses on achieving high packing density and mechanical stability to minimize electrode expansion during cycling. However, as we move toward the nanoscopic and atomic scales, the optimization of these properties becomes increasingly complex, as each level of design introduces new challenges and opportunities for synergy.

At the nanoscale, architectures such as 3D porous networks, hollow structures, and core–shell designs are particularly effective at buffering the large volumetric strain typically associated with high-capacity anode materials like silicon (Si) and tin (Sn). These designs allow for the accommodation of stress by creating space within the structure, preventing catastrophic fracture or delamination. For example, in yolk–shell Si@C/graphene composites, the hollow carbon shell acts as a buffer, allowing the Si core to expand and contract during cycling without losing structural integrity. At the atomic level, the incorporation of Si–C bonding at the interface ensures electrical continuity, mitigates particle pulverization, and enhances cycling stability by preventing the loss of active material.

This multiscale approach leverages the strengths of each scale to optimize overall anode performance. However, the challenge lies in achieving a harmonious integration of these scales, as the mechanical, electrical, and chemical properties at each level interact in complex ways. Future research should focus on refining these multiscale strategies, using advanced computational models and *in situ* characterization tools to better understand the interactions between the different scales. Such efforts will be key to advancing high-performance anodes capable of sustaining the next generation of energy storage devices.

7.2.6. Complexity in quantifying interface effects. The interrelation between strain accommodation, Li^+ diffusion, and interface configurations presents significant challenges in quantification, particularly in composite anode systems. The intricate behavior of interfaces, which evolve dynamically under cycling, involves multiple factors such as electrochemical reactions, mechanical stress, and phase transformations, each contributing to the overall performance. In many advanced composite anodes, multiple interface modes (PtP, LtL, and StS contact interfaces) operate simultaneously. These different interface types, each with distinct characteristics in terms of charge transfer, mechanical stability, and strain accommodation, interact in complex ways, making it difficult to isolate and quantify their individual contributions. For example, in core–shell or yolk–shell designs, interfaces at both the outer shell and inner core exhibit unique properties that influence the overall performance, but their simultaneous effects can be challenging to disentangle.

Moreover, the coupling between strain and Li^+ diffusion is highly dynamic, as mechanical deformation during cycling can impact ionic pathways and create localized inhomogeneities in diffusion rates. As these interfaces evolve under strain, new sites for ionic conduction may emerge, while others may be

obstructed or degraded. Traditional experimental methods, though valuable, often struggle to capture these transient, multi-dimensional interactions in real-time, especially when dealing with heterogeneous, multi-phase systems.

7.2.7. Limitations in simulation–experiment correlation. Current simulation models for heterostructured contact interfaces often rely on idealized assumptions that do not fully capture the complexities of real-world morphologies observed in experimental systems. These models typically simplify the interface by assuming uniform geometries, smooth surfaces, and static interaction patterns, which contrast with the highly dynamic and heterogeneous nature of actual interfaces in large-volume-strain anodes. In practice, contact interfaces are influenced by a multitude of factors such as surface roughness, nanoscale defects, electrochemical reactions, and the evolving SEI, all of which contribute to the material's performance in ways that are difficult to simulate accurately. As a result, discrepancies between modeled and actual contact interfaces can arise, limiting the practical relevance and predictive power of simulation results.

Furthermore, the parameters used in simulations, such as interfacial adhesion, diffusion coefficients, and stress distribution, are often based on idealized assumptions or extrapolated from simplified experimental conditions. These assumptions may not capture the complex, time-dependent changes that occur under realistic cycling conditions, such as interface degradation, crack propagation, or SEI evolution. This gap between simulation and experiment is a major barrier to the design of robust anode materials, as the lack of real-world accuracy in simulations may lead to over-optimistic predictions or incorrect design guidelines.

Bridging this gap requires improved structural models that more accurately reflect the complexity of contact interfaces, as well as more precisely inform the simulations. Incorporating real-time, high-resolution experimental measurements, such as *operando* imaging, X-ray tomography, and cryo-TEM, into simulation frameworks will be essential to refine these models. By better aligning simulation predictions with experimental realities, we can improve the design and optimization of next-generation anodes.

7.2.8. Limitations in scalable preparation. Many contact interface-engineering strategies are discussed, such as yolk–shell architectures, hierarchical 3D scaffolds, and conformal multi-layer coatings, which are highly effective at the laboratory scale, yet their translation to scalable and cost-effective manufacturing remains a major hurdle. In practice, a large fraction of state-of-the-art designs relies on multi-step templating/etching routes, delicate self-assembly, or low-throughput coating processes, which complicate scale-up and increase cost. For example, typical yolk–shell constructs often require sacrificial interlayers followed by acid/alkali (or even HF-based) etching and extensive washing, posing concerns in yield, safety, and waste management. Likewise, many 3D scaffold electrodes are fabricated through freeze-drying, supercritical/ambient drying, or template-assisted aerogel routes; while structurally powerful, these methods can be batch-limited and energy-intensive when translated to ton-scale production. Another practical constraint is that complex nano-architectures frequently trade volumetric metrics for gravimetric performance. Highly porous yolk–shell or aerogel-like scaffolds may suffer from low tap density and high surface area, which inflate SEI formation and first-cycle Li^+ loss, and are unfavorable for industrial electrodes with high areal loading and calendaring requirements.[523]

Encouragingly, several manufacturing routes that are already compatible with industrial material lines can approximate or simplify these advanced contact interface concepts. Spray-drying/spray-pyrolysis offers a continuous, high-throughput approach to produce micro-spherical Si/carbon composites and even yolk–shell-like voided structures at scale and has been repeatedly demonstrated as an industrially adaptable method for high-strain anodes.[524] Mechanochemical blending/ball milling with pitch or polymer precursors, followed by standard carbonization, provides another scalable route to create robust StS-type bonding and buffered composite interfaces without complicated sacrificial templates. In addition, continuous CVD coating, already mature in roll-to-roll industries, enables uniform Si or carbon interlayers with controlled thickness, although current cost and energy intensity still require further reduction.[525,526] For 3D conductive frameworks, electrospinning is increasingly scalable through multi-nozzle/needleless and roll-to-roll setups, making fibrous LtL/StS scaffold electrodes more manufacturable than previously assumed. Finally, the use of low-cost Si feedstocks (*e.g.*, photovoltaic kerf-loss waste) coupled with simple wet-coating/carbonization processes provides a realistic pathway to reduce raw-material cost while retaining key interface-buffering benefits.

Overall, bridging the lab-to-industry gap requires contact interface designs to be evaluated not only by electrochemical metrics, but also by manufacturing-relevant criteria, including process continuity, yield, solvent/etchant recyclability, energy consumption, tap/areal density, and batch-to-batch consistency. Future interface engineering should therefore co-optimize performance and manufacturability, favoring simplified, continuous, and environmentally benign routes that can reproduce the essential contact-buffering mechanisms at industrial scales.

7.2.9. Limitations of AI-driven design. While Section 6.5 outlines how AI and data-driven workflows could, in principle, accelerate contact-interface engineering, their practical deployment is still limited by several issues that prevent the outlook from becoming a truly actionable and transferable roadmap. The first bottleneck is the absence of standardized, quantitative ground-truth labels for contact interfaces. Key concepts such as PtP/LtL/StS fractions, real contact-area evolution, or weak/strong interaction regimes are often inferred qualitatively, reported with inconsistent criteria, or measured indirectly under non-comparable conditions. As a result, datasets pooled from the literature may contain systematic label noise, and models can learn author- or platform-specific conventions rather than robust interface physics.

A second limitation is domain shift across realistic operating regimes. Models developed from coin-cell half-cells, low areal loadings, and excess-electrolyte testing frequently degrade when transferred to high-loading electrodes, lean-electrolyte conditions, aggressive formation protocols, or full-cell configurations where interphase growth, transport limitation, and stress states

differ fundamentally. Without explicit cross-domain validation, AI recommendations may appear convincing yet fail under industrially relevant constraints.

Third, *operando* evidence remains insufficiently model-addressable. Even when advanced *operando* tools are available, the extracted observables are not always converted into reproducible, interface-native metrics (*e.g.*, connectivity decay rates, contact-loss kinetics, and interphase thickening rates) that can be directly compared to model variables and used for falsification. This weakens the ability to calibrate models, diagnose failure modes, and update predictions as interfaces evolve.

Finally, scalability is not just a constraint, but a reliability problem: manufacturable electrodes must satisfy not only tap density and areal loading targets, but also slurry/process robustness, batch-to-batch consistency, and tolerances to calendering and aging. Therefore, meaningful AI-driven design requires community-level benchmarks and reporting standards that couple interface descriptors to realistic cell configurations and reproducible validation pipelines. Until such a measurement and protocol infrastructure is established, AI should be viewed as an enabling tool rather than a standalone solution for interface design in high-strain anodes.

Conclusions and outline

In this review, we first explain the importance and necessity of studying contact interfaces and introduce in Section 2 the major high-volume-strain anode materials (Si-, Sn-, Ge-, oxide- and P-based systems) together with typical structural design motifs that have been proposed to buffer large expansion. Section 3 then proposes a geometric classification of internal contact interfaces—point-to-point (PtP), line-to-line (LtL), and surface-to-surface (StS)—and illustrates how these contact interface types coexist and dynamically evolve within realistic composite electrodes under cycling. Building on this, Section 4 focuses on the physical and chemical nature of contact interfaces, distinguishing weak *versus* strong interactions and heterointerfaces and discussing how electronic structure and bonding govern charge transfer and mechanical robustness. Section 5 extends the contact interface concept to the electrode level, analysing active material–binder, active material–conductive additive, and active material–current collector contacts and further discusses solid–solid contact interfaces in Si-based all-solid-state batteries, culminating in an integrated mechanistic chain from volume-strain generation to contact interface degradation and electrochemical failure. Section 6 reviews advanced characterization and modelling tools for probing these contact interfaces across scales, including 2D/3D imaging, *in situ* and cryogenic techniques, spectroscopies, multiscale simulations, and AI-driven design, and maps each method onto the PtP/LtL/StS framework. Finally, Section 7 summarizes design principles and engineering strategies for constructing mechanically compliant, electronically and ionically percolated contact interfaces, and outlines remaining challenges and future research directions.

Declaration of generative AI and AI-assisted technologies in the writing process

During the preparation of this work, the authors used ChatGPT to generate individual elements of the figures, which were subsequently assembled and designed into the final figures by the authors. All scientific decisions regarding figure content and presentation were made solely by the authors. After using this tool, the authors reviewed and edited the content as needed and took full responsibility for the content of the published article.

Author contributions

G. Y., F. W., and H. H. proposed the topic and wrote the manuscript; J. L., H. Z. and X. L. collected the data; Y. Z., J. F., Z. G. and Y. Z. helped the figure organization; F. W., H. H., and Y. Y. are responsible for the work; all authors helped revise the manuscript and have approved for the submission.

Conflicts of interest

The authors declare that they have no known competing financial interests or personal relationships that could have appeared to influence the work reported in this paper.

Abbreviations

Li^+	Lithium-ion
LIBs	Lithium-ion batteries
PVDF	Polyvinylidene fluoride
Si	Silicon
O	Oxygen
Sn	Tin
P	Phosphorus
SnS_2	Tin disulfide
RP	Red phosphorus
BP	Black phosphorus
SnP	Tin phosphide
MOs	Metal oxides
M	Metal
3D	Three-dimensional
LtL	Line to line
FEM	Finite element method
StS	Surface-to-surface
CVD	Chemical vapour deposition
EIS	Electrochemical impedance spectroscopy
RG/Fe_3O_4	Fe_3O_4/graphene composites with strong interaction
SEM	Scanning electron microscope
AFM	Atomic force microscope
XPS	X-ray photoelectron spectroscopy
XANES	X-ray absorption near-edge structure
SAED	Selected area electron diffraction
CB	Carbon black

FEA	Finite element analysis
1D	One-dimensional
4D	Four-dimensional
XAS	X-ray absorption spectroscopy
FEA	Finite-element analysis
AI	Artificial intelligence
Li_2O	Lithium oxide
PAA	Polyacrylic acid
CMC	Carboxymethyl cellulose
ASSBs	All-solid-state batteries
S-LHCEs	Solidified localized high-concentration electrolytes
ATR-FTIR	Attenuated total reflection Fourier transform infrared spectroscopy
MLPs	Machine learning potentials
DL	Deep learning
MIEC	Mixed ionic-electronic conductor
SEI	Solid electrolyte interface
SiO	Silicon monoxide
SiO_2	Silicon dioxide
SiO_x	Non-stoichiometric silicon oxide
TEM	Transmission electron microscope
Ge	Germanium
SnS	Tin sulfide
S	Sulfur
PP	Purple phosphorus
P–S	Phosphorus–sulfur
GeP	Germanium phosphide
GeO_2	Germanium oxide
DFT	Density functional theory
PtP	Point-to-point
StS	Surface-to-surface
2D	Two-dimensional
YS-Si/C	Electrode materials with a bridge joint point contact
GO	Graphene oxide
TEOS	Tetraethyl orthosilicate
RG + Fe_3O_4	Mechanical mixing Fe_3O_4/graphene composites
FIB	Focused ion beam
EDS	Energy dispersive X-ray spectrometer
DOS	Density of states
FT-IR	Fourier transform infrared spectroscopy
MD	Molecular dynamics
CNTs	Carbon nanotubes
Cu	Copper
CEM	Cryogenic electron microscopy
XRD-CT	X-ray CT
C	Coulombic efficiency
PVDF	Polyvinylidene fluoride
NEB	Nudged elastic band
SGA	Graphene aerogel
M	Metal nanoparticles
–COOH	Carboxylic acid groups
SE	Solid electrolytes
X-CT	High-throughput *operando* X-ray computed tomography
ReaxFF	Reactive force field
DP	Deep potentials
CZM	Cohesive zone models
MCI	Mixed conducting interphase

Data availability

Data availability is not applicable to this article as no new data were created or analyzed in this study.

Acknowledgements

This work was supported by the National Natural Science Foundation of China (No. 52402365, 52525203, 52394170, 52394171, U24A2067, 52522212, 52222210, U24A2064, 52372239, 52472261, U23A20579, and 524B2026), Yunnan Fundamental Research Projects (202401BE070001-010), the Liaoning Binhai Laboratory (Grant No. LBLF-2023-03), the State Key Laboratory of Catalysis (No: 2024SKL-B-003), the Strategic Priority Research Program of Chinese Academy of Sciences (Grant No. XDA0400202), Commanding heights of science and technology of Chinese Academy of Sciences (Grant No. LDES15 0000) and the Fundamental Research Funds for the Central Universities (Grant No. WK9990000170, WK2060250119 and YD2060002042).

References

1 W. Li, J. H. Wang and Y. Li, *et al.*, Element screening of high-entropy silicon anodes for superior Li-storage performance of Li-ion batteries, *J. Am. Chem. Soc.*, 2024, **146**(31), 21320–21334.
2 H. Liu, Z. Zhu and Q. Yan, *et al.*, A disordered rock salt anode for fast-charging lithium-ion batteries, *Nature*, 2020, **585**(7823), 63–67.
3 H. Zhang, Y. Shan and R. Li, *et al.*, Rising Air-conditioning use intensifies global warming, *Nat. Commun.*, 2026, **17**(1), 1961.
4 X. Wang, X. Zhang and G. Zhao, *et al.*, Ether–water hybrid electrolyte contributing to excellent Mg ion storage in layered sodium vanadate, *ACS Nano*, 2022, **16**(4), 6093–6102.
5 F. Wang, L. Xia and X. Li, *et al.*, Nano-ferric oxide embedded in graphene oxide: high-performance electrocatalyst for nitrogen reduction at ambient conditions, *Energy Environ. Mater.*, 2021, **4**(1), 88–94.
6 F. Wang, X. Liao and H. Wang, *et al.*, Bioinspired mechanically interlocking holey graphene@SiO_2 anode. Interdisciplinary, *Materials*, 2022, **1**(4), 517–525.
7 F. Wang, X. Wei and X. Dong, *et al.*, Defective two-dimensional $Al_2Si_2O_5(OH)_4$ as a promising nitrogen reduction reaction electrocatalyst, *Appl. Clay Sci.*, 2023, **232**, 106805.
8 L. Luo, B. Wang and J. Wang, *et al.*, Vacancy engineering of WO_{3-x} nanosheets for electrocatalytic NRR process – a first-principles study, *Phys. Chem. Chem. Phys.*, 2021, **23**(31), 16658–16663.

9 H. Yu, H. Liang and Z. Gu, *et al.*, Waste-to-wealth: low-cost hard carbon anode derived from unburned charcoal with high capacity and long cycle life for sodium-ion/lithium-ion batteries, *Electrochim. Acta*, 2020, **361**, 137041.
10 Y. Zhang, Y. Wang and W. Zhao, *et al.*, Delocalized electronic engineering of $TiNb_2O_7$ enables low temperature capability for high-areal-capacity lithium-ion batteries, *Nat. Commun.*, 2024, **15**(1), 6299.
11 X. Lei, Y. Wang and J. Wang, *et al.*, Si-based high-entropy anode for lithium-ion batteries, *Small Methods*, 2024, **8**(1), 2300754.
12 Y. An, Y. Tian and C. Wei, *et al.*, Recent advances and perspectives of 2D silicon: synthesis and application for energy storage and conversion, *Energy Storage Mater.*, 2020, **32**, 115–150.
13 J. Liu, F. Wang and J. Mao, Silica quantum dots coupled with N-doping carbon achieving zero-strain, *Diamond Relat. Mater.*, 2025, **152**, 111905.
14 F. Wang, T. Deng, J. Liu, R. Tan, D. Lin and J. Mao, Si-C atomic line achieving efficient electrocatalytic nitrogen, *Colloids Surf., A*, 2024, **703**, 135216.
15 J. Liu, F. Wang and J. Mao, Si Single-atom sites anchored carbon anode achieving the zero-strain feature and superior Li^+ storage performance, *ChemSusChem*, 2024, e202400397.
16 K. J. Griffith, Y. Harada and S. Egusa, *et al.*, Titanium niobium oxide: from discovery to application in fast-charging lithium-ion batteries, *Chem. Mater.*, 2021, **33**(1), 4–18.
17 X. Li, Z. Lin and N. Jin, *et al.*, Perovskite-type $SrVO_3$ as high-performance anode materials for lithium-ion batteries, *Adv. Mater.*, 2021, **34**(46), 2107262.
18 D. Qiu, C. Kang and M. Li, *et al.*, Biomass-derived mesopore-dominant hierarchical porous carbon enabling ultra-efficient lithium ion storage, *Carbon*, 2020, **162**, 595–603.
19 X. Zhu, J. Xiao and Y. Chen, *et al.*, A high-performance nano-Sn/G@C composite anode prepared by waste carbon residue from spent lithium-ion batteries, *Chem. Eng. J.*, 2022, **450**, 138113.
20 X. Wang, T. Su and Y. Luo, *et al.*, Achieving superior lithium storage performances of $CoMoO_4$ anode for lithium-ion batteries by Si-doping dual vacancies engineering, *Acta Mater.*, 2022, **225**, 117600.
21 Y. Li, P. Xiong and L. Zhang, *et al.*, A class of Ga-Al-P-based compounds with disordered lattice as advanced anode materials for Li-ion batteries, *J. Energy Chem.*, 2023, **79**, 12–21.
22 Z. Li, G. Wu and Y. Yang, *et al.*, An ion-conductive grafted polymeric binder with practical loading for silicon anode with high interfacial stability in lithium-ion batteries, *Adv. Energy Mater.*, 2022, **12**(29), 2201197.
23 H. Zhang, D. Xu and F. Yang, *et al.*, A high-capacity Sn metal anode for aqueous acidic batteries, *Joule*, 2023, **7**(5), 971–985.
24 J. Wang, X. Ren, Q. Xiang, J. Jiang, F. Wang, Y. Guan, H. Xu and P. Wu, Double unit-cell Silicogermanate nanosheets developed by Salting-out mechanism for biomass conversion, *J. Am. Chem. Soc.*, 2024, **27**(146), 18418–18426.
25 F. Liang, L. Yang and R. Hu, *et al.*, Mechanisms, development, and applications of silicon-based anodes in solid state batteries, *Chem. Sci.*, 2026, **17**(2), 738–771.
26 R. Fu, J. Ji and L. Yun, *et al.*, Graphene wrapped silicon suboxides anodes with suppressed Li-uptake behavior enabled superior cycling stability, *Energy Storage Mater.*, 2021, **35**, 317–326.
27 Y. Wang, L. Chen and H. Liu, *et al.*, Cornlike ordered N-doped carbon coated hollow Fe_3O_4 by magnetic self-assembly for the application of Li-ion battery, *Chem. Eng. J.*, 2019, **356**, 746–755.
28 S. Choi, G. Nam and S. Chae, *et al.*, Robust pitch on Silicon nanolayer-embedded graphite for suppressing undesirable volume expansion, *Adv. Energy Mater.*, 2019, **9**(4), 1803121.
29 Y. Zhang, Z. Wang and K. Hu, *et al.*, Anchoring Silicon on the basal plane of graphite via a three-phase heterostructure for highly reversible lithium storage, *Energy Storage Mater.*, 2021, **34**, 311–319.
30 J. Wang, Y. Gao and Z. He, *et al.*, Regulating structural units and morphology of SiOC anode for enhanced high-rate storage and long-life lithium ion batteries, *J. Power Sources*, 2024, **621**, 235238.
31 K. Li, G. Yuan and X. Liu, *et al.*, On the practical applicability of rambutan-like SiOC anode with enhanced reaction kinetics for lithium-ion storage, *Adv. Funct. Mater.*, 2023, **33**(43), 2302348.
32 X. Hong, J. Kim and S. Shi, *et al.*, Ultrafast charge transfer in atomically thin MoS_2/WS_2 heterostructures, *Nat. Nanotechnol.*, 2014, **9**(9), 682–686.
33 M. H. Parekh, V. P. Parikh and P. J. Kim, *et al.*, Encapsulation and networking of silicon nanoparticles using amorphous carbon and graphite for high-performance Li-ion batteries, *Carbon*, 2019, **148**, 36–43.
34 S. Zhang, Y. Zhang and Z. Zhang, *et al.*, Bi Works as a Li reservoir for promoting the fast-charging performance of phosphorus anode for Li-ion batteries, *Adv. Energy Mater.*, 2022, **12**(19), 2103888.
35 B. Wang, X. Li and X. Zhang, *et al.*, Contact-engineered and void-involved silicon/carbon nanohybrids as Lithium-ion-battery anodes, *Adv. Mater.*, 2013, **25**(26), 3560–3565.
36 Y. Guo, Q. Niu, F. Pei, Q. Wang, Y. Zhang, L. Du, Y. Zhang, Y. Zhang, Y. Zhang, L. Fan and Q. Zhang, Interface engineering toward stable lithium–sulfur batteries, *Energy Environ. Sci.*, 2024, **17**, 1330.
37 G. Liu, J. Yang, J. Wu, Z. Peng and X. Yao, Inorganic sodium solid electrolytes: structure design, interface engineering and application, *Adv. Mater.*, 2024, **36**, 2311475.
38 L. Wang, J. Yu, S. Li, F. Xi, W. Ma, K. Wei, J. Lu, Z. Tong, B. Liu and B. Luo, Recent advances in interface engineering of silicon anodes for enhanced lithium-ion battery performance, *Energy Storage Mater.*, 2024, **66**, 103243.
39 Y. Yang, S. Yang, X. Xue, X. Zhang, Q. Li, Y. Yao, X. Rui, H. Pan and Y. Yu, Inorganic all-solid-state sodium batteries: electrolyte designing and interface engineering, *Adv. Mater.*, 2024, **36**, 2308332.

40 G. Hu, H. Liu and Y. Luo, *et al.*, Two-dimensional sandwich-like silica@carbon@silica nanosheets for superior lithium storage, *Mater. Lett.*, 2022, **308**, 131288.
41 K. C. Wasalathilake, S. N. S. Hapuarachchi and Y. Zhao, *et al.*, Unveiling the working mechanism of graphene bubble film/silicon composite anodes in Li-ion batteries: from experiment to modeling, *ACS Appl. Energy Mater.*, 2020, **3**(1), 521–531.
42 J. Guo, D. Dong and J. Wang, *et al.*, Silicon-based lithium ion battery systems: state-of-the-art from half and full cell view point, *Adv. Funct. Mater.*, 2021, **31**(34), 2102546.
43 H. Luo, X. Zhang and Z. Wang, *et al.*, Vanadium-tailored silicon composite with furthered ion diffusion behaviors for longevity lithium-ion storage, *ACS Appl. Mater. Interfaces*, 2023, **15**(3), 4166–4174.
44 J. Xu, J. Zhao and N. Zhang, *et al.*, Improved electrochemical performance of SBA-15-based SiO_2 anodes with N-doping porous carbon, *J. Electroanal. Chem.*, 2023, **928**, 117019.
45 W. Li, Q. Ma and X. Liu, *et al.*, Enhanced reaction kinetics enabled by a bi-element co-doping strategy for high-performance ternary Si-based anodes of Li-ion batteries, *Chem. Eng. J.*, 2023, **453**, 139567.
46 G. Liu, T. Jiao and Y. Cheng, *et al.*, Interfacial enhancement of Silicon-based anode by a lactam-type electrolyte additive, *ACS Appl. Energy Mater.*, 2021, **4**(9), 10323–10332.
47 C. Zhang, F. Wang and J. Han, *et al.*, Challenges and recent progress on silicon-based anode materials for next-generation lithium-ion batteries, *Small Structures*, 2021, **2**(6), 2100009.
48 Y. Huang, B. Shao and Y. Wang, *et al.*, Solid-state silicon anode with extremely high initial coulombic efficiency, *Energy Environ. Sci.*, 2023, **16**(4), 1569–1580.
49 H. Li, H. Li and Y. Lai, *et al.*, Revisiting the preparation progress of nano-structured Si anodes toward industrial application from the perspective of cost and scalability, *Adv. Energy Mater.*, 2022, **12**(7), 2102181.
50 L. Zhang, M. Al-Mamun and L. Wang, *et al.*, The typical structural evolution of silicon anode, *Cell Rep. Phys. Sci.*, 2022, **3**(4), 100811.
51 K. Shi, F. Yang and H. Xu, *et al.*, Silicon oxide anodes: advances and challenges toward practical applications, *Coord. Chem. Rev.*, 2026, **550**, 217394.
52 X. Zhang, L. Huang and Q. Shen, *et al.*, Hollow boron-doped Si/SiO_x nanospheres embedded in the vanadium nitride/nanopore-assisted carbon conductive network for superior lithium storage, *ACS Appl. Mater. Interfaces*, 2019, **11**(49), 45612–45620.
53 G. Ge, G. Li and X. Wang, *et al.*, Manipulating oxidation of silicon with fresh surface enabling stable battery anode, *Nano Lett.*, 2021, **21**(7), 3127–3133.
54 S. Gao, S. Li and L. Yang, *et al.*, Zero-strain Li_2VSiO_5 for high-performance lithium storage, *Chem. Mater.*, 2023, **35**(10), 4048–4056.
55 F. Wang, J. Mao and Y. Zhao, Crystal engineering of silica anode achieving intrinsic zero-strain, *Adv. Mater.*, 2023, **35**(51), 2307908.
56 Z. Liu, Q. Yu and Y. Zhao, *et al.*, Silicon oxides: a promising family of anode materials for lithium-ion batteries, *Chem. Soc. Rev.*, 2019, **48**(1), 239–285.
57 W. Chang, C. Park and J. Kim, *et al.*, Quartz (SiO_2): a new energy storage anode material for Li-ion batteries, *Energy Environ. Sci.*, 2012, **5**(5), 6895–6899.
58 C. Wang, X. Li and Z. Wang, *et al.*, In situ TEM investigation of congruent phase transition and structural evolution of nanostructured silicon/carbon anode for lithium ion batteries, *Nano Lett.*, 2012, **12**(3), 1624–1632.
59 L. Sun, Y. Liu and R. Shao, *et al.*, Recent progress and future perspective on practical silicon anode-based lithium ion batteries, *Energy Storage Mater.*, 2022, **46**, 482–502.
60 G. Huang, J. Han and Z. Lu, *et al.*, Ultrastable silicon anode by three-dimensional nanoarchitecture design, *ACS Nano*, 2020, **14**(4), 4374–4382.
61 B. S. Lee, S. Oh and Y. J. Choi, *et al.*, SiO-induced thermal instability and interplay between graphite and SiO in graphite/SiO composite anode, *Nat. Commun.*, 2023, **14**(1), 150.
62 Y. Wei, Z. Xiao and Y. Huang, *et al.*, Insights into the SiO_2 stress effect on the electrochemical performance of Si anode, *Small*, 2024, **20**(20), 2310240.
63 F. Wang, Z. Hu and L. Mao, *et al.*, Nano-silicon @ soft carbon embedded in graphene scaffold: high-performance 3D free-standing anode for lithium-ion batteries, *J. Power Sources*, 2020, **450**, 227692.
64 Y. Lei, X. Li and F. Ding, *et al.*, SiO_2 for electrochemical energy storage applications, *J. Power Sources*, 2024, **623**, 235494.
65 V. V. Kozik, L. P. Borilo and E. S. Lyutova, *et al.*, Preparation of $CaO@TiO_2$ –SiO_2 biomaterial with a sol–gel method for bone implantation, *ACS Omega*, 2020, **5**(42), 27221–27226.
66 S. Fan, X. Zhou and J. Tang, *et al.*, Insights to the variation of oxygen content and reasons for improved electrochemical performance of annealing SiO_x anodes for Li-ion battery, *Appl. Surf. Sci.*, 2022, **579**, 152179.
67 Z. Li, M. Du and P. Liu, *et al.*, Exploring the influence of oxygen distribution on the performance of SiO anode materials, *J. Power Sources*, 2025, **625**, 235720.
68 Y. He, X. Yu and G. Li, *et al.*, Shape evolution of patterned amorphous and polycrystalline silicon microarray thin film electrodes caused by lithium insertion and extraction, *J. Power Sources*, 2012, **216**, 131–138.
69 X. Zhan, M. Li and S. Li, *et al.*, Challenges and opportunities towards silicon-based all-solid-state batteries, *Energy Storage Mater.*, 2023, **61**, 102875.
70 M. A. Rahman, G. Song and A. I. Bhatt, *et al.*, Nanostructured silicon anodes for high-performance lithium-ion batteries, *Adv. Funct. Mater.*, 2016, **26**(5), 647–678.
71 S. Pan, J. Han and Y. Wang, *et al.*, Integrating SEI into layered conductive polymer coatings for ultrastable silicon anodes, *Adv. Mater.*, 2022, **34**(31), 2203617.
72 K. Kitada, O. Pecher, P. C. Magusin, M. F. Groh, R. S. Weatherup and C. P. Grey, Unraveling the reaction mechanisms of SiO anodes for Li-ion batteries by combining in situ 7Li and ex situ 7Li/29Si solid-state NMR spectroscopy, *J. Am. Chem. Soc.*, 2019, **141**(17), 7014–7027.

73 C. Chou and G. S. Hwang, Lithiation behavior of silicon-rich oxide ($SiO_{1/3}$): a first-principles study, *Chem. Mater.*, 2013, **25**(17), 3435–3440.
74 M. Khan, X. Ding and H. Zhao, *et al.*, SiO_2-based lithium-ion battery anode materials: a brief review, *J. Electron. Mater.*, 2022, **51**(7), 3379–3390.
75 H. X. Chen, D. X. Xu and G. Li, *et al.*, Phase engineering of lithium silicate in SiO_x anodes for fast-charging lithium-ion batteries, *ACS Appl. Mater. Interfaces*, 2026, **18**(1), 1854–1864.
76 Y. Yang, Y. Liu, X. Jiang, L. Zhao, P. Wang and Y. Zhang, Rational design of SiO_x based anode materials for next generation lithium-ion batteries, *Mater. Adv.*, 2024, **5**, 896.
77 S. C. Jung, H. Kim and J. Kim, *et al.*, Atomic-level understanding toward a high-capacity and high-power silicon oxide (SiO) material, *J. Phys. Chem. C*, 2016, **120**(2), 886–892.
78 X. Zhu, B. Liu and J. Shao, *et al.*, Fundamental mechanisms and promising strategies for the industrial application of SiO_x anode, *Adv. Funct. Mater.*, 2023, **33**(17), 2213363.
79 H. Li, H. Li and Z. Yang, *et al.*, SiO_x anode: from fundamental mechanism toward industrial application, *Small*, 2021, **17**(51), 2102641.
80 J. Yang, Y. Takeda, N. Imanishi and O. Yamamoto, Ultrafine Sn and $SnSb_{0.14}$ powders for lithium storage matrices in lithium-ion batteries, *Science*, 1999, **11**(146), 4009–4013.
81 J. R. González, R. Alcántara and F. Nacimiento, *et al.*, Optimization of tin intermetallics and composite electrodes for lithium-ion batteries obtained by sonochemical synthesis, *J. Solid State Electrochem.*, 2013, **17**(9), 2495–2501.
82 H. Ying and W. Q. Han, Metallic Sn-based anode materials: application in high-performance lithium-ion and sodium-ion batteries, *Adv. Sci.*, 2017, **4**(11), 1700298.
83 M. Chen, P. Xiao and K. Yang, *et al.*, Sn anodes protected by intermetallic $FeSn_2$ layers for long-lifespan sodium-ion batteries with high initial coulombic efficiency of 93.8%, *Angew. Chem., Int. Ed.*, 2023, **62**(16), e202219177.
84 L. Wei, X. Ren and S. Hou, *et al.*, SnO_2/Sn particles anchored in moderately exfoliated graphite as the anode of lithium-ion battery, *Electrochim. Acta*, 2023, **442**, 141908.
85 F. Liang, H. Dong and J. Dai, *et al.*, Fast energy storage of SnS_2 anode nanoconfined in hollow porous carbon nanofibers for lithium-ion batteries, *Adv. Sci.*, 2024, **11**(4), 2306711.
86 R. Thangavel, A. Samuthira Pandian and H. V. Ramasamy, *et al.*, Rapidly synthesized, few-layered pseudocapacitive SnS2 anode for high-power sodium ion batteries, *ACS Appl. Mater. Interfaces*, 2017, **9**(46), 40187–40196.
87 Z. Chen, T. Wang and Y. Liu, *et al.*, Hydrogen-titanate-protected SnO_2@C coaxial nanocables as new nanocomposite anode materials for lithium-ion batteries, *Chem. Eng. J.*, 2024, **483**, 149381.
88 W. Dong, R. Li and J. Xu, *et al.*, Long-life and high volumetric capacity $Bi_2Sn_2O_7$ anode with interpenetrating Bi–O and Sn–O networks, *Cell Rep. Phys. Sci.*, 2022, **3**(11), 101109.
89 H. G. Nam, J. Y. Park and J. M. Yuk, *et al.*, Phase transformation mechanism and stress evolution in Sn anode, *Energy Storage Mater.*, 2022, **45**, 101–109.
90 T. L. Nguyen, D. S. Kim and J. Hur, *et al.*, Ni-Sn-based hybrid composite anodes for high-performance lithium-ion batteries, *Electrochim. Acta*, 2018, **278**, 25–32.
91 Z. Yang, X. Qin and K. Lin, *et al.*, Realizing ultra-stable SnO_2 anodes via in-situ formed confined space for volume expansion, *Carbon*, 2022, **187**, 321–329.
92 X. Lan, X. Xiong and J. Liu, *et al.*, Insight into reversible conversion reactions in SnO_2-based anodes for lithium storage: a review, *Small*, 2022, **18**(26), 2201110.
93 N. Kamboj, B. Debnath and S. Bhardwaj, *et al.*, Ultrafine mix-phase SnO-SnO_2 nanoparticles anchored on reduced graphene oxide boost reversible Li-ion storage capacity beyond theoretical limit, *ACS Nano*, 2022, **16**(9), 15358–15368.
94 G. Xu, Y. Gong and C. Miao, *et al.*, Sn nanoparticles embedded into porous hydrogel-derived pyrolytic carbon as composite anode materials for lithium-ion batteries, *Rare Met.*, 2022, **41**(10), 3421–3431.
95 Y. S. Mun, T. N. Pham and V. K. Hoang Bui, *et al.*, Tin oxide evolution by heat-treatment with tin-aminoclay (SnAC) under argon condition for lithium-ion battery (LIB) anode applications, *J. Power Sources*, 2019, **437**, 226946.
96 J. J. Lee, S. H. Kim and S. H. Jee, *et al.*, Characteristics of Sn/Li_2O multilayer composite anode for thin film micro-battery, *J. Power Sources*, 2008, **178**(1), 434–438.
97 J. Y. Kim, D. E. King and P. N. Kummta, *et al.*, Chemical synthesis of tin oxide-based materials for Li-ion battery anodes: influence of process parameters on the electrochemical behavior, *J. Electrochem. Soc.*, 2000, **147**(12), 4411–4420.
98 J. Liu, Y. Chang and K. Sun, *et al.*, Sheet-like stacking SnS_2/rGO heterostructures as ultrastable anodes for lithium-ion batteries, *ACS Appl. Mater. Interfaces*, 2022, **14**(9), 11739–11749.
99 A. Glibo, N. Eshraghi and Y. Surace, *et al.*, Comparative study of electrochemical properties of SnS and SnS_2 as anode materials in lithium-ion batteries, *Electrochim. Acta*, 2023, **441**, 141725.
100 K. Yin, M. Zhang and Z. D. Hood, *et al.*, Self-assembled framework formed during lithiation of SnS_2 nanoplates revealed by in situ electron microscopy, *Acc. Chem. Res.*, 2017, **50**(7), 1513–1520.
101 S. Guan, X. Fu and B. Zhang, *et al.*, Cation-exchange-assisted formation of NiS/SnS_2 porous nanowalls with ultrahigh energy density for battery–supercapacitor hybrid devices, *J. Mater. Chem. A*, 2020, **8**(6), 3300–3310.
102 M. N. Obrovac and V. L. Chevrier, Alloy negative electrodes for Li-ion batteries, *Chem. Rev.*, 2014, **114**(23), 11444–11502.
103 L. L. Lu, Z. X. Zhu and T. Ma, *et al.*, Superior fast-charging Lithium-ion batteries enabled by the high-speed solid-state lithium transport of an intermetallic Cu_6Sn_5 network, *Adv. Mater.*, 2022, **34**(32), 5502688.
104 H. Kim, Y. J. Kim and D. G. Kim, *et al.*, Mechanochemical synthesis and electrochemical characteristics of Mg_2Sn as an anode material for Li-ion batteries, *Solid State Ionics*, 2001, **144**(1), 41–49.
105 S. Wang, M. He and M. Walter, *et al.*, Monodisperse $CoSn_2$ and $FeSn_2$ nanocrystals as high-performance anode materials for lithium-ion batteries, *Nanoscale*, 2018, **10**(15), 6827–6831.

106 M. Park, D. Lee and H. Jung, *et al.*, Sn-based nanocomposite for Li-ion battery anode with high energy density, rate capability, and reversibility, *ACS Nano*, 2018, **12**(3), 2955–2967.
107 J. Moon, T. D. Hoang and S. Soo Park, *et al.*, Intrinsic electrochemical activity of Ni in Ni_3Sn_4 anode accommodating high capacity and mechanical stability for fast-charging lithium-ion batteries, *J. Energy Chem.*, 2022, **71**, 470–477.
108 H. Lee, S. Jang and S. Lee, *et al.*, Lithium storage properties of nanocrystalline Ni_3Sn_4 alloys prepared by mechanical alloying, *J. Power Sources*, 2002, **112**(1), 8–12.
109 Y. Liu, S. Zhang and T. Zhu, Germanium-based electrode materials for lithium-ion batteries, *ChemElectroChem*, 2014, **1**(4), 706–713.
110 J. Liang, X. Li and Z. Hou, *et al.*, Honeycomb-like macro-germanium as high-capacity anodes for lithium-ion batteries with good cycling and rate performance, *Chem. Mater.*, 2015, **27**(11), 4156–4164.
111 Y. Yan, Y. Liu and Y. Zhang, *et al.*, Improving the cycling stability of three-dimensional nanoporous Ge anode by embedding Ag nanoparticles for high-performance lithium-ion battery, *J. Colloid Interface Sci.*, 2021, **592**, 103–115.
112 X. Liu, X. Wu and B. Chang, *et al.*, Recent progress on germanium-based anodes for lithium ion batteries: efficient lithiation strategies and mechanisms, *Energy Storage Mater.*, 2020, **30**, 146–169.
113 L. Y. Lim, S. Fan and H. H. Hng, *et al.*, Storage capacity and cycling stability in Ge anodes: relationship of anode structure and cycling rate, *Adv. Energy Mater.*, 2015, **5**(15), 1500599.
114 X. Li, C. Shang and R. Wei, *et al.*, GeO_2 crystals embedded germanium phosphate glass with high electrochemical properties as an anode for lithium-ion battery, *J. Am. Ceram. Soc.*, 2024, **107**(5), 2940–2948.
115 S. Haghighat-Shishavan and M. Nazarian-Samani, *et al.*, Exceptionally reversible Li-/Na-ion storage and ultrastable solid-electrolyte interphase in layered GeP_5 anode, *ACS Appl. Mater. Interfaces*, 2019, **11**(36), 32815–32825.
116 S. Dong, L. Wang and X. Huang, *et al.*, Challenges and prospects of phosphorus-based anode materials for secondary batteries, *Batteries Supercaps*, 2023, **6**(12), e202300265.
117 X. Lan, Z. Li and Y. Zeng, *et al.*, Phosphorus-based anodes for fast-charging alkali metal ion batteries, *EcoMat*, 2024, **6**(5), e12452.
118 Z. Shu, X. Y. Cui and B. W. Wang, *et al.*, Fast intercalation of lithium in semi-metallic γ-GeSe nanosheet: a new group-IV monochalcogenide for lithium-ion battery application, *ChemSusChem*, 2022, **15**(15), e202200564.
119 B. Wang, W. C. Du and Y. Yang, *et al.*, Two-dimensional germanium sulfide nanosheets as an ultra-stable and high capacity anode for lithium ion batteries, *Chem. – Eur. J.*, 2020, **26**(29), 6554–6560.
120 A. Avila Cardenas, N. Herlin-Boime and L. Monconduit, *et al.*, Si–Ge alloys as promising anodes for sulfide-based solid-state batteries: role of the powder morphology on performance, *J. Energy Storage*, 2025, **132**, 117912.
121 Y. Subramanian, K. Kaliyappan and K. S. Ramakrishnan, Facile hydrothermal synthesis and characterization of Co_2GeO_4/r-GO@C ternary nanocomposite as negative electrode for Li-ion batteries, *J. Colloid Interface Sci.*, 2017, **498**, 76–84.
122 W. Li, X. Wang and B. Liu, *et al.*, Single-crystalline metal germanate nanowire–carbon textiles as binder-free, self-supported anodes for high-performance lithium storage, *Nanoscale*, 2013, **5**(21), 10291.
123 W. Wei, F. Jia and K. Wang, *et al.*, Synthesis of graphene/$Ca_2Ge_7O_{16}$ nanofibers composite as anode materials for lithium-ion batteries, *Mater. Lett.*, 2017, **196**, 157–160.
124 W. Li, D. Chen and G. Shen, Encapsulating $Ca_2Ge_7O_{16}$ nanowires within graphene sheets as anode materials for lithium-ion batteries, *J. Mater. Chem. A*, 2015, **3**(41), 20673–20680.
125 T. Lv, X. Li and J. Ma, Hydrothermal synthesis of hollow $Ca_2Ge_7O_{16}$ microspheres as high-capacity anodes for Li-ion batteries with long cycling life, *RSC Adv.*, 2014, **4**(91), 49942–49945.
126 J. S. Kim, A. Kim and Y. W. Byeon, *et al.*, Porous Zn_2GeO_4 nanowires with uniform carbon-buffer layer for lithium-ion battery anodes with long cycle life, *Electrochim. Acta*, 2016, **195**, 43–50.
127 G. Cosio-Aguilar, J. R. Rodríguez and C. Belman-Rodríguez, *et al.*, Understanding the Li-Ion storage mechanism of h-Zn_2GeO_4 nanoparticles: experimental and theoretical studies, *Electrochim. Acta*, 2025, **521**, 145850.
128 R. Yi, J. Feng and D. Lv, *et al.*, Amorphous Zn_2GeO_4 nanoparticles as anodes with high reversible capacity and long cycling life for Li-ion batteries, *Nano Energy*, 2013, **2**(4), 498–504.
129 M. V. Reddy, T. Yu and C. H. Sow, *et al.*, Fe_2O_3 nanoflakes as an anode material for Li-ion batteries, *Adv. Funct. Mater.*, 2007, **17**(15), 2792–2799.
130 Y. Kang, M. Song and J. Kim, *et al.*, A study on the charge–discharge mechanism of Co_3O_4 as an anode for the Li ion secondary battery, *Electrochim. Acta*, 2005, **50**(18), 3667–3673.
131 J. Ding, Y. Huang and Z. Liu, *et al.*, $Fe_2Mo_3O_8$/MoO_2@C composites with pseudocapacitive properties and fast diffusion kinetics for the anode of Lithium-Ion batteries, *Chem. Eng. J.*, 2022, **431**, 133984.
132 F. Pu, Y. Bai and J. Lv, *et al.*, Yolk–shell Cu_2O@CuO-decorated RGO for high-performance lithium-ion battery anode, *Energy Environ. Mater.*, 2022, **5**(1), 253–260.
133 Y. Zhu, X. Ji and S. Cheng, *et al.*, Fast energy storage in two-dimensional MoO_2 enabled by uniform oriented tunnels, *ACS Nano*, 2019, **13**(8), 9091–9099.
134 Y. S. Choi, W. Choi and W. Yoon, *et al.*, Unveiling the genesis and effectiveness of negative fading in nanostructured iron oxide anode materials for lithium-ion batteries, *ACS Nano*, 2022, **16**(1), 631–642.
135 F. Wang, X. Qi and L. Mao, *et al.*, Aligned ferric oxide/graphene with strong coupling effect for high-performance anode, *ACS Appl. Energy Mater.*, 2021, **4**(1), 331–340.
136 X. Cheng, Y. Li and H. Shi, *et al.*, Rate-dependent electrochemical reaction mechanism of spinel metal oxide anode studied by in situ TEM, *J. Alloys Compd.*, 2018, **763**, 349–354.

137 E. Muchuweni, E. T. Mombeshora and C. M. Muiva, *et al.*, Lithium-ion batteries: recent progress in improving the cycling and rate performances of transition metal oxide anodes by incorporating graphene-based materials, *J. Energy Storage*, 2023, **73**, 109013.
138 T. Kim, K. H. Kim and H. Kim, *et al.*, New suggestion of highly durable electrode design for ordered mesoporous Ni–Mn binary transition metal oxide anode material in lithium-ion batteries, *Small*, 2024, **21**(5), 2570032.
139 C. Shang, X. Li and R. Wei, *et al.*, Research progress of metal oxide glass anode materials for lithium-ion batteries: a review, *J. Non-Cryst. Solids*, 2023, **618**, 122547.
140 E. Mao, W. Wang and M. Wan, *et al.*, Confining ultrafine Li_3P nanoclusters in porous carbon for high-performance lithium-ion battery anode, *Nano Res.*, 2020, **13**(4), 1122–1126.
141 M. Bichat, T. Politova and H. Pfeiffer, *et al.*, Cu_3P as anode material for lithium ion battery: powder morphology and electrochemical performances, *J. Power Sources*, 2004, **136**(1), 80–87.
142 M. Li, W. Li and Y. Hu, *et al.*, New insights into the high-performance black phosphorus anode for lithium-ion batteries, *Adv. Mater.*, 2021, **33**(35), 2101259.
143 X. Han, H. Gong and H. Li, *et al.*, Fast-charging phosphorus-based anodes: promises, challenges, and pathways for improvement, *Chem. Rev.*, 2024, **124**(11), 6903–6951.
144 J. F. Qian, D. Qiao and X. P. Ai, *et al.*, Reversible 3-Li storage reactions of amorphous phosphorus as high capacity and cycling-stable anodes for Li-ion batteries, *Chem. Commun.*, 2012, **48**(71), 8931–8933.
145 Z. X. Yu, J. X. Song and M. L. Gordin, *et al.*, Phosphorus-graphene nanosheet hybrids as lithium-ion anode with exceptional high-temperature cycling stability, *Adv. Sci.*, 2015, **2**(1–2), 1400020.
146 R. Amine, A. Daali and X. Zhou, *et al.*, A practical phosphorus-based anode material for high-energy lithium-ion batteries, *Nano Energy*, 2020, **74**, 104849.
147 S. Said, Z. Zhang and R. R. C. Shutt, *et al.*, Black phosphorus degradation during intercalation and alloying in batteries, *ACS Nano*, 2023, **17**(7), 6220–6233.
148 H. C. Jin, S. Xin and C. H. Chuang, *et al.*, Black phosphorus composites with engineered interfaces for high-rate high-capacity lithium storage, *Science*, 2020, **370**(6513), 192.
149 H. Tian, J. Wang and G. Lai, *et al.*, Renaissance of elemental phosphorus materials: properties, synthesis, and applications in sustainable energy and environment, *Chem. Soc. Rev.*, 2023, **52**(16), 5388–5484.
150 F. Liberale, M. Fiore and R. Ruffo, *et al.*, Red phosphorus decorated electrospun carbon anodes for high efficiency lithium ion batteries, *Sci. Rep.*, 2020, **10**(1), 13233.
151 J. Wang, J. Zhu and Y. Cai, *et al.*, Multicomponent solid-solution alloy negative electrode for Li-metal batteries, *Nat. Commun.*, 2026, DOI: 10.1038/s41467-026-70301-w.
152 Y. Xing, C. Cao and Z. Huang, *et al.*, A first-principles study of 2D single-layer SiP as anode materials for lithium-ion batteries and sodium-ion batteries, *Phys. Chem. Chem. Phys.*, 2024, **26**(8), 7072–7082.
153 H. Kwon, C. K. Lee and K. Jeon, *et al.*, Silicon diphosphide: a Si-based three-dimensional crystalline framework as a high-performance Li-ion battery anode, *ACS Nano*, 2016, **10**(6), 5701–5709.
154 Y. Kuai, C. Chen and S. Gao, *et al.*, Two-dimensional SiP_3 monolayer as promising anode with record-high capacity and fast diffusion for alkali-ion battery, *Appl. Surf. Sci.*, 2022, **586**, 152510.
155 R. Reinhold, D. Mikhailova and T. Gemming, *et al.*, Silicon monophosphide as a possible lithium battery anode material, *J. Mater. Chem. A*, 2018, **6**(41), 19974–19978.
156 X. N. Li, J. W. Liang and Y. Lu, *et al.*, Sulfur-rich phosphorus sulfide molecules for use in rechargeable lithium batteries, *Angew. Chem., Int. Ed.*, 2017, **56**(11), 2937–2941.
157 K. N. Wood, K. X. Steirer and S. E. Hafner, *et al.*, *Operando* X-ray photoelectron spectroscopy of solid electrolyte interphase formation and evolution in Li_2S-P_2S_5 solid-state electrolytes, *Nat. Commun.*, 2018, **9**(1), 2490.
158 S. Sun, W. Wang and F. Kong, *et al.*, Application and prospective of Sn-P based anodes for alkali-ion batteries, *Energy Storage Mater.*, 2021, **40**, 292–311.
159 H. Shen, Y. Huang and Y. Chang, *et al.*, Narrowing working voltage window to improve layered GeP anode cycling performance for lithium-ion batteries, *ACS Appl. Mater. Interfaces*, 2020, **12**(15), 17466–17473.
160 X. Wang, H. Kim and Y. Xiao, *et al.*, Nanostructured metal phosphide-based materials for electrochemical energy storage, *J. Mater. Chem. A*, 2016, **4**(39), 14915–14931.
161 P. Wu, S. Chen and A. Liu, The influence of contact engineering on silicon-based anode for Li-ion batteries, *Nano Select*, 2021, **2**, 468–491.
162 J. Lee, J. Moon and S. A. Han, *et al.*, Everlasting living and breathing gyroid 3D network in Si@SiOx/C nanoarchitecture for lithium ion battery, *ACS Nano*, 2019, **13**(8), 9607–9619.
163 C. Huang, M. Dontigny and K. Zaghib, *et al.*, Low-tortuosity and graded lithium ion battery cathodes by ice templating, *J. Mater. Chem. A*, 2019, **7**(37), 21421–21431.
164 S. H. Choi, G. Nam and S. Chae, *et al.*, Robust pitch on silicon nanolayer–embedded graphite for suppressing undesirable volume expansion, *Adv. Energy Mater.*, 2019, **9**(4), 1803121.
165 Y. Hsu, C. Hsieh and W. Liu, Synthesis of double core-shell carbon/silicon/graphite composite anode materials for lithium-ion batteries, *Surf. Coat. Technol.*, 2020, **387**, 125528.
166 Q. Pan, P. Zuo and S. Lou, *et al.*, Micro-sized spherical silicon@carbon@graphene prepared by spray drying as anode material for lithium-ion batteries, *J. Alloys Compd.*, 2017, **723**, 434–440.
167 M. Molaei, A. R. Bahador and M. Karimipour, Green synthesis of ZnSe and core–shell ZnSe@ZnS nanocrystals (NCs) using a new, rapid and room temperature photochemical approach, *J. Lumin.*, 2015, **166**, 101–105.
168 K. Min, K. Kim and H. An, *et al.*, Yolk-shell-structured SiO_2@N, P co-doped carbon spheres as highly stable anode materials for lithium ion batteries, *J. Power Sources*, 2022, **543**, 231849.

169 R. Yu, R. Jiang and Z. Zhou, Yolk-shell SiO_2 wrapped by reduced graphene oxide for high performance lithium-ion battery anode, *J. Alloys Compd.*, 2023, **937**, 168324.
170 A. Jamaluddin, B. Umesh and F. Chen, *et al.*, Facile synthesis of core–shell structured Si@graphene balls as a high-performance anode for lithium-ion batteries, *Nanoscale*, 2020, **12**(17), 9616–9627.
171 F. Zhang, X. Yang and Y. Xie, *et al.*, Pyrolytic carbon-coated Si nanoparticles on elastic graphene framework as anode materials for high-performance lithium-ion batteries, *Carbon*, 2015, **82**, 161–167.
172 Y. Park, N. Choi and S. Park, *et al.*, Si-encapsulating hollow carbon electrodes via electroless etching for lithium-ion batteries, *Adv. Energy Mater.*, 2013, **3**(2), 206–212.
173 J. Zhang, K. Wang and Q. Xu, *et al.*, Beyond yolk–shell nanoparticles: Fe_3O_4@Fe_3C core@shell nanoparticles as yolks and carbon nanospindles as shells for efficient lithium ion storage, *ACS Nano*, 2015, **9**(3), 3369–3376.
174 S. Chen, L. Shen and P. A. van Aken, *et al.*, Dual-functionalized double carbon shells coated silicon nanoparticles for high performance lithium-ion batteries, *Adv. Mater.*, 2017, **29**(21), 1605650.
175 X. Hu, X. Liu, K. Chen, G. Wang and H. Wang, Core–shell MOF-derived N-doped yolk–shell carbon nanocages homogenously filled with ZnSe and $CoSe_2$ nanodots as excellent anode materials for lithium- and sodium-ion batteries, *J. Mater. Chem. A*, 2019, **7**(18), 11016–11037.
176 V. Shrivastav, P. Dubey, S. Sundriyal, U. K. Tiwari and A. Deep, Recent advances on core-shell metal-organic frameworks for energy storage applications: controlled assemblies and design strategies, *Coord. Chem. Rev.*, 2024, **499**, 215497.
177 F. Li, G. Luo and J. Yu, *et al.*, Terminal hollowed Fe_2O_3@SnO_2 heterojunction nanorods anode materials with enhanced performance for lithium-ion battery, *J. Alloys Compd.*, 2019, **773**, 778–787.
178 Z. X. Xiao, X. Q. Lin and C. X. Zhang, *et al.*, Insights into the coating integrity and its effect on the electrochemical performance of core-shell structure SiO_x@C composite anodes, *Small Methods*, 2023, **7**(6), 2201623.
179 F. Li, Z. Liu and J. Shen, *et al.*, A nanorod-like Ni-rich layered cathode with enhanced Li^+ diffusion pathways for high-performance lithium-ion batteries, *J. Mater. Chem. A*, 2021, **9**(5), 2830–2839.
180 R. Huang, Y. Li and Y. Song, *et al.*, Facial preparation of N-doped carbon foam supporting Co_3O_4 nanorod arrays as free-standing lithium-ion batteries' anode, *J. Alloys Compd.*, 2020, **818**, 152839.
181 Q. Liu, Z. Cui and R. Zou, *et al.*, Surface coating constraint induced anisotropic swelling of silicon in Si–Void@SiO_x nanowire anode for lithium-ion batteries, *Small*, 2017, **13**(13), 1603754.
182 B. C. Steimle, J. L. Fenton and R. E. Schaak, Rational construction of a scalable heterostructured nanorod megalibrary, *Science*, 2020, **367**(6476), 418–424.
183 Y. Yang, W. Yuan, W. Kang, Y. Ye, Q. Pan, X. Zhang, Y. Ke, C. Wang, Z. Qiu and Y. Tang, A review on silicon-nanowires-based anodes for next-generation high-performance lithium-ion batteries from a material-based perspective, *Sustainable Energy Fuels*, 2020, **4**, 1577–1594.
184 S. Nam, S. Umrao and S. Oh, *et al.*, Sonochemical self-growth of functionalized titanium carbide nanorods on Ti_3C_2 nanosheets for high capacity anode for lithium-ion batteries, *Composites, Part B*, 2020, **181**, 107583.
185 J. Li, L. Han and X. Zhang, *et al.*, Multi-role TiO_2 layer coated carbon@few-layered MoS_2 nanotubes for durable lithium storage, *Chem. Eng. J.*, 2021, **406**, 126873.
186 B. Wang, X. Li and X. Zhang, *et al.*, Contact-engineered and void-involved silicon/carbon nanohybrids as lithium-ion-battery anodes, *Adv. Mater.*, 2013, **25**(26), 3560–3565.
187 F. Du, Y. Ni and Y. Wang, *et al.*, Green fabrication of silkworm cocoon-like silicon-based composite for high-performance Li-ion batteries, *ACS Nano*, 2017, **11**(9), 8628–8635.
188 Q. He, J. Xing and F. Wang, *et al.*, Electrolyte-induced interphase programming for aprotic high-energy lithium metal batteries, *ACS Energy Lett.*, 2026, **11**(2), 1397–1422.
189 H. Zhang, X. Huang and O. Noonan, *et al.*, Tailored yolk–shell Sn@C nanoboxes for high-performance lithium storage, *Adv. Funct. Mater.*, 2017, **27**(8), 1606023.
190 H. Zhang, L. Zhou and O. Noonan, *et al.*, Tailoring the void size of iron oxide@carbon yolk–shell structure for optimized lithium storage, *Adv. Funct. Mater.*, 2014, **24**(27), 4337–4342.
191 S. Du, C. Wu and L. Ao, *et al.*, Significantly enhanced lithium storage by in situ grown CoS_2@MoS_2 core–shell nanorods anchored on carbon cloth, *Chem. Eng. J.*, 2021, **420**, 127714.
192 G. Nava, J. Schwan and M. G. Boebinger, *et al.*, Silicon-core–carbon-shell nanoparticles for lithium-ion batteries: rational comparison between amorphous and graphitic carbon coatings, *Nano Lett.*, 2019, **19**(10), 7236–7245.
193 L. Zhou, Z. Zhuang and H. Zhao, *et al.*, Intricate hollow structures: controlled synthesis and applications in energy storage and conversion, *Adv. Mater.*, 2017, **29**(20), 1602914.
194 Y. Zhang, S. Deng, Y. Shen, B. Liu, G. Pan, Q. Liu, X. Wang, Y. Wang, X. Xia and J. Tu, Construction of 1T-$MoSe_2$@TiC/C branch-core arrays as advanced anodes for enhanced sodium ion storage, *ChemSusChem*, 2020, **16**(13), 1575–1581.
195 T. F. Yi, J. P. Qu and X. Lai, *et al.*, Toward high-performance Li storage anodes: design and construction of spherical carbon-coated $CoNiO_2$ materials, *Mater. Today Chem.*, 2021, **19**, 100407.
196 J. Zheng, Y. Wu and Y. Sun, *et al.*, Advanced anode materials of potassium ion batteries: from zero dimension to three dimensions, *Nano-Micro Lett.*, 2021, **13**, 1.
197 F. Wang, G. Chen and N. Zhang, *et al.*, Engineering of carbon and other protective coating layers for stabilizing silicon anode materials, *Carbon Energy*, 2019, **1**(2), 219–245.
198 Y. Park, Y. Myung and J. Lee, Facile and scalable synthesis of porous Si/SiO_x nanoplates from talc for lithium-ion battery anodes, *ACS Appl. Energy Mater.*, 2020, **3**(9), 8803–8811.

199 R. Purbia and S. Paria, Yolk/shell nanoparticles: classifications, synthesis, properties, and applications, *Nanoscale*, 2015, **7**(47), 19789–19873.
200 H. Su, A. A. Barragan and L. Geng, *et al.*, Colloidal synthesis of silicon–carbon composite material for lithium-ion batteries, *Angew. Chem., Int. Ed.*, 2017, **56**(36), 10780–10785.
201 X. Xia, Y. Wang and D. Wang, *et al.*, Atomic-layer-deposited iron oxide on arrays of metal/carbon spheres and their application for electrocatalysis, *Nano Energy*, 2016, **20**, 244–253.
202 L. Zhang, C. Wang and Y. Dou, *et al.*, A yolk–shell structured silicon anode with superior conductivity and high tap density for full lithium-ion batteries, *Angew. Chem., Int. Ed.*, 2019, **58**(26), 8824–8828.
203 Y. Zeng, H. Zhong and Y. Luo, *et al.*, Interfacial engineering principles for hard carbon anodes in sodium-ion batteries: from mechanisms to synergistic strategies, *Energy Environ. Sci.*, 2026, **19**(6), 1775–1836.
204 C. Kim, S. Choi and S. Yoo, *et al.*, A facile route for growth of CNTs on Si@hard carbon for conductive agent incorporating anodes for lithium-ion batteries, *Nanoscale*, 2015, **7**(26), 11286–11290.
205 T. Kim, Y. H. Mo and K. S. Nahm, *et al.*, Carbon nanotubes (CNTs) as a buffer layer in silicon/CNTs composite electrodes for lithium secondary batteries, *J. Power Sources*, 2006, **162**(2), 1275–1281.
206 Z. Jiang, J. Li and Y. Yang, *et al.*, Machine-learning-revealed statistics of the particle-carbon/binder detachment in lithium-ion battery cathodes, *Nat. Commun.*, 2020, **11**(1), 2310.
207 X. Lu, A. Bertei and D. P. Finegan, *et al.*, 3D microstructure design of lithium-ion battery electrodes assisted by X-ray nano-computed tomography and modelling, *Nat. Commun.*, 2020, **11**(1), 2079.
208 Y. Zhang, C. Zhao and Z. Guo, Simulation of crack behavior of secondary particles in Li-ion battery electrodes during lithiation/de-lithiation cycles, *Int. J. Mech. Sci.*, 2019, **155**, 178–186.
209 X. Jin, B. Javaregowda and J. Sun, *et al.*, Structured for success: conjugated polymer binders with tailored composition and architecture for lithium-ion batteries, *EES Batteries*, 2026, **2**, 112–129.
210 L. Xue, G. Xu and Y. Li, *et al.*, Carbon-coated Si nanoparticles dispersed in carbon nanotube networks as anode material for lithium-ion batteries, *ACS Appl. Mater. Interfaces*, 2013, **5**(1), 21–25.
211 W. Wang and P. N. Kumta, Nanostructured hybrid silicon/carbon nanotube heterostructures: reversible high-capacity lithium-ion anodes, *ACS Nano*, 2010, **4**(4), 2233–2241.
212 C. Xie, N. Xu and P. Shi, *et al.*, Flexible and robust silicon/carbon nanotube anodes exhibiting high areal capacities, *J. Colloid Interface Sci.*, 2022, **625**, 871–878.
213 W. An, B. Xiang and J. Fu, *et al.*, Three-dimensional carbon-coating silicon nanoparticles welded on carbon nanotubes composites for high-stability lithium-ion battery anodes, *Appl. Surf. Sci.*, 2019, **479**, 896–902.
214 S. J. Fan, H. Wang and J. F. Qian, *et al.*, Covalently bonded silicon/carbon nanocomposites as cycle-stable anodes for Li-ion batteries, *ACS Appl. Mater. Interfaces*, 2020, **12**(14), 16411–16416.
215 Z. S. Li, Z. Y. Zhao and S. Y. Pan, *et al.*, Covalent coating of micro-sized silicon with dynamically bonded graphene layers toward stably cycled lithium storage, *Adv. Energy Mater.*, 2023, **13**(28), 2300874.
216 F. Wang, X. Liao and H. Wang, *et al.*, Bioinspired mechanically interlocking holey graphene@SiO_2 anode, *Interdiscip. Mater.*, 2022, **1**(4), 517–525.
217 H. Yang, F. F. Fan and W. T. Liang, *et al.*, A chemo-mechanical model of lithiation in silicon, *J. Mech. Phys. Solids*, 2014, **70**, 349–361.
218 O. B. Tapar, J. Epp and M. Steinbacher, *et al.*, In-situ synchrotron X-ray diffraction investigation of microstructural evolutions during low-pressure carburizing, *Metall. Mater. Trans. A*, 2021, **52**(4), 1427–1442.
219 M. H. Ryou, J. Kim and I. Lee, *et al.*, Mussel-inspired adhesive binders for high-performance silicon nanoparticle anodes in lithium-ion batteries, *Adv. Mater.*, 2013, **25**(11), 1571–1576.
220 M. H. Lee, O. Mukhan and C. T. Mpupuni, *et al.*, The impact of volume expansion on thermodynamic and kinetic properties of graphite/Si alloy composite anodes, *RSC Adv.*, 2025, **15**(56), 47790–47802.
221 M. Matsumoto, Y. Sakka and C. C. Zhong, *et al.*, *Operando* micro- and nano-computed tomography reveals silicon-electrolyte interface dynamics and anisotropic contact loss in all-solid-state batteries, *ACS Nano*, 2025, **19**(41), 36527–36535.
222 X. H. Wu, J. Billaud and I. Jerjen, *et al.*, *Operando* visualization of morphological dynamics in all-solid-state batteries, *Adv. Energy Mater.*, 2019, **9**(34), 1901547.
223 F. Han, W. Li and M. Li, *et al.*, Fabrication of superior-performance SnO_2@C composites for lithium-ion anodes using tubular mesoporous carbon with thin carbon walls and high pore volume, *J. Mater. Chem.*, 2012, **22**(19), 9645–9651.
224 N. Liu, H. Wu and M. T. McDowell, *et al.*, A yolk-shell design for stabilized and scalable Li-ion battery alloy anodes, *Nano Lett.*, 2012, **12**(6), 3315–3321.
225 V. A. Sethuraman, M. J. Chon and M. Shimshak, *et al.*, In situ measurements of stress evolution in silicon thin films during electrochemical lithiation and delithiation, *J. Power Sources*, 2010, **195**(15), 5062–5066.
226 P. Wu, C. Guo and J. Han, *et al.*, Fabrication of double core–shell Si-based anode materials with nanostructure for lithium-ion battery, *RSC Adv.*, 2018, **8**(17), 9094–9102.
227 J. Entwistle, A. Rennie and S. Patwardhan, A review of magnesiothermic reduction of silica to porous silicon for lithium-ion battery applications and beyond, *J. Mater. Chem. A*, 2018, **6**(38), 18344–18356.
228 Y. Jin, S. Li and A. Kushima, *et al.*, Self-healing SEI enables full-cell cycling of a silicon-majority anode with a coulombic efficiency exceeding 99.9%, *Energy Environ. Sci.*, 2017, **10**(2), 580–592.
229 L. J. Yan, H. W. Zhang and Z. H. Li, *et al.*, Millimeter silicon-derived secondary submicron materials as high-

initial coulombic efficiency anode for lithium-ion batteries, *ACS Appl. Energy Mater.*, 2020, **3**(10), 10255–10260.
230 Z. Y. Jiang, C. Li and J. Q. Huang, *et al.*, Engineering SnO_2 decoration on the Si surface of Si/C anode toward enhanced lithium storage, *J. Alloys Compd.*, 2025, **1039**, 183245.
231 S. Q. Cui, S. M. Chen and L. B. Deng, Si nanoparticles encapsulated in CNTs arrays with tubular sandwich structure for high performance Li ion battery, *Ceram. Int.*, 2020, **46**(3), 3242–3249.
232 F. Li, G. Luo and J. Yu, *et al.*, Terminal hollowed Fe_2O_3@SnO_2 heterojunction nanorods anode materials with enhanced performance for lithium-ion battery, *J. Alloys Compd.*, 2019, **773**, 778–787.
233 S. Zhang, S. Chen and Y. Wang, *et al.*, Fabrication of polypyrrole-coated silicon nanoparticle composite electrode for lithium-ion battery, *Ionics*, 2024, **30**(12), 7869–7879.
234 K. Min, K. Kim and H. An, *et al.*, Yolk-shell-structured SiO_2@N, P co-doped carbon spheres as highly stable anode materials for lithium ion batteries, *J. Power Sources*, 2022, **543**, 231849.
235 T. F. Yi, J. P. Qu and X. Lai, *et al.*, Toward high-performance Li storage anodes: design and construction of spherical carbon-coated $CoNiO_2$ materials, *Mater. Today Chem.*, 2021, **19**, 100407.
236 S. H. Choi, G. Nam and S. Chae, *et al.*, Robust pitch on silicon nanolayer-embedded graphite for suppressing undesirable volume expansion, *Adv. Energy Mater.*, 2019, **9**(4), 1803121.
237 F. Z. Pu, Y. L. Bai and J. Lv, *et al.*, Yolk-shell Cu_2O@CuO-decorated RGO for high-performance lithium-ion battery anode, *Energy Environ. Mater.*, 2022, **5**(1), 253–260.
238 K. Z. Li, G. Q. Yuan and X. F. Liu, *et al.*, On the practical applicability of rambutan-like SiOC anode with enhanced reaction kinetics for lithium-ion storage, *Adv. Funct. Mater.*, 2023, **33**(43), 2302348.
239 Z. H. Zhang, W. C. Chen and J. Tian, *et al.*, Two-dimensional nitrogen-doped carbon nanosheets-coated porous SiO composites sponges for durable anode materials of high-energy lithium-ion batteries, *Chem. Eng. J.*, 2025, **518**, 164269.
240 Y. Y. Yu, C. Yang and Y. Jiang, *et al.*, Robust nitrogen/sulfur co-doped carbon frameworks as multifunctional coating layer on Si anodes toward superior lithium storage, *Adv. Energy Mater.*, 2025, **15**(17), 2403086.
241 Q. Y. Wang, M. Zhu and G. R. Chen, *et al.*, High-performance microsized Si anodes for lithium-ion batteries: insights into the polymer configuration conversion mechanism, *Adv. Mater.*, 2022, **34**(16), 2109658.
242 S. Kim, D. Y. Han and G. Song, *et al.*, Resilient binder network with enhanced ionic conductivity for high-areal-capacity Si-based anodes in Lithium-ion batteries, *Chem. Eng. J.*, 2023, **473**, 145441.
243 H. C. Jin, S. Xin and C. H. Chuang, *et al.*, Black phosphorus composites with engineered interfaces for high-rate high-capacity lithium storage, *Science*, 2020, **370**(6513), 192.
244 H. W. Liu, Y. Q. Zou and L. Tao, *et al.*, Sandwiched thin-film anode of chemically bonded black phosphorus/graphene hybrid for lithium-ion battery, *Small*, 2017, **13**(33), 1700758.
245 Z. S. Wu, W. C. Ren and L. Wen, *et al.*, Graphene anchored with Co_3O_4 nanoparticles as an anode of lithium ion batteries with enhanced reversible capacity and cyclic performance, *ACS Nano*, 2010, **4**(6), 3187–3194.
246 G. M. Zhou, D. W. Wang and F. Li, *et al.*, Graphene-wrapped Fe_3O_4 anode material with improved reversible capacity and cyclic stability for lithium ion batteries, *Chem. Mater.*, 2010, **22**(18), 5306–5313.
247 S. Niu, W. Lv and C. Zhang, *et al.*, One-pot self-assembly of graphene/carbon nanotube/sulfur hybrid with three dimensionally interconnected structure for lithium–sulfur batteries, *J. Power Sources*, 2015, **295**, 182–189.
248 F. Wang and J. Mao, Nacre-like graphene oxide/waterborne styrene butadiene rubber composite and its reusable anti-corrosion behavior on Al-2024, *Prog. Org. Coat.*, 2019, **132**, 191–200.
249 E. Antolini, Composite materials: an emerging class of fuel cell catalyst supports, *Appl. Catal., B*, 2010, **100**(3–4), 413–426.
250 M. Gobbi, E. Orgiu and P. Samorì, When 2D materials meet molecules: opportunities and challenges of hybrid organic/inorganic van der Waals heterostructures, *Adv. Mater.*, 2018, **30**(18), 1706103.
251 C. Rest, R. Kandanelli and G. Fernández, Strategies to create hierarchical self-assembled structures via cooperative non-covalent interactions, *Chem. Soc. Rev.*, 2015, **44**, 2543–2572.
252 H. Hashim, M. S. Salleh and M. Z. Omar, Homogenous dispersion and interfacial bonding of carbon nanotube reinforced with aluminum matrix composite: a review, *Rev. Adv. Mater. Sci.*, 2019, **58**, 295–303.
253 Y. Liu, Y. Ma and S. Guang, *et al.*, Facile fabrication of three-dimensional highly ordered structural polyaniline–graphene bulk hybrid materials for high performance supercapacitor electrodes, *J. Mater. Chem. A*, 2014, **2**(3), 813–823.
254 F. Zhong, Y. He and P. Wang, *et al.*, Self-assembled graphene oxide-graphene hybrids for enhancing the corrosion resistance of waterborne epoxy coating, *Appl. Surf. Sci.*, 2019, **488**, 801–812.
255 Y. Ren, L. Xiang and X. Yin, *et al.*, Ultrathin Si nanosheets dispersed in graphene matrix enable stable interface and high rate capability of anode for lithium-ion batteries, *Adv. Funct. Mater.*, 2022, **32**(16), 2110046.
256 X. Tan, T. Liu and W. Zhou, *et al.*, Enhanced electromagnetic shielding and thermal conductive properties of polyolefin composites with a $Ti_3C_2T_x$ MXene/graphene framework connected by a hydrogen-bonded interface, *ACS Nano*, 2022, **16**(6), 9254–9266.
257 H. Wang, Q. Hao and X. Yang, *et al.*, Effect of graphene oxide on the properties of its composite with polyaniline, *ACS Appl. Mater. Interfaces*, 2010, **2**(3), 821–828.
258 C. Martin, A. Martin-Pacheco and A. Naranjo, *et al.*, Graphene hybrid materials? the role of graphene materials in the final structure of hydrogels, *Nanoscale*, 2019, **11**(11), 4822–4830.

259 J. Liu, J. Tang and J. J. Gooding, Strategies for chemical modification of graphene and applications of chemically modified graphene, *J. Mater. Chem.*, 2012, **22**(25), 12435–12452.
260 J. Zhang, L. Jia and H. Lin, *et al.*, Advances and prospects of 2D graphene-based materials/hybrids for lithium metal–sulfur full battery: from intrinsic property to catalysis modification, *Adv. Energy Sustainability Res.*, 2022, **3**(4), 2100187.
261 N. V. Medhekar, A. Ramasubramaniam and R. S. Ruoff, *et al.*, Hydrogen bond networks in graphene oxide composite paper: structure and mechanical properties, *ACS Nano*, 2010, **4**(4), 2300–2306.
262 J. Meng, Y. Cao and Y. Suo, *et al.*, Facile fabrication of 3D SiO_2@graphene aerogel composites as anode material for lithium ion batteries, *Electrochim. Acta*, 2015, **176**, 1001–1009.
263 M. Wang, Y. Niu and J. Zhou, *et al.*, The dispersion and aggregation of graphene oxide in aqueous media, *Nanoscale*, 2016, **8**(30), 14587–14592.
264 L. Svoboda, R. Škuta and V. Matějka, *et al.*, Graphene oxide and graphitic carbon nitride nanocomposites assembled by electrostatic attraction forces: synthesis and characterization, *Mater. Chem. Phys.*, 2019, **228**, 228–236.
265 J. Hong, K. Shin and O. S. Kwon, *et al.*, A strategy for fabricating single layer graphene sheets based on a layer-by-layer self-assembly, *Chem. Commun.*, 2011, **47**(25), 7182.
266 M. Sun, Z. Xu and K. Liu, *et al.*, Construction of rice husk-derived SiO_x nanoparticles encapsulated with graphene aerogel hybrid for high-performance lithium ion batteries, *Electrochim. Acta*, 2022, **422**, 140572.
267 R. Zacharia, H. Ulbricht and T. Hertel, Interlayer cohesive energy of graphite from thermal desorption of polyaromatic hydrocarbons, *Phys. Rev. B:Condens. Matter Mater. Phys.*, 2004, **69**(15), 155406.
268 S. Jun, M. Jeong and B. Jang, *et al.*, Electron-conductive binder for silicon negative electrode enabling low-pressure all-solid-state batteries, *Nat. Commun.*, 2025, **17**(1), 156.
269 M. H. Ryou, J. Kim and I. Lee, *et al.*, Mussel-inspired adhesive binders for high-performance silicon nanoparticle anodes in lithium-ion batteries, *Adv. Mater.*, 2013, **25**(11), 1571–1576.
270 Z. Zhang, C. Lee and W. Zhang, Vertically aligned graphene nanosheet arrays: synthesis, properties and applications in electrochemical energy conversion and storage, *Adv. Energy Mater.*, 2017, **7**(23), 1700678.
271 Z. Jiang, Q. Li and M. Chen, *et al.*, Mechanical reinforcement fibers produced by gel-spinning of poly-acrylic acid (PAA) and graphene oxide (GO) composites, *Nanoscale*, 2013, **5**(14), 6265.
272 J. Su, M. Cao and L. Ren, *et al.*, Fe_3O_4–graphene nanocomposites with improved lithium storage and magnetism properties, *J. Phys. Chem. C*, 2011, **115**(30), 14469–14477.
273 C. Lu, C. Yu and Y. Yeh, Engineering nanocomposite hydrogels using dynamic bonds, *Acta Biomater.*, 2021, **130**, 66–79.
274 C. I. Idumah and C. M. Obele, Understanding interfacial influence on properties of polymer nanocomposites, *Surf. Interfaces*, 2021, **22**, 100879.
275 Y. Liang, W. Zhang and D. Wu, *et al.*, Interface engineering of carbon-based nanocomposites for advanced electrochemical energy storage, *Adv. Mater. Interfaces*, 2018, **5**(14), 1800430.
276 F. Wang, X. Qi and L. Mao, *et al.*, Aligned ferric oxide/graphene with strong coupling effect for high-performance anode, *ACS Appl. Energy Mater.*, 2021, **4**(1), 331–340.
277 P. Chen, N. Zhang and S. Wang, *et al.*, Interfacial engineering of cobalt sulfide/graphene hybrids for highly efficient ammonia electrosynthesis, *Proc. Natl. Acad. Sci. U. S. A.*, 2019, **116**(14), 6635–6640.
278 Q. Li, M. Yuan and Y. Ji, *et al.*, Atomically dispersed Sn incorporated into carbon matrix for stable electrochemical lithium storage, *Chem. Eng. J.*, 2022, **437**, 135340.
279 F. Wang, L. Mao and X. Wei, *et al.*, Reversible lithium ions stored by lithium clusters, *Chem. Eng. J.*, 2022, **450**, 138235.
280 X. Guo, H. Xu and W. Li, *et al.*, Embedding atomically dispersed iron sites in nitrogen-doped carbon frameworks-wrapped silicon suboxide for superior lithium storage, *Adv. Sci.*, 2023, **10**(4), 2206084.
281 X. Lu, E. Owen and W. Du, *et al.*, Unravelling electro-chemo-mechanical processes in graphite/silicon composites for designing nanoporous and microstructured battery electrodes, *Nat. Nanotechnol.*, 2025, **20**, 1656–1666.
282 M. Shi, D. Bao and S. Li, *et al.*, Anchoring PdCu amorphous nanocluster on graphene for electrochemical reduction of N_2 to NH_3 under ambient conditions in aqueous solution, *Adv. Energy Mater.*, 2018, **8**(21), 1800124.
283 J. Peng, R. Shao and S. Huang, *et al.*, An interface-enhanced continuous 2D-carbon network enabling high-performance Si anodes for Li-ion batteries, *J. Mater. Chem. A*, 2022, **10**(43), 23008–23014.
284 Y. Zheng, T. Zhou and C. Zhang, *et al.*, Boosted charge transfer in SnS/SnO_2 heterostructures: toward high rate capability for sodium-ion batteries, *Angew. Chem., Int. Ed.*, 2016, **55**(10), 3408–3413.
285 J. Yao, M. Zhang and X. Ma, *et al.*, Interfacial electronic modulation of CoP-CoO p-p type heterojunction for enhancing oxygen evolution reaction, *J. Colloid Interface Sci.*, 2022, **607**, 1343–1352.
286 S. Fu, Y. Ma and X. Yang, *et al.*, Defect and interface engineering of hexagonal Fe_2O_3/$ZnCo_2O_4$ n-n heterojunction for efficient oxygen evolution reaction, *Appl. Catal., B*, 2023, **333**, 122813.
287 M. Li, S. Zhang and L. Li, *et al.*, Construction of highly active and selective polydopamine modified hollow ZnO/Co_3O_4 p-n heterojunction catalyst for photocatalytic CO_2 reduction, *ACS Sustainable Chem. Eng.*, 2020, **8**(30), 11465–11476.
288 T. Meng, Y. Hao and J. Qin, *et al.*, Interface-engineering-induced electric field effect and atomic disorder in cobalt selenide for high-rate and large-capacity lithium storage, *ACS Sustainable Chem. Eng.*, 2019, **7**(5), 4657–4665.
289 G. Liu, H. Wu and Q. Meng, *et al.*, Role of the anatase/TiO_2(B) heterointerface for ultrastable high-rate lithium and sodium energy storage performance, *Nanoscale Horiz.*, 2020, **5**(1), 150–162.

290 S. Huang, M. Wang and P. Jia, *et al.*, N-graphene motivated SnO_2@SnS_2 heterostructure quantum dots for high performance lithium/sodium storage, *Energy Storage Mater.*, 2019, **20**, 225–233.

291 J. Wu, B. Liu and X. Xia, *et al.*, GaN/graphene heterostructures as promising anode materials for Li-ion batteries, *Surf. Interfaces*, 2023, **42**, 103333.

292 H. Lin, N. Lou and D. Yang, *et al.*, Janus MoSSe/graphene heterostructures: potential anodes for lithium-ion batteries, *J. Alloys Compd.*, 2021, **854**, 157215.

293 T. Meng, B. Li and Q. Wang, *et al.*, Large-scale electric-field confined silicon with optimized charge-transfer kinetics and structural stability for high-rate lithium-ion batteries, *ACS Nano*, 2020, **14**(6), 7066–7076.

294 N. A. Salleh, S. Kheawhom, A. Ashrina and N. Hamid, *et al.*, Electrode polymer binders for supercapacitor applications: a review, *J. Mater. Res. Technol.*, 2023, **23**, 3470–3491.

295 T. Chen, L. Pan and X. Liu, *et al.*, A comparative study on electrochemical performances of the electrodes with different nanocarbon conductive additives for lithium ion batteries, *Mater. Chem. Phys.*, 2013, **142**(1), 345–349.

296 B. Jin, H. Gu and W. Zhang, *et al.*, Effect of different carbon conductive additives on electrochemical properties of $LiFePO_4$-C/Li batteries, *J. Solid State Electrochem.*, 2008, **12**(12), 1549–1554.

297 Y. Huang, Z. Li and S. Jin, *et al.*, Carbon nanohorns/nanotubes: an effective binary conductive additive in the cathode of high energy-density zinc-ion rechargeable batteries, *Carbon*, 2020, **167**, 431–438.

298 P. Ren, M. Torkamanzadeh and X. Zhang, *et al.*, Conductive carbon additives: friend or foe of capacitive deionization with activated carbon?, *Carbon*, 2023, **213**, 118191.

299 Y. Cho, E. Lee and K. S. Lee, *et al.*, CNT ink as an electrode additive for an effective hybrid conductive network in silicon microparticle/graphite anodes, *Electrochim. Acta*, 2023, **447**, 142134.

300 J. Ahn, B. Park and J. Kim, *et al.*, Multifunctional additives for high-energy-density lithium-ion batteries: improved conductive additive/binder networks and enhanced electrochemical properties, *ACS Appl. Mater. Interfaces*, 2021, **13**(17), 19970–19982.

301 F. Su, C. You and Y. He, *et al.*, Flexible and planar graphene conductive additives for lithium-ion batteries, *J. Mater. Chem.*, 2010, **20**(43), 9644.

302 X. Ji, Y. Mu and J. Liang, *et al.*, High yield production of 3D graphene powders by thermal chemical vapor deposition and application as highly efficient conductive additive of lithium ion battery electrodes, *Carbon*, 2021, **176**, 21–30.

303 I. A. Kinloch, J. Suhr and J. Lou, *et al.*, Composites with carbon nanotubes and graphene: an outlook, *Science*, 2018, **362**(6414), 547–553.

304 X. Li, P. Huang and H. Peng, *et al.*, Study on the improvement of rate capability of spinel $Li_4Ti_5O_{12}$ with graphene/carbon nanotubes binary conductive additive, *Int. J. Electrochem. Sci.*, 2014, **9**(11), 6258–6265.

305 S. Komaba, K. Shimomura and N. Yabuuchi, *et al.*, Study on polymer binders for high-capacity SiO negative electrode of Li-ion batteries, *J. Phys. Chem. C*, 2011, **115**(27), 13487–13495.

306 A. Magasinski, B. Zdyrko and I. Kovalenko, *et al.*, Toward efficient binders for Li-ion battery Si-based anodes: polyacrylic acid, *ACS Appl. Mater. Interfaces*, 2010, **2**(11), 3004–3010.

307 S. Jiang, J. Zhou and H. Yang, *et al.*, Ionic liquid fabricated PVDF binder for cathode toward stable and high-rate lithium-ion batteries, *J. Power Sources*, 2025, **633**, 236439.

308 J. S. Bridel, T. Azaïs and M. Morcrette, *et al.*, Key parameters governing the reversibility of Si/carbon/CMC electrodes for Li-ion batteries, *Chem. Mater.*, 2010, **22**(3), 1229–1241.

309 J. H. Park, S. H. Kim and K. H. Ahn, Role of carboxymethyl cellulose binder and its effect on the preparation process of anode slurries for Li-ion batteries, *Colloids Surf., A*, 2023, **664**, 131130.

310 S. Hidayat, T. Cahyono and J. Y. Mindara, *et al.*, The optimization of CMC concentration as graphite binder on the anode of $LiFePO_4$ battery, *IOP Conf. Ser.:Mater. Sci. Eng.*, 2017, **196**(1), 196.

311 L. Qiu, Z. Shao and D. Wang, *et al.*, Carboxymethyl cellulose lithium (CMC-Li) as a novel binder and its electrochemical performance in lithium-ion batteries, *Cellulose*, 2014, **21**(4), 2789–2796.

312 D. Munao, J. W. M. van Erven and M. Valvo, *et al.*, Role of the binder on the failure mechanism of Si nano-composite electrodes for Li-ion batteries, *J. Power Sources*, 2011, **196**(16), 6695–6702.

313 P. Parikh, M. Sina and A. Banerjee, *et al.*, Role of polyacrylic acid (PAA) binder on the solid electrolyte interphase in silicon anodes, *Chem. Mater.*, 2019, **31**(7), 2535–2544.

314 H. Li, L. Wang and Y. Song, *et al.*, Significance of current collectors for high performance conventional lithium-ion batteries: a review, *Adv. Funct. Mater.*, 2023, **33**(49), 2305515.

315 Y. Jiang, F. Guo and Y. Liu, *et al.*, Three-dimensional printing of graphene-based materials for energy storage and conversion, *SusMat*, 2021, **1**(3), 304–323.

316 W. Luo, J. Hayden and S. H. Jang, *et al.*, Highly conductive, light weight, robust, corrosion-resistant, scalable, all-fiber based current collectors for aqueous acidic batteries, *Adv. Energy Mater.*, 2018, **8**(9), 1702615.

317 P. Gorji, M. Ghahramani and M. Haghighi-Yazdi, The electrochemical performance of $LiFePO_4$ electrodes based on polyurethane binder and carbon fiber current collector for lithium-ion batteries, *J. Energy Storage*, 2024, **99**, 113249.

318 X. Wu, S. Chen and D. Liu, *et al.*, Polymer@Cu composite foils with through-hole arrays as lightweight and flexible current collectors for lithium-ion batteries, *J. Energy Storage*, 2023, **74**, 109208.

319 Y. Yue and H. Liang, 3D current collectors for lithium-ion batteries: a topical review, *Small Methods*, 2018, **2**(8), 1800056.

320 S. R. Gowda, A. Leela Mohana Reddy and X. Zhan, *et al.*, 3D nanoporous nanowire current collectors for thin film microbatteries, *Nano Lett.*, 2012, **12**(3), 1198–1202.

321 C. Yang, Y. Yin and S. Zhang, *et al.*, Accommodating lithium into 3D current collectors with a submicron skeleton towards long-life lithium metal anodes, *Nat. Commun.*, 2015, **6**(1), 8058.
322 S. Jin, Y. Jiang and H. Ji, *et al.*, Advanced 3D current collectors for lithium-based batteries, *Adv. Mater.*, 2018, **30**(48), 1802014.
323 M. Li, J. Zhang and Y. Gao, *et al.*, A water-soluble, adhesive and 3D cross-linked polyelectrolyte binder for high-performance lithium–sulfur batteries, *J. Mater. Chem. A*, 2021, **9**(4), 2375–2384.
324 S. Wen, Z. Li and C. Zou, *et al.*, Improved performances of lithium-ion batteries by conductive polymer modified copper current collector, *New J. Chem.*, 2021, **45**(23), 1541–1548.
325 S. Scott, J. Terreblanche and D. L. Thompson, *et al.*, Gelatin and alginate binders for simplified battery recycling, *J. Phys. Chem. C*, 2022, **126**(19), 8489–8498.
326 H. Wang, H. Yang and D. Wang, *et al.*, Designing chemical bonds between active materials and current collectors for packaging a high-performance supercapacitor, *Nanotechnology*, 2019, **31**(10), 105402.
327 L. Ketter, N. Greb and T. Bernges, *et al.*, Using resistor network models to predict the transport properties of solid-state battery composites, *Nat. Commun.*, 2025, **16**(1), 1411.
328 B. W. Li, Z. J. Chen and M. K. Sun, *et al.*, Advances in silicon-based anodes for all-solid-state lithium batteries: material modification and structural design, *J. Energy Storage*, 2025, **135**, 118309.
329 F. Liang, L. Yang and R. Hu, *et al.*, Mechanisms, development, and applications of silicon-based anodes in solid state batteries, *Chem. Sci.*, 2026, **17**(2), 738–771.
330 R. Liu, C. Mi and X. Jiang, *et al.*, Zinc oxide-reinforced silicon anodes for high-performance all-solid-state lithium-ion batteries, *EES Batteries*, 2026, DOI: 10.1039/D5EB00238A.
331 Z. Y. Zhang, X. L. Zhang and Y. Liu, *et al.*, Silicon-based all-solid-state batteries operating free from external pressure, *Nat. Commun.*, 2025, **16**(1), 1013.
332 H. Y. Huo, M. Jiang and Y. Bai, *et al.*, Chemo-mechanical failure mechanisms of the silicon anode in solid-state batteries, *Nat. Mater.*, 2024, **23**(4), 543–551.
333 R. Koerver, W. B. Zhang and L. de Biasi, *et al.*, Chemo-mechanical expansion of lithium electrode materials - on the route to mechanically optimized all-solid-state batteries, *Energy Environ. Sci.*, 2018, **11**(8), 2142–2158.
334 J. M. Yao, Z. X. Yu and J. Ma, *et al.*, Revealing interfacial failure mechanism of silicon based all solid state batteries via cryogenic electron microscopy, *Nat. Commun.*, 2025, **16**(1), 9731.
335 C. Lee, J. Y. Kim and K. Y. Bae, *et al.*, Enhancing electrochemomechanics: how stack pressure regulation affects all-solid-state batteries, *Energy Storage Mater.*, 2024, **66**, 103196.
336 M. J. Wang, R. Choudhury and J. Sakamoto, Characterizing the Li-solid-electrolyte interface dynamics as a function of stack pressure and current density, *Joule*, 2019, **3**(9), 2165–2178.
337 M. Yamamoto, M. Takatsu and R. Okuno, *et al.*, Nanoporous silicon fiber networks in a composite anode for all-solid-state batteries with superior cycling performance, *Sci. Rep.*, 2023, **13**(1), 17051.
338 D. Santhanagopalan, D. Qian and T. McGilvray, *et al.*, Interface limited lithium transport in solid-state batteries, *J. Phys. Chem. Lett.*, 2014, **5**(2), 298–303.
339 Z. Y. Wang, D. Santhanagopalan and W. Zhang, *et al.*, In situ STEM-EELS observation of nanoscale interfacial phenomena in all-solid-state batteries, *Nano Lett.*, 2016, **16**(6), 3760–3767.
340 J. K. Zhang, J. C. Lv and W. Lu, *et al.*, $Li_{10}GeP_2S_{12}$-based solid electrolyte induced by high pressure for all-solid-state batteries: a facile strategy of low-grain-boundary-resistance, *Chem. Eng. J.*, 2024, **487**, 150452.
341 D. D. Wang, X. Y. Wu and Y. P. Ren, *et al.*, A review of interface optimization strategies for solid electrolytes and anode materials, *Nanoscale Adv.*, 2025, **7**(15), 4535–4550.
342 J. M. Yao, Z. X. Yu and J. Ma, *et al.*, Revealing interfacial failure mechanism of silicon based all solid state batteries via cryogenic electron microscopy, *Nat. Commun.*, 2025, **16**(1), 9731.
343 D. L. Nelson, S. E. Sandoval and J. Pyo, *et al.*, Fracture dynamics in silicon anode solid-state batteries, *ACS Energy Lett.*, 2024, **9**(12), 6085–6095.
344 D. Tan, Y. S. Meng and J. Jang, Scaling up high-energy-density sulfidic solid-state batteries: a lab-to-pilot perspective, *Joule*, 2022, **6**(8), 1755–1758.
345 Q. B. Cao, Z. T. Sun and K. Ye, *et al.*, Stacking pressure homogenizes the electrochemical lithiation reaction of silicon anode in solid-state batteries, *Energy Storage Mater.*, 2024, **67**, 103246.
346 D. Tan, Y. T. Chen and H. D. Yang, *et al.*, Carbon-free high-loading silicon anodes enabled by sulfide solid electrolytes, *Science*, 2021, **373**(6562), 1494.
347 S. Jun, M. Jeong and B. Jang, *et al.*, Electron-conductive binder for silicon negative electrode enabling low-pressure all-solid-state batteries, *Nat. Commun.*, 2025, **17**(1), 156.
348 X. Qin, L. Zhao and J. Han, *et al.*, Self-pressure silicon–carbon anodes for low-external-pressure solid-state Li-ion batteries, *ACS Nano*, 2025, **19**(18), 17760–17773.
349 R. Okuno, M. Yamamoto and A. Kato, *et al.*, Microscopic observation of nanoporous Si-Li_3PS_4 interface in composite anodes with stable cyclability, *Electrochem. Commun.*, 2021, **130**, 107100.
350 S. Asano, J. I. Hata and K. Watanabe, *et al.*, Formation processes of a solid electrolyte interphase at a silicon/sulfide electrolyte interface in a model all-solid-state Li-ion battery, *ACS Appl. Mater. Interfaces*, 2024, **16**(6), 7189–7199.
351 J. M. Yao, Z. X. Yu and J. Ma, *et al.*, Revealing interfacial failure mechanism of silicon based all solid state batteries via cryogenic electron microscopy, *Nat. Commun.*, 2025, **16**(1), 9731.
352 T. Famprikis, P. Canepa and J. A. Dawson, *et al.*, Fundamentals of inorganic solid-state electrolytes for batteries, *Nat. Mater.*, 2019, **18**(12), 1278–1291.

353 S. Wen, T. Lei and D. Kr, *et al.*, Interphase formation on lithium solid electrolytes—An in situ approach to study interfacial reactions by photoelectron spectroscopy, *Solid State Ionics*, 2015, **275**, 98–105.
354 H. Y. Huo and J. Jan, Silicon as emerging anode in solid-state batteries, *ACS Energy Lett.*, 2022, **7**(11), 4005–4016.
355 C. H. Wang, Y. Zhao and Q. Sun, *et al.*, Stabilizing interface between $Li_{10}SnP_2S_{12}$ and Li metal by molecular layer deposition, *Nano Energy*, 2018, **53**, 168–174.
356 L. Chen, Z. N. Huang and R. Shahbazian-Yassar, *et al.*, Directly formed alucone on lithium metal for high-performance Li batteries and Li-S batteries with high sulfur mass loading, *ACS Appl. Mater. Interfaces*, 2018, **10**(8), 7043–7051.
357 S. Lee, K. S. Lee and S. Kim, *et al.*, Design of a lithiophilic and electron-blocking interlayer for dendrite-free lithium-metal solid-state batteries, *Sci. Adv.*, 2022, **8**(30), eabq0153.
358 J. W. Cui, L. Zhang and M. Wang, *et al.*, The interface compatibility between solid-state electrolytes and lithium/silicon anodes: challenges, recent progress and perspectives, *J. Energy Storage*, 2024, **101**, 113774.
359 H. Y. Huo, J. Y. Sun and C. Chen, *et al.*, Flexible interfaces between Si anodes and composite electrolytes consisting of poly(propylene carbonates) and garnets for solid-state batteries, *J. Power Sources*, 2018, **383**, 150–156.
360 L. Z. Fan, H. C. He and C. W. Nan, Tailoring inorganic-polymer composites for the mass production of solid-state batteries, *Nat. Rev. Mater.*, 2021, **6**(11), 1003–1019.
361 X. Lu, Y. M. Wang and X. Y. Xu, *et al.*, Polymer-based solid-state electrolytes for high-energy-density lithium-ion batteries - review, *Adv. Energy Mater.*, 2023, **13**, 38.
362 J. Wu, L. Shen and Z. Zhang, *et al.*, All-solid-state lithium batteries with sulfide electrolytes and oxide cathodes, *Electrochem. Energy Rev.*, 2021, **4**(1), 101–135.
363 S. C. Sand, J. Rupp and B. Yildiz, A critical review on Li-ion transport, chemistry and structure of ceramic-polymer composite electrolytes for solid state batteries, *Chem. Soc. Rev.*, 2025, **54**(1), 178–200.
364 K. S. Oh, J. E. Lee and Y. H. Lee, *et al.*, Elucidating ion transport phenomena in sulfide/polymer composite electrolytes for practical solid-state batteries, *Nano-Micro Lett.*, 2023, **15**(1), 179.
365 X. Lan, Z. Li and C. Zhao, *et al.*, Superionic composite electrolytes with continuously perpendicular-aligned pathways for pressure-less all-solid-state lithium batteries, *Nat. Nanotechnol.*, 2026, **11**, 9690.
366 A. M. Li, Z. Y. Wang and T. P. Pollard, *et al.*, High voltage electrolytes for lithium-ion batteries with micro-sized silicon anodes, *Nat. Commun.*, 2024, **15**(1), 1206.
367 Q. Q. Huang, J. X. Song and Y. Gao, *et al.*, Supremely elastic gel polymer electrolyte enables a reliable electrode structure for silicon-based anodes, *Nat. Commun.*, 2019, **10**, 1206.
368 T. Vorauer, J. Schöggl and S. G. Sanadhya, *et al.*, Impact of solid-electrolyte interphase reformation on capacity loss in silicon-based lithium-ion batteries, *Commun. Mater.*, 2023, **4**(1), 44.
369 W. Li, S. Xu and C. Zhong, *et al.*, A LiF-pie-structured interphase for silicon anodes, *Nano-Micro Lett.*, 2025, **17**(1), 322.
370 N. Liu, H. Wu and M. T. McDowell, *et al.*, A yolk-shell design for stabilized and scalable Li-ion battery alloy anodes, *Nano Lett.*, 2012, **12**(6), 3315–3321.
371 L. Yang, H. S. Chen and H. Q. Jiang, *et al.*, Failure mechanisms of 2D silicon film anodes: in situ observations and simulations on crack evolution, *Chem. Commun.*, 2018, **54**(32), 3997–4000.
372 L. Y. Guo, F. F. Huang and M. Z. Cai, *et al.*, Organic-inorganic hybrid SEI induced by a new lithium salt for high-performance metallic lithium anodes, *ACS Appl. Mater. Interfaces*, 2021, **13**(28), 32886–32893.
373 X. Y. Liu, X. J. Zhu and D. Pan, Solutions for the problems of silicon-carbon anode materials for lithium-ion batteries, *R. Soc. Open Sci.*, 2018, **5**(6), 172370.
374 A. P. Wang, S. Kadam and H. Li, *et al.*, Review on modeling of the anode solid electrolyte interphase (SEI) for lithium-ion batteries, *NPJ Comput. Mater.*, 2018, **4**, 15.
375 T. Vorauer, J. Schöggl and S. G. Sanadhya, *et al.*, Impact of solid-electrolyte interphase reformation on capacity loss in silicon-based lithium-ion batteries, *Commun. Mater.*, 2023, **4**(1), 44.
376 S. Alam, M. Ubaidullah and R. K. Sharma, *et al.*, Interface chemistry in solid-state batteries: advances, challenges, and future prospects, *Results Chem.*, 2025, **18**, 102832.
377 Y. F. Zeng, X. S. Li and G. H. Jin, *et al.*, Breaking barriers in silicon-based anodes: multifaceted strategies for high-performance next-generation lithium-ion batteries, *J. Alloys Compd.*, 2025, **1048**, 185224.
378 L. von Kolzenberg, A. Latz and B. Horstmann, Chemo-mechanical model of SEI growth on silicon electrode particles, *Batteries Supercaps*, 2022, **5**(2), e202100216.
379 M. T. McDowell, S. W. Lee and J. T. Harris, *et al.*, In situ TEM of two-phase lithiation of amorphous silicon nanospheres, *Nano Lett.*, 2013, **13**(2), 758–764.
380 V. A. Sethuraman, M. J. Chon and M. Shimshak, *et al.*, In situ measurements of stress evolution in silicon thin films during electrochemical lithiation and delithiation, *J. Power Sources*, 2010, **195**(15), 5062–5066.
381 D. Mazouzi, Z. Karkar and C. R. Hernandez, *et al.*, Critical roles of binders and formulation at multiscales of silicon-based composite electrodes, *J. Power Sources*, 2015, **280**, 533–549.
382 S. Müller, P. Pietsch and B. Brandt, *et al.*, Quantification and modeling of mechanical degradation in lithium-ion batteries based on nanoscale imaging, *Nat. Commun.*, 2018, **9**, 2340.
383 Y. He, L. Jiang and T. W. Chen, *et al.*, Progressive growth of the solid-electrolyte interphase towards the Si anode interior causes capacity fading, *Nat. Nanotechnol.*, 2021, **16**(10), 1113.
384 S. Pal, S. S. Damle and S. H. Patel, *et al.*, Modeling the delamination of amorphous-silicon thin film anode for lithium-ion battery, *J. Power Sources*, 2014, **246**, 149–159.
385 K. Shitaw, Y. Nikodimos and T. Hagos, *et al.*, Failure mechanisms and scalability of anode-free lithium-metal and lithium–sulfur batteries, *Nat. Rev. Clean Technol.*, 2026, **2**, 19–37.

386 Z. S. Jiang, J. Z. Li and Y. Yang, *et al.*, Machine-learning-revealed statistics of the particle-carbon/binder detachment in lithium-ion battery cathodes, *Nat. Commun.*, 2020, **11**(1), 2310.

387 O. von Kessel, A. Avdyli and D. Vrankovic, *et al.*, Swelling, pressure evolution and aging in high-silicon/graphite composite lithium-ion batteries, *J. Power Sources*, 2024, **610**, 234582.

388 F. K. Tareq and S. Rudra, Enhancing the performance of silicon-based anode materials for alkali metal (Li, Na, K) ion battery: a review on advanced strategies, *Mater. Today Commun.*, 2024, **39**, 108653.

389 L. Y. Yang, H. Z. Li and J. Liu, *et al.*, Dual yolk-shell structure of carbon and silica-coated silicon for high-performance lithium-ion batteries, *Sci. Rep.*, 2015, **5**, 10908.

390 J. R. He, C. Das and F. Yang, *et al.*, Crosslinked poly(acrylic acid) enhances adhesion and electrochemical performance of Si anodes in Li-ion batteries, *Electrochim. Acta*, 2022, **411**, 140038.

391 Y. Zhao, P. Stein and Y. Bai, *et al.*, A review on modeling of electro-chemo-mechanics in lithium-ion batteries, *J. Power Sources*, 2019, **413**, 259–283.

392 S. Hao, J. J. Bailey and F. Iacoviello, *et al.*, 3D imaging of lithium protrusions in solid-state lithium batteries using X-ray computed tomography, *Adv. Funct. Mater.*, 2021, **31**(10), 2007564.

393 J. Z. Lee, T. A. Wynn and M. A. Schroeder, *et al.*, Cryogenic focused ion beam characterization of lithium metal anodes, *ACS Energy Lett.*, 2019, **4**(2), 489–493.

394 P. Huang, L. T. Gao and Z. Guo, Electrochemo-mechanical response of all solid-state batteries: finite element simulations supported by image-based 3D reconstruction of X-ray microscopy tomography, *Electrochim. Acta*, 2023, **463**, 142873.

395 H. Duan, C. Wang and R. Yu, *et al.*, In situ constructed 3D lithium anodes for long-cycling all-solid-state batteries, *Adv. Energy Mater.*, 2023, **13**(24), 2300815.

396 H. Iwai, N. Shikazono and T. Matsui, *et al.*, Quantification of SOFC anode microstructure based on dual beam FIB-SEM technique, *J. Power Sources*, 2010, **195**(4), 955–961.

397 C. Zhu, S. Chen and K. Li, *et al.*, Quantitative analysis of the structural evolution in Si anode via multi-scale image reconstruction, *Sci. Bull.*, 2023, **68**(4), 408–416.

398 A. Etiemble, A. Tranchot, T. Douillard, H. Idrissi, E. Maire and L. Roué, Evolution of the 3D microstructure of a Si-based electrode for Li-ion batteries investigated by FIB/SEM tomography, *J. Electrochem. Soc.*, 2016, **8**, A1550–A1559.

399 A. J. Sanchez, E. Kazyak, Y. Chen, J. Lasso and N. P. Dasgupta, Lithium stripping: anisotropic evolution and faceting of pits revealed by *operando* 3D microscopy, *J. Mater. Chem. A*, 2021, **9**, 21013–21023.

400 X. Li, B. Han and X. Yang, *et al.*, Three-dimensional visualization of lithium metal anode via low-dose cryogenic electron microscopy tomography, *iScience*, 2021, **24**(12), 103418.

401 Y. Fei, L. Cong and W. Bryan, *et al.*, Ordering heterogeneity of $[MnO_6]$ octahedra in tunnel-structured MnO_2 and its influence on ion storage, *Joule*, 2019, **3**(2), 471–484.

402 Z. Deng, X. Lin and Z. Huang, *et al.*, Recent progress on advanced imaging techniques for lithium-ion batteries, *Adv. Energy Mater.*, 2021, **11**(2), 2000806.

403 T. Qin, X. Zhao and Y. Sui, *et al.*, Heterointerfaces: unlocking superior capacity and rapid mass transfer dynamics in energy storage electrodes, *Adv. Mater.*, 2024, **36**(32), 2402644.

404 R. Zhu, Z. Wang and X. Hu, *et al.*, Silicon in hollow carbon nanospheres assembled microspheres cross-linked with N-doped carbon fibers toward a binder free, high performance, and flexible anode for lithium-ion batteries, *Adv. Funct. Mater.*, 2021, **31**, 33.

405 J. An, H. Zhang and L. Qi, *et al.*, Self-expanding ion-transport channels on anodes for fast-charging lithium-ion batteries, *Angew. Chem., Int. Ed.*, 2022, **61**(7), e202113313.

406 C. Sun, Y. Wang and H. Gu, *et al.*, Interfacial coupled design of epitaxial graphene@SiC Schottky junction with built-in electric field for high-performance anodes of lithium ion batteries, *Nano Energy*, 2020, **77**, 105092.

407 M. Matsumoto, Y. Sakka and C. C. Zhong, *et al.*, *Operando* micro- and nano-computed tomography reveals silicon-electrolyte interface dynamics and anisotropic contact loss in all-solid-state batteries, *ACS Nano*, 2025, **19**(41), 36527–36535.

408 D. Vidal, C. Leys and B. Mathieu, *et al.*, Si-C/G based anode swelling and porosity evolution in 18650 casing and in pouch cell, *J. Power Sources*, 2021, **514**, 230552.

409 T. Holderle, D. Petz and V. Kochetov, *et al.*, Structural response of silicon-containing graphite anodes on lithium intercalation, *Energy Storage Mater.*, 2025, **75**, 104042.

410 D. P. Finegan, A. Vamvakeros and L. Cao, *et al.*, Spatially resolving lithiation in silicon-graphite composite electrodes via in situ high-energy x-ray diffraction computed tomography, *Nano Lett.*, 2019, **19**(6), 3811–3820.

411 A. Pfrang, A. Kersys and A. Kriston, *et al.*, Deformation from formation until end of life: micro x-ray computed tomography of silicon alloy containing 18650 Li-ion cells, *J. Electrochem. Soc.*, 2023, **170**(3), 030548.

412 R. F. Ziesche, T. Arlt and D. P. Finegan, *et al.*, 4D imaging of lithium-batteries using correlative neutron and X-ray tomography with a virtual unrolling technique, *Nat. Commun.*, 2020, **11**(1), 777.

413 D. Goers, M. Holzapfel and W. Scheifele, *et al.*, In situ neutron radiography of lithium-ion batteries: the gas evolution on graphite electrodes during the charging, *J. Power Sources*, 2004, **130**(1), 221–226.

414 D. P. Finegan, E. Tudisco and M. Scheel, *et al.*, Quantifying bulk electrode strain and material displacement within lithium batteries via high-speed *operando* tomography and digital volume correlation, *Adv. Sci.*, 2016, **3**(3), 1500332.

415 D. S. Eastwood, V. Yufit and J. Gelb, *et al.*, Lithiation-induced dilation mapping in a lithium-ion battery electrode by 3D X-ray microscopy and digital volume correlation, *Adv. Energy Mater.*, 2014, **4**(4), 1300506.

416 P. Blazek, P. Westenberger and S. Erker, *et al.*, Axially and radially inhomogeneous swelling in commercial 18650 Li-ion battery cells, *J. Energy Storage*, 2022, **52**, 104563.

417 Y. Z. Li, Y. B. Li and A. L. Pei, *et al.*, Atomic structure of sensitive battery materials and interfaces revealed by cryo-electron microscopy, *Science*, 2017, **358**(6362), 506–510.
418 X. F. Wang, Y. J. Li and Y. S. Meng, Cryogenic electron microscopy for characterizing and diagnosing batteries, *Joule*, 2018, **2**(11), 2225–2234.
419 S. Xiang, L. Zhu and L. Fu, *et al.*, Cryogenic and in situ characterization techniques for electrode interphase analysis, *eScience*, 2025, **5**(1), 100291.
420 A. Brennhagen, D. Saha and I. C. Berdiell, *et al.*, Mechanical deformations in battery current collectors observed by *operando* X-ray diffraction on Si/graphite anodes, *Chem. Commun.*, 2025, **61**(98), 19485–19488.
421 D. P. Finegan, A. Vamvakeros and L. Cao, *et al.*, Spatially resolving lithiation in silicon-graphite composite electrodes via in situ high-energy X-ray diffraction computed tomography, *Nano Lett.*, 2019, **19**(6), 3811–3820.
422 D. P. Finegan, A. Vamvakeros and C. Tan, *et al.*, Spatial quantification of dynamic inter and intra-particle crystallographic heterogeneities within lithium ion electrodes, *Nat. Commun.*, 2020, **11**(1), 631.
423 J. Swallow, M. W. Fraser and N. Kneusels, *et al.*, Revealing solid electrolyte interphase formation through interface-sensitive *operando* x-ray absorption spectroscopy, *Nat. Commun.*, 2022, **13**(1), 6070.
424 F. Apfelbeck, G. E. Wittmann and M. P. Le Dû, *et al.*, Local crystallization inside the polymer electrolyte for lithium metal batteries observed by *operando* nanofocus WAXS, *Nat. Commun.*, 2025, **16**(1), 8958.
425 R. F. Ziesche, N. Kardjilov and W. Kockelmann, *et al.*, Neutron imaging of lithium batteries, *Joule*, 2022, **6**(1), 35–52.
426 Y. Z. Li, Y. B. Li and A. L. Pei, *et al.*, Atomic structure of sensitive battery materials and interfaces revealed by cryo-electron microscopy, *Science*, 2017, **358**(6362), 506–510.
427 D. P. Finegan, A. Vamvakeros and L. Cao, *et al.*, Spatially resolving lithiation in silicon-graphite composite electrodes via in situ high-energy x-ray diffraction computed tomography, *Nano Lett.*, 2019, **19**(6), 3811–3820.
428 J. Swallow, M. W. Fraser and N. Kneusels, *et al.*, Revealing solid electrolyte interphase formation through interface-sensitive *operando* x-ray absorption spectroscopy, *Nat. Commun.*, 2022, **13**(1), 6070.
429 H. F. Shi, X. Q. Liu and R. Wu, *et al.*, In situ SEM observation of structured Si/C anodes reactions in an ionic-liquid-based lithium-ion battery, *Appl. Sci.*, 2019, **9**(5), 956.
430 L. H. Zhao, M. Feng and C. S. Wu, *et al.*, Imaging the evolution of lithium-solid electrolyte interface using *operando* scanning electron microscopy, *Nat. Commun.*, 2025, **16**(1), 4283.
431 Z. Liu, Y. Chen-Wiegart and J. Wang, *et al.*, Three-phase 3D reconstruction of a $LiCoO_2$ cathode via FIB-SEM tomography, *Microsc. Microanal.*, 2016, **22**(1), 140–148.
432 X. Lu, A. Bertei and D. P. Finegan, *et al.*, 3D microstructure design of lithium-ion battery electrodes assisted by x-ray nano-computed tomography and modelling, *Nat. Commun.*, 2020, **11**(1), 2079.
433 I. Yoon, D. P. Abraham and B. L. Lucht, *et al.*, In situ measurement of solid electrolyte interphase evolution on silicon anodes using atomic force microscopy, *Adv. Energy Mater.*, 2016, **6**(12), 1600099.
434 S. Y. Luchkin, S. A. Lipovskikh and N. S. Katorova, *et al.*, Solid-electrolyte interphase nucleation and growth on carbonaceous negative electrodes for Li-ion batteries visualized with in situ atomic force microscopy, *Sci. Rep.*, 2020, **10**(1), 8550.
435 C. K. Chan, R. Ruffo and S. S. Hong, *et al.*, Surface chemistry and morphology of the solid electrolyte interphase on silicon nanowire lithium-ion battery anodes, *J. Power Sources*, 2009, **189**(2), 1132–1140.
436 Z. V. Zivcová, F. J. Sonia and M. Jindra, *et al.*, Structural and chemical changes in Si nanoparticle-based anodes in lithium-ion batteries during the (de)lithiation processes studied by in situ Raman spectroelectrochemistry, *ACS Appl. Energy Mater.*, 2025, **8**(9), 5729–5737.
437 S. Tardif, E. Pavlenko and L. Quazuguel, *et al.*, *Operando* Raman spectroscopy and synchrotron x-ray diffraction of lithiation/delithiation in silicon nanoparticle anodes, *ACS Nano*, 2017, **11**(11), 11306–11316.
438 Y. Gu, Y. Hu and W. Wang, *et al.*, An in-situ Raman spectroscopic study on the interfacial process of carbonate-based electrolyte on nanostructured silver electrode, *J. Electrochem.*, 2023, **29**(12), 2301261.
439 X. Wang, M. Zhang and J. Alvarado, *et al.*, New insights on the structure of electrochemically deposited lithium metal and its solid electrolyte interphases via cryogenic TEM, *Nano Lett.*, 2017, **17**(12), 7606–7612.
440 X. Lu, A. Bertei and D. P. Finegan, *et al.*, 3D microstructure design of lithium-ion battery electrodes assisted by x-ray nano-computed tomography and modelling, *Nat. Commun.*, 2020, **11**(1), 2079.
441 D. Y. Cheng, T. A. Wynn and X. F. Wang, *et al.*, Unveiling the stable nature of the solid electrolyte interphase between lithium metal and LiPON via cryogenic electron microscopy, *Joule*, 2020, **4**(11), 2484–2500.
442 S. Misra, N. Liu and J. Nelson, *et al.*, In situ x-ray diffraction studies of (de)lithiation mechanism in silicon nanowire anodes, *ACS Nano*, 2012, **6**(6), 5465–5473.
443 U. Boesenberg, D. Sokaras and D. Nordlund, *et al.*, Electronic structure changes upon lithium intercalation into graphite - insights from ex situ and *operando* X-ray Raman spectroscopy, *Carbon*, 2019, **143**, 371–377.
444 S. C. Nagpure, R. G. Downing and B. Bhushan, *et al.*, Neutron depth profiling technique for studying aging in Li-ion batteries, *Electrochim. Acta*, 2011, **56**(13), 4735–4743.
445 E. D. Rus and J. A. Dura, In situ neutron reflectometry study of solid electrolyte interface (SEI) formation on tungsten thin-film electrodes, *ACS Appl. Mater. Interfaces*, 2019, **11**(50), 47553–47563.
446 K. L. Browning, A. S. Westover and J. F. Browning, *et al.*, In situ measurement of buried electrolyte–electrode interfaces

for solid state batteries with nanometer level precision, *ACS Energy Lett.*, 2023, **8**(4), 1985–1991.

447 S. Liao, J. Chen and S. Cui, *et al.*, CoS2 enhanced SnO_2@rGO heterostructure quantum dots for advanced lithium-ion battery anode, *J. Power Sources*, 2023, **553**, 232265.

448 K. Leung, DFT modelling of explicit solid - solid interfaces in batteries: methods and challenges, *Phys. Chem. Chem. Phys.*, 2020, **22**, 10412.

449 S. Wei, Z. Qi and Y. Xia, *et al.*, Monolayer thiol engineered covalent interface toward stable zinc metal anode, *ACS Nano*, 2022, **16**(12), 21152–21162.

450 Y. Qian, Y. Liang and W. Zhang, *et al.*, Thermal polymerization of ion-modified carbon dots into multi-functional LiF-carbon interface for stabilizing SiO anode, *Energy Storage Mater.*, 2023, **63**, 102996.

451 X. He, X. Ji and B. Zhang, *et al.*, Tuning interface lithiophobicity for lithium metal solid-state batteries, *ACS Energy Lett.*, 2022, **7**(1), 131–139.

452 M. Wan, S. Zhao and Z. Zhang, *et al.*, Two-dimensional BeB_2 and MgB_2 as high capacity Dirac anodes for Li-ion batteries: a DFT study, *J. Phys. Chem. C*, 2022, **126**(23), 9642–9651.

453 E. Olsson and Z. H, Atomic-scale design of anode materials for alkali metal (Li/Na/K)-ion batteries: progress and perspectives, *Adv. Energy Mater.*, 2022, **12**, 2200662.

454 H. Huang, D. Xie and J. Zhao, *et al.*, Boosting reversibility and stability of Zn anodes via manipulation of electrolyte structure and interface with addition of trace organic molecules, *Adv. Energy Mater.*, 2022, **12**(38), 2202419.

455 X. Tan, M. Chen and J. Zhang, *et al.*, Decoding electrochemical processes of lithium-ion batteries by classical molecular dynamics simulations, *Adv. Energy Mater.*, 2024, **14**(22), 2400564.

456 X. Wang, M. Chen and S. Li, *et al.*, Inhibiting dendrite growth via regulating the electrified interface for fast-charging lithium metal anode, *ACS Central Sci.*, 2021, **7**(12), 2029–2038.

457 K. Wang, T. Qiu and L. Lin, *et al.*, Interface solvation regulation stabilizing the Zn metal anode in aqueous Zn batteries, *Chem. Sci.*, 2023, **14**(30), 8076–8083.

458 P. Hu, Y. Wu and X. Gao, *et al.*, N/O dual coordination of cobalt single atom for fast kinetics sodium-sulfur batteries, *Rare Met.*, 2025, **44**(1), 288–299.

459 J. Wang, X. Zhang and Y. Qiu, *et al.*, Germanosilicates for selective etherification of biomass-derived furfuryl alcohol, *Appl. Catal., B*, 2025, **365**, 124956.

460 K. Srinivas, Z. Chen and A. Cao, *et al.*, Dual single-atom sites coupled with graphene-encapsulated core-shell, *J. Mater. Chem. A*, 2024, **12**, 28398–28413.

461 L. Zhang and D. Feng, *et al.*, Interlayer and O-vacancy engineering co-boosting fast kinetics and stable, *Chem. Eng. J.*, 2025, **506**, 159920.

462 W. Gao, P. Xiao and G. Henkelman, *et al.*, Interfacial adhesion between graphene and silicon dioxide by density functional theory with van der Waals corrections, *J. Phys. D: Appl. Phys.*, 2014, **47**(25), 255301.

463 J. Sołtys, J. Piechota and P. Strak, *et al.*, Electronic charge transfer contribution in adsorption of silicon at the SiC(0001) surface—A density functional theory (DFT) study, *Appl. Surf. Sci.*, 2017, **393**, 168–179.

464 V. V. Kulish, M. Ng and O. I. Malyi, *et al.*, Improved binding and stability in Si/CNT hybrid nanostructures via interfacial functionalization: a first-principles study, *RSC Adv.*, 2013, **3**(22), 8446–8453.

465 M. Bhati and T. P. Senftle, Identifying adhesion properties at Si/polymer interfaces with ReaxFF, *J. Phys. Chem. C*, 2019, **123**(44), 27036–27047.

466 A. Peguiron, G. Moras and M. Walter, *et al.*, Activation and mechanochemical breaking of C–C bonds initiate wear of diamond (110) surfaces in contact with silica, *Carbon*, 2016, **98**, 474–483.

467 Z. Ao, M. Jiang and Z. Wen, *et al.*, Density functional theory calculations on graphene/α-SiO2(0001) interface, *Nanoscale Res. Lett.*, 2012, **7**(1), 158.

468 S. Adloo, S. Nasresfahani and R. Safaiee, A DFT screening of CH_4 detection by (8,0) single-walled carbon nanotubes decorated with small tin oxide clusters, *Surf. Interfaces*, 2024, **54**, 105123.

469 Q. Lai, Y. Dou and C. Tsui, *et al.*, Atomic Sn clusters engineered electron-deficient carbon nanofibers enable bulk-interface synergy for high-capacity and durable lithium-ion batteries, *Nano Energy*, 2025, **139**, 110987.

470 S. Zhang, C. Liu and H. Wang, *et al.*, A covalent P–C bond stabilizes red phosphorus in an engineered carbon host for high-performance lithium-ion battery anodes, *ACS Nano*, 2021, **15**(2), 3365–3375.

471 Y. B. Ma, K. Wang and Y. N. Xu, *et al.*, Black phosphorus covalent bonded by metallic antimony toward high-energy lithium-ion capacitors, *Adv. Energy Mater.*, 2024, **14**(18), 2304408.

472 F. Wang, X. Qi and L. M. Mao, *et al.*, Aligned ferric oxide/graphene with strong coupling effect for high-performance anode, *ACS Appl. Energy Mater.*, 2021, **4**(1), 331–340.

473 K. C. Wasalathilake, N. Hu and S. Fu, *et al.*, High capacity and mobility in germanium sulfide/graphene (GeS/Gr) van der Waals heterostructure as anode materials for sodium–ion batteries: a first-principles investigation, *Appl. Surf. Sci.*, 2021, **536**, 147779.

474 H. Tang, S. Chowdhury and J. M. Tao, *et al.*, Density functionals combined with van der Waals corrections for graphene adsorbed on layered materials, *Phys. Rev. B*, 2020, **101**(19), 195426.

475 W. Tao, H. Chun and S. Hyun, *et al.*, Design a multiphase interfaced Ge(GeOx)/T-Nb2O5−x/C anode with synergistic high capacity and durability for Li-ion batteries, *Appl. Surf. Sci.*, 2023, **640**, 158424.

476 S. B. Olou'ou Guifo, J. E. Mueller and T. Markus, Molecular dynamics simulations of interfacial lithium–silicon interdiffusion in lithium-ion-battery anodes, *J. Phys. Chem. C*, 2024, **128**(12), 4891–4904.

477 K. S. Yun, S. J. Pai and B. C. Yeo, *et al.*, Simulation protocol for prediction of a solid-electrolyte interphase on the

silicon-based anodes of a lithium-ion battery: ReaxFF reactive force field, *J. Phys. Chem. Lett.*, 2017, **8**(13), 2812–2818.

478 L. F. Zhang, J. Q. Han and H. Wang, *et al.*, Deep potential molecular dynamics: a scalable model with the accuracy of quantum mechanics, *Phys. Rev. Lett.*, 2018, **120**(14), 143001.

479 S. Pan, W. Fang and J. Yan, *et al.*, Multiscale coupled electron–ion transport in semi-solid lithium flow batteries, *Energy Environ. Sci.*, 2025, **18**(12), 5868–5896.

480 X. Zhang, T. Gupta and Z. Wang, *et al.*, A treatment of particle–electrolyte sharp interface fracture in solid-state batteries with multi-field discontinuities, *J. Mech. Phys. Solids*, 2024, **182**, 105490.

481 T. Zhang, M. Kamlah and R. M. McMeeking, Modeling storage particle delamination and electrolyte cracking in cathodes of solid state batteries, *J. Mech. Phys. Solids*, 2024, **185**, 105551.

482 M. Liu, Finite element analysis of lithiation-induced decohesion of a silicon thin film adhesively bonded to a rigid substrate under potentiostatic operation, *Int. J. Solids Struct.*, 2015, **67–68**, 263–271.

483 W. L. Ai, B. Wu and E. Martinez-Paneda, A coupled phase field formulation for modelling fatigue cracking in lithium-ion battery electrode particles, *J. Power Sources*, 2022, **544**, 231805.

484 R. D. Deshpande and D. M. Bernardi, Modeling solid-electrolyte interphase (SEI) fracture: coupled mechanical/chemical degradation of the lithium ion battery, *J. Electrochem. Soc.*, 2017, **164**(2), A461–A474.

485 A. F. Bower, P. R. Guduru and V. A. Sethuraman, A finite strain model of stress, diffusion, plastic flow, and electrochemical reactions in a lithium-ion half-cell, *J. Mech. Phys. Solids*, 2011, **59**(4), 804–828.

486 A. Bagheri, J. Arghavani and R. Naghdabadi, On the effects of hydrostatic stress on Li diffusion kinetics and stresses in spherical active particles of Li-ion battery electrodes, *Mech. Mater.*, 2019, **137**, 103134.

487 S. L. Zhang, Chemomechanical modeling of lithiation-induced failure in high-volume-change electrode materials for lithium ion batteries. NPJ Computational, *Materials*, 2017, **3**, 7.

488 A. R. Akbarzadeh, V. Ozolins and C. Wolverton, First-principles determination of multicomponent hydride phase diagrams: application to the Li-Mg-N-H system, *Adv. Mater.*, 2007, **19**(20), 3233–3239.

489 B. Ransom, A. Ramdas and E. Lomeli, *et al.*, Electrolyte coatings for high adhesion interfaces in solid-state batteries from first principles, *ACS Appl. Mater. Interfaces*, 2023, **15**(37), 44394–44403.

490 M. Aykol, S. Kim and V. I. Hegde, *et al.*, High-throughput computational design of cathode coatings for Li-ion batteries, *Nat. Commun.*, 2016, **7**, 13779.

491 L. Y. Shen, Z. L. Wang and S. J. Xu, *et al.*, Harnessing database-supported high-throughput screening for the design of stable interlayers in halide-based all-solid-state batteries, *Nat. Commun.*, 2025, **16**(1), 3687.

492 H. Jung, M. Lee and B. C. Yeo, *et al.*, Atomistic observation of the lithiation and delithiation behaviors of silicon nanowires using reactive molecular dynamics simulations, *J. Phys. Chem. C*, 2015, **119**(7), 3447–3455.

493 J. Q. Gao, G. Wang and K. H. Luo, Formation of solid electrolyte interphase in Li-ion batteries: insights from temperature-accelerated ReaxFF molecular dynamics, *Appl. Energy*, 2024, **371**, 123708.

494 W. Shin and K. Min, Machine learning interatomic potential enables interface-level insights into cathode/solid electrolyte adhesion in sodium-ion batteries, *J. Energy Storage*, 2026, **154**, 121104.

495 Z. J. Sun, X. Li and Y. M. Wu, *et al.*, Machine learning-assisted simulations and predictions for battery interfaces, *Adv. Intell. Syst.*, 2025, **7**(6), 2400626.

496 M. Duquesnoy, C. Y. Liu and D. Z. Dominguez, *et al.*, Machine learning-assisted multi-objective optimization of battery manufacturing from synthetic data generated by physics-based simulations, *Energy Storage Mater.*, 2023, **56**, 50–61.

497 G. Tom, S. P. Schmid and S. G. Baird, *et al.*, Self-driving laboratories for chemistry and materials science, *Chem. Rev.*, 2024, **124**(16), 9633–9732.

498 Z. L. Wang, W. G. Zeier and F. Q. You, Toward AI ecosystems for electrolyte and interface engineering in solid-state batteries, *Sci. Adv.*, 2025, **11**(48), eaea0638.

499 Y. H. Xiao, L. J. Miara and Y. Wang, *et al.*, Computational screening of cathode coatings for solid-state batteries, *Joule*, 2019, **3**(5), 1252–1275.

500 Y. H. Xiao, L. J. Miara and Y. Wang, *et al.*, Computational screening of cathode coatings for solid-state batteries, *Joule*, 2019, **3**(5), 1252–1275.

501 Z. S. Jiang, J. Z. Li and Y. Yang, *et al.*, Machine-learning-revealed statistics of the particle-carbon/binder detachment in lithium-ion battery cathodes, *Nat. Commun.*, 2020, **11**(1), 2310.

502 Y. H. Xiao, L. J. Miara and Y. Wang, *et al.*, Computational screening of cathode coatings for solid-state batteries, *Joule*, 2019, **3**(5), 1252–1275.

503 H. Y. Huo, M. Jiang and Y. Bai, *et al.*, Chemo-mechanical failure mechanisms of the silicon anode in solid-state batteries, *Nat. Mater.*, 2024, **23**(4), 543–551.

504 A. Bhowmik, M. Berecibar and M. Casas-Cabanas, *et al.*, Implications of the BATTERY 2030+ AI-assisted toolkit on future low-TRL battery discoveries and chemistries, *Adv. Energy Mater.*, 2022, **12**(17), 2102698.

505 Y. H. Xiao, Y. Wang and S. H. Bo, *et al.*, Understanding interface stability in solid-state batteries, *Nat. Rev. Mater.*, 2020, **5**(2), 105–126.

506 Y. H. Xiao, L. J. Miara and Y. Wang, *et al.*, Computational screening of cathode coatings for solid-state batteries, *Joule*, 2019, **3**(5), 1252–1275.

507 M. Aykol, S. Kim and V. I. Hegde, *et al.*, High-throughput computational design of cathode coatings for Li-ion batteries, *Nat. Commun.*, 2016, **7**, 13779.

508 B. Ransom, A. Ramdas and E. Lomeli, *et al.*, Electrolyte coatings for high adhesion interfaces in solid-state batteries from first principles, *ACS Appl. Mater. Interfaces*, 2023, **15**(37), 44394–44403.

509 A. Dave, J. Mitchell and S. Burke, *et al.*, Autonomous optimization of non-aqueous Li-ion battery electrolytes via robotic experimentation and machine learning coupling, *Nat. Commun.*, 2022, **13**(1), 5454.

510 A. G. Kusne, H. S. Yu and C. M. Wu, *et al.*, On-the-fly closed-loop materials discovery via Bayesian active learning, *Nat. Commun.*, 2020, **11**(1), 5966.

511 L. Y. Chen and Y. P. Li, Uncertainty quantification with graph neural networks for efficient molecular design, *Nat. Commun.*, 2025, **16**(1), 3262.

512 M. Kulichenko, K. Barros and N. Lubbers, *et al.*, Uncertainty-driven dynamics for active learning of interatomic potentials, *Nat. Comput. Sci.*, 2023, **3**(3), 230.

513 T. Qin, H. Yang and Q. Li, *et al.*, Design of functional binders for high-specific-energy lithium-ion batteries: from molecular structure to electrode properties, *Ind. Chem. Mater.*, 2024, **2**(2), 191–225.

514 J. S. Chen, M. Asachi and A. Hassanpour, *et al.*, Modelling of lithium-ion battery electrode calendering: a critical review, *J. Energy Storage*, 2025, **123**, 116702.

515 G. X. Lu, Z. Y. Han and L. Shi, *et al.*, Decoding single-crystal lithium growth through solid electrolyte interphase omics, *Nat. Commun.*, 2025, **16**(1), 9323.

516 D. Micieli, T. Minniti and L. M. Evans, *et al.*, Accelerating neutron tomography experiments through artificial neural network based reconstruction, *Sci. Rep.*, 2019, **9**(1), 2450.

517 I. Z. Borshon, V. Jabbari and T. A. Kingston, *et al.*, Deep learning analysis of solid-electrolyte interphase microstructures in lithium-ion batteries, *Adv. Mater. Interfaces*, 2025, **12**(21), e00558.

518 C. Leau, Y. Wang and C. Gervillié-Mouravieff, *et al.*, Tracking solid electrolyte interphase dynamics using *operando* fibre-optic infra-red spectroscopy and multivariate curve regression, *Nat. Commun.*, 2025, **16**(1), 757.

519 M. Duquesnoy, C. Y. Liu and D. Z. Dominguez, *et al.*, Machine learning-assisted multi-objective optimization of battery manufacturing from synthetic data generated by physics-based simulations, *Energy Storage Mater.*, 2023, **56**, 50–61.

520 T. Lookman, P. V. Balachandran and D. Z. Xue, *et al.*, Active learning in materials science with emphasis on adaptive sampling using uncertainties for targeted design, *NPJ Comput. Mater.*, 2019, **5**, 21.

521 R. van Gorp, M. van der Heijden and M. A. Sadeghi, *et al.*, Bottom-up design of porous electrodes by combining a genetic algorithm and a pore network model, *Chem. Eng. J.*, 2023, **455**, 139947.

522 J. P. Pender, G. Jha and D. H. Youn, *et al.*, Electrode degradation in lithium-ion batteries, *ACS Nano*, 2020, **14**(2), 1243–1295.

523 Y. Jin, S. Li and A. Kushima, *et al.*, Self-healing SEI enables full-cell cycling of a silicon-majority anode with a coulombic efficiency exceeding 99.9%, *Energy Environ. Sci.*, 2017, **10**(2), 580–592.

524 M. Li, X. Hou and Y. Sha, *et al.*, Facile spray-drying/pyrolysis synthesis of core–shell structure graphite/silicon-porous carbon composite as a superior anode for Li-ion batteries, *J. Power Sources*, 2014, **248**, 721–728.

525 E. S. Polsen, D. Q. McNerny and B. Viswanath, *et al.*, High-speed roll-to-roll manufacturing of graphene using a concentric tube CVD reactor, *Sci. Rep.*, 2015, **5**, 10257.

526 Q. Ma, J. K. Qu and X. Chen, *et al.*, Converting micro-sized kerf-loss silicon waste to high-performance hollow-structured silicon/carbon composite anodes for lithium-ion batteries, *Sustainable Energy Fuels*, 2020, **4**(9), 4780–4788.

